Image-guided High Intensity Focused Ultrasound Treatment for Uterine Leiomyomata

Arthur Ho-Yin Chan

A dissertation submitted in partial fulfillment of the
requirements for the degree of

Doctor of Philosophy

University of Washington

2003

Program Authorized to Offer Degree: Department of Bioengineering

UMI Number: 3090974

ProQuest Information and Learning Company
300 North Zeeb Road
P.O. Box 1346
Ann Arbor, MI 48106-1346

In presenting this dissertation in partial fulfillment of the requirements for the Doctoral degree at the University of Washington, I agree that the Library shall make its copies freely available for inspection. I further agree that extensive copying of the dissertation is allowable only for scholarly purposes, consistent with "fair use" as prescribed in the U.S. Copyright Law. Requests for copying or reproduction of this dissertation may be referred to Proquest Information and Learning, 300 North Zeeb Road, Ann Arbor, MI 48106-1346, to whom the author has granted "the right to reproduce and sell (a) copies of the manuscript in microform and/or (b) printed copies of the manuscript made from microform."

Signature 

Date 28 May 2003

University of Washington
Graduate School

This is to certify that I have examined this copy of a doctoral dissertation by

Arthur Ho-Yin Chan

And have found that it is complete and satisfactory in all respects,
and that any and all revisions required by the final
examining committee have been made.

Chair of Supervisory Committee:

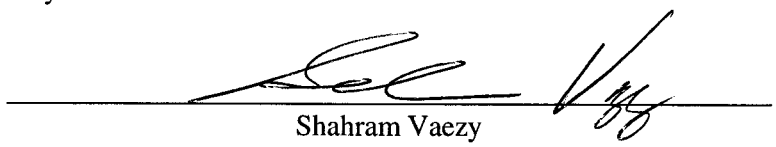

Shahram Vaezy

Reading Committee:

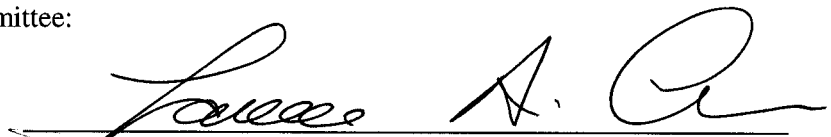

Lawrence A. Crum

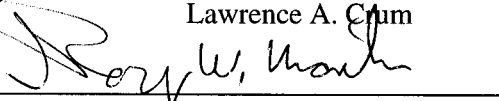

Roy W. Martin

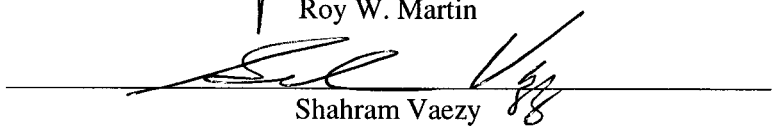

Shahram Vaezy

Date: May 16 2003

University of Washington

Abstract

Image-guided High Intensity Focused Ultrasound Treatment for Uterine Leiomyomata

Arthur Ho-Yin Chan

Chair of the Supervisory Committee:

Shahram Vaezy
Research Assistant Professor
Department of Bioengineering

High Intensity Focused Ultrasound, or HIFU, is capable of treating tissue deep in the body without the need for surgery. With this premise, an ultrasound image-guided HIFU device has been developed for treating submucosal uterine fibroids, which are benign tumors common in women of reproductive age. Fibroids may cause bleeding, discomfort, and lead to infertility, and is the largest indication for hysterectomy. HIFU treatment has the potential for women to retain their uterus while suppressing symptomatic fibroids.

The device was designed based on the female anatomy. It consisted of a commercially available abdominal image probe and a transvaginal HIFU transducer operating at 4.0 MHz. A piezoelectric crystal affixed to an aluminum lens focused ultrasound energy at a fixed distance of 4 cm from the transducer. A graphite embedded epoxy matching layer placed in front of the lens increased the transducer efficiency by approximately 6%. The HIFU transducer was mechanically aligned to the image probe such that the HIFU focus was in the image plane allowing image-guided therapy. A latex condom filled with circulated water covered the transducer providing a sterile covering, acoustic coupling, and transducer cooling. A targeting system using position sensors mounted on the device was used to track the location of the HIFU focus relative to the ultrasound image. Computer software tracked the HIFU focus location and superimposed a visual target on the ultrasound image based on the data acquired by the position sensors.

The device was characterized using acoustic measurement techniques of hydrophone field mapping and radiation force balance. Image-guided therapy was then performed in vitro in a tissue-mimicking phantom and in turkey breast tissue. Treated regions, or lesions, were created at the intended location, and appeared in the ultrasound image as hyperechoic spots above a specific intensity threshold. An ergonomic study without treatment, using human volunteers, was performed. The HIFU transducer, uterus, and pelvic structures were visualized in the ultrasound image. There was no patient discomfort when the device was placed in situ.

The device was used to create lesions in vivo in sheep uterus. Gross and microscopic analysis was performed for 4 different time periods post-treatment. A full bladder and adequate transducer cooling were needed for a successful treatment. During treatment, lesions were visible as hyperechoic spots at HIFU intensities above 2200 W/cm^2. HIFU treated areas were coagulative necrosis lesions consisting of a necrotic center surrounded by a ring of blood congestion. Over a period of 30 days, necrotic tissue was phagocytosed by macrophages, ablated myometrium was partially regenerated, and scar tissue formed in the treated area.

Image-guided HIFU has the potential to become a minimally-invasive treatment option for women with symptomatic uterine fibroids.

TABLE OF CONTENTS

LIST OF FIGURES

LIST OF TABLES

Acknowledgements

I would like to thank the Whitaker Foundation and the Natural Sciences and Engineering Research Council (NSERC) of Canada for their generous funding in support of the work presented in this dissertation. This four year journey through graduate school has brought me in contact with many wonderful people who have contributed immensely to my personal development as a scientist and engineer, and to the development of image-guided HIFU therapy.

First, I am grateful to my committee members. Foremost, my advisor, mentor and friend Shahram Vaezy whose enthusiasm towards my education since the day I stepped into his laboratory has allowed me to excel and be passionate about this project. I am honored to have had Shahram as a role model and be his first Ph.D. student. Next, I would like to thank Larry Crum, who continually encouraged me to pursue my research and career goals. His words of wisdom contributed immensely to my success. Thanks to Roy Martin, who was first to teach me about the basics of ultrasound and how to build a transducer, and whose humor and laughter made our lab a fun place to work. Finally, I am thankful to Peter Kaczkowski, a fellow Canadian who has provided me with vast technical advice. Peter's perfectionist attitude, ethics, and meticulousness were exemplary characteristics that I was proud to adopt in my daily work.

I would like to thank my collaborators at the Center for Industrial and Medical Ultrasound (CIMU) and Applied Physics Laboratory at the University of Washington: our sonographer, Marla Paun, who made sure every ultrasound image during our sheep treatments and human ergonomic studies came out perfect; animal technician Rusty Starr who the animals seemed to understand and who made the sheep experiments a success; mechanical technicians Andrew Proctor and Francis Olson, who were instrumental in helping with the design and construction of the device; electronic technician Terry Myntti who guided me through fixing everything with wires; Mike Bailey, Wen Chen, Bryan Cunitz and Cyril Lafon for their assistance in ultrasound characterization methods and forgiving me for rendering a hydrophone inoperable; Emil Chi for his expertise in looking at histology images; and Lori Ferro, Dorothy Lowell and Marilee Andrew for their administrative support.

I am grateful for the involvement of our two Ob/Gyns who I considered as thought leaders in the field: Dr. Donald Moore and Dr. Victor Fujimoto, provided valuable suggestions from a physician's perspective and assisted in the ergonomic and in vivo studies. They have also been great advocates and promoted our device and treatment to their peers and to the public.

I had the honor of mentoring two outstanding Bioengineering undergraduate students who contributed greatly to this project. Grace Huynh assisted in transducer temperature measurements and acoustic characterization of materials and Robert Held aided in the development of the targeting system. My colleagues in the Vaezy lab have contributed tremendously to my experiments and providing me with assistance. I would especially like to thank Vesna Zderic, a commendable graduate student whose dedication and willingness to help should be recognized. Also, I would like to thank Jonathan Yuen, a great friend and a real smart guy who is a great problem solver, and Joo Ha Hwang, for his medical advice and expertise.

There are many wonderful friends of mine who devoted their time and energy into providing valuable feedback and moral support to my work, especially Jeff Anderl, Janet Cuy, Jennifer Flexman, Misty Noble, Brian Rabkin, and Annabel Tsai. Finally, I would like to thank my parents Raymond and Philomena, my sister Alma, my parents in law Lauren and Susan Brown, and my loving wife Lisa for believing in me since day one, and for supporting my ambitions and dreams.

Dedication

This dissertation is dedicated to my family,
especially my parents Raymond and Philomena Chan.

This dissertation is also dedicated to those who are suffering from uterine fibroids and other HIFU treatable conditions, and to those whose creative endeavors will further research in therapeutic ultrasound.

1.0 CHAPTER 1 INTRODUCTION AND MOTIVATION

1.1 MOTIVATION

Uterine leiomyomata, or fibroids, are the most common pelvic tumor among women of reproductive age. These benign tumors are present in 75% of the world's female population and are symptomatic in approximately one-third of all cases. Fibroids may be associated with menstrual problems, pressure induced pain, and reproductive problems such as infertility and miscarriage. Although the significance is great, there has yet to be a truly desirable treatment for eliminating fibroids. Fibroids are the most common indication for hysterectomy (the complete removal of the uterus). Although this is a permanent solution, many women elect more conservative fibroids management options in order to potentially be able to bear children and avoid surgical complications. Unfortunately, these alternatives to hysterectomy often result in recurrence of the fibroids and may result in surgical complications. Women are usually restricted in their everyday activities for 2-4 weeks after current fibroids treatment methods due to pain, immobility and possible bleeding, and the recurrence of fibroids means their quality of life may not be better even after treatment.

In this dissertation project, the goal was to investigate the potential for using an image-guided high intensity focused ultrasound (HIFU) device to treat fibroids and, in general, anomalies and tumors in the uterus. A previous study in our laboratory had proven that HIFU treated fibroids in nude mice had shrunk and did not recur. We believe that an ergonomic device can be developed that will be able to accurately treat fibroids in the uterus in a minimally-invasive manner. This device and method for treatment would have the potential in the near future to be a desired alternative to hysterectomy for women suffering from symptomatic uterine fibroids and other uterine and pelvic anomalies.

1.2 A DEVICE FOR MINIMALLY INVASIVE THERAPY

An aspiration in the field of medicine has been to provide patients with therapy that is non-invasive. With such therapies, infections and blood loss would be minimized, surgery time shortened, and procedures done on an outpatient basis. The results would be a reduction in recovery time and reduced health care costs. In reaching the eventual goal of non-invasive therapy, minimally invasive procedures are being explored, which may not be completely non-invasive when first introduced, but are a much less invasive option than currently available treatments.

The vision of developing minimally invasive procedures has become reality due to the advances in medical device technology of the past two decades. Laparoscopic surgery, where miniature surgical apparatus are positioned within the body using tubes inserted via small abdominal incisions, has become common practice. Radiofrequency tissue ablation, endoscopic neurological surgery, laser vision treatments, brachytherapy for prostate cancer, and the modality explored in this thesis: high intensity focused ultrasound (HIFU), are just a few of the many other forms of minimally invasive surgery currently available or under investigation. These techniques are being rapidly developed due to physician and patient interest and demand.

What is common amongst forms of minimally-invasive surgery is that some method of image-guidance is utilized. Millimeter-sized high-resolution video cameras, magnetic resonance imaging (MRI), and ultrasound are examples of techniques used for providing image-guided therapy.

The device presented in this dissertation will explore the use of ultrasound image-guided HIFU for treating uterine fibroids. The device has the potential to allow a physician to visualize, target and ablate a fibroid in real-time.

1.3 PRINCIPAL GOALS

The intentions of this research are to advance the understanding of image-guided HIFU treatment, promote the use of therapeutic ultrasound as a method of minimally-invasive therapy, and apply it to a real-world application. The end-goal for this dissertation is to perform *in vivo* HIFU uterus treatment in a simulated clinical setting using a large animal model. The principal goals of this dissertation are as follows:

First, an ultrasound image-guided HIFU device for treating uterine fibroids will be designed. The various ergonomic and ultrasound parameters chosen for the device will be explored and justified. A method for constructing such a device will be presented.

Second, characterize this device will be characterized using known acoustic measurement techniques and test this device using a gel phantom and in tissue *in vitro*. The device will also be tested for ergonomics in humans. Based on these initial tests, modifications will be recommended, and a second iteration of the device will be built.

Third, in order for this device to be safe and efficacious, a targeting system will be developed that uses computer monitoring of position sensors to determine where the HIFU treatment will occur. Testing of this targeting system and error analysis will be performed.

Fourth, the safety and efficacy of this device *in vivo* will be explored. The device will be tested in a sheep animal model. A qualitative and quantitative analysis of the lesions formed will be presented. This *in vivo* study also involves the survival of animals and the changes in the treated regions will be investigated over a period of 30 days.

Fifth, an analysis of lesion visibility in the ultrasound image will be presented. In the course of this investigation, many HIFU lesions will be created in various media. These lesions will be characterized based on their shape and size, and whether or not they were visible in the ultrasound image.

Finally, insight will be provided for use of this device in humans. The next logical step for continuation of this dissertation is the treatment of humans using image-guided HIFU. Proposed methods for human treatments, clinical concerns, and future work will be presented.

1.4 HYPOTHESES AND SPECIFIC AIMS

To pursue the objectives listed in section 1.3, several hypotheses were formulated and tested as specific aims, listed in Table 1.1.

Table 1.1 Hypotheses and specific aims for this dissertation

Hypothesis	Specific aim
A transvaginal HIFU transducer can be integrated with a commercially available abdominal ultrasound image probe to provide image-guided HIFU treatment.	Design a novel HIFU transducer and integrate it with a SonoSite abdominal image probe in an ergonomic hand-held device. Evaluate treatment repeatability, reliability, and image-guidance of the device *in vitro*
The device will be ergonomically suitable for human use and be able to potentially treat various locations of the human uterus with ultrasound image-guidance.	Test device ergonomics *in vivo*. Test the feasibility of using a water-filled acoustically transparent membrane for acoustic coupling, varying the treatment location, and transducer cooling during treatment. Test its functionality *in vitro and in vivo*.
The location of the treatment can be accurately targeted prior to the onset of HIFU	Develop a computer controlled targeting system to provided treatment targeting, guidance, and visualization of treated regions. The computer software would also control the HIFU treatment parameters.
The device can be used to perform image-guided HIFU treatment of the uterus *in vivo*	Determine the feasibility of using sheep as an animal model. Develop a protocol for treatment, and perform a safety, efficacy and survival study *in vivo* in sheep.

1.5 SIGNIFICANCE AND IMPACT OF THIS PROJECT

The overall significance of this project can be summarized as follows:

First, the device presented in this dissertation demonstrates the feasibility of an intracavitary HIFU transducer guided by external diagnostic ultrasound. The device reveals the simplicity and effectiveness of such a device whereby a commercially available image probe is mechanically aligned with a HIFU transducer. The device shows the potential for ultrasound image-guided HIFU as a clinically accepted form of minimally-invasive therapy.

Next, this dissertation provides an insight on the potential for using HIFU as a minimally-invasive treatment for uterine fibroids and other uterine anomalies. With accurate visualization, targeting, and localized treatment, this device demonstrates the safety and efficacy of *in vivo* uterus treatment. Besides uterine fibroids, this device may be useful for ovarian cancer and cysts, endometriosis, uterine artery treatment, and endometrial polyps.

The work presented in this dissertation may allow physicians and patients to realize that image-guided HIFU may be a safe and promising minimally-invasive treatment alternative to surgery and drug and hormone therapy.

1.6 ORGANIZATION OF THE DISSERTATION

The dissertation is divided into eleven chapters following this introduction.

Chapter 2 explores high intensity focused ultrasound (HIFU) and principles of acoustics applicable to image-guided HIFU therapy, along with HIFU device design considerations.

Chapter 3 discusses uterine leiomyoma. Their significance, epidemiology, symptoms, and current treatments will be explored.

Chapter 4 introduces the first version of the image-guided HIFU device for uterine fibroids. Optimized parameters, transducer modeling, and construction methods will be discussed. A characterization of the HIFU transducer using known ultrasound testing methods is presented. The use of an acoustically transparent membrane for acoustic coupling, treatment stand-off (separation between the HIFU transducer and the tissue to be treated) and cooling will be explored.

Chapter 5 presents *in vitro* test results using the first version of the device. Image-guided therapy in a gel phantom and in turkey breast tissue will be described. Results from the *in vivo* ergonomics study will also be discussed in this chapter.

Chapter 6 examines device improvements deemed necessary after the characterization and *in vitro* testing of the first version of the device. The design, construction, characterization and initial testing of a second generation device will be presented.

Chapter 7 presents the HIFU integrated targeting system (HITS). Hardware selection, software implementation, system calibration and testing will be explored. An error analysis will be performed to determine the expected accuracy of the system.

Chapter 8 explores the *in vivo* safety, efficacy, and survival study performed in adult female sheep. The protocol will be explored, and gross and microscopic analyses will be presented.

Chapter 9 discusses the use of ultrasound imaging to visualize HIFU therapy. The ability to observe HIFU treated areas as hyperechoic spots on the ultrasound image, and the changes in hyperechoic spot brightness as a function of intensity and time will be examined.

Chapter 10 provides insight into the use of this device in humans and discusses the potential for HIFU to become clinically acceptable for minimally-invasive treatment of uterine fibroids. Possible future studies for continuation of this dissertation are discussed.

Chapter 11 provides a conclusion to this dissertation.

2.0 CHAPTER 2 HIGH INTENSITY FOCUSED ULTRASOUND

2.1 ULTRASOUND

A sound wave is a mechanical disturbance that induces oscillatory movements in particles of a medium. This sound wave is composed of regions in which the medium is stretched and compressed alternately, as shown in Figure 2.1, resulting in areas of high and low pressure. These regions of high and low pressure travel in materials at various speeds depending on the material traversed. As a result, particles of material oscillate back and forth. In a longitudinal sound wave, the particle motion is parallel to the direction of wave propagation. In a transverse sound wave, particle motion is perpendicular to the direction of wave propagation. Sound is audible to the human ear between 20 cycles per second (20 Hz) and 20 kHz in air. Sound above frequencies of 20 kHz is called ultrasound, and below 20 Hz, infrasound.

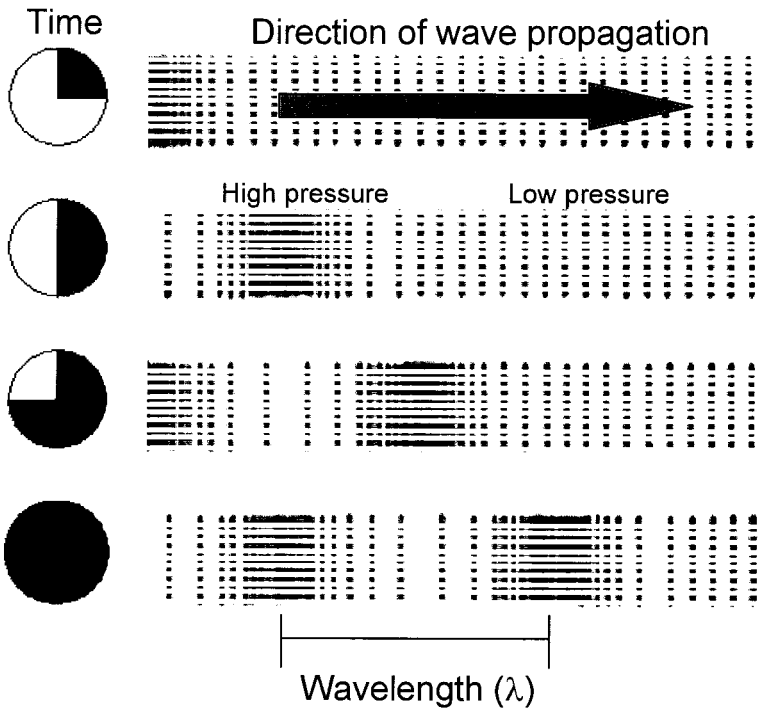

Figure 2.1 A propagating sound wave induces regions of stretching and compression in media resulting in areas of high and low pressure.

2.2 ULTRASOUND GENERATION AND PIEZOCERAMIC MATERIALS

Ultrasound is usually generated by resonant electrical excitation of thin plates of anisotropic piezoceramic material. Lead zirconate titanate (PZT) is the most commonly used piezoceramic material and was originally developed in 1955 by Jaffe *et al.*. (Jaffe, Roth *et al.* 1955) There are many variations of PZT, each with slightly different characteristics due to variations in transmissivity, dielectric constant, permittivity, density, velocity, impedance. These variations resulted from different chemical and thermal treatments, and different mass fractions of lead, zirconate, and titanate. Thus, certain PZT types are more suited for specific applications such as HIFU, than others. PZT-4 and PZT-8 materials are often used in HIFU applications since the internal electrical loss (dielectric loss) in them is low enabling high power transmission of ultrasound. The differences in dielectric loss is due to the differences in the ferroelectric properties of the material (American Piezoceramics, Mackeyville, PA). Generally, materials effective in transmitting are poor receivers. However PZT-5 is a material suitable for both receiving and transmitting (Morgan Electro Ceramics, Bedford, OH, and American Piezoceramics), and is often used for imaging applications.

Pieces of piezoceramic materials can come in a variety of shapes and sizes, and are commonly known as piezoceramic crystals. To generate ultrasound, these crystals are placed in a device that enables electrical excitation of the crystal, hereafter called a transducer.

2.3 ACOUSTIC WAVE PROPAGATION

It is important to understand the theory behind acoustic wave propagation to understand how ultrasound travels through different materials. When acoustic waves propagate through different media, interactions such as interference, diffraction, reflection, refraction and scattering occur.

2.3.1 Reflection and Transmission

Part of the energy is reflected and part is transmitted when a plane acoustic wave passes through two different fluid media at an angle of incidence. This relationship depends on the densities and propagation speed of sound in the media, as shown in Figure 2.2, and by Eq. 2.1 through Eq. 2.12 where the transmission of acoustic pressure is calculated as the sound wave travels from media 1 to media 2.

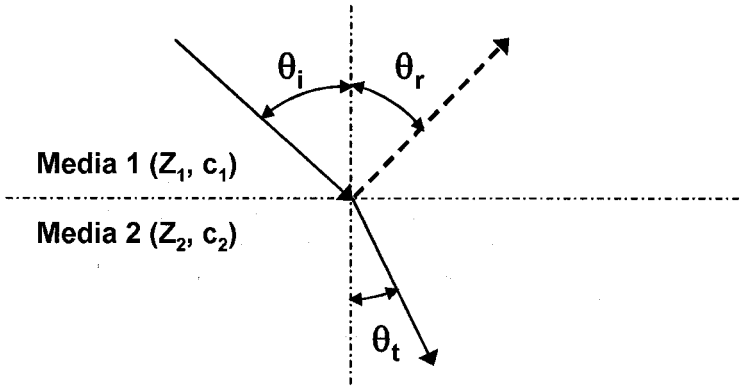

Figure 2.2 A longitudinal wave encountering a fluid boundary has part of the energy reflected and part of the energy transmitted at angles determined by the angle of incidence.

First, it should also be noted that the wave propagation velocity (c) is dependent on the compressibility (κ) and the average density (ρ_o) of a material. For a simple homogenous liquid, the wave propagation velocity (c) can be defined as:

Eq. 2.1 $$c = \sqrt{\frac{1}{\rho_o \kappa}}$$

Next, the specular reflection law (angle of incidence θ_i = angle of reflection θ_r), and Snell's law of refraction apply to plane acoustic waves. Snell's law states that if a wave encounters a boundary between two materials differing in phase velocities at an oblique angle of incidence, the angle of propagation of the transmitted wave will differ from the angle of incidence according to Eq. 2.2:

Eq. 2.2 $$\frac{\sin\theta_i}{\sin\theta_t} = \frac{c_1}{c_2}$$

where c_1 and c_2 are the propagation velocities in media 1 and 2 respectively, which can also be related to wavelength (λ) and frequency (f) by:

Eq. 2.3 $$c = f\lambda$$

The acoustic pressure reflection coefficient, R, is the ratio of reflected to incident acoustic pressures (p_r) and (p_i) respectively, defined as:

Eq. 2.4 $$R = \frac{p_r}{p_i} = \frac{(Z_2/\cos\theta_t) - (Z_1/\cos\theta_i)}{(Z_2/\cos\theta_t) + (Z_1/\cos\theta_i)}$$

It should be noted that p_r and p_i are commonly derived from solutions to the wave equation, and Z_1 and Z_2 are the characteristic impedances of media 1 and 2 respectively, related to density (ρ_o) and wave propagation velocity (c), defined as:

Eq. 2.5 $$Z = \rho_o c$$

Z is most commonly measured in Rayleighs (Rayl), where 1 Rayl = 10 Kg/(s m^2). For an acoustic wave encountering a boundary between two media at normal incidence ($\theta i = \theta t = 0$), Eq. 2.4 reduces to

Eq. 2.6 $$R = \frac{p_r}{p_i} = \frac{Z_2 - Z_1}{Z_2 + Z_1}$$

In addition to the reflection coefficient, it is often useful to determine the pressure transmission coefficient, defined by the transmitted pressure p_t:

Eq. 2.7 $$T = \frac{p_t}{p_i} = 1 + R$$

Acoustic intensity (I) and acoustic power ($\boldsymbol{P_a}$) are proportional to the square of peak acoustic pressure (p), and are most commonly measured in W/cm^2 and W respectively:

Eq. 2.8 $$I = \frac{p^2}{2Z}$$

Eq. 2.9 $$\boldsymbol{P_a} = IA$$

where A is a defined cross sectional area of the acoustic beam (usually the full width at half maximum pressure profile). Using Eq. 2.8, the intensity reflection coefficient, R_I, can be calculated as the ratio of reflected intensity (I_r) to transmitted intensity (I_i):

Eq. 2.10 $$R_I = \frac{I_r}{I_i} = \frac{p_r/(2Z_1)}{p_i/(2Z_1)} = \frac{p_r^{\,2}}{p_i^{\,2}}$$

From Eq. 2.6, the intensity reflection coefficient (R_I) is simply R^2, and the intensity transmission (T_I) coefficient is

Eq. 2.11

$$T_I = \frac{I_t}{I_i} = \left(\frac{p_t/z_2}{p_i/z_1}\right)^2 = \frac{4Z_2Z_1}{(Z_2+Z_1)^2} = (1+R)^2\left(\frac{Z_1}{Z_2}\right) = T^2\left(\frac{Z_1}{Z_2}\right)$$

Finally, the ratio of transmitted power ($\boldsymbol{P_t}$) to incident beam power ($\boldsymbol{P_i}$) is given by

Eq. 2.12 $$\frac{\boldsymbol{P_t}}{\boldsymbol{P_i}} = \frac{I_t A_t}{I_i A_i} = 1 - \frac{I_r}{I_i} = 1 - R^2$$

Note that because the cross-sectional area of the acoustic beam is equal for both media, the ratios of incident to reflected powers and intensities are equal.

Finally, it is important to note the critical angle of incidence ($\theta_{i,\,crit}$) for which the angle of refraction in media 2 is 90° (occurs when $c_2 > c_1$):

Eq. 2.13
$$\theta_{i,crit} = \sin^{-1}\left(\frac{c_1}{c_2}\right)$$

When $\theta_i > \theta_{i,\,crit}$, no waves are transmitted into media 2.

2.3.2 *Mode conversions in solids*

The device developed in this thesis involved propagation of ultrasound waves through an aluminum acoustic lens and a solid matching layer. Therefore, it should be noted that when a longitudinal wave encounters a solid-solid interface, mode conversion may occur where part of the longitudinal wave is converted into a shear wave along with the production of reflected and transmitted longitudinal waves, as shown in Figure 2.3. In a shear wave, particle motion is perpendicular to the direction of wave propagation. Snell's law can be used to calculate the angles of the various waves in Figure 2.3 if the various wave propagation velocities are known.

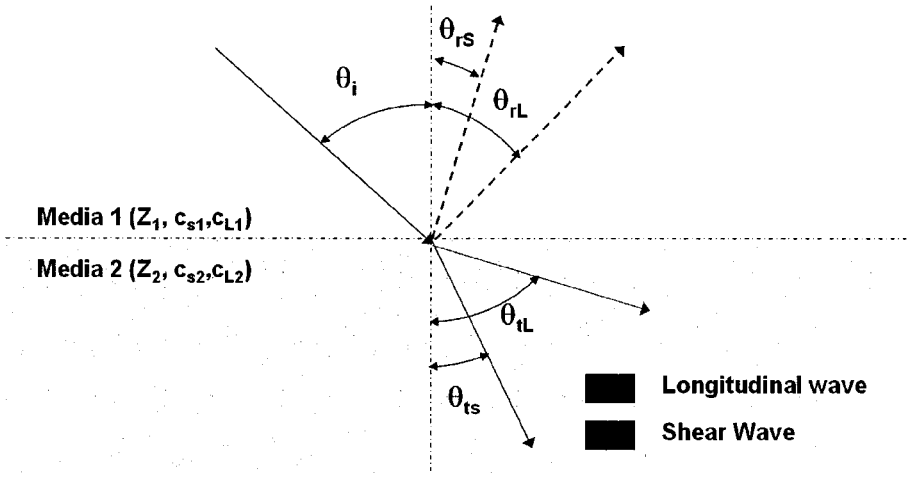

Figure 2.3 Mode conversion at solid-solid boundary results in part of the longitudinal wave being converted into a shear wave.

For example, to determine the angle of shear wave reflection, the shear wave velocity is used in Snell's law, such that

Eq. 2.14 $$\theta_{rs} = \sin^{-1}\left[\sin(\theta_i)\times\left(\frac{c_{S1}}{c_{L1}}\right)\right]$$

where c_{S1} and c_{L1} are the shear and longitudinal wave velocities, in media 1, respectively. Transverse waves always have a propagation velocity lower than longitudinal waves, and as a result, are closer to the normal than the incident wave.

To determine whether longitudinal or shear waves will be transmitted, critical angles, similar to those calculated in equation Eq. 2.13, can be used. For a transmitted shear wave, the critical angle is:

Eq. 2.15 $$\theta_{i,crit} = \sin^{-1}\left(\frac{c_{S1}}{c_{S2}}\right)$$

For a transmitted longitudinal wave, the critical angle is:

Eq. 2.16 $$\theta_{i,crit} = \sin^{-1}\left(\frac{c_{L1}}{c_{L2}}\right)$$

Again, if $\theta_i > \theta_{i,crit}$, no waves are transmitted into media 2.

2.4 ATTENUATION

As an ultrasonic wave travels through a medium, energy is lost due to attenuation in the medium. The attenuation encountered during a HIFU treatment will determine the energy deliverable to the treatment site and the energy a particular type of tissue can uptake. Attenuation is due to two mechanisms: absorption and scattering. The majority of attenuation (60-80%) is due to absorption (Duck 1990; ter Haar 1999). Absorption is the process by which mechanical ultrasound energy is converted into heat. Scattering describes a phenomenon where the incident ultrasonic beam encounters multiple reflections while passing through the tissue. These multiple reflections are due to tissue inhomogenieties and may result in the ultrasound energy being radiated and absorbed outside the main beam.

Due to attenuation, the pressure and intensity amplitude of an ultrasound wave decrease logarithmically as the distance from the ultrasound source increases (Christensen 1988).

The coefficient of decay, or the amplitude attenuation coefficient for small attenuations where $\alpha^2 << k^2$ (k = wave constant), is expressed as:

Eq. 2.17 $$\alpha = \frac{[(4\eta_s/3)+\eta_b]\omega^2}{2\rho_o c^3}$$

where $\omega = 2\pi f$ and f is the frequency, and η_s and η_b are the dynamic coefficients of shear and bulk viscosity respectively. This attenuation coefficient is usually obtained using acoustic properties tables, such as the well known publication by F.A. Duck, (Duck 1990) and is reported in units of dB/cm or Nepers/cm where *1 dB/cm = 0.115 NP/cm.*

Since attenuation generally increases with increasing frequency (higher frequencies are more rapidly absorbed), the attenuation coefficient (α) is usually stated for a specific frequency (*f*) or reported as a function of frequency according to a power function where *a* and *b* are constants:

Eq. 2.18 $$\alpha = af^b$$

The constant *a* is expressed in NP/cm/MHz and *b* is usually in the range of 1 to 1.5 for most soft tissue and 2 for water. Most reported attenuation measurements were empirically determined. Therefore, using this equation for frequencies outside the frequency range tested should be done so with caution.

The ratio of intensity at a location x (I_x) to the incident intensity (I_o) is determined by:

Eq. 2.19 $$I_x = I_o e^{-2\alpha x}$$

Where x is the distance traversed in the media by the ultrasound wave. If the ultrasound wave propagates through several media, each with their own attenuation coefficient, the ratio becomes:

Eq. 2.20 $$I_x = I_o e^{-2(\alpha_1 x_1 + \alpha_2 x_2 + \cdots + \alpha_i x_i)}$$

where α_i and x_i represents the attenuation coefficients and thicknesses of various media respectively.

2.5 HIGH INTENSITY FOCUSED ULTRASOUND: THE FUNDAMENTALS

Ultrasound energy can be focused similar to how a magnifying glass focuses light energy, as depicted in Figure 2.4. The focusing of ultrasound can result in high acoustic intensities (measured as power density in W/cm^2) at the focus. An intensity gain of 100 to 1000 times can be achieved in the cross-sectional area of the beam at the focus, resulting in intensities upward of 1000 W/cm^2, 4-5 orders of magnitude greater than that of diagnostic ultrasound systems (<0.1 W/cm^2). The high focal intensities result in localized thermal and mechanical effects, discussed in detail in Section 2.7, that can cause irreversible lethal damage to cells (coagulative necrosis, protein denaturation and apoptosis) within 1 to 2 seconds. HIFU generators, or transducers, generally operate at frequencies between 1 and 10 MHz, and focus ultrasound using a curved piezoceramic crystal, a piezoceramic crystal attached to an acoustic lens, or a phased array, as discussed in Section 2.11.

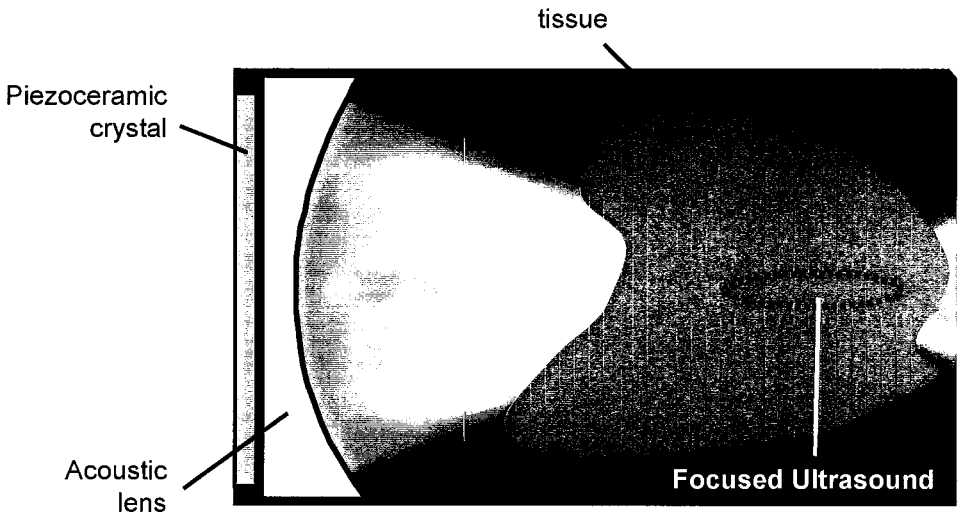

Figure 2.4 Focused ultrasound is produced when electrical energy is applied to a piezoceramic crystal which generates mechanical vibrations at ultrasound frequencies that are then focused to a small spot in tissue via an acoustic lens.

The localized effects of HIFU and its accurate focusing capability make it an attractive tool for extracorporeal treatment of deep seated tissue targets at discrete locations in the body without surgical exposure, particularly for non-operative treatment of tumors. HIFU focal dimensions are similar to those of a grain of rice, up to 2 mm in width and 5-15 mm in length. The intensities of ultrasound proximal and distal to the focus are low, preventing tissue damage outside the focal point. Therefore, tissue damage due to HIFU effects occur solely at the focus, while intervening tissues (between the HIFU source and target areas) remain intact due to lower physiologically tolerable intensities.

Compared to other minimally invasive techniques, HIFU can be a more attractive treatment option since it can provide a remote treatment with better control of the treatment location. Incisions are necessary with catheter based lasers and RF ablation, thermal gradients are wider and the transition from coagulated tissue to normal tissue is less sharp than with HIFU. As a result, irregular target volumes cannot be treated with the same precision as with HIFU. It is no wonder that HIFU, or focused ultrasound surgery (FUS) has received so much attention both in research, and recently in clinical applications, since it was first discovered in the mid 20th century. The history of HIFU and a summary of some of the HIFU research completed in the past 10 years are discussed in the following section and published studies are tabulated in Appendix A.

2.6 HISTORY OF HIGH INTENSITY FOCUSED ULTRASOUND

2.6.1 Pioneers of HIFU

The history of ultrasound as a therapeutic modality dates back to the early 20th century, much earlier than when ultrasound was first used as a diagnostic tool. The ability of high intensity ultrasound to induce biological effects in tissue was first observed and studied in unicellular organisms, frogs, and fish by Wood and Loomis in 1926 (Wood and Loomis 1927). Eight years later in 1935, Gruetzmacher placed a concave surface to a piezoelectric generator and discovered that ultrasound could be focused (Gruetzmacher 1935). In 1942, Lynn *et al.* (Lynn, Zwemer *et al.* 1942) pioneered the use of high intensity focused ultrasound (HIFU) for therapeutic effects. They produced HIFU lesions deep in bovine liver without damaging surrounding tissue. William Fry, his brother Frank, and others (Fry, Barnard *et al.* 1942) developed a HIFU device that mechanically aligned four focused ultrasound generators. This device produced focal lesions in cat brain. Research of using HIFU to destroy central nervous system (CNS) tissue for therapeutic purposes was advanced in the 1950s (Wall, Fry *et al.* 1951). In 1956, human clinical studies began after animal testing proved accurate aiming and precise lesion formation was possible. HIFU was also used to produce lesions in the pallidofugal and nigral complexes of the brains of patients with hyperkinetic and hypertonic disorders (Meyers, Fry *et al.* 1959). Several cases of Parkinson's disease were treated successfully with HIFU, but the study was halted due to difficulties in imaging and targeting of treatment sites in the brain. The introduction of L-dopa drug treatment at that time also reduced the popularity of HIFU. However, research in the application of HIFU to the CNS continued (Lele 1962; Fry 1965; Lele 1967).

2.6.2 Developments from the 1950-1980s

HIFU was thought to be a useful modality for cancer treatment, however, shortly after the Wood and Loomis experiments, ultrasound was reported to have no effect on Ehrlich's carcinoma (Szent-Gyorgi 1933). Twenty years would pass until the investigation of HIFU for cancer treatment recommenced. Burov and Andreevskaya used high-intensity pulsed ultrasound for treating tumors implanted in rabbit testes, and cutaneous melanoma in humans (Burov and Andreevskaya 1956). In the 1960s and 70s, Oka reported using HIFU to treat thyroid and breast cancers (Oka 1964; Oka 1977). Research in the 1970s with animal tumor models continued to indicate that HIFU had significant promise for cancer treatment. HIFU was effective in treatment of murine gliomas implanted in abdominal walls (Kishi, Mishima *et al.* 1975), medulloblastomas in hamster flank (Fry and Johnson 1978), and liver tumors (Linke, Carstensen *et al.* 1973). In-depth experiments testing dosimetry and lesion formation thresholds were also performed during this time (Fry, Kossoff *et al.* 1970; Johnston and Dunn 1976; Frizzell, Linke *et al.* 1977). Although there were promising results in the 1980s from experiments using HIFU for ophthalmological applications: for treating glaucoma and retinal detachment, and for sealing traumatic capsular tears (Coleman, Lizzi *et al.* 1985; Rosecan, Iwamoto *et al.* 1985; Silverman, Vogelsang *et al.* 1991). HIFU therapy did not gain much clinical acceptance until the 1990s.

2.6.3 HIFU in the 1990s

The late 1980s saw a surge in research devoted to HIFU, along with the advancement in technology and its emergence in clinical use. In 1987, Hynynen *et al.* studied temperature elevation at the muscle-bone interface during HIFU using a scanned four transducer HIFU system (Hynynen, Roemer *et al.* 1987; Hynynen and DeYoung 1988). Ter Haar and collegues in the UK (ter Haar, Sinnett *et al.* 1989) demonstrated that focal lesions could be induced in porcine liver in vitro. In the early 1990s, Yang, Sanghvi *et al.* at the Indiana University School of Medicine also investigated the use of HIFU for ablating liver tissue. The group initially used HIFU with a rat hepatoma model and showed improved survival rates in HIFU treated animals (Yang, Reilly *et al.* 1991). Later, HIFU was used on subcutaneous murine neuroblastoma in mice and showed

reduced tumor growth (Yang, Reilly *et al.* 1992). A group in Lyon, France (INSERM) examined the effects of HIFU on liver tumors and showed significant tumor size reduction (Sibille, Prat *et al.* 1993; Prat, Centarti *et al.* 1995). This group, led by Gelet and Chapelon, also proved that irreversible HIFU lesions in prostate tissue can be created through the rectal wall (Gelet, Chapelon *et al.* 1993). Their counterparts in Paris, led by Vallancien, conducted a feasibility study that used extracorporeal HIFU for treating benign prostatic hyperplasia, and kidney and liver metastases in human patients. It was shown that precise focal ablations were possible, but with a side effect of skin burn (Vallancien, Chartier-Kastler *et al.* 1993). In the mid-1990s, animal studies continued showing that HIFU effectively produces lesions in the kidney, liver and prostate (Adams, Moore *et al.* 1996; Kincaide, Sanghvi *et al.* 1996; Rowland, Rivens *et al.* 1997; Watkin, Morris *et al.* 1997).

2.6.4 *Recent research outside the University of Washington*

HIFU is currently in clinical use for the treatment of prostate cancer and benign prostatic hyperplasia (Mulligan, Lynch *et al.* 1997; Nakamura, Baba *et al.* 1997; Sullivan, McLoughlin *et al.* 1997; Sanghvi, Foster *et al.* 1999; Gelet, Chapelon *et al.* 2000; Uchida, Sanghvi *et al.* 2002). ter Haar's group is leading clinical trials in a variety of stage 4 primary and metastatic cancer tumors of the kidney, liver, and ovaries in humans (Visioli, Rivens *et al.* 1999). Kidney ablation using HIFU, for the purpose of treating renal carcinomal, is being studied in the US (Paterson, Barret *et al.* 2003) and Germany (Kohrmann, Michel *et al.* 2002). Hynynen *et al.* at the Brigham and Women's Hospital are using HIFU to treat human benign breast fibroadenomas (Hynynen, Pomeroy *et al.* 2001), and they are investigating the use of HIFU for ablating tumors in the brain using a rabbit model (Hynynen, McDannold *et al.* 2001; Vykhodtseva, McDannold *et al.* 2001). Hynynen's group has also investigated the use of using gas bubbles at the HIFU focus to enhance ultrasound absorption, which resulted in larger lesions more consistent in shape (Sokka, King *et al.* 2003). HIFU is being evaluated as an alternative to vasectomy. Canine vas deferens and epididymis were treated with HIFU and occluded (Fried, Roberts *et al.* 2002; Roberts, Chan *et al.* 2002; Roberts, Wright *et al.* 2002).

A group in Chongqing, China, led by Wu *et al.*, has shown HIFU treatment in 164 patients with liver cancer, breast cancer, malignant bone tumor, and soft tissue sarcoma to be safe, effective and feasible (Wu, Chen *et al.* 2001). Tumor vessels have also shown cessation of blood flow after treatment (Wu, Chen *et al.* 2002). Dr. Wu's group has in all, treated thousands of patients using HIFU, perhaps the most widespread use of HIFU for tumor treatment. Other groups in China are using HIFU for treating bone, liver, pancreas and other malignant tumors (Chen, Wang *et al.* 2002; Chen, Wang *et al.* 2002; Wang and Sun 2002; Li, Xu *et al.* 2003). Closest to our work, a HIFU-based treatment for fibroids using MRI guidance is currently being used clinically in Europe and in clinical trials in the USA (Tempany, Stewart *et al.* 2003).

2.6.5 *Recent HIFU investigation at the University of Washington*

Given the rich history of HIFU research, the Center for Industrial and Medical Ultrasound (CIMU) at the University of Washington can be considered a newcomer in the field of HIFU. In 1997, it was shown that HIFU can be used for hemostasis, or the stopping of bleeding, in rabbit liver (Vaezy, Martin *et al.* 1997). Since then, HIFU has been used at CIMU to study hemostasis of punctured vessels (Martin, Vaezy *et al.* 1999), spleen (Vaezy, Martin *et al.* 1999, Noble, 2002 #243; Vaezy, Martin *et al.* 1999) and kidney. Methods of characterizing HIFU lesions using ultrasound for image-guidance (Yuen 2001), and dynamic elastometry (Shi, Martin *et al.* 1999) have been studied. A transparent tissue-mimicking phantom for studying HIFU treatments was formulated at CIMU (Lafon, Kaczkowski *et al.* 2001). Mesiwala and Mourad have also used HIFU to open the blood brain barrier without damage to brain tissue (Mesiwala, Farrell *et al.* 2002).

A study was completed in 1999 showing that HIFU effectively reduced the size of uterine fibroid tumors in a nude mouse model (Vaezy, Fujimoto *et al.* 2000). HIFU device development at CIMU also commenced around the same time with the introduction of the solid cone HIFU applicator for hemostasis (Brentnall, Martin *et al.* 2001).

The work presented in this thesis attempts to advance HIFU device development by creating a practical and efficient transvaginal transducer, while investigating the promising idea of using HIFU for treating the uterus.

2.7 EFFECTS OF HIFU

The high energy concentration at the HIFU focus results in an area of localized tissue destruction or what is known as a HIFU lesion. The mechanisms behind this tissue destruction are primarily temperature increase and cavitation. Wave energy is converted to heat by various mechanisms such as absorption, a result of viscous shearing effects and relaxation processes (ter Haar 1988; Vaezy, Andrew *et al.* 2001). Thermal damage was shown to occur at relatively low intensities (below 1000 W/cm^2) with long exposure times (> 1s) (Frizzell, Linke *et al.* 1977). At higher intensities, acoustic fields stimulate gas bubbles into motion resulting in a phenomenon known as cavitation or vaporization at the focus. The effects of HIFU treatment, lesion properties, and the resulting tissue changes at the HIFU lesion are explored here.

2.7.1 Thermal effects

HIFU can cause rapid localized temperature increases at the focus causing protein denaturation and tissue coagulation (Robinson and Lele 1972; Reilly 1991; Sibille, Prat *et al.* 1993). The extent of thermal destruction depends on HIFU intensity, frequency, and exposure time (Fry, Kossoff *et al.* 1970; Pond 1970; Frizzell, Linke *et al.* 1977; Lele 1977). Several studies have shown a steep decline in temperature outside the focus (10°C / mm) (Hynynen, Colucci *et al.* 1996; Vaezy, Martin *et al.* 1997). However, it was also shown that if a HIFU treatment affected vasculature and compromises blood supply, indirect damage in surrounding areas may occur due to ischemia (Chen, Rivens *et al.* 1993; Chen, ter Haar *et al.* 1999).

The temperature obtained at the focus is of interest to HIFU research. Temperature measurements at the center of the focus may be difficult to perform due to the difficulty in situating a thermocouple at the focus, the thermocouple interfering with the HIFU energy distribution, and effects of cavitation and tissue vaporization (Waterman, Nerlinger *et al.* 1990). Several researchers have attempted to study temperature increases in the area surrounding the focus, as shown in Table 2.1. Sanghvi *et al.* stated that without heat transfer considerations, the temperature increase is related to specific heat, intensity, absorption coefficient and time duration (Sanghvi and Hawes 1994).

Table 2.1 HIFU thermal measurement studies

Study	Temperature increase	Time
Chen *et al.*, (Chen, Rivens *et al.* 1993) peak temperature at the focus in rat liver measured using a needle thermocouple	70 – 100°C	1 s
Graham *et al.*, (Graham, Chen *et al.* 1999) MRI focal temperature measurements in excised pig liver treated with 1.681 MHz HIFU at 40-150 W/cm^2 I_{SPTA}	55°C	1 s
Reilly *et al.*, (Reilly 1991) temperature of rat liver using 4 MHz HIFU at 550 W/cm^2 I_{SPTA}	80 – 100°C	5 s
Vallancien *et al.*, (Vallancien, Chartier-Kastler *et al.* 1993) animal kidney focal peak temperatures	108°C	0.25 s
Sanghvi *et al.*, (Sanghvi and Hawes 1994) 4 MHz HIFU at 900 W/cm^2 I_{SPTA} in liver tissue	80°C	1 s

Vallancien also showed that perfusion may be an important factor to consider in treatment planning (Vallancien, Chartier-Kastler *et al.* 1993). In humans, a temperature at the focus of 250°C was reached in 0.25 sec due to HIFU. However, after 4 to 7 seconds, the temperature stabilized around 270 – 300°C (Vallancien, Chartier-Kastler *et al.* 1993). Therefore, increased treatment time may not result in a continual increase in temperature. This is due to perfusion effects of tissue which may carry heat away from the focal zone resulting in a less precise or less localized treatment. HIFU treatments can be made perfusion independent by providing thermal delivery without significant cooling using higher intensity treatments for shorter exposure durations (Ibbini and Cain 1990; Dorr and Hynynen 1992; Vaezy, Martin *et al.* 1999).

Furthermore, studies have demonstrated that HIFU exposures greater than 1 second do not induce any additional increase in the peak temperature, but result in a more gradual return to baseline temperature (Hynynen, Shimm *et al.* 1990; Vallancien, Chartier-Kastler *et al.* 1993). These studies also showed that when repeated HIFU exposures were delivered to the same point, peak temperatures did not increase by much after the first exposure, most likely due to perfusion. In another set of experiments where repeated

HIFU exposures were used, the minimum temperature increased and the peak temperature decreased at each exposure (Vallancien, Chartier-Kastler *et al.* 1991; Barkman, Almquist *et al.* 1999).

Heat flow in the body depends on the tissue specific heat and thermal conduction, and perfusion that transfers the applied heat away from the source. The extent to which thermal effects prevail for given HIFU treatment parameters is dependent on tissue properties as modeled the bio-heat transfer equation (BHTE). Initially proposed by Pennes (Pennes 1948), this equation allows the temperature rise (T) to be modeled in living tissue by adding a perfusion term to the heat conduction equation. It is shown in its transient explicit form as:

Eq. 2.21
$$\rho_t c_t \frac{\partial T}{\partial t} + w_b c_b (T - T_a) = k\nabla^2 T + (Q_p + Q_m)$$

The variables in Eq. 2.21 and commonly used values are represented in Table 2.2.

Table 2.2 Thermal properties used in BHTE

Symbol	Description	Common value	Units
ρ_t	Tissue density	1	g/cm^3
c_t	Specific Heat (tissue)	4.2	$J/cm^3/^oC$
c_b	Specific Heat (blood)	4.2	$J/cm^3/^oC$
t	Time	Variable range	S
T	Temperature	Variable	°C
T_a	Initial tissue temperature	37	°C
w_b	Blood perfusion rate	0.01	$g/cm^3/s$
k	Thermal conductivity (tissue)	0.006	$W/cm/^oC$
Q_p	Ultrasound Power Deposition	Variable	W/cm^3
Q_m	Local metabolic rate	Assumed as 0	W/cm^3

It is often useful to define the thermal diffusivity (D) and the perfusion time constant (τ_w):

Eq. 2.22
$$D = \frac{k}{c_t}$$

Eq. 2.23
$$\tau_w = \frac{\rho_t}{w_b}$$

The ultrasonic power deposition, Q_p, is usually expressed as a function of position *f(x,y,z)*

Eq. 2.24 $$Q_p = q_o f(x, y, z)$$

where q_o is a scalar representing the heat at a rate of heat production per unit volume that can be determined using the rate of heating method (Fry and Fry 1954):

Eq. 2.25 $$q_o = 2\alpha_a I$$

Here I is focal intensity, and α_a is the absorption coefficient and can be approximated by 0.7 * attenuation coefficient α, since absorption accounts for 60 – 80 % of total attenuation in reality as discussed in section 2.4. As shown in Figure 2.5 using a program I wrote in MatLAB (Mathworks Inc., Natick, MA), thermal modeling using the BHTE may be helpful in determining spatial distribution of heat generated by a HIFU treatment. This image depicts the normalized temperature distribution of a 3 second HIFU treatment and the normalized temperature distribution 3 seconds after HIFU, using 1500 W/cm^2 of HIFU focal intensity in turkey breast tissue. The HIFU focus was modeled as an ellipse with dimensions of 11 mm (length) and 1.2 mm (width). It should be noted that modeling heat flow in living tissue is complicated by variability in the vascular distribution and temperature sensitive vasodilation that equilibrate the body temperature to 37°C .

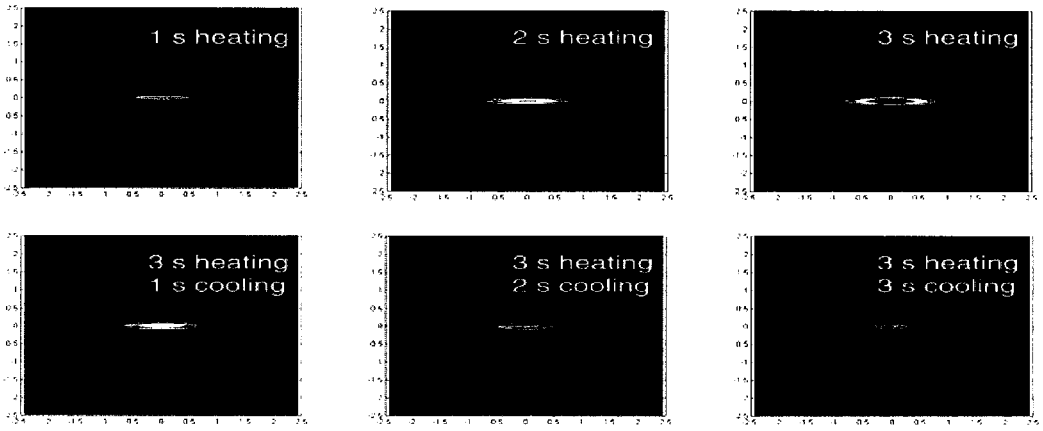

Figure 2.5 BHTE modeling of a HIFU treatment can be used to determine the spatial distribution of heat generated by a HIFU treatment over time.

Although the modeling shown above incorporated the full BHTE, this solution can be complex if many points in the radiation field of a transducer are used (high spatial resolution modeling). The modeling can be simplified by ignoring perfusion and diffusivity under certain conditions. Perfusion can be ignored if high intensities of HIFU are applied for short exposure times. Ignoring diffusivity results in a higher modeled temperature unless the point considered exists in a uniform field that extends far beyond the point modeled. If perfusion and diffusivity are ignored, the BHTE reduces to:

Eq. 2.26
$$T = \frac{2\alpha_a It}{c_t} + T_o$$

2.7.2 Cavitation effects

Cavitation refers to the dynamic behavior of gas bubbles due to pressure changes within regions of compression and rarefaction in a medium caused by a propagating ultrasound wave. As a result, bioeffects may occur and are dependant on the extent and type of cavitation. Cavitation can be sorted into two types: stable and inertial.

2.7.2.1 Stable cavitation

Stable cavitation usually refers to the expansion and contraction of bubbles already present in the medium due to pressure oscillations. These preexisting bubbles are often referred to as cavitation nucleation sites. The bubbles may exhibit this behavior in a cyclic manner without collapse. These bubble oscillations are controlled by the density and compliance of the gas *inside the bubble*. The bubble size is dependent on the frequency: as frequency increases, the size of the bubble required for resonance decreases. Gas bubble oscillations may produce high shearing forces resulting in microstreaming (the rapid movement of fluid near the bubble - section 2.7.4). Ter Haar has reported stable cavitation at spatial peak intensities of 80 mW/cm^2 (ter Haar, Daniels *et al.* 1986), and O'Brien theorized that stable cavitation may occur at spatial peak intensities as low as 0.1 mW/cm^2 (O'Brien 1980). For HIFU applications, a form of cavitation known as inertial cavitation, discussed in the next section, is usually more prevalent. It should be noted that stable cavitation may lead to inertial cavitation.

2.7.2.2 Inertial Cavitation

Inertial cavitation refers to cavitation that is dictated by the density and compliance of the *media surrounding the bubble*. With the depression induced by the negative part of the ultrasound wave, water may enter the vapor phase leading to the development of microbubbles. During inertial cavitation, bubbles rapidly grow to their resonance size and then collapse violently due to the positive and negative sinusoidal oscillation of pressure in the ultrasound field respectively. This bubble collapse is associated with a large concentration of energy causing high acoustic pressure and the propagation of a shock wave. High pressure (20000 – 30000 bars) and high temperatures (1000 – 20000 K) often result in tissue destruction (Apfel 1982; Flynn 1982). Asymmetric bubble collapse may also result in the formation of high-speed liquid jets. Shock waves and liquid jets can destroy tissue and cells due to the high shear forces generated.

Inertial cavitation (hereafter referred to as cavitation for this section) has shown to occur at high peak intensities and brief exposure periods (Dunn and Fry 1971; Flynn 1982). Cavitation effects were shown to be brief in nature, and increased when repeated HIFU exposures were delivered (Vallancien, Chartier-Kastler *et al.* 1993). The degree of cavitation due to HIFU exposure is dependent on HIFU intensity and frequency (Dunn, Lohnes *et al.* 1975). As shown by Hynynen *et al.*, higher intensities are required to trigger cavitation at higher frequencies (1000 W/cm^2 with 1 MHz, 2800 W/cm^2 with 3 MHz in dog muscle) (Hynynen 1991). This research also stated that there is a linear relationship between cavitation threshold and pressure of about 5.3 MPa/MHz at 37°C between 0.246 and 1.68 MHz (Hynynen 1991). In earlier experiments, cavitation was observed at 2000 W/cm^2 with 1 MHz (Fry, Kossoff *et al.* 1970), 1000 – 1500 W/cm^2 with 2.7 MHz HIFU in cat's brain *in vivo* and calf liver *in vitro* (Lele 1977) and 2500 W/cm^2 with 3 MHz HIFU in cat liver *in vivo* (Frizzell 1988).

2.7.2.3 Predicting Cavitation

The mechanical index (MI) is a measure used by the American Institute of Ultrasound in Medicine (AIUM) and the FDA to gauge the probability of inertial cavitation. It is stated as:

Eq. 2.27 $$MI = \frac{p}{\sqrt{f}}$$

where p is the peak negative or rarefactional ultrasound pressure (MPa) and f is frequency (MHz) (Holland and Apfel 1990). A MI less than 0.7 means that even if bubbles exist in a medium, conditions are not adequate for bubble expansion leading to cavitation. A MI greater than 0.7 means that conditions are sufficient for significant cavitation activity (Holland and Apfel 1990). It should be noted that the likelihood of cavitation increases proportionally with ultrasound intensity and pressure, gas content, and temperature, and decreases proportionally with ambient pressure and frequency (at a given intensity).

Caviation at the focus during ultrasound image-guided HIFU treatment has been described as a "popcorn" and "cloud" mechanism by Sanghvi *et al.* (Sanghvi, Foster *et al.* 1999). The popcorn action refers to an audible "pop" sound heard during HIFU treatment that resulted in the formation of a cavity. This was discovered to occur at intensities around 1700 W/cm^2 (4 MHz) in humans and at peak intensities between 2200 and 3400 W/cm^2 in dogs. The "cloud" refers to the formation of a bright hyperechoic spot in an ultrasound image during ultrasound guided HIFU treatment, described in section 2.9.1.1.

2.7.3 Radiation force and other phenomenon

The change in momentum of the propagating ultrasound waves due to absorption or reflection of the waves may result in radiation forces during HIFU. This force may generate mechanical pressure at the focus in tissue and produce streaming in a fluid medium. Radiation pressure results when a force presses against a reflecting or absorbing solid. When the force due to ultrasound pressure is capable of moving a liquid, streaming occurs. If a HIFU transducer is held underwater such that the focus is at the surface of the water, a jet of water (similar to a fountain) can shoot up to a meter into the air, indicative of high mechanical forces. The atomization of water, or formation of a water mist in the air, may also occur.

2.7.4 Other tissue effects

HIFU can also induce other mechanical effects in tissue besides thermal and cavitation effects. A few examples are given here: (a) as the ultrasound wave propagates through tissue, particles undergo changes in velocity, (b) the acoustic pressure due to an ultrasound field may result in translational or rotational motion of cells and other small particles, (c) rapid fluid motion in a small area, or microstreaming, may be a result of higher intensity ultrasound waves. Microstreaming is often induced by stable cavitation and produces high shear forces close to the bubble that can potentially disrupt cell membranes playing a role in ultrasound-enhanced drug delivery.

2.7.5 Non-linearities of HIFU treatment

Propagation non-linearity may also be encountered at high pressure amplitudes (>5 MPa). Non-linearity results in waveform distortion (the wave distortion that occurs is usually from a sinusoidal shape to a sawtooth shape), and can be considered as transferring energy from original fundamental acoustic frequency to higher harmonics (frequencies 2 – 4 times higher than the fundamental frequency). At these higher frequencies absorption coefficients in tissue are greater than that of the fundamental frequency. Consequently, there may be an increase in energy deposition in the focal region where non-linear behavior occurs due to the greater absorption coefficients (Hill and ter Haar 1995). This increase in energy deposition can potentially enhance heat generation by 50% (Swindell

1985). Although advantageous, its magnitude and occurrence is difficult to predict. Propagation non-linearity may also result in a change in shape and width of the acoustic beam profile due to wavelength dependence of the ultrasound diffraction pattern. This leads to uncertainties in the relationships between beam acoustic power and intensity (Hill, Rivens *et al.* 1994).

2.7.6 The Lesion

The small area of tissue that is significantly affected by the HIFU treatment is referred to as a HIFU lesion. Biophysical mechanisms and properties behind lesion formation have not been carefully studied although lesion dosimetry has been researched. Lesion size and shape is dependent on tissue properties, HIFU parameters, and the mechanism behind which the lesion was formed (thermal or mechanical) (Yuen 2001). Lesion size increases proportionally to the average energy delivered to the tissue during treatment (ter Haar, Sinnett *et al.* 1989; Barkman, Almquist *et al.* 1999; Yuen 2001).

Thermally induced lesions are formed at intensities below the cavitation threshold. These lesions are, for the most part, short in width and long in axial dimension (cigar-shaped) (Sanghvi and Hawes 1994). Thermal lesions are affected by the absorption coefficient of thermal energy which varies widely from tissue to tissue (Goss, Frizzell *et al.* 1979). Lesions produced at higher intensities usually have larger central cavities, presumed due to tissue boiling and cavitation surrounded by thermally altered tissue (Hill and ter Haar 1995). These lesions have been shown to be shaped like tadpoles or ellipsoids (Yuen 2001). Confirming this hypothesis, Chapelon showed that lesion shape in rat kidney changed from coagulation necrosis to a "punched out" cavity (induced by cavitation) due to increased intensity and shortened exposure time (Chapelon, Margonari *et al.* 1992). Bailey *et al.* showed that the lesions formed in an overpressure environment (5.6 MPa) were more cigar-shaped than lesions formed with no overpressure (0.1 MPa) (Bailey, Couret *et al.* 2001). With overpressure, there was less likelihood of cavitation resulting in thermally produced ellipsoidal lesions.

Lesions usually start at the focus and develop towards the HIFU transducer. ter Haar showed in liver that lesion volume increased, but developed towards the tissue surface in front of the focal plane, with increasing applied intensity but constant exposure time. The

formation of a lesion in front of the focus has been hypothesized to be caused by changes in acoustic properties of the tissue while the lesion is being formed (Vallancien, Chartier-Kastler *et al.* 1991; Watkin, Morris *et al.* 1997; Barkman, Almquist *et al.* 1999). At least two actions contribute to the growth of the lesion towards the front of the focus. First, tissue absorption increases as the temperature rises. Second, once thermal damage occurs, ultrasound absorption further increases (Keshavarzi, Vaezy *et al.* 2001). These actions result in higher attenuation of ultrasound at the site of the lesion thus reducing transmitted ultrasound energy beyond the lesion. As the temperature increases in front of the lesion with continued ultrasound exposure, the lesion grows towards the HIFU transducer (Bush, Rivens *et al.* 1993).

It was also discovered that when intensity was kept constant and exposure time increased, lesion size increased to maximum after which longer exposure time did not cause larger lesions (Bush, Rivens *et al.* 1993). At a certain time, the lesion stops propagating towards the transducer because it has reached a location where the near-field HIFU beam is not powerful enough to induce additional lesion formation. The arrest of lesion growth may also be due to thermal conduction considerations. The understanding of the effect of existing treated tissue on subsequent HIFU treatments is crucial to treatment planning and HIFU parameter selection.

The actual location of the lesion may be different (1-2 mm) from the predicted focal location of the HIFU transducer due to a phenomenon known as thermal lensing (Connor and Hynynen 2002). There is a change in the acoustic properties of the targeted tissue and tissue surrounding it when localized heating of tissue by HIFU occurs. The incoming acoustic wavefront then becomes distorted and the lesion position may be offset. The lesion may also be offset from the focus due to the formation of bubbles at the focus and the reflection of ultrasound waves by these bubbles.

2.7.7 Biological effects of HIFU

There have been many studies that looked at the histology and biological effects of HIFU treated tissue. These biological effects will be explored in this section.

2.7.7.1 Coagulation necrosis

Coagulative necrosis is the most obvious bioeffect of HIFU. It is a result of elevated tissue temperatures. Coagulative necrosis leading to instantaneous cell death occurs (Section 2.7.7.2) at temperatures over 60°C (for a 1 second exposure) and is a primary method of tumor cell destruction by HIFU. Wu *et al.* has performed a study investigating the pathology of malignant tumors resected up to 14 days after HIFU treatment (Wu, Chen *et al.* 2001). This evaluation showed that within the first 7 days, homogeneous areas of coagulative necrosis existed with no residual viable tumor cells. Between 7-14 days post HIFU, granulation tissue replaced the necrotic tissue and the boundary between treated and untreated tissue was replaced by fibrous scar tissue. Coagulative necrosis lesions due to HIFU are often indicated by a white or yellow necrotic center, surrounded by a dark red inflamed area of blood congestion. The blood congestion may be due to disrupted capillaries in the necrosed area.

Other studies have shown there is a sharp demarcation of approximately 3 to 7 cell layers between viable and necrotic HIFU treated tissue (Madersbacher, Kratzik *et al.* 1998; Visioli, Rivens *et al.* 1999; Wu, Chen *et al.* 2001) or a transition between viable and necrotic tissue of approximately 50 μm in width (ter Haar, Rivens *et al.* 1991).

2.7.7.2 Cellular damage and apoptosis

Cellular damage due to HIFU include coagulated hepatocytes with leukocyte infiltration along margins of necrosis immediately after treatment (Yang, Reilly *et al.* 1991; Chen, Rivens *et al.* 1993), loss of nuclei, calcium deposits, cytoplasmic leakage and vaporization, detached epithelium and interstitial edema (Susani, Madersbacher *et al.* 1993; Wu, Chen *et al.* 2001). In another study, torn endothelium and smooth muscle were seen after treatment while collagenous fibers still remained (Chen, Rivens *et al.* 1993).

Although the majority of HIFU damage is due to thermally induced cell necrosis, apoptosis has also been reported as an effect of HIFU. Apoptosis refers to the self-programmed destruction of the nucleus and rapid degradation of DNA by endonucleases. Cell death by HIFU induced hyperthermia has been shown primarily due to apoptosis (Vykhodtseva, McDannold *et al.* 2001). Apoptosis has also been shown to occur in leukemic cells exposed to both low intensity ultrasound (7 W/cm^2, 1.8 MHz) (Lagneaux, de Meulenaer *et al.* 2002) and ultrasound induced cavitation (at 54.6 and 103.7 W/cm^2, 750 KHz) (Ashush, Rozenszajn *et al.* 2000), both without contrast agents present.

2.7.7.3 Cell membrane damage

HIFU induced cavitation may have a role in disrupting cell membranes. In fact, ultrasound mediated drug and gene delivery relies on this mechanism to affect targeted cells. Tachibana *et al.* have shown pores in cell membranes after ultrasound exposure at 255 kHz and 0.4 W/cm^2 intensity for 30 seconds with a photosensitive drug present (Tachibana, Uchida *et al.* 1999). Cell monolayers in cultures have also been disrupted during ultrasound exposure with gas-filled microbubbles present (Brayman, Lizotte *et al.* 1999; Miller and Quddus 2001).

2.7.7.4 Capillary disruption and blood congestion

Capillary rupture and disruption has been shown to occur due to ultrasound induced cavitation at high intensity levels (Skyba, Price *et al.* 1998; Miller and Quddus 2000). In the presence of contrast agent, these effects have even been noted at diagnostic ultrasound levels (Miller and Quddus 2000; Miller and Quddus 2001). In a study by Zhong *et al.*, capillary disruption is believed to be due to microbubble expansion during the rarefaction part of the ultrasound wave or due to forces exerted during inertial cavitation (Zhong, Zhou *et al.* 2001). Capillary disruption may also affect local blood circulation. Chen et al showed that on a macroscopic scale, liver tissue treated directly by HIFU had blanching and a rough surface. The occlusion to the local blood supply after treatment resulted in areas surrounding the HIFU treatment to also be affected. Blanching in these areas were to a lesser degree (Chen, ter Haar *et al.* 1999). HIFU treated areas, as shown later in this dissertation (Chapter 8), often have a ring of red

surrounding necrotic tissue. This ring of red is due to congested blood resulting from local blood supply disruption.

2.7.7.5 Recovery from HIFU treatment

Chen *et al.* has shown that within 2 months after HIFU treatment, most damage appeared to be removed by phagocytes (Chen, ter Haar *et al.* 1999). Linke *et al.* showed that a discrete fibrous scar resulted from the healing of a HIFU lesion (Linke, Carstensen *et al.* 1973). The duration of exposure appeared to be proportional to the time required for tissue repair due to the treated area, or HIFU lesion, being smaller in size. Noble *et al.* showed that HIFU treated spleen regenerated along with the formation of scar tissue (Noble, Vaezy *et al.*).

2.8 LIMITATIONS OF HIFU

As with any medical treatment, HIFU has its limitations. The major drawbacks of HIFU treatment are presented here.

2.8.1 Treatment time consideration

Large areas to be treated and large tumors will result in long treatment times. This is due to the small focal area, and multiple overlapping lesions required for treating a volume of tissue. The majority of the total treatment time required is due to transducer cooling in between lesions and device repositioning. Shorter treatment times are desired to minimize patient discomfort and anesthesia required, and decrease costs associated with the treatment procedure. Strategies for decreasing treatment time include:

- decreasing the number of required sonications by increasing focal dimensions or intensities
- using multiple or patterned foci generated with phased arrays
- determining optimal sonication patterns tailored for a specific tumor to avoid treatment duplication while ensuring all tissue is ablated
- optimizing transducer cooling mechanisms

- using phased arrays to change treatment locations electronically instead of repositioning the transducer mechanically

- operating the transducer continuously while scanning across a region to be treated, analogous to "painting a stripe" using the transducer versus "making treatment spots"

2.8.2 *Acoustic pathway limitations*

HIFU treatment is usually limited to regions of the body which are accessible through soft tissue or fluid pathways since ultrasound in the MHz frequency range is poorly transmitted through air or bone. Impedance mismatch and subsequent reflection at gas-soft tissue or bone-soft tissue interfaces can be an impairment to treatment. However, focused ultrasound was shown to cause thermal lesions in animal brains through skull (Fry 1977). It has also been shown that substantial attenuation of ultrasonic power due to bone can be compensated by strong focusing, increased intensity, and the reduction of beam distortion (Thomas and Fink 1996; Hynynen and Jolesz 1998; Clement, Sun *et al.* 2000). However, a treatment path comprised of soft tissue and fluid is still preferred since a more homogenous tissue path free of bone will result in less variation in lesion characteristics (Daum, Smith *et al.* 1999).

Furthermore, acoustic coupling between the HIFU transducer and tissue must be provided to minimize the differences in acoustic impedances between the transducer and the layers of tissue to be treated. Since ultrasound propagates through water with negligible attenuation, water enclosed in a sealed flexible membrane that can contour to both the HIFU transducer and tissue at the site of interest is commonly used. Examples of this include a degassed water bolus encapsulated by a latex membrane (Bush, Rivens *et al.* 1993; Sanghvi, Foster *et al.* 1999; Chan, Fujimoto *et al.* 2002), and a water filled bag placed between the transducer and the subject to be treated (Hynynen, Pomeroy *et al.* 2001).

2.8.3 Tissue mobility during treatment

Since the HIFU focal region is so small, any slight movement of the tissue being treated may lead to treatment of undesired areas, random regions of tissue under-treatment, or incomplete tissue ablation. Movement of the tissue may sometimes be unavoidable due to respiration. For example, the liver can move up to 10 cm during deep respiration (Daum, Smith *et al.* 1999). To minimize tissue movement, techniques such as stomach deflation, synchronizing treatment with breathing, and finding an optimal acoustic window least susceptible to movement may be necessary. A tracking system that guides HIFU treatment based on image recognition of tissue location may be another possibility to compensate for tissue mobility.

2.8.4 Noted side effects

There have not been many published discussions related to undesired biological side effects of HIFU. However, the high acoustic absorption coefficient of skin could potentially lead to a skin burn (Visioli, Rivens *et al.* 1999). Fry and Johnson also observed severe skin burns (Fry and Johnson 1978), as did Moore, who used 4 MHz HIFU at intensities between 500-700 W/cm^2 (Moore, Lopez *et al.* 1989). Moore attributed the skin burn to the fact that the subcutaneous implanted tumor required the focal area to be close to the skin.

Treatment in undesired locations was noted in a few experiments. Indirect tissue destruction can occur in tissue that becomes completely isolated from its blood supply due to the ablation of an adjacent region (Hill and ter Haar 1995). Unwanted HIFU effects may also be formed at tissue-bone or tissue-air interfaces due to the reflection of high intensity ultrasound waves (Taylor and Connolly 1969). Finally, Fry *et al.* observed an increase in tumor metastases after HIFU tumor treatment when compared with a control group (Fry and Johnson 1978). This was hypothesized as due to tumor cells being redistributed due to HIFU effects, but was not confirmed in other studies (Goss and Fry 1984; Chapelon, Margonari *et al.* 1992; Oosterhof, Cornel *et al.* 1997).

2.9 IMAGE-GUIDANCE

An integrated imaging component is just as important as the HIFU transducer in focused ultrasound therapy. It is crucial to have some means of assessing the treatment location, tracking the position of the focal point, and verifying that power is being delivered to the proper location. It is also necessary to determine when the critical thermal dose has been reached at each location and ascertaining whether tissue destruction has occurred, and if so, at what location and to what extent. This feedback allows lesion formation to be controlled and confined to areas planned for tissue destruction. Post-treatment imaging for mapping the treated region is also necessary for treatment follow-up or continued therapy (Vaezy, Andrew *et al.* 2001). Fortunately, several modalities are available for monitoring HIFU therapy, as shown in Table 2.3.

Table 2.3 Comparison of various modalities for monitoring HIFU treatment

Modality	Invasiveness*	Cost#	Advantages	Disadvantages
B-mode ultrasound	-	+	Real time, portability possible	Thermal and tissue property measurement techniques not fully developed yet, images may be hard to decipher
MRI	+	+++	Image resolution and contrast, thermal monitoring	Delay time for image generation, contrast agent may be required, non-portable
X-ray	++	++	Good for cardiovascular procedures	Poor image resolution, contrast agent required, x-ray protection needed
Visual	--	--	Accurate visualization, little interpretation and/or post-processing necessary	Suitable only for intraoperative procedure where the treatment site can be seen (not suitable for minimally-invasive procedures)
Thermocouples	+	-	Easy to use, minimal adjunct equipment needed	Obstruction of thermal measurements, not practical for image-guided therapy: positioning and monitoring difficult

**Invasiveness: amount of patient discomfort required*
#*Cost: equipment and procedure costs*

2.9.1 Ultrasound

Ultrasound is the modality of choice for HIFU treatment visualization at the Center for Industrial and Medical Ultrasound at the University of Washington (except for intra-operative hemostasis where visual guidance is sufficient). Ultrasound is inexpensive compared to MRI, and with advances in miniature systems, has the potential to provide portable image-guidance. Pioneering work on using ultrasound as a diagnostic modality started in the 1940's, paralleling the early developments of the electronic computer. In 1966, Lele studied detectable changes in ultrasonic images following creation of focused ultrasound lesions (Lele 1966). However, it was not until the mid-1970s that image-guided ultrasound therapy was developed as the quality of diagnostic ultrasound images improved (Fry, Sanghvi *et al.* 1976). The primary ultrasound modality for detecting lesion formation is B-mode (brightness mode), in which lesions appear as hyperechoic spots on the ultrasound image. However, it is also desirable to monitor temperature and tissue property changes to allow more accurate and reliable therapy guidance. Therefore, researchers have come up with novel ways of using ultrasound imaging in assisting HIFU treatments. It should be noted that ultrasound has already been proven to provide adequate image-guidance for extracorporeal lithotripsy (Neisius and Moll 1989).

2.9.1.1 *Lesions as Hyperechoic Spots*

The amplitude of the reflected signal, or detected echo strength in B-mode ultrasound, is represented by the brightness of a dot on the ultrasound screen. B-mode can be used to map the target area and indicate where HIFU treatments are taking place as lesions show up as hyperechoic spots in real-time (Yang, Sanghvi *et al.* 1992; Yang, Kopecky *et al.* 1993; Madersbacher, Pedevilla *et al.* 1995; Sanghvi, Foster *et al.* 1999; Gelet, Chapelon *et al.* 2000; Vaezy, Shi *et al.* 2001). The echo strength may range from no echo to diffuse hyperechogenicity within a treatment area. The hyperechoic spot forms at the focal point and increases in size while growing towards the HIFU transducer as treatment continues. A greater intensity results in a more rapid lesion formation and growth. The underlying causes for these differences in echogenicity are not fully understood, but were proposed to be due to differences in intracellular water content (Madersbacher, Pedevilla *et al.* 1995). With higher water content, there was a higher chance of microbubble generation

during HIFU, resulting in echogenicity changes. However, changes in echogenicity have been shown to have no impact on the size, location, or quality of HIFU necrosis (Madersbacher, Pedevilla *et al.* 1995). Vaezy *et al.* proved that hyperechoic spots fade as a function of time (Vaezy, Shi *et al.* 2001). A larger hyperechoic area was measured for higher HIFU exposure levels, and the duration of HIFU application needed for visualizing the hyperechoic spot as inversely proportional to HIFU intensity. There was also an intensity threshold below which no visualization occurred. Bailey *et al.* showed that hyperechoic spots of thermally induced lesions formed in an overpressure environment disappeared quicker (Bailey, Couret *et al.* 2001).

ter Haar and Hynynen reported that hyperechoic zones were observed when ultrasound imaging was used to monitor cavitation (ter Haar, Sinnett *et al.* 1989; Hynynen 1991). This inferred that the existence of microbubbles was related to cavitation, although another study showed no systematic correlation between the appearance of the hyperechoic zone and indications of cavitation effects in the treated tissue upon physical dissection and examination (Vallancien, Chartier-Kastler *et al.* 1991). Finally, Bailey *et al.* found that lesions formed where a hyperechoic spot was visible appeared more irregular than when the spot does not occur (Bailey, Couret *et al.* 2001), inferring cavitation induced hyperechogenicity.

2.9.1.2 Tissue property measurements using ultrasound

It may appear then that ultrasound visualization based on hyperechoic spot formation is dependent on microbubble formation based on the points noted in Section 2.9.1.1. This means that B-mode ultrasound imaging may be insensitive to purely thermal lesions and may only respond when the lesioning process has proceeded to the point of cavity formation (Hill and ter Haar 1995). However, there are substantial changes in the attenuation coefficient, sound speed, and thermal expansion of tissue during HIFU treatment with only thermal effects, that can make ultrasound detection and visualization of purely thermal lesions (with no backscatter due to cavitation) possible (Bush, Rivens *et al.* 1993; Seip and Ebbini 1995). Another method of detecting changes due to HIFU is sonoelastic imaging, which uses ultrasound echoes transmitted to the tissue interrogated to determine tissue stiffness (Kallel, Stafford *et al.* 1999; Shi, Martin *et al.* 1999). These

new methods of tissue characterization may provide a more quantitative approach to lesion investigation in the future.

2.9.2 Magnetic Resonance Imaging (MRI)

MRI has emerged as an effective tool for monitoring HIFU therapy. MRI offers good tissue contrast for localization of the target volume and can characterize temperature (diffusion of thermal energy), perfusion, and blood flow in tissue. This enables the detection of tissue damage induced by thermal ablation. Hynynen *et al.* has shown that tissue changes that resulted from treatment were visible after exposure, and that MRI can be used to monitor temperature elevation (Cline, Schenck *et al.* 1992; Hynynen, Darkazanli *et al.* 1993). Temperature resolution has been shown to be better than 1°C (Bohris, Schreiber *et al.* 1999). However, MRI is expensive compared to ultrasound and minimal use of metal is necessary in the HIFU transducer assembly to prevent distortion of MR images (source: Philips Medical Systems, Bothell, WA).

When MRI guidance is used, a test pulse of low energy that allows MRI to detect a small thermal change but does not cause permanent tissue damage, is initially used to test targeting and treatment location (Cline, Hynynen *et al.* 1995; Hynynen, Pomeroy *et al.* 2001). The treatment location is usually initially outlined on a series of MRI scans for reference. During treatment, the tissue temperature is shown after a slight delay as it takes approximately 3 seconds to acquire the MR sequence and a few seconds to process the temperature image. Unfortunately, this delay may result in an inaccurate tissue temperature measurement and lengthen the HIFU treatment session.

2.9.3 Other forms of HIFU treatment guidance

There exist treatment scenarios where external image-guidance is not necessary. An example would be intraoperative acoustic hemostasis where blood vessels and other sources of bleeding are surgically exposed for HIFU treatment. Visual guidance using the human eye is necessary in this case, although conical attachments for transducers that pinpoint the treatment location and guide the ultrasound have been developed (Vaezy, Martin *et al.* 1999; Brentnall, Martin *et al.* 2001). Another study used Doppler ultrasound to guide HIFU treatment of punctured vessels. Doppler indicated that the

HIFU focus was at the bleeding site and this detection reduced the time for complete hemostasis by five times compared to simply using visual guidance (Martin, Vaezy *et al.* 1999). X-rays have also been utilized for therapeutic ultrasound treatment. Besides being used for mapping treatment areas and monitoring HIFU therapy in Parkinson's disease experiments (Meyers, Fry *et al.* 1959), X-rays have also been used in intravascular therapeutic ultrasound thrombolysis (Gunn, Cumberland *et al.* 2001). Catheter systems are used to deliver ultrasound energy performed under X-ray guidance. However, X-ray doses require radiation shielding for both the patient and the clinicians administering treatment. King *et al.* has recently investigated the use of an "acoustic camera" as a real-time imaging device for focused ultrasound surgery (King, Clement *et al.* 2003). This camera used a PVDF (polyvinylidene difluoride) array divided into 128 by 128 pixels, similar to a CCD camera. A transmission transducer sent ultrasound through a HIFU treated tissue sample. The ultrasound was then focused onto the array of elements via a lens and the intensity of the received ultrasound correlated to the degree of HIFU treatment.

More invasive forms of treatment monitoring have also been studied. When thermocouples were used to measure lesion temperature, temperatures measured were higher than the actual temperature due to both frictional forces acting between the probe and the tissue during sonication, as well as energy absorption in the probe (Hynynen, Darkazanli *et al.* 1993). The acoustic field may also be disturbed if the thermocouple is of a different impedance than the surrounding tissue. Hynynen *et al.* showed that thermocouples with diameters equal to or greater than $0.5\lambda^{1/2}$ scattered and reflected waves, thus distorting the ultrasound field. However, smaller thermocouples down to $\lambda^{1/2}/5$ in diameter had a small local effect, which would probably not have had a significant effect on the overall temperature distribution (Hynynen and Edwards 1989). In addition, it was stated that temperature measurement probes with low energy absorbance were desirable (Hynynen and Edwards 1989).

2.10 DEVICE DESIGN: INTRODUCTION

The work presented in this thesis relates to the design and development of an image-guided HIFU device for uterine fibroids treatment. Therefore, it is crucial to define parameters and variables that will need to be taken into consideration in designing such a device. The following sections provide an overview of concepts considered in the design of the transvaginal HIFU device presented in this thesis.

2.11 METHOD OF FOCUSING ULTRASOUND

Focusing of high intensity ultrasound is most commonly achieved using a curved piezoceramic crystal, a flat crystal attached to an acoustic lens, or an electronic delay circuit (phased array), as shown in Figure 2.6. An overview of each of these modalities is provided here and compared in Table 2.4. It should be noted that the focal intensity (power density) gain is related to the ratio of the transducer area (A_T) to the focal area (A_F) for a given acoustic power:

Eq. 2.28
$$Gain = \frac{A_T}{A_F}$$

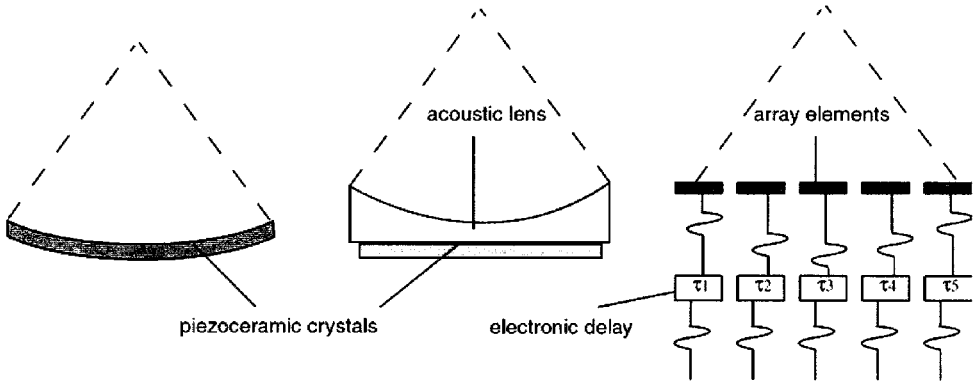

Figure 2.6 Methods of focusing ultrasound include the use of a curved piezoceramic crystal, a flat pizezoceramic crystal affixed to an acoustic lens, and an electronic time delay phased array with multiple array elements. τ_1 through τ_5 indicate various sequenced crystal excitation times.

2.11.1 Curved ceramic crystal

A spherically curved piezoelectric crystal will converge at a distance corresponding to its radius of curvature (Chapelon, Margonari *et al.* 1992). Perhaps the most well known article discussing the theory of spherically curved crystals was written by Kossoff (Kossoff 1979).

It is important for the curved crystal to have a constant thickness for uniform ultrasound generation across its surface at a particular frequency. Curved ceramic crystals with tight tolerances on thickness required spherical lapping techniques. Consequently, they are expensive relative to comparable flat crystals (cost of curved crystals ~ 10x that of flat crystals, Source: American Piezo Ceramics, Mackeyville, PA). Therefore, for simplicity and reduced costs of production, a flat crystal attached to an acoustic lens may be used for HIFU generation.

2.11.2 Acoustic lens

An acoustic lens functions similarly to an optical lens in that focusing is due to refraction. Ultrasound waves are focused at a point in space when waves from an ultrasound source arrive in phase (Ziskin and Lewan 1993). A concave lens is required if the acoustic velocity of the lens material (e.g. plastic, metal) is greater than the acoustic velocity of the material that the sound waves propagate into (e.g. water, tissue). Sections 4.3.3 and 4.3.4 discusses acoustic lens geometry and modeling.

Since acoustic lenses often attenuate the transmitted ultrasound, spherically focused crystals are more efficient than lens-focused transducers. However, the shape of the ultrasound field using a spherically focused crystal is fixed. Lenses offer a simple and inexpensive method to produce a variety of acoustic power deposition patterns. For example, lenses were used to simulate 2D phased arrays with 500-2000 elements using a single crystal (Lalonde, Worthington *et al.* 1993) and pseudo-inverse field conjugate lenses were used to generate multipoint foci (Ebbini and Cain 1991). As a further benefit, lenses may permit impedance matching between the crystal and surrounding medium, improving the power output from the crystal for a given driving voltage (Fry and Dunn 1962).

It is necessary to minimize the energy reflected or absorbed by the lens since reflected energy reduces the power entering the treatment area and absorbed energy can lead to lens damage over prolonged use due to high temperatures, as well as transducer heating which may potentially damage tissue adjacent to the transducer. Therefore, acoustic lens materials should have a good impedance match to water, a low acoustic attenuation coefficient, and a high melting temperature (Sette 1949).

Most commonly, aluminum or plastic lenses (polystyrene, Plexiglas, araldite) are used for focusing ultrasound (Tarnoczy 1965; Beard, Magin *et al.* 1982). Plastics generally have low acoustic impedances compared to metals but their high absorption and attenuation reduces output power (Bronzo and Anderson 1952; Robinson and Lele 1972). In the search for an optimal acoustic lens, less common materials have been used, such as lithium and TPX (polymethylpentane) (Beard, Magin *et al.* 1982). An acoustic lens also protects the piezoceramic element, important for when the transducer is placed in saline solutions, body fluids, or tissue, or when used intraoperatively.

2.11.3 Electronically controlled phased array

Electronic control or "steering" of the ultrasound beam can allow the HIFU focal distance to be electronically varied. Transducers with many diced elements, each driven by a delayed signal, are used for electronic focal control. Known as phased arrays, these transducers can also allow the number and pattern of focal spots to be varied during HIFU treatment. By using electronic steering and multiple focus fields to enlarge the treated area, phased arrays have been shown to greatly increase the rate (volume per unit time) of tissue coagulation (Fan and Hynynen 1996). Arrays have been developed that are annular, linear and two-dimensional. However, since multiple piezoelectric ceramic elements are required complex circuitry is usually needed (Vallancien, Chartier-Kastler *et al.* 1993). The theory behind the development of phased arrays is complex and will not be discussed in depth in this thesis.

Table 2.4 Comparison of focusing methods

Focusing method	Curved crystal	Acoustic lens + flat crystal	Phased array
Cost	Moderate. Spherical lapping techniques make curved crystals expensive >$150 ea (2-4 cm in diameter)	Low – lenses cost ~ $40 ea machined, flat crystals cost < $10 ea (2-4 cm in diameter)	High. Dicing and assembly is expensive, completed transducers >$1000
Transducer construction	Mounting curved surfaces may be more challenging	Bonding a flat crystal onto a lens is simple.	Difficult due to many miniscule elements and complex wiring.
Durability	Poor without protective layer covering the crystal.	Good – the lens acts as a barrier to the external environment	Good – usually a protective layer is placed over the array elements
Variable focus	No	No	Yes
Attenuation loss	None	Depends on thickness and material of the lens used	Depends on whether a protective layer is present
Electronics needed	Minimal – waveform generator and amplifier	Minimal – waveform generator and amplifier	Complex – multi-channel waveform generator and multiple amplifiers

2.12 TRANSDUCER PROPERTIES

2.12.1 Frequency selection

The frequency of ultrasound affects focusing and penetration, and thus becomes an important parameter to consider in HIFU therapy. If the crystal is operating in "thickness" mode (shown in Figure 2.7), as in the case of transducer discussed in this thesis, the wavelength (and thus frequency) of the ultrasound is governed by the thickness of the piezoceramic crystal. In thickness mode, the crystal operates at a half-wavelength thickness resonance as per Eq. 2.29.

Eq. 2.29 $$thickness = \frac{\lambda}{2}$$

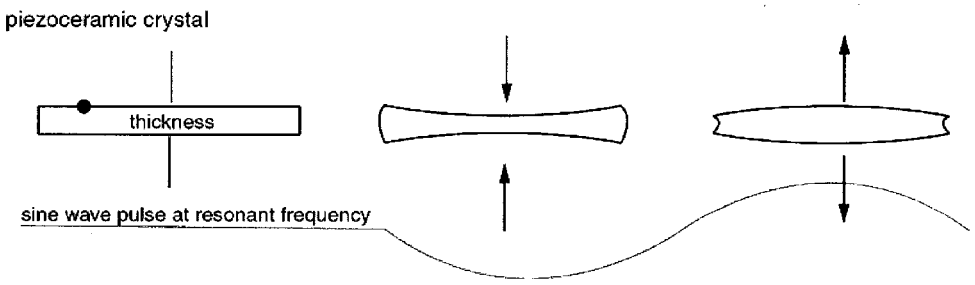

Figure 2.7 A piezoceramic crystal operating in thickness mode deforms in shape at various stages of the acoustic wave.

The absorption of HIFU energy in tissue is largely based on the attenuation of the tissue, which is frequency dependent. Also, the focal area spot width (defined by diffraction absent any tissue aberrations), is negatively correlated to frequency, as shown later in Eq. 2.30 (Zanelli, DeMarta *et al.* 1993).

A frequency should be chosen that is high enough to achieve a tight focus and adequate absorption in the target tissue at the treatment site without being so high as to lead to excessive attenuation in overlying tissues. Theoretical modeling suggested a choice of frequency that led to an overlying tissue attenuation of ~ 10 dB down to the target depth (Hill 1994). This modeling implies optimum frequencies of 1.4 MHz for a depth of 10 cm and 2.6 MHz for a 5 cm depth using a representative value for tissue attenuation

coefficient of 0.7 dB/cm/MHz. Figure 2.8 shows a plot of the optimum frequency for depths ranging from 1 to 7 cm.

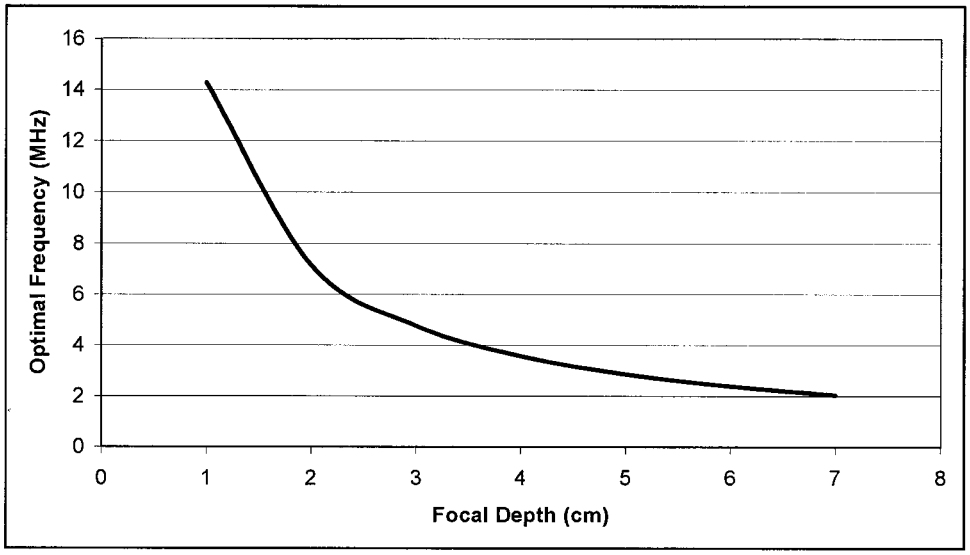

Figure 2.8 Plot showing the optimal HIFU frequency for treatments at various depths. The optimal frequency is the frequency that would result in an attenuation of 10 dB at the focus using a tissue attenuation coefficient of 0.7 dB/cm/MHz.

2.12.2 Transducer size, focal distance, and focal shape

The focal beam dimensions depend on the physical dimensions of the HIFU transducer: the front face diameter d and focal length l_f (which is the radius of curvature for a spherically curved piezoceramic crystal) (Zanelli, DeMarta *et al.* 1993). The f-number, defined as l_f/d, should be close to 1 in order to produce high intensities in focal zone (Sanghvi and Hawes 1994). In comparison, imaging transducers generally have an f-number of 2 to 5 (in this case, the f-number is defined as the ratio of the focal length to the crystal diameter) allowing for a longer and more uniform focal region.

The width of the ultrasound beam is twice the distance between the first off-axis intensity minimum and the geometric focus. Known as the focal width (FW), this width is based on the Fraunhofer diffraction equation and can be stated as (Christensen 1988):

Eq. 2.30 $$FW = 2.44\left(\frac{l_f}{d}\right)\lambda$$

This relationship holds true for a lens focusing an ultrasound beam (Christensen 1988). It should also be noted that the focal depth (FD) is defined as the axial distance over which the beam maintains its cross-sectional diameter defined by the focal width equation above, and can be approximated as (Christensen 1988):

Eq. 2.31 $$FD \approx \frac{LR^2}{2\lambda} \approx 3\left(\frac{l_f}{d}\right)^2 \lambda$$

Based on Eq. 2.30 and Eq. 2.31, and with l_f / d greater than or equal to 1, $FD > FW$ and therefore the focal region of a focused ultrasound beam is asymmetrical, with focal depth being greater than focal width.

The maximum HIFU power and gain is dependent on the size of the HIFU transducer. Larger aperture transducers generate more power at the focus for a given F-number due to higher focal gains. However, the size of transducer is usually dictated by the specific application for which the device is to be used. The HIFU focal sizes, transducer sizes, and beam dimensions may also be limited by the acoustic window available for the ultrasound beam to reach the tissue intended for treatment.

2.12.3 Acoustic Impedance matching

A major challenge in transducer design is matching the high acoustic impedance of the piezoceramic crystal (30-36 Mrayl) to the relatively low impedance of water or tissue (~1.5 Mrayl). Without matching, this impedance mismatch results in a poor transmission from the piezoceramic crystal to the media that ultrasound is radiating into (using Eq. 2.12 and Z_{PZT} = 31.25 and Z_{TISSUE}=1.5, P_t/P_i= 17.5%). Matching also has a large effect on the operating efficiency of the transducer, affect the intensity at the treatment site, and prevent overheating of the transducer. Acoustic impedance matching also has the potential for increasing the bandwidth for which a transducer can effectively operate.

Classical transmission line theory states that matching can be provided by using sections of material with a thickness equal to integer multiples of a quarter wavelength "matching layer" placed between the transducer and the surrounding media. Since increased thickness results in increased attenuation, matching layers that are one quarter wavelength thick are most commonly used. One or two layers of material can be used for matching, and the optimal acoustic impedances for matching (Z_{m1} and Z_{m2}) can be calculated as the geometric means of the crystal (Z_c) and surrounding medium, such as water (Z_w) (Collins 1957):

Eq. 2.32 $$Z_{m1} = \sqrt{Z_c Z_w}$$

for a single layer match, and

Eq. 2.33 $$Z_{m1} = Z_c^{3/4} Z_w^{1/4}$$

Eq. 2.34 $$Z_{m2} = Z_c^{1/4} Z_w^{3/4}$$

for a two layer match.

Assuming Z_c = 31.25 Mrayl for piezoceramic material used in the transducer and Z_w = 1.5 Mrayl, Z_{m1} = 6.84 Mrayl for a single layer match and Z_{m1} = 14.6 Mrayl and Z_{m2} = 3.2 Mrayl for a dual layer match. A matching layer design is discussed in section 6.5.1.

Although the above equations are commonly used for designing matching layers, it has been shown that it may be more effective to match the output mechanical impedance (Z_{mech}) of the transducer. The output mechanical impedance of a transducer was derived from assuming that the transducer propagating into a loading medium can be modeled as a Thevenin equivalent mechanical circuit. The transducer was a force generator and the mechanical impedance was calculated as:

Eq. 2.35 $$Z_{mech} = \frac{F}{u}$$

where F was the mechanical force exerted by the transducer, and u was the particle velocity, analogous to the voltage and electrical current respectively, in an electrical Thevenin equivalent circuit. The mechanical impedance has a real and complex

component and varies with frequency. Martin[a] has shown that if the transducer acoustic impedance Z_o was equal to Z_{mech} at the center frequency of the transducer, a peak transmission will occur at the center frequency. Z_{mech} is often modeled using Thevenin equivalent equations. The transducer acoustic impedance was calculated as the specific acoustic impedance (Z) multiplied by the area of the transducer (A):

Eq. 2.36 $$Z_o = AZ$$

2.12.4 Electrical impedance matching

It is desirable to maximize the net electrical power for driving the HIFU transducer. The net electrical power (P_e) is defined as the difference between forward and reflected power (excluding any electrical impedance matching described below) measured using an in-line RF power meter:

Eq. 2.37 $$P_e = P_{forward} - P_{reflected}$$

Radiofrequency amplifiers used for HIFU generation typically have an output impedance of 50 Ω. However, the impedance of the HIFU transducer is often not 50 Ω. Thus, to minimize the reflected power, a matching network is designed to tune the real part of the transducer impedance to 50 Ω and cancel any imaginary component. A detailed discussion on impedance measurements and the matching network used for our device is presented in section 4.3.5.5.

[a] Professor Roy Martin, Department of Bioengineering, University of Washington, personal communications

2.12.5 Transducer efficiency

Not all of the incident energy delivered by the amplifier goes toward the generation of ultrasound waves. Some of this energy may be lost due to heat dissipation in the electronics or device components. The incident energy actually used for ultrasound generation is defined by the transducer electroacoustic efficiency η:

Eq. 2.38 $$\eta = \frac{P_a}{P_e}$$

where P_a is the acoustical power output, and P_e is the electrical power input. Acoustic power output is often determined using radiation force balance techniques (Section 4.4.3).

2.13 HARDWARE OPERATION PARAMETERS

In terms of hardware, the generation of HIFU requires, at minimum, a radio frequency (RF) amplifier and a waveform generator. The specific hardware and apparatus used for the device presented in this thesis is discussed in detail in Section 4.3.6. The selection of appropriate hardware to operate the HIFU transducer will ensure that treatment intensities, desired wave parameters, and pulsing regimes will be achievable.

2.13.1 Burst mode versus continuous wave

A transducer operates in continuous wave (CW) mode if electrical power is continually supplied to the transducer assuming linear propagation. However, it is often advantageous to operate the transducer in burst mode meaning that electrical power is periodically supplied. As discussed in Section 2.7.2, if cavitation effects are desired, the treatment should be of high intensities and short excitation times. Burst mode may also be preferred over continuous wave operation to prevent overheating of the transducer. Furthermore, burst mode may also be used to implement image-guided therapy where B-mode imaging is synchronized to HIFU pulses (Vaezy, Shi *et al.* 2001). Values that are important in burst mode operation are presented here, and illustrated in Figure 2.9.

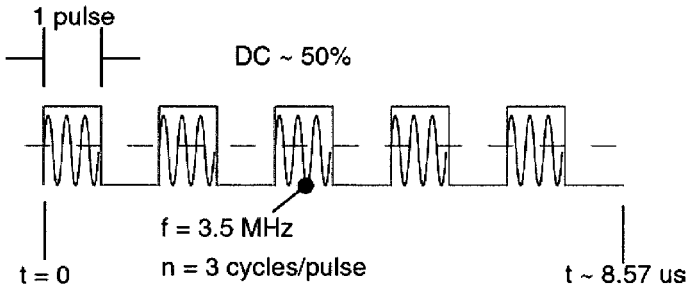

Figure 2.9 Example of burst mode operation at a duty cycle of 50% shows that five complete bursts or pulses, each with three cycles of 3.5 MHz ultrasound, takes a total time of 8.57 us.

The pulse repetition frequency (PRF) is defined as the number of times per second the crystal is generating an ultrasound pulse or burst. The pulse duration (PD) is the time that the transducer is generating the ultrasound burst. Some authors have defined it as the number of half cycles in which the peak amplitude is greater than 0.25 of the maximum pulse amplitude (Ziskin and Lewan 1993).

It can be calculated as:

Eq. 2.39 $$PD = \frac{n}{f}$$

where n is the number of cycles in the pulse, and f is the operating frequency of the transducer. Multiplying the PRF by the PD results in the duty cycle (DC), or the fraction of time the transducer is on:

Eq. 2.40 $$DC = (PD)(PRF)$$

A phenomenon known as ringing may occur when a transducer is subjected to a short excitation pulse, resulting in the continued expansion and contraction of a crystal after the excitation pulse is turned off. In diagnostic ultrasound, damping mechanisms are often required to reduce ringing artifacts, which adversely affects the axial resolution of the transducer (Ziskin and Lewan 1993). However, in HIFU, the pulse durations are long enough to avoid ringing.

2.13.2 Power settings

The higher the acoustic power output from the transducer, the higher the intensity at the HIFU focus. As discussed in Section 2.12.5, the acoustic power is dependent on the electrical power input and the transducer efficiency. The electrical power is limited by the power the amplifier can generate. On the other hand, operating the transducer at powers greater than it can handle may result in overheating and transducer failure. At continuous wave operation, the electrical output power is dependent on the amplifier gain as well as the excitation voltage applied to the amplifier input, set using a waveform generator. During pulsed mode operation, the electrical output power is also dependent on the duty cycle.

2.14 HIFU INTENSITY

Determining the energy density required and deliverable to the tissue of interest is of great importance to any HIFU application. This energy density is commonly referred to as the HIFU focal intensity. The intensity of ultrasound at the transducer surface is dependent on hardware and operator defined parameters, and then decreases as the wave propagates through tissue due to attenuation (absorption and scattering) and reflections at tissue interfaces, as shown in Figure 2.10.

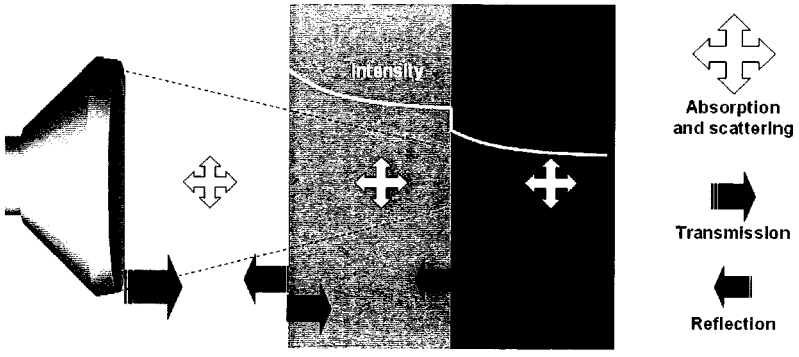

Figure 2.10 Changes in focal intensity during HIFU energy propagation is due to absorption and scattering through layers of media, and transmission and reflection at the boundaries between two media of different acoustic impedances.

Focal intensity is dependent on a multitude of parameters explored in this chapter, and is summarized in the following equations. The overall intensity at the focus is defined as:

Eq. 2.41

$$I_{focus} = (I_{transducer})(Gain)(DC)(Transmission_{total})(Attenuation_{total})$$

$I_{transducer}$ is defined as the emitted intensity at the lens surface of the HIFU transducer:

Eq. 2.42

$$I_{transducer} = \frac{P_A}{A_T}$$

where A_T is the area of the transducer and P_A is the acoustic power emitted by the transducer. P_A can be defined as:

Eq. 2.43

$$P_A = P_E \eta$$

where P_E is the electrical power feeding the transducer, measured using an electrical power meter, and η is the transducer electroacoustic efficiency, determined using a radiation force balance, described in Chapter 4.

The transducer gain is the ratio of transducer area A_T to the cross-sectional area of the focus, determined using a needle hydrophone generated acoustic field map, described in Chatper 4.

Eq. 2.44

$$Gain = \frac{A_T}{A_F}$$

The duty cycle (DC) is defined in Eq. 2.40, and is dependant on the pulse duration (or burst length) and pulse repetition frequency of the waveform signal feeding the ultrasound transducer.

The total transmission is the product of all intensity transmission coefficients at boundaries between media (Figure 2.10), defined in Eq. 2.11 as

Eq. 2.45

$$Transmission_{total} = \left(\frac{4Z_2Z_1}{(Z_2+Z_1)^2}\right)\left(\frac{4Z_4Z_3}{(Z_4+Z_3)^2}\right)\left(\frac{4Z_iZ_j}{(Z_i+Z_j)^2}\right)....etc$$

where $Z_{1,2,3,4,i,\text{ and } j}$ are the acoustic impedances of different media that the ultrasound travels through, defined by Eq. 2.5 as the density multiplied by the speed of sound of the specific medium.

The total attenuation is defined by the attenuation coefficients (α) of the different media that the ultrasound travels through, and the depth of each medium (x):

Eq. 2.46 $$Attenuation_{total} = e^{-2(\alpha_1 x_1 + \alpha_2 x_2 + \ldots + \alpha_i x_i)}$$

Figure 2.11 shows how these formulas fit together to define intensity. If the acoustic impedances between tissue layers are similar, the transmission values will be close to 1 and can be ignored.

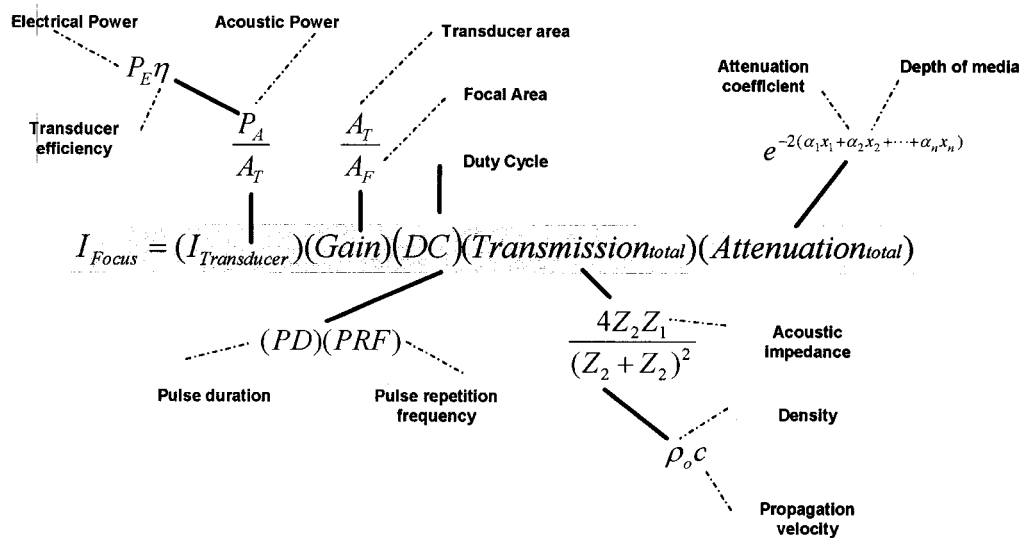

Figure 2.11 Focal intensity is dependent on many HIFU hardware settings and properties of various media that the HIFU propagates through

Intensity can be defined in different ways depending on how it was measured, as shown in Figure 2.12. It is important to define whether the intensity is averaged or a peak value in time or space. Spatial average is often defined as the full-width at half-maximum (FWHM) intensity or the average intensity over a -6dB contour of an acoustic field map (described in detail in section 4.4.2). Intensity can also be defined at the transducer surface as $I_{SATA,T}$, which is the time average intensity over the transducer aperture.

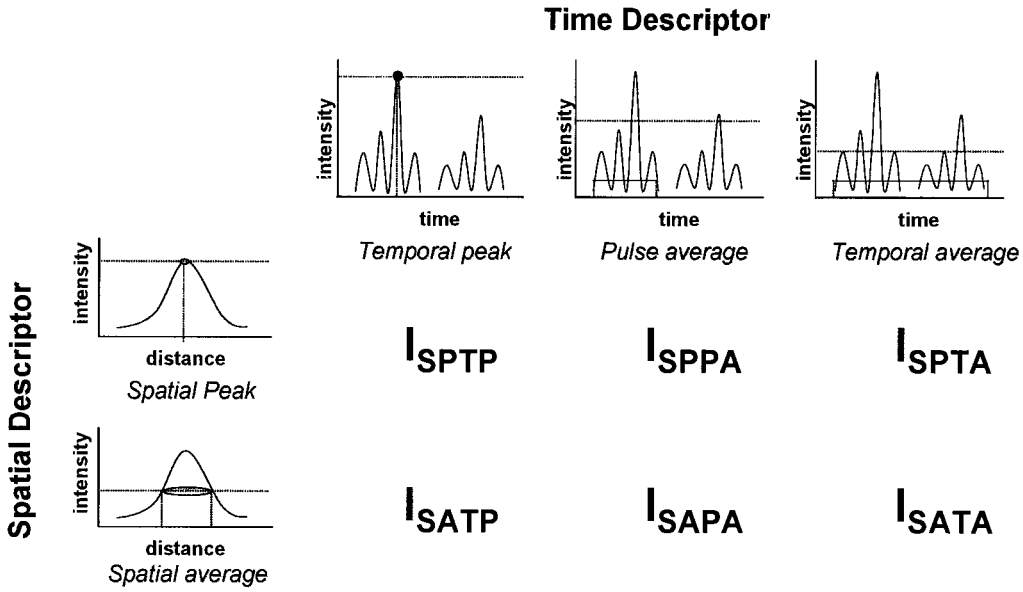

Figure 2.12 Definitions of intensity are based on averaging over time or space and is commonly defined in six different ways. The horizontal black lines indicate intensity value and the horizontal red lines indicate the time over which the intensity is averaged.

3.0 CHAPTER 3 UTERINE LEIOMYOMA

3.1 INTRODUCTION

Uterine leiomyoma (plural: leiomyomata, also known as fibroids or myoma) are benign smooth-muscle tumors of the uterus common in women of reproductive age. Fibroids are a major cause of abnormal uterine bleeding and their growth has been shown to be dependent on estrogen and progesterone, both ovarian steroid hormones (Nowak 1999). Genetic predisposition may also have a role in the formation and growth of these tumors, although a specific gene responsible for the development of leiomyomata has not been identified (Cramer 1992). Fibroids usually range in size between 1 and 20 cm in diameter, and leiomyomata as large as 100 pounds have been reported (Stovall 2001). This chapter provides an insight into uterine leiomyomata: their significance, pathology, symptoms, and currently available treatments. A review of literature addressing ultrasonic characteristics of fibroids relevant to leiomyomata will also be presented.

3.2 SIGNIFICANCE AND EPIDEMIOLOGY

Uterine fibroids are the most common indication for hysterectomy. Uterine fibroids accounted for approximately half of all hysterectomies (600,000 procedures / year) in the United States between 1980 and 1993 (Lepine, Hillis et al. 1997), costing $2-3 billion US / year. It has been shown that they may be present in as many as 77% of women of reproductive age (Buttram and Reiter 1981), although are only symptomatic in about 25% (Cramer and Patel 1990; Andersen and Barbieri 1995). Most women are in their 30s and 40s when fibroids become symptomatic, and symptomatic fibroids increase to more than 40% of women over 40 years of age (Hendrickson and Kempson 1980). In one study, 69% of 1,245 women who underwent hysterectomy for non-cancerous reasons had leiomyoma (Kjerulff, Langenberg et al. 1996). This study also showed variability among ethnic groups, suggesting genetic predisposition: 89% of black women and 59% of white women had leiomyomata. Black women were also shown to be younger at the time of diagnosis and hysterectomy, and had a more severe problem in terms of higher uterine weights and a greater chance of anemia. Prospective studies showed that premenopausal

black women were more than three times as likely as white women to develop fibroids. (Marshall, Spiegelman et al. 1997)

Besides age and race, other factors have been proven to affect the likelihood of uterine fibroids. Although contraindicated for women with myomas, oral contraceptives proved to protect against clinically evident fibroids (Ross, Pike et al. 1986; Marshall, Spiegelman et al. 1998; Chiaffarino, Parazzini et al. 1999). However, one study showed that exposure to oral contraceptives between ages 13 and 16 increased the relative risk of fibroids, while use in general showed protection in direct proportion to the duration of use (Marshall, Spiegelman et al. 1998). Since there was the reduction or absence of the menstrual cycle in taking contraceptives or being pregnant respectively, a hypothesis was made that myoma may be formed as an injury response to hypoxia in myometrial cells during menstruation (Stewart and Nowak 1998).

3.3 PATHOLOGY OF UTERINE LEIOMYOMATA

Leiomyomata are benign smooth-muscle tumors that affect the body of the uterus, but may also be found in the cervix, broad ligament, and even the ovary. Myoma development is comprised of two components: transformation of normal myocytes into abnormal myocyctes, and their growth into clinically apparent tumors via clonal expansion (Stewart 2001). As shown in Figure 3.1 and Table 3.1, leiomyomata develop in various locations throughout the myometrium, are classified based on their location, and have different symptoms (these symptoms are discussed in detail in section 3.4). Submucosal fibroids, which account for 5% of all leiomyoma, are the most symptomatic since they may induce atrophy or erosion of the mucosal surface and cause intermenstrual bleeding. Fibroids located near the endometrium or serosa layers of the uterus are named submucosal and subserosal, respectively. Submucosal and subserosal fibroids may protrude into the uterine cavity or into the peritoneal cavity.

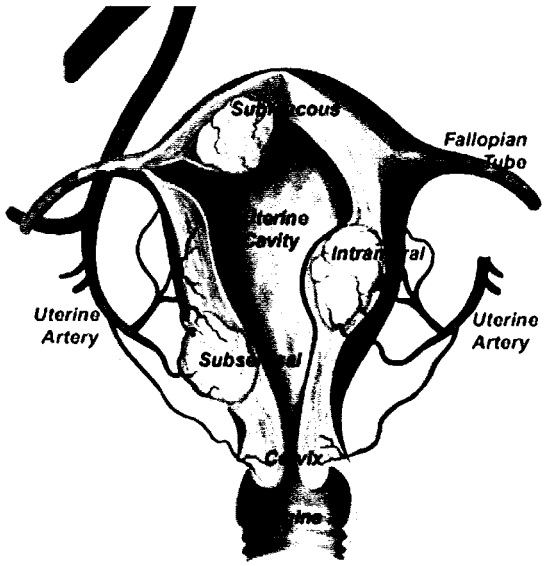

Figure 3.1 The various types of leiomyomata are classified based on their location in the uterus

Table 3.1 Summary of uterine fibroid types and their symptoms

Fibroid type	Location	Symptoms
Subserosal	Under the outside covering of the uterus and expand outward through the wall, may be pedunculated and appear to be an ovarian mass	Pelvic pain, back pain, generalized pressure in abdominal region
Intramural	Within the lining of the uterus, expand inward, most common fibroids	Heavier menstrual bleeding, pelvic pain, back pain, pressure
Submucosal	Under the endometrium or lining of the uterus, least common fibroids	Cause the most problems – heavy bleeding

Fibroids have a distinct histopathological appearance. Fibroid were described as firm and rubber-like to the touch, and a cut surface of a fibroid exhibited a spiral pattern of fibers (Robboy, Bentley et al. 2000). Fibroids may also be surrounded by a thin capsule. This encapsulation is most apparent in intramural fibroids and contains a blood supply and smooth muscle bundles interspersed with connective tissue strands (Robboy, Bentley et al. 2000). Fibroids were noted as more pale than the surrounding tissue and a sharp line of demarcation between the tumor and the surrounding myometrium has been observed

(Robboy, Bentley et al. 2000). This sharp demarcation was prominent under microscopic analysis: normal smooth-muscle cells were elongated and had eosinophilic cytoplasm and elongated cigar-shaped nuclei, whereas the smooth-muscle cells of a leiomyoma were more closely packed than those of the surrounding myometrium, had uniform nuclei, absent mitotic figures, and abundant reticulin (Robboy, Bentley et al. 2000).

3.4 SYMPTOMS OF UTERINE LEIOMYOMATA

3.4.1 Abnormal bleeding

The most common symptom among women with leiomyomata is abnormal or excessive bleeding. An increase in blood loss per month, menorrhagia and prolonged vaginal bleeding may occur. A recent study showed that women with abnormal bleeding were significantly more likely to have either an intramural (58% vs. 13%) or submucous leiomyoma (21% vs. 1%) than women with normal bleeding (Clevenger-Hoeft, Syrop et al. 1999). Growth factors associated with leiomyomata may have had effects on vascular function and angiogenesis triggering vascular abnormalities that lead to menorrhagia (Stewart and Nowak 1996). Other proposed mechanisms of abnormal vaginal bleeding included an increase in the endometrial surface area and vascular flow, interference with normal uterine contractility, and endometrial ulceration over a submucous leiomyoma. (Stovall 2001)

3.4.2 Pelvic pain and urinary symptoms

Pelvic pain or pressure, analogous to the discomfort women experience during pregnancy, is the second most common symptom of leiomyomata. The severity and location of pain or pressure is usually associated with the location and size of the leiomyoma (Stovall 2001). Leiomyomata may cause lower abdominal pain, pain during urination and pregnancy, and may even compromise respiratory function. Women with leiomyomata may experience difficulty with urination, and experience incontinence due to bladder capacity changes and compromised ureters.

3.4.3 Reproductive dysfunction

Although no data has been published to assess whether the proportion of infertile women with leiomyomata is greater than the proportion of normal fertile women with leiomyomata, there have been several proposed mechanisms for how leiomyomata may impair reproductive function. One study hypothesized that large leiomyomata may impair the rhythmic uterine contractions that facilitate sperm motility through the uterus (Coutinho and Maia 1971). Since the histology of endometrial tissue near a fibroid is altered, implantation of the embryo and compliance for uterine growth may also be affected (Deligdish and Loewenthal 1970). Furthermore, leiomyomata have been documented to alter vascular flow which may lead to reduced hormone delivery and endometrial hyperplasia resulting in reproductive dysfunction (Stovall 2001).

3.4.4 Complications during pregnancy

During pregnancy, there is an increase in both estrogen and progesterone, hormones associated with the growth of fibroids. However, only 20-30% of leiomyomata increase in size during pregnancy and leiomyomata that did increase in volume did not increase by more than 25% (Aharoni, Reiter et al. 1988; Rosati, Exacoustos et al. 1992; Strobelt, Ghidini et al. 1994). Coronado et al. recently performed the only large population based study investigating the effects of fibroids on pregnancy complications and found that the pregnancies of women with leiomyomata had significantly higher risk for first-trimester bleeding, premature rupture of membranes, prolonged labor, breech babies, caesarian section, and low birth-weight (Coronado, Marshall et al. 2000).

3.4.5 Leiomyoma growth and transition to leiomyosarcoma

In the past, leiomyosarcomas (uterine cancer) were thought to be associated with rapid growth of fibroids. This thought would dictate clinical treatment because hysterectomy would be chosen over lower-key fibroid management techniques (Stovall 2001). Recently, a study of over 1300 hysterectomies that were due to rapidly growing fibroids showed that only 0.3% had leiomyosarcomas. This study also showed that leiomyosarcomas were not diagnosed any more frequently in women who had rapidly growing fibroids than in women who had fibroids that were not rapidly growing. It is

still important not to misinterpret benign fibroids as malignant leiomyosarcoma. Endometrial biopsy, ultrasound, and MRI are useful in differentiating sarcomas from myomas (Schwartz, Diamond et al. 1993).

3.5 MOST COMMON TREATMENTS FOR UTERINE LEIOMYOMATA

Table 3.2 summarizes the currently available treatments for uterine fibroids, their advantages and disadvantages.

Table 3.2 Uterine fibroid treatments

Treatment	Description	Advantages / successes	Disadvantages / side-effects
Gonadotropin releasing hormone agonists (GnRH)	GnRH is a drug treatment that causes uterus shrinkage and leiomyomata to decrease in size 35-65% (Shaw 1991). Coagulative necrosis may occur (Colgan, Pendergast et al. 1993).	When used as an adjunct to surgery, shrinkage of fibroid may reduce need for transfusion (Stjernquist 1997).	Most fibroids return to their original size once the treatment is stopped or within a year even if treatment is continued.
Uterine Artery Embolization (UAE)	Selective arterial embolization involves puncturing the femoral artery. Catheterization of the hypogastric and uterine arteries is performed, then polyvinyl alcohol particles are introduced until complete devascularization is achieved.	80% of women have had sufficient improvement in symptoms to avoid subsequent surgical treatment (Pelage, Le Dref et al. 2000). Fibroid shrinkage 48-78 % (Spies, Scialli et al. 1999). Shorter hospital stays than hysterectomy or myomectomy (Wong, Muir et al. 2000).	Pelvic pain 12-18 hours after UAE, temporary amenorrhea and post-procedure menopause (Smith 2000). Serious complications of major sepsis or death are rare but more likely when there is a single large myoma (Goodwin and Walker 1998; Wong, Muir et al. 2000).
Hysterectomy	Removal of entire uterus.	Eliminates symptoms and chance of recurrence	Reproductive potential lost, risk for urinary tract infection

Treatment	Description	Advantages / successes	Disadvantages / side-effects
Abdominal Myomectomy	Removal of myomas via open abdominal surgery, suitable for large or multiple fibroids .	Uterus conservation Permits healthy pregnancies after surgery (risk of uterine rupture low).	Recurrence is high – 50% of women at 5 years (Pelage, Le Dref et al. 2000). Recurrence after second operation ranges from 11 to 26 % (Malone 1969; Buttram and Reiter 1981).
Laparoscopic myomectomy	Laparoscopic removal of small subserosal or intramural fibroids .	Shorter recovery period than with abdominal myomectomy (Donnez, Mathieu et al. 1996).	Larger, multiple or deep fibroids problematic (Donnez, Mathieu et al. 1996).
Laparoscopic Myolysis	Variation of laparoscopic myomectomy in which the fibroid tissue is coagulated rather than removed (Goldfarb 2000).	Less complicated than removal, no suturing	Localized destruction without repair may increase the chance of uterine rupture (Arcangeli and Pasquarette 1997).
Hysteroscopic myomectomy	Treatment for accessible submucosal fibroids - endoscope is inserted in cervix and fibroid is resected	Outpatient procedure that has short recovery period	32% failure rate in 2 years with high rate of endometriosis (52%) (Hallez 1996). Endometriosis is the presence of endometrial glands and supporting tissues in the muscle of the uterus where it would not occur normally.

3.6 ACOUSTIC PROPERTIES OF UTERINE LEIOMYOMATA

It is important to know the acoustic properties of the targeted tissue in calculating HIFU treatment energy absorption and transmission. More specifically, the attenuation coefficients and speed of sound for myometrium and fibroids are of interest. Fortunately, these properties have been empirically determined in several studies, with results shown in Table 3.3.

Table 3.3 Acoustic properties of uterine tissue and fibroid tissue

Study	Type	Test Freq (MHz)	Sound Speed (m/s)		Attenuation (dB/cm/MHz)	
			Myometrium	Fibroid	Myometrium	Fibroid
Keshavarzi et al. (2001) (Keshavarzi, Vaezy et al. 2001)	*In vitro*	3.0	1615 ± 10	1617 ± 5	0.5 ± 0.1	0.77 ± 0.1
Bhatia and Singh (2001) (Bhatia and Singh 2001)	*In vitro*	3.5	1553	1550	0.86	1.23
Masaoka et al. (1987) (Masaoka, Akamatsu et al. 1987)	*In vivo*	3.5			0.89 ± 0.2	0.61 – 1.75
Siddiqi et al. (1999)	*In vivo*	3.0			0.6 ± 0.5	
Mean					0.713	1.06

The study by Masaoka et al. showed that the attenuation coefficient varied proportional to the amount of calcium in the fibroid (Masaoka, Akamatsu et al. 1987). Kesharvarzi et al. demonstrated that after 40-60 seconds of HIFU at 3.5 MHz and 2000 W/cm^2, measured attenuation coefficients and sound speed were respectively 1-2 dB/cm and 1-15 m/s higher than before HIFU (Keshavarzi, Vaezy et al. 2001). The increase in attenuation was attributed to the loss of tissue fluid and presence of gas bubbles in the HIFU treated area. These acoustic properties allow for estimating HIFU intensity during treatment, as explored in section 10.1.

3.7 PREVIOUS WORK ON HIFU AND UTERINE FIBROIDS

Three studies performed at the University of Washington prior to this project demonstrated the potential for HIFU to be used for treating uterine tumors. The first study involved HIFU treatment of athymic nude mice that were subcutaneously inoculated with ELT-3 uterine fibroid tumor cells (Vaezy, Fujimoto et al. 2000). HIFU used at an intensity of 2000 W/cm^2 and a frequency of 3.5 MHz at exposure durations of 30 to 60 seconds resulted in complete tumor shrinkage in 16 out of 28 animals within 3 to 4 weeks. 11 out of the 28 animals showed tumor re-growth, of which 5 were given a second treatment resulting in complete tumor shrinkage. A second study was performed on an Eker rat model, a validated animal model for fibroids, allowing an *in situ* study to be performed (Keshavarzi, Vaezy et al. 2002). HIFU (3.5 MHz) at an intensity of 2000 W/cm^2 was used for treating fibroids, and 70% of the treated animals had a reduction in tumor volume after HIFU application. Finally, 65 athymic nude mice with uterine leiomyosarcoma (ELT-5B) cancer cells were treated with 2.0 MHz HIFU at an intensity of 2000 W/cm^2 (Keshavarzi, Vaezy et al. 2002). In all but one animal, a complete reduction in tumor volume was observed after a single HIFU treatment. In the animal that continued tumor growth, a second treatment resulted in a complete reduction in tumor volume. Sham and control animals saw tumor growth up to 5 times initial size. These studies led to the desire to develop a device for HIFU treatment of fibroids, and study the potential for such a device to be used clinically.

4.0 CHAPTER 4 IMAGE-GUIDED HIFU DEVICE VERSION 1: DESIGN, DEVELOPMENT AND CHARACTERIZATION

4.1 INTRODUCTION

Chapters 2 and 3 explored the capabilities of HIFU, the significance of uterine leiomyoma, and indicated potential for image-guided HIFU in treating uterine leiomyoma. An image-guided transvaginal HIFU device was designed and constructed to explore this potential. The first iteration of the device was named "Version 1" as modifications to the applicator were later performed, detailed in Chapter 6. Section 4.2 provides an overview of the device. The following section (4.3) provides an in-depth analysis of the device design and development: preliminary calculations, ultrasound lens design and modeling, and device construction. Finally, section 4.4 discusses acoustic measurement techniques used to characterize the HIFU transducer.

4.2 DEVICE OVERVIEW

4.2.1 Modality of imaging and HIFU

The first goal in designing this device was to determine how the HIFU was to be administered to the uterus. The two approaches were a treatment path via the abdomen (transabdominal) or via the vagina (transvaginal). A transvaginal versus transabdominal treatment approach was chosen since it provided the shortest acoustic path to the uterus, as shown in Figure 4.1 (0.5 cm from the vaginal fornix to the uterus versus > 4 cm via the abdomen depending on bladder size and the amount of subcutaneous fat). As shown in Section 2.14, treatment path distance and the number of tissue layers the treatment propagates through should be minimized to maximized HIFU intensity at the focus. Therefore, a transvaginal approach was chosen since large attenuation losses are associated with the abdominal path (due to losses in skin, fat, abdominal wall and bladder fluid) (Siddiqi, O'Brien et al. 1992; Siddiqi, Miodovnik et al. 1999). An estimate of the total attenuation associated with each path is shown in Table Table 4.1. With the estimated depths of each tissue type shown in Table 4.1 and attenuation values presented, the intensity at the focus using a transvaginal treatment path is 75% of the incident intensity at the transducer, versus 4% using a transabdominal path. Therefore, based on these assumed depths and attenuation values, the transvaginal treatment path results in 18.6 times more HIFU intensity at the focus than the transabdominal treatment path for a given incident intensity.

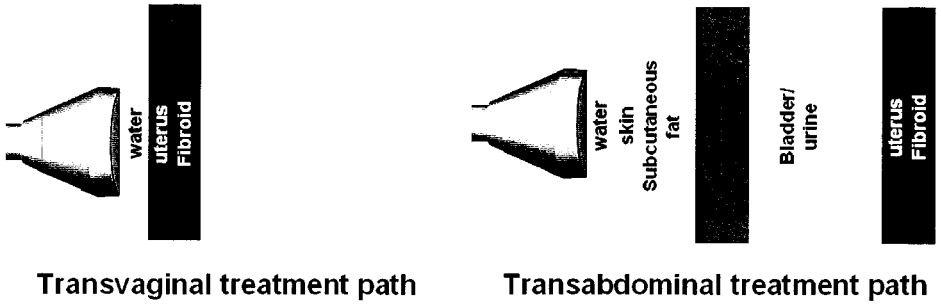

Figure 4.1 Comparing the transvaginal versus transabdominal treatment path shows that fewer tissue layers are traversed using a transvaginal approach resulting in less attenuation through tissue layers and reflection between tissue layers.

Table 4.1 Estimated intensities at the focus (Ix) for a given intensity emitted by the HIFU transducer (Io) for the transvaginal and transabdominal treatment paths.

Transvaginal path	attenuation coefficient Np/cm	estimated depth cm	Ix / Io	Source
uterus	0.0820	1	0.849	Table 3.3
fibroid	0.1219	0.5	0.885	Table 3.3
		Total depth	Total Ix/Io	
		1.5	0.751	

Transabdominal path	attenuation coefficient Np/cm	estimated depth cm	Ix / Io	Source
skin	0.197	0.1	0.961	NCRP
subcutaneous fat	0.245	2	0.375	NCRP
abdominal muscle	0.250	1.5	0.472	NCRP
bladder wall (muscle)	0.700	0.4	0.571	NCRP
urine	0.099	3	0.551	NCRP
uterus	0.082	1	0.849	Table 3.3
fibroid	0.122	0.5	0.885	Table 3.3
		Total depth	Total Ix/Io	
		8.5	0.0403	

Attenuation values were derived from Table 3.3 or from the National Council on Radiation Protection (NCRP) report No. 74.

The next step was to determine how the ultrasound image-guidance would be incorporated. The problem was approached initially by attaching a transvaginal HIFU transducer to a transvaginal ultrasound image probe (C9-5, Philips Medical Systems, Bothell, WA) as shown in Figure 4.2. The device ended up being larger than deemed acceptable for human use (the maximum diameter of the transducer was > 5 cm). The attachment of the HIFU transducer also partially obscured the ultrasound image.

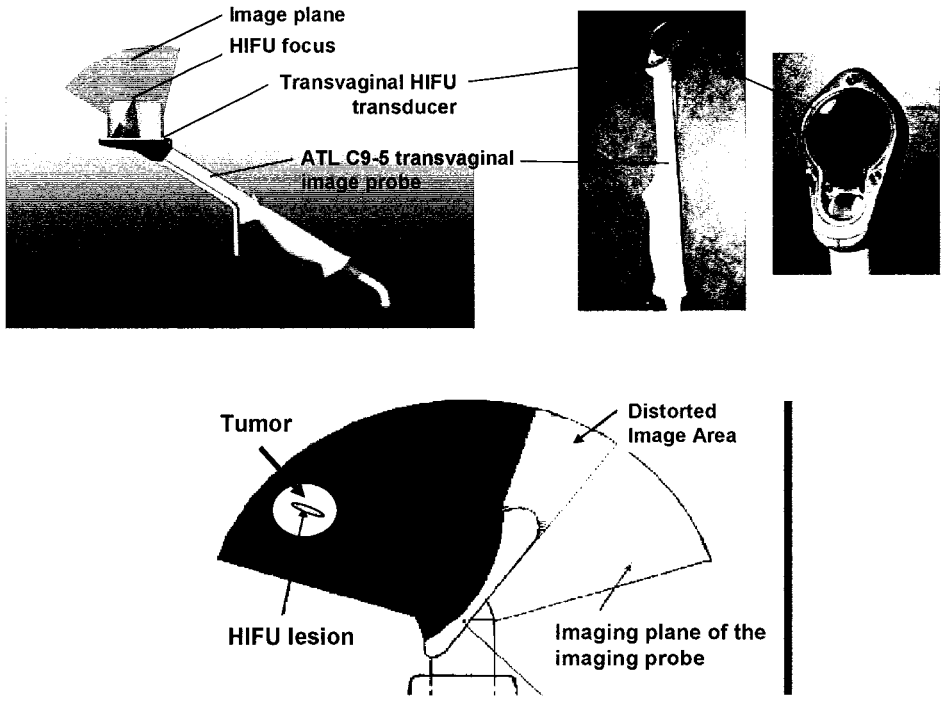

Figure 4.2 Prototype vaginal HIFU transducer attached to transvaginal image probe was deemed too large for human use. The position of the HIFU transducer also distorted the image plane of the imaging probe.

It was then determined that the ultrasound image-guidance would be best performed transabdominally while the HIFU would still be applied transvaginally. However, this required the image probe and the HIFU transducer to be aligned so that the HIFU focus was coincident with the image plane of the image probe at all times. A rather simple but novel approach emerged. A conceptual drawing of the device, and how it would be placed in a human is shown in Figure 4.3.

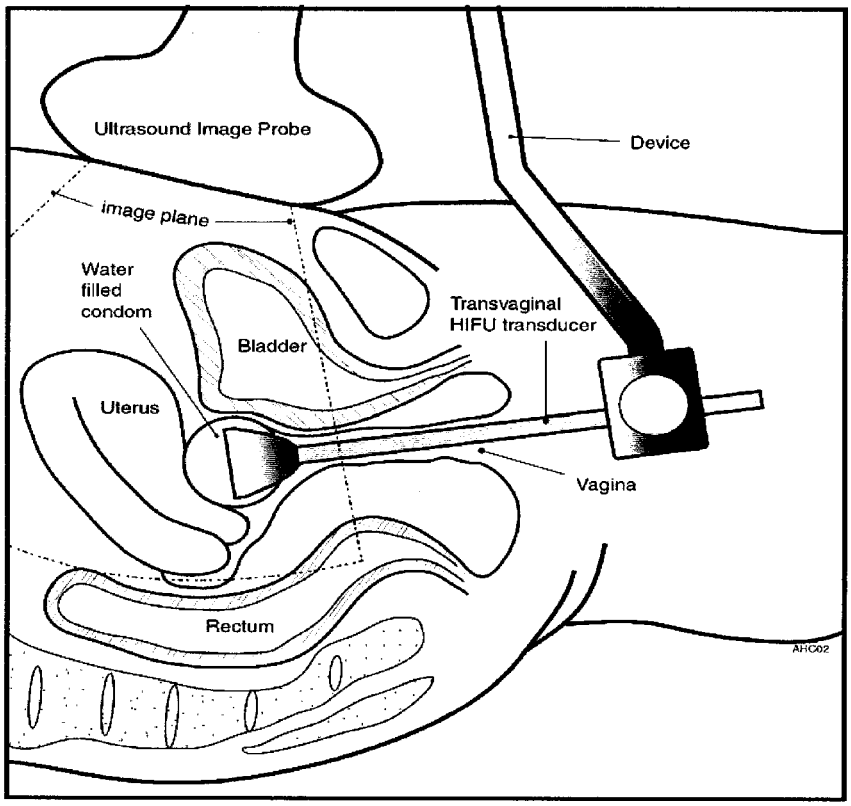

Figure 4.3 Conceptual drawing of device in use in a human. An abdominal image probe is used to visualize the transvaginal HIFU transducer and pelvic structures including the uterus. (Drawing is not to scale – for illustration only)

4.2.2 *Selection of ultrasound image probe*

Following the abdominal imaging approach, a curved array transducer would be used for the imaging component of the device. Two abdominal imaging probes were considered due to availability in our laboratory: C7-4 (Philips Medical Systems, Bothell, WA) and C60 (SonoSite Inc., Bothell, WA). The foremer operates at 7-4 MHz, and the latter at 4-2 MHz. Both imaging probes could be easily integrated into the device and both were suitable (in terms of weight and size) for a hand-held device. The selection was thus based on the ultrasound machine that the probe would be compatible with. The C7-4 would be used with an HDI 1000 or 5000 (Philips Medical Systems, Bothell, WA), and the C60 would be used with the SonoSite (SonoSite Inc., Bothell, WA). Although the HDI machines have Doppler capabilities and better resolution, the portability of the SonoSite unit was more appealing for our device. The SonoSite would also be more practical if the device were to be used in a clinical setting where the device would be moved from room to room to treat patients. Therefore, the C60 image probe was selected for the imaging component of the device.

4.2.3 Design requirements

A set of criteria was defined for the initial design requirements, shown in Table 4.2. These were based on feedback received from clinicians, physicians, and technicians involved with this project.

Table 4.2 Design Criteria and Solutions

Parameter	Criteria	Design Solution
Weight / comfort	The device was to be hand held and used for treatment times up to an hour.	The majority of device components would be made of hollowed out lightweight aluminum (6061-T6).
Sterility	The device must be sterilizable, and a means for covering the device with a sterile membrane must be provided.	The device could be gas sterilized, and the transvaginal HIFU transducer would provide means for attaching a sterile condom
Accommodation	The device should accommodate women of various mass and vaginal lengths.	The device would allow horizontal adjustment of the HIFU transducer and varying of the distance between the HIFU transducer and the image probe
Functionality	The device must be simple to use requiring little time for set-up.	Adjustment knobs would be used to enable device set-up and operation without external tools. All moveable components of the device could be locked in place.
Compatibility with image probes	The device should be able to be used with various makes and models of abdominal ultrasound image probes.	An adjustable two-piece clamp would be used to lock the image probe in place.
Image control	The device should enable fine-tuning of the ultrasound image position while ensuring the focus can still be visualized.	Rotation of the image probe would be allowed in one plane to allow fine tuning while ensuring the focus was still in the image plane.
Aperture size	The HIFU transducer must be small enough to be used in the human vagina while large enough to provide adequate HIFU energy for treatment.	The HIFU transducer would have a maximum diameter of 40 mm. From previous experimentation (not shown here), transducers with piezoceramic crystals of 23 mm have demonstrated deep lesion formation.
Focal Length	The HIFU focal location should be able to reach fibroids in various locations of the uterus while ensuring that the f-number (focal distance divided by aperture diameter) is close to 1.	The HIFU transducer would have a HIFU focal distance of 40 mm. An anatomical study (Section 4.2.5) proved that this should be sufficient for treating fibroids in various locations of the uterus.

4.2.4 Frequency Selection

The frequency chosen should be low enough for the HIFU to penetrate the uterine tissue to the focal depth, while high enough to ensure a small enough focal spot to achieve high intensities at the focus. Also, since the absorption of HIFU energy by tissue is positively correlated with frequency, the frequency needed to be high enough to ensure sufficient absorption for lesion formation. As shown previously in Figure 2.8, the optimal frequency for a HIFU transducer should result in an attenuation loss in tissue (0.7 dB/cm/MHz) of about 10 dB at the focal depth (Hill 1994). A treatment depth of 4 cm was deemed appropriate for treating the entire uterus while the transducer is in the vaginal fornix. Therefore, a frequency of 3.5 MHz was chosen for the transducer. This frequency of HIFU was also shown to be successful in treating fibroids in a mouse model (Keshavarzi, Vaezy et al. 2002).

4.2.5 Anatomical constraints and geometry

A study of the female pelvic anatomy was performed to determine the optimal geometry and dimensions of the device. Images from the Visible Human Project (National Library of Medicine, National Institute of Health), Gray's anatomy (Gray 1918), pelvic ultrasounds, and uterine fibroid patient data files were used. The anatomical study revealed vaginal lengths ranging from 6 to 11 cm, uterine lengths from 5 to 9 cm and uterine widths ranging from 2 to 6 cm. A focal length of 4 cm was deemed sufficient for this device to treat fibroids through the width of the uterus from the vaginal fornix as shown in Figure 4.3. Existing transvaginal ultrasound image probe dimensions were also used for reference. Commercially available transvaginal image probes had lengths ranging from 120 to 180 mm, and maximum diameters from 18.5 to 31 mm (excluding the handle). Various configurations of the device (not shown) were modeled with SolidWorks (SolidWorks corporation, Concord, MA) design software to determine optimal sizes of device components and geometry based on these findings.

4.2.6 Device mobility

A conceptual image of the device is shown in Figure 4.4. With the exception of the transducer housing (section 4.2.7), all device components were made of aluminum. The device allowed motion in three degrees as shown by the numbers in Figure 4.4: (1) 90° rotation of the image probe independently of the device allowing for the image probe to contour to the body and for image adjustment while ensuring the HIFU focus remained in the image plane, (2) horizontal movement of the image probe and HIFU transducer to accommodate vaginal lengths between 6 and 15 cm and various fibroid locations, and (3) variable vertical separation of 5-15 cm between the image probe and HIFU transducer enabling it to be used in women of different sizes and with varying amounts of body fat.

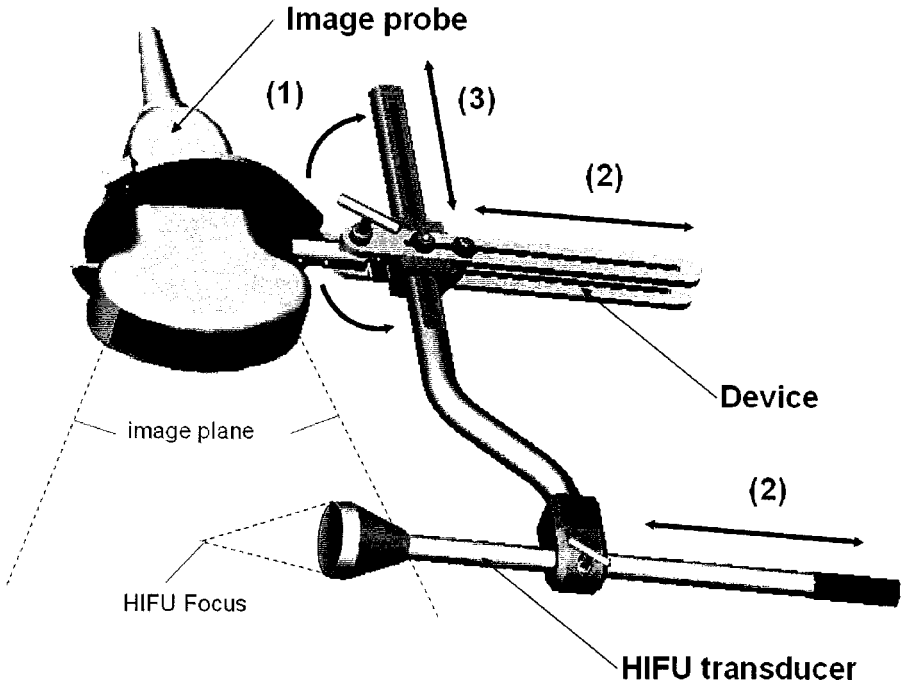

Figure 4.4 Conceptual drawing of "Version 1" device. The image probe can be moved vertically and horizontally relative to the HIFU transducer, and can also be rotated to adjust the image position for optimal visualization. The device was mechanically aligned such that the HIFU focus was in the image plane of the image probe.

4.2.7 *HIFU Transducer and water-filled condom*

The transvaginal HIFU transducer design consisted of a piezoceramic element attached to an aluminum lens, a brass housing, and an aluminum handle, and is shown in Figure 4.5. The design specifics and construction procedure are discussed later in section 4.3.

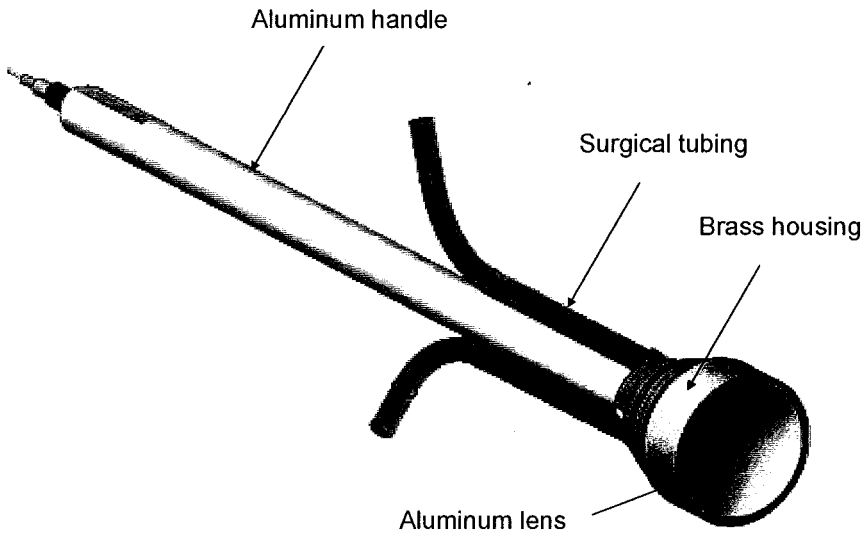

Figure 4.5 The transvaginal HIFU transducer consisted of a flat disk piezoceramic element (not shown) attached to an aluminum lens that focused the ultrasound. The lens and element were contained in a brass housing connected to an aluminum handle. Surgical tubing attached to the brass housing allowed water to be supplied to the transducer for cooling.

Effective acoustic coupling from the ultrasound transducer to the tissue of interest is crucial for successful treatment. There was the potential of air to be trapped between the transducer and the vaginal wall when used *in vivo*, so a method of acoustic coupling to eliminate the pocket of air was devised. As shown in Figure 4.6, the transducer design enabled a latex condom to be fastened to the outside of the brass housing using a rubber o-ring. This condom could be filled with degassed water from a reservoir using surgical plastic tubing (Tygon S-50-HL, Saint Gobain Performance Plastics, Akron, OH) connected using custom made barb fittings to 1.8 mm diameter channels machined into the brass housing. The water-filled condom provided acoustic coupling from the ultrasound transducer to the treatment site. The water in the condom also circulated to cool the adjacent vaginal wall tissue during treatment, and provide transducer cooling, discussed in Section 4.3.7.

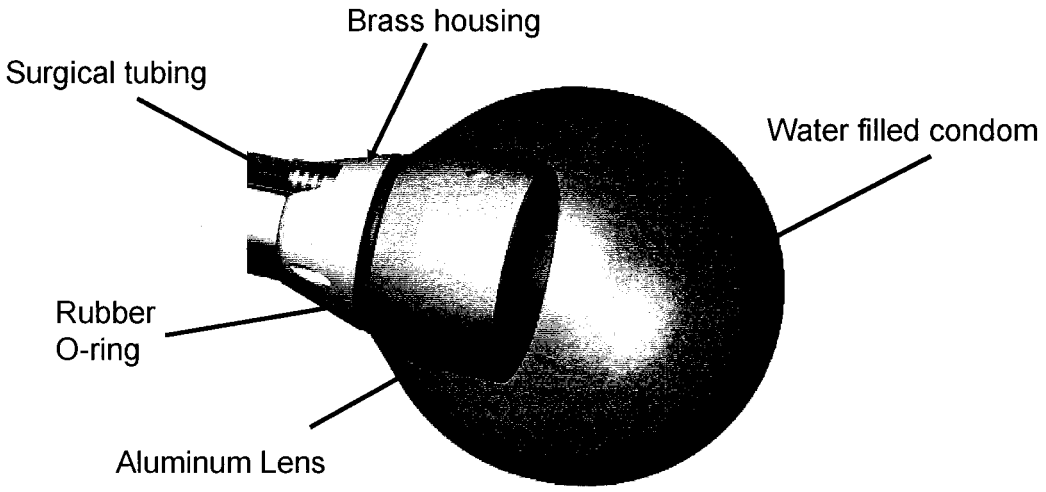

Figure 4.6 A water filled condom was attached to HIFU transducer using a rubber o-ring. Water was supplied to the condom via surgical tubing and holes machined into the brass housing. The water in the condom was circulated to provide cooling.

It was important to ensure that the HIFU transducer can be used to treat various areas of the uterus with a fixed focal length. This was accomplished using two methods, depicted in Figure 4.7. First, the treatment site (depth in the uterus) could be varied by inflating and deflating the condom with water effectively providing a variable treatment stand-off. Second, transducer mobility within the water filled condom and in the vagina would allow the HIFU to be applied to the fundus, mid-uterus, and cervix.

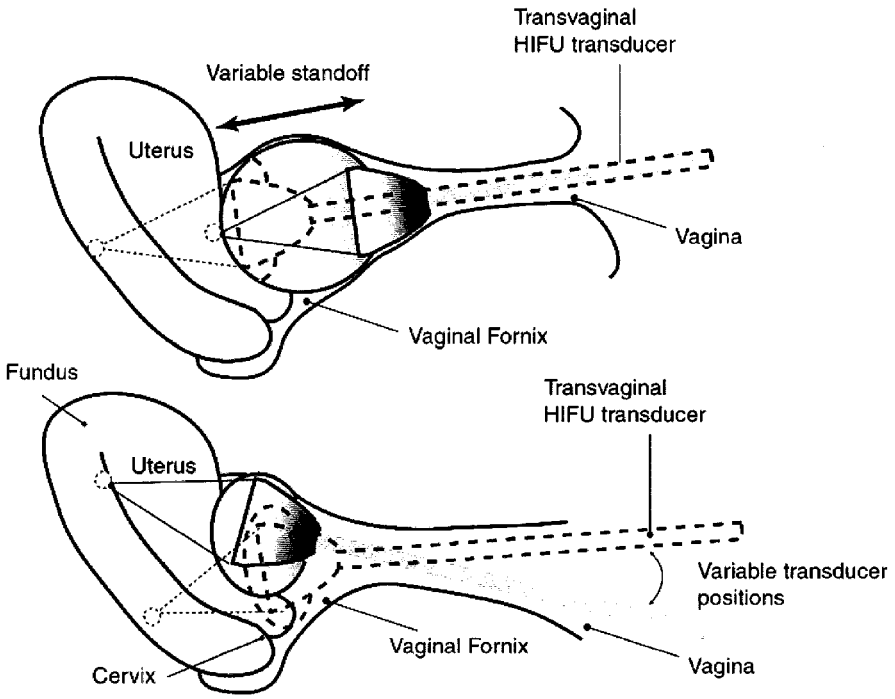

Figure 4.7 The treatment location can be varied by inflating and deflating the water filled condom, and by moving the HIFU transducer within the vagina.

4.3 DEVICE DEVELOPMENT

4.3.1 Preliminary calculations

Several design specific calculations will be discussed in this section. Using equations described in section 2.12.2, a focal distance of 40 mm and a proposed aperture diameter of 25.4 mm (area = 506 mm^2) resulted in a F-number of 1.57. Using Eq. 2.30 and Eq. 2.31, and assuming a frequency of 3.5 MHz, the focal width and focal depth were calculated as 1.6 mm and 3.19 mm respectively in tissue (c~1500 m/s). Using the focal width, the cross sectional focal area was 2 mm^2. Thus, the gain (Eq. 2.28) should theoretically be 253. For a flat disk transducer (proposed for use in this device), the near-field far-field transition distance can be calculated as:

Eq. 4.1 $$d_{ff} = \frac{d^2}{4\lambda}$$

and for d = 25.4 mm, and a frequency of 3.5 MHz in tissue (c~1500 m/s), λ was 0.428 mm and d_{ff} was 376 mm. Therefore a focal distance of 40 mm is in the near field of the transducer beam. This was important to note since convergence of the emitted ultrasound in the near field is preferred. In the far field, the transducer beam diverges.

4.3.2 Piezoceramic selection

A flat crystal and lens design versus a curved crystal was used due to crystal availability, cost, and the possibility of using various lens geometries and focal configurations in the future. We decided to use a PZT-8 equivalent material, APC 880 (American Piezo Ceramics, Duck Run, PA), with c=4113 m/s, and Z=31.26 MRayl. This was selected over the popular PZT-4 material for focused ultrasound surgical applications since PZT-8 is more efficient and thus more powerful[b]. Although PZT-8 is more subject to fracture than PZT-4[c], the lens affixed to the piezoceramic crystal would provide protection for the crystal.

---

[b] PZT-8 is approximately 10% more efficient over the intensity range proposed (1000-5000 W/cm^2): Personal Communications, Butch Bartley, American Piezo Ceramics, Duck Run, PA

[c] Personal communications: Butch Bartley, American Piezoceramics, Duck Run, PA

4.3.3 Acoustic lens design

An aluminum lens (6061-T6, c=6363 m/s, Z=17 MRayl) was used for focusing ultrasound waves. The elliptical concave curved surface of the aluminum lens was calculated such that waves from each point on the surface of the piezoceramic crystal would pass through the lens and arrive at the focus simultaneously, satisfying the in-phase requirement of an acoustic lens, discussed in section **2.11.2**. Aluminum was chosen as material for the lens due to our group's positive experience with using aluminum solid cones for guiding HIFU (Brentnall, Martin et al. 2001). Compared to plastics commonly used for acoustic lenses (section 3.1.2), an experiment using the acoustic calipers method (Bloch 1998) demonstrated that aluminum has a lower attenuation than most plastics (Huynh, Chan et al. 2002). Aluminum is also more durable and scratch resistant than plastic. Furthermore, aluminum also has a relatively low acoustic impedance and attenuation compared to most metals (Selfridge 1985). Aluminum may allow for effective transducer cooling via water circulation over the surface of the lens since it has a high coefficient of thermal conductivity. Referring to Figure 4.8, equations used to determine the shape of the lens are as follows:

Eq. 4.2 $$t_{1i} + t_{2i} = t_o \quad \textbf{where } t_o = \frac{x_f}{c_2} \quad t_{1i} = \frac{x_i}{c_1} \quad t_{2i} = \frac{\sqrt{(x_f - x_i)^2 + (y_i)^2}}{c_2}$$

Where t_{1i} is the time it takes the ultrasound wave to travel through the aluminum lens, t_{2i} is the time it takes the ultrasound wave to travel from the surface of the aluminum lens to the focus through water, and t_o is the direct path to the ultrasound wave in water. The lens shape is defined by equating t_o to t_{1i} plus t_{2i} therefore yielding a quadratic equation in the form of

Eq. 4.3 $$x_i^2\left(1 - \frac{c_2^2}{c_1^2}\right) + x_i\left(2x_f \frac{c_2}{c_1} - 2x_f\right) + \left(y_i^2\right) = 0$$

Solving for coordinates (x_i) in terms of (y_i) results in the solution to the quadratic in the form

Eq. 4.4 $$x_i = \frac{-b \pm \sqrt{b^2 - 4ac}}{2a}$$ **where**

$$a = 1 - \frac{c_2^{\,2}}{c_1^{\,2}} \qquad b = 2x_f\left(\frac{c_2}{c_1} - 1\right) \qquad c = y_i^{\,2}$$

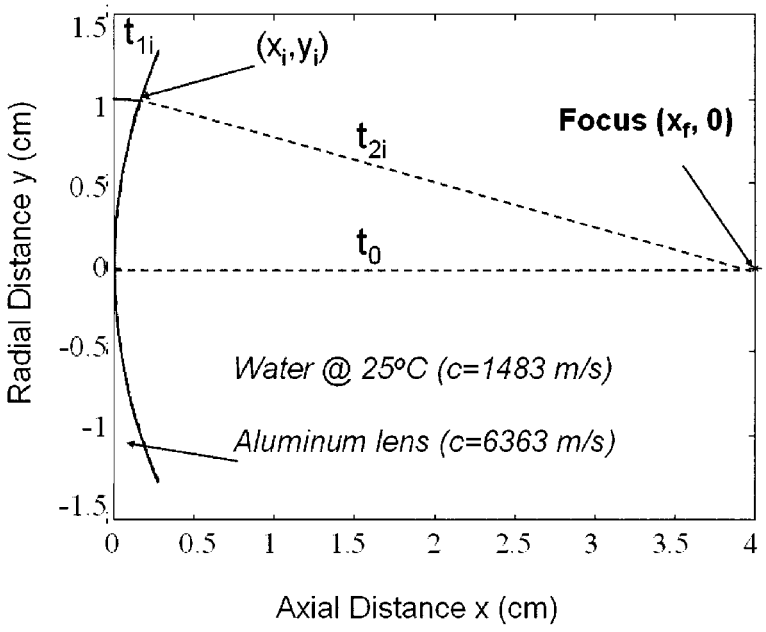

Figure 4.8 This figure shows the curvature of the aluminum lens for ultrasound waves propagating into water. Parameters used in determining elliptical lens curvature are indicated. Since aluminum has a greater speed of sound that water, the lens shape is concave as defined by the equations 4.2 through 4.4 (Chan, Fujimoto et al. 2002).

These equations assume that the minimum thickness of the lens is 0 mm at the center of the lens. However, in reality, the lens will have a small thickness to allow for structural rigidity. As long as the thickness added onto the flat side of the lens is equal at all points, the waves will still arrive at the focus simultaneously. A thicker lens results in higher attenuation, and therefore, the thinnest lens that can be machined and still be structurally rigid was made (lens minimum thickness was 0.3 mm, corresponding to 0.165λ and 0.188λ for aluminum (c=6363 m/s) at 3.5 and 4.0 MHz respectively). The shape of the lens was generated using Matlab code shown in Appendix B, and data points converted to a text file compatible with the CNC lathe used to machine the lenses.

4.3.4 Wave 2000 Pro modeling

Numerical modeling was used to determine the effectiveness of the aluminum lens in focusing ultrasound emitted by a piezoceramic crystal. Wave2000 Pro (Cyberlogic, New York, NY), a software package for computational ultrasonics that analyzed shear and longitudinal waves, was used to determine particle displacements in the acoustic field. The program computed the finite difference solution to the 2-dimensional wave equation. The solution was solved in the form of a mathematical grid in both spatial and temporal domains, based on a published algorithm (Schechter, Chaskelis et al. 1994). Shear and compression coupling and viscous loss attenuation were included in the algorithm. The minimum wavelength of the frequency used in the simulation was used to determine the size each element in the finite difference grid. The format of the wave equation solved by Wave2000 Pro is (Schechter, Chaskelis et al. 1994)

Eq. 4.5
$$\rho\left(\frac{\partial^2 \xi}{\partial t^2}\right)=\left(\mu_L+v_s\frac{\partial}{\partial t}\right)\nabla^2\xi+\left(\lambda_L+\mu_L+v_b\frac{\partial}{\partial t}+\frac{1}{3}v_s\frac{\partial}{\partial t}\right)\nabla(\nabla\bullet\xi)$$

where t represents time, ρ is the material density (kg/m^3), γ_L is the first Lame constant (N/m^2), μ_L is the second Lame constant (N/m^2), v_S is the shear viscosity (N-s/m^2), v_b is the bulk viscosity (N-s/m^2), and ξ is a two-dimensional column vector consisting of the x and y components of displacement of the medium at location (x,y) at a specified time, i.e.

Eq. 4.6
$$\xi=\begin{bmatrix}\xi_x(x,y,t)\\ \xi_y(x,y,t)\end{bmatrix}$$

The Lame constants are elastic constants (named for French mathematician Gabriel Lame. μ_L is the shear modulus defined as:

Eq. 4.7
$$\mu_L=\frac{\Delta F/A}{\Delta L/L}$$

where ΔF is the shear stress, A is the area, ΔL is the distance between shearing planes, and L is the shear displacement. The other Lame constant, γ_L, is the bulk modulus less two-thirds of the shear modulus:

Eq. 4.8 $$\gamma_L = k - \frac{2}{3}\mu_L$$

The particle displacement can be stated as

Eq. 4.9 $$\xi = \xi_o e^{j(\omega t - kx)} = \xi_o \cos(\omega t - kx) + j\xi_o A \sin(\omega t - kx)$$

where ξ_o is the initial particle position, $\omega=2\pi f$, f is the frequency, k is the wave constant, t is the time, A is the amplitude, and x is the wave propagation distance. The particle velocity (u) is the derivative of displacement with a 90° phase difference:

Eq. 4.10 $$u = \frac{\partial \xi}{\partial t} = j\omega\xi_o e^{j(\omega t - kx)} = j\omega\xi$$

and the pressure (p) and intensity (I) can be determined by:

Eq. 4.11 $$p = uZ_o = k\omega\xi Z_o$$

Eq. 4.12 $$I = \frac{u^2 Z_o}{2} = \frac{\omega^2 \xi^2 Z_o}{2}$$

The crystal and lens, material properties, ultrasound source parameters and receivers were incorporated into the model. The geometry, shown in Figure 4.9, consisted of a simplified model of the transducer: a 25.4 mm diameter air-backed piezoceramic crystal (APC 880, American Piezo Ceramics, a PZT-8 equivalent) affixed to a 28.5 mm diameter aluminum lens with a 0.025 mm thin epoxy bond layer (not shown). The thickness of the crystal was 0.59 mm, based on the half-wavelength thickness of APC 880 at 3.5 MHz. A Source pulse of 3 μs (10.5 wave periods at 3.5 MHz) was modeled in a simulated treatment path consisting of water at 25°C and uterine tissue. Receivers for particle displacement measurement were located at the focus and at various points along the focal axes (1, 2, 5, 10, and 20 mm to the left and right of the focus, and 1, 2, and 5 mm above and below the focus) as depicted in Figure 4.9. The time that each simulation was allowed to run was 45 μs allowing the wave to propagate a few centimeters past the focus. Normalized particle displacement data as extracted from the simulations. The parameters used in the simulation are summarized in Table 4.3.

Table 4.3 Wave2000 model simulation parameters

Parameter*	Value
Display brightness	63 (default)
Grid per pixel	0.3258
Points per cycle	10
Resolution	72 pixels / mm
Resolving wavelength	0.4277 mm
Simulation time	50 μs
Simulation Time step	0.0046 μs
Source frequency	3.5 MHz
Source pulse duration	3 μs
Source wave type	Sinusoid
Time step scale	0.8

* Refer to Wave 2000 Pro users guide for definitions of the parameters

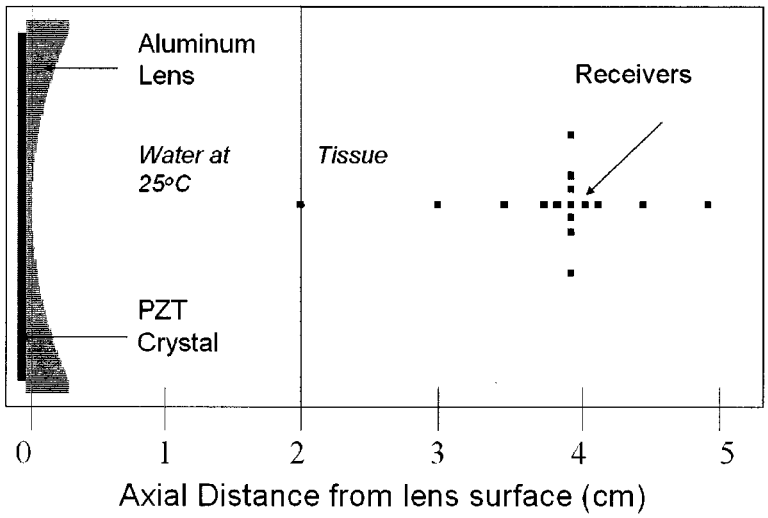

Figure 4.9 The geometry used for generating the wave propagation model in Wave 2000 Pro consisted of a piezoceramic (PZT) crystal affixed to an aluminum lens. The ultrasound was propagated first into water and then into tissue. Multiple receivers recorded the particle displacement at various locations along the focal plane (Chan, Fujimoto et al. 2002). A 0.025mm epoxy bond layer was included in the model, between the PZT crystal and the aluminum lens, but cannot be seen in this figure.

The Wave 2000 Pro simulations demonstrated the feasibility of using the aluminum lens design in focusing ultrasound. A propagating 3 μs pulse for a 3.5 MHz sinusoidal ultrasound source focusing at 4 cm is shown at various times during the simulation in Figure 4.10. The program created a black background during simulation for contrast, and the various minima and maxima of the wave are shown in white, with areas that remain black showing locations where the waveform has zero amplitude. The image at 30 μs

shows the wave front having just passed the focus. The normalized magnitudes of peak particle displacement amplitudes, determined from various receiver locations, are shown in Figure 4.11. Since particle displacement is linearly proportional to acoustic pressure, the half pressure maximum beam dimensions were expected to be approximately 5 mm in length by 1 mm in width. The length and width is similar to the focal depth (3.19 mm) and focal width (1.6 mm) calculated in section 4.3.1.

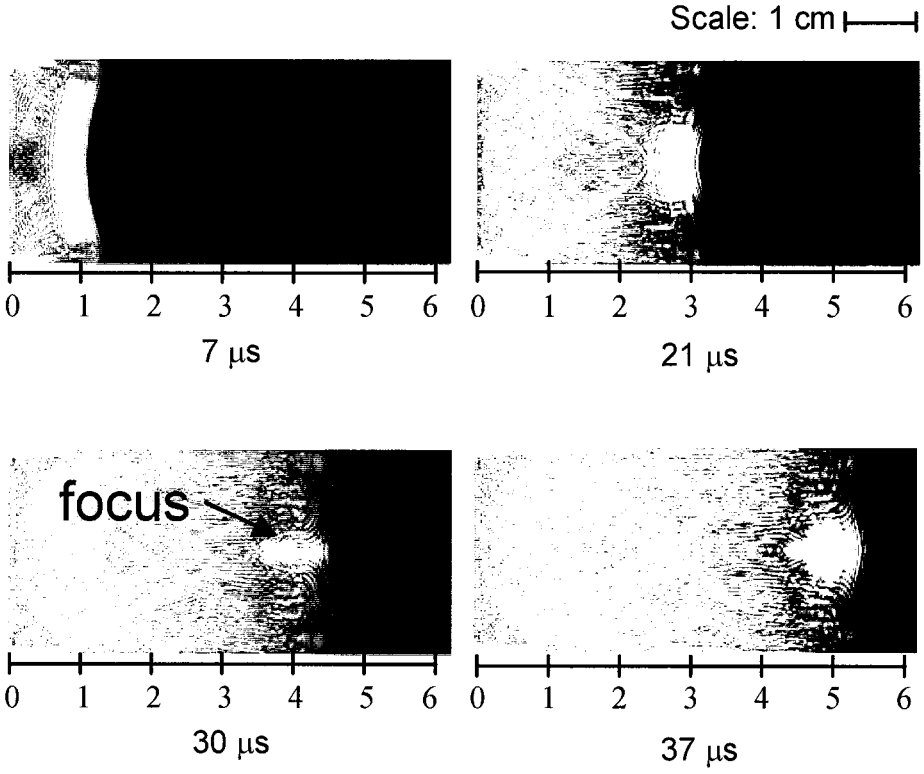

Figure 4.10 Images from a Wave 2000 Pro simulation, showing a 3.5 MHz, 3 μs sinusoidal wave. At 7 us, the wave had propagated 1 cm and is converging towards the focus. At 21 us, the ultrasound energy continues to converge until it reaches the focus at approximately 30 us. The lens was designed to focus the ultrasound energy at 4 cm, confirmed in this image. At 37 us, the ultrasound has propagated past the focus and begins to diverge (Chan, Fujimoto et al. 2002).

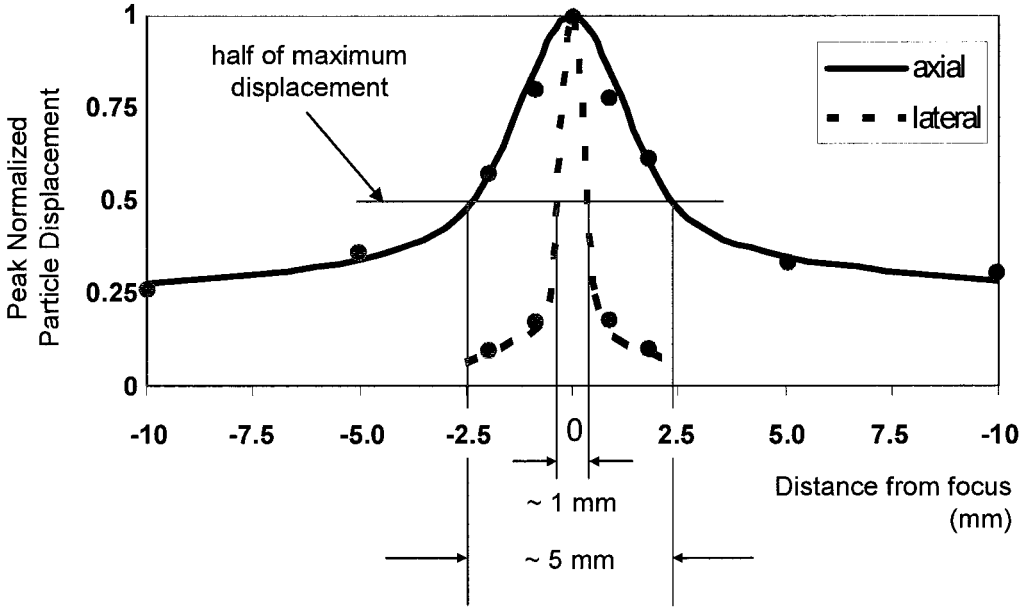

Figure 4.11 Peak normalized particle displacements collected from simulation receiver data show that the full width at half maximum focal dimensions are approximately 1 mm by 5 mm (Chan, Fujimoto et al. 2002).

4.3.5 HIFU transducer construction

The transducer construction protocol is outlined in the following sections. The individual components of the HIFU transducer: aluminum handle, brass housing, and aluminum lens, were machined at Twintec Inc. (Kent, WA) using a Hardinge T-42 Conquest Super Precision CNC lathe (Hardinge Inc., Elmira, NY) with a turning tool that had a radius of 0.127 mm.

4.3.5.1 Preparation of the housing and handle (Refer to Figure 4.12)

1. A 9.52mm (3/8") outer diameter hollow tube aluminum handle was attached to the brass housing using a metal to metal adhesive (Threadlocker 271, Loctite Corporation, Rocky Hill, CT).

2. Custom made stainless steel tubing barb connectors were inserted into the brass housing and secured with the metal adhesive.

3. Tygon tubing (S-50-HL, 3/32" ID, Saint-Gorbain Performance Plastics, Wayne, NJ) was attached to the tubing connectors and secured using epoxy (Hysol RE2039 and HD3561, Loctite Corporation, Rocky Hill, CT). This tubing was used to connect the transducer to the water circulation system, described in 4.3.7.

4. A RG-58 coaxial cable, approximately 10 cm longer than the handle, was fed through the handle and its braiding was attached to the inside of the brass housing with a 4-40 screw for a ground connection. The core lead was left exposed for soldering onto the piezoceramic crystal assembly (section 4.3.5.3).

5. The braiding and the screw were coated with epoxy (Hysol RE2039 and HD3561, Loctite Corporation, Rocky Hill, CT) providing isolation from the exposed coaxial cable center. This prevented electrical shorting.

6. The exposed coaxial cable at the end of the handle was encased in plastic Tygon tubing (R3603, ½" ID, Saint-Gorbain Performance Plastics, Wayne, NJ), and the tubing was secured to the handle using a plastic tubing connector to waterproof the transducer.

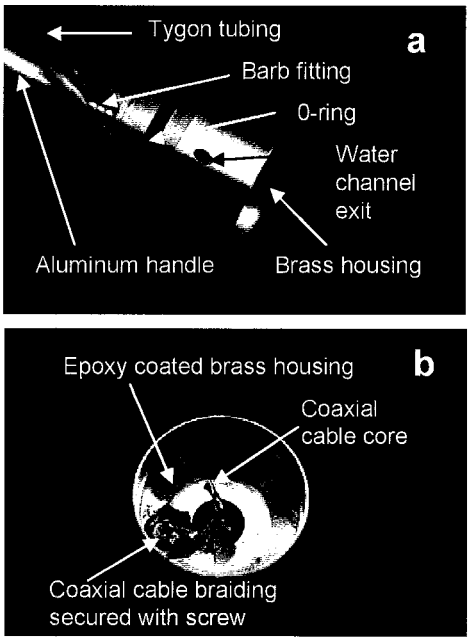

The aluminum handle and tubing were attached to brass housing. Plastic (Tygon) tubing was connected to the brass housing via custom made barbs fittings. Channels machined into the brass housing allowed water cooling and circulation into a condom attached to the transducer (not shown) using an o-ring.

The coaxial cable was fed through the aluminum handle and into the brass housing. The braiding of the cable was attached to the brass housing using a screw. The surface of the brass housing, the braiding, and the screw was coated with epoxy.

Figure 4.12 Preparation of the brass housing, coaxial cable, and transducer handle.

4.3.5.2 Affixing crystal to lens (Refer to Figure 4.13)

7. The negative (grounding) surface of a flat, circular disk piezoceramic crystal (Figure 4.13a) (APC 880, American Piezoceramics, Mackeyville, PA), 25.4 mm in diameter and 0.59 mm in thickness (corresponding to half wavelength of APC 880 at 3.5 MHz) was roughened with a fiberglass brush and cleaned with acetone in an ultrasonic cleaner. (The positive side of the piezoceramic crystal was marked with a black dot by the manufacturer).

8. The flat surface of the aluminum lens (Figure 4.13a) was also roughened with a fiberglass brush and the lens was subsequently cleaned with acetone in an ultrasonic cleaner. This roughening and cleaning procedure optimized the surfaces for bonding.

9. A custom built plastic (delrin) fixture and molds composed of silicone rubber (RTV 630 A and B, 10:1 by mass, GE Silicones, Waterford, NY) were made. This fixture ensured concentric alignment of the crystal and the lens and consisted of a base, a central cylinder, and a top that was molded to the shape of the aluminum lens (Figure 4.13b).

10. The base of the mold was inserted into the central cylinder, and the crystal was placed on top of the base with the negative (bonding) side facing upwards.

11. A small drop of degassed epoxy (Hysol RE2039 and HD3561, Loctite Corporation, Rocky Hill, CT), corresponding to a thin layer (approximately 0.025 mm) over the surface of the crystal, was applied to the crystal (Figure 4.13c).

12. The aluminum lens was placed on top of the epoxy and crystal, and the top of the mold was lowered onto the lens (Figure 4.13d). The lens was placed gently on top of the epoxy to prevent the formation of air bubbles in the epoxy mixture. Air bubbles may reduce the bond strength of the epoxy or distort the emitted ultrasound beam. It was assumed that there was no air bubbles in between in the epoxy layer. Although this was not explicitly tested for, a method developed by

Sapozhnikov et al.[d] can potentially be used to detect for imperfections in the bond layer. This method evaluates the normal velocity distribution along the vibrating surface of a piezoceramic transducer. Anomalies in the velocity distribution may indicate a flaw in the epoxy such as the presence of an air bubble.

13. The mold fixture was placed in a clamp (Figure 4.13e) and the crystal and lens were bonded under pressure (approximately 400 kPa).

14. The epoxy was allowed to set at a temperature of 25°C for 24 hours.

15. The lens and crystal assembly was extracted from the mold fixture (Figure 4.13f) and excess epoxy was cleaned.

[d] The details of this procedure are outlined in an article in Sapozhnikov, O.A., Pishchalnikov, Y.A., Morozov, A.V., "Reconstruction of Normal Velocity Distribution at the Surface of an Ultrasound Transducer on the Base of Acoustic Pressure Measurements along a Control Surface", published in the Russian journal , Acoustical Journal (2003) 49(3), 376-384.

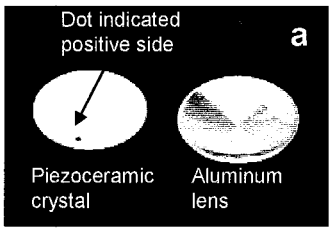

The bonding surfaces of the piezoceramic crystal and aluminum lens were cleaned.

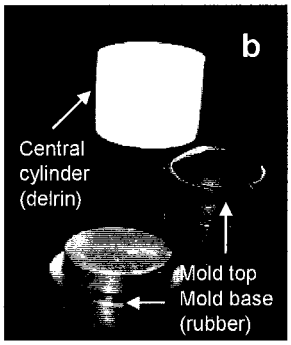

A custom mold, made of delrin plastic and rubber, ensured concentric bonding of the crystal and lens.

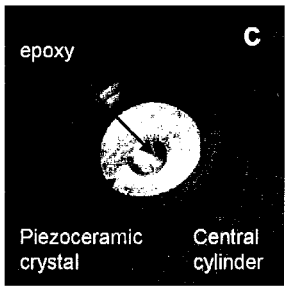

The piezoceramic crystal was placed in the central cylinder and epoxy was applied.

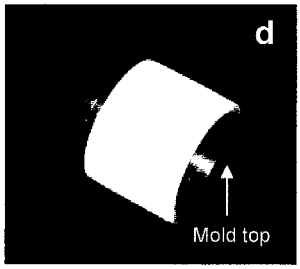

The aluminum lens (not shown) was placed on the epoxy and the crystal and the top of the mold was placed on top.

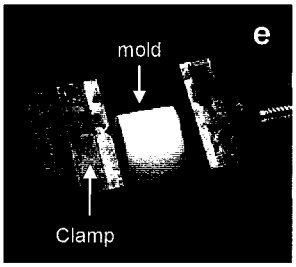

The mold fixture was placed in a clamp for the lens and crystal to be bonded under pressure.

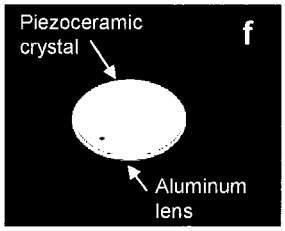

The lens and crystal assembly was extracted from the mold after 24 hours.

Figure 4.13 Procedure for affixing the piezoceramic crystal to the aluminum lens.

4.3.5.3 Attachment of lens/crystal assembly to housing (Refer to Figure 4.14)

16. A "conductive spider" (shown in Figure 4.14a) was cut out of 0.25 mm thick gold foil.

17. One end of the "conductive spider" was soldered onto the center core lead of the coaxial cable and the other end was soldered to the crystal (Figure 4.14b) providing an electrical connection to the crystal.

18. The lens/crystal assembly was placed into the brass housing and secured with epoxy (Hysol RE2039 and HD3561, Loctite Corporation, Rocky Hill, CT) around the circumference in contact with the brass housing as illustrated in the cross sectional drawing in Figure 4.15. It should be noted that the crystal was air backed to ensure minimum energy loss through the back-side (so that the majority of the ultrasound energy would be radiated to through the lens).

The completed transvaginal HIFU transducer is shown in Figure 4.14d.

The electrical excitation of the piezoceramic crystal is shown in Figure 4.15. The positive side of the crystal was connected to the center of the coax cable via the "conductive spider". The negative side of the crystal was grounded via the aluminum lens and the brass housing. The braiding of the coaxial cable was connected directly to the brass housing, and the aluminum lens also had electrical contact with the brass housing. Because the aluminum lens and piezoceramic crystal were roughened prior to bonding with epoxy, areas of direct contact provided a pathway for the electrical energy to travel from the lens to the crystal, as shown in Figure 4.16.

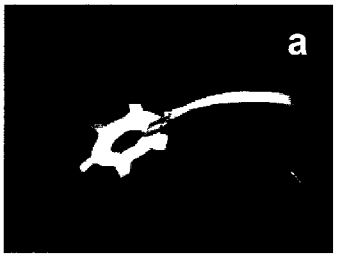

A "conductive spider" was cut out of gold foil.

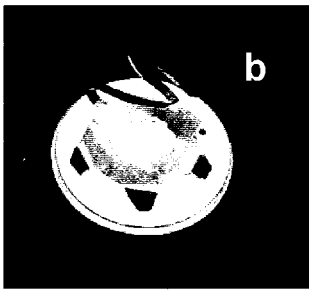

The "spider" was soldered to the positive (exposed) side of the piezoceramic crystal

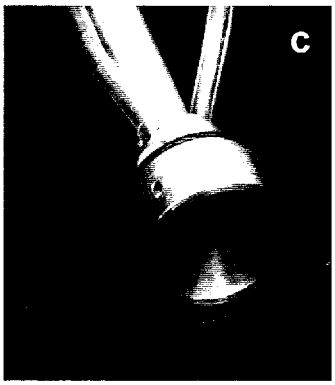

The lens-crystal-spider assembly was placed into the brass housing and secured with epoxy. The spider was soldered to the coaxial cable core (not shown).

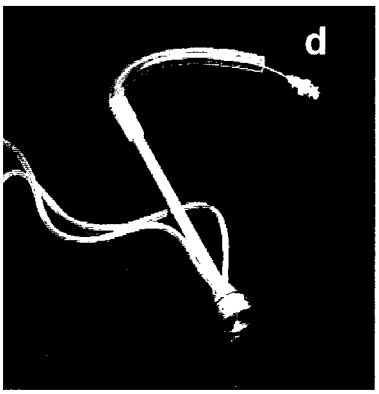

Photo of the completed transvaginal HIFU transducer.

Figure 4.14 The conductive spider and the completion of the HIFU transducer

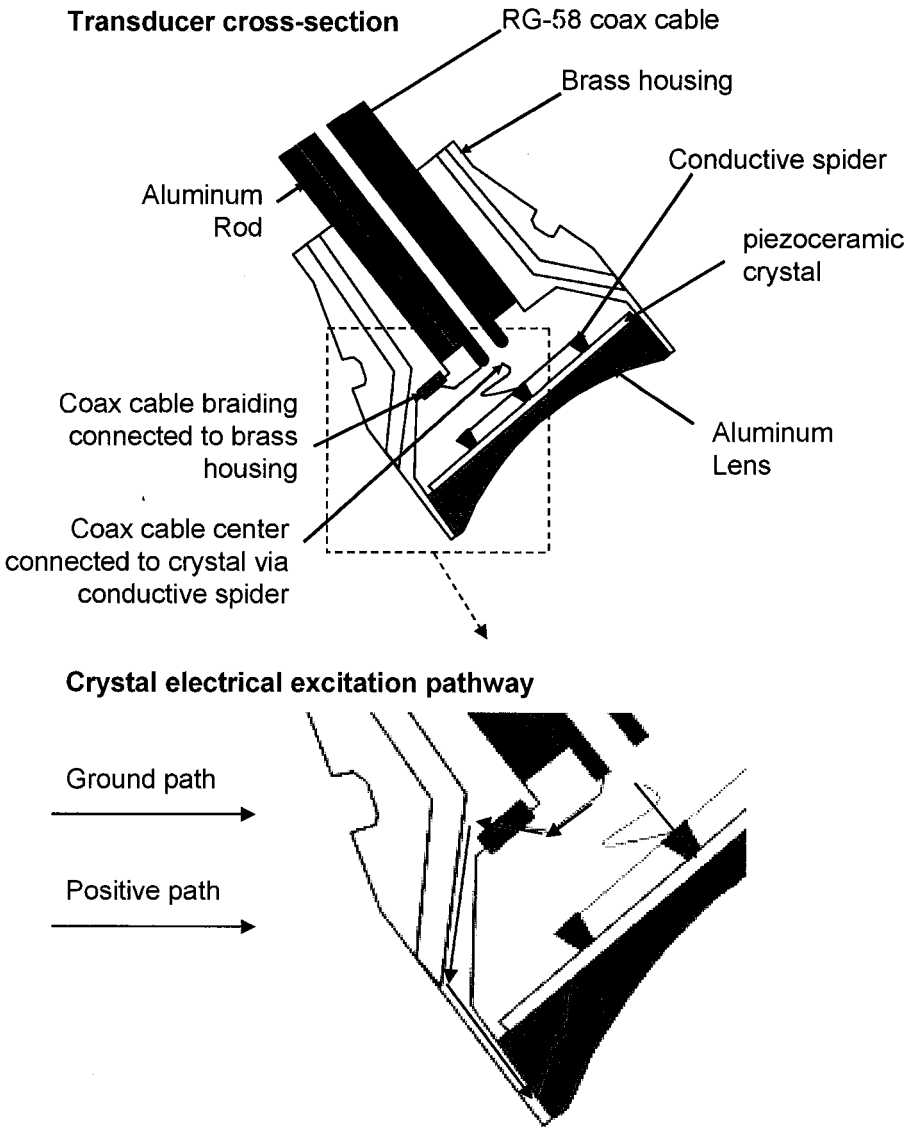

Figure 4.15 Cross section view of transducer shows the electrical connection between the coaxial cable and the piezoceramic crystal via the conductive spider and aluminum lens. The center core of the coaxial cable was soldered to the conductive spider. The braiding of the coax cable was connected to the brass housing and the aluminum lens was touching the brass housing providing grounding to the crystal.

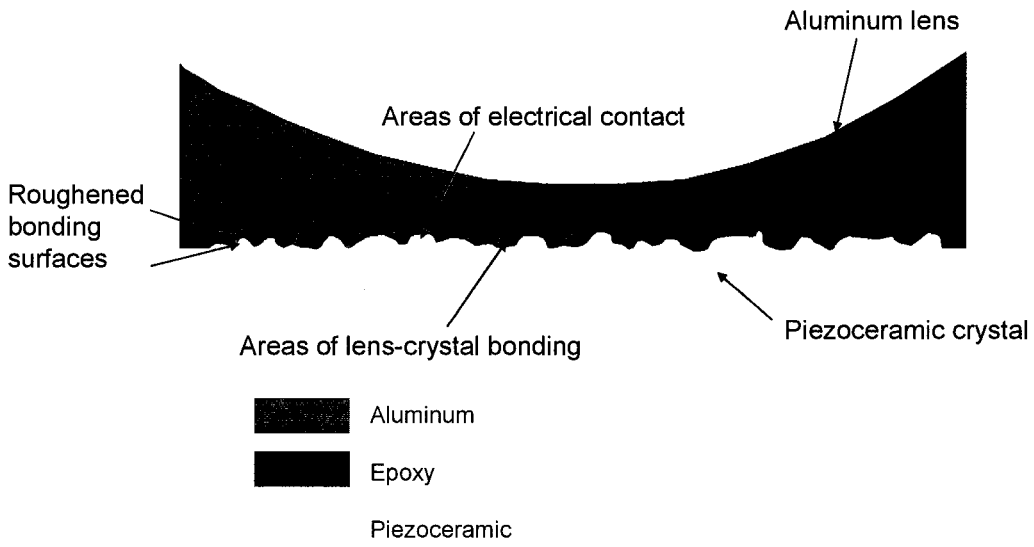

Figure 4.16 The roughened bonding surfaces of the aluminum lens and the piezoceramic crystal allow the lens and crystal to be bonded using epoxy while providing areas of electrical contact for the crystal to be grounded. (Not to scale, the roughened bonding surfaces have been exaggerated to demonstrate the bonding and conducting principle).

4.3.5.4 The completed device

The device was constructed at the Applied Physics Laboratory machine shop at the University of Washington, Seattle, WA. Figure 4.17 shows the completed HIFU transducer and the device. There is potential for the device to allow abdominal imaging probes of various makes and models to be used, as well as HIFU transducers of various frequencies and focal lengths.

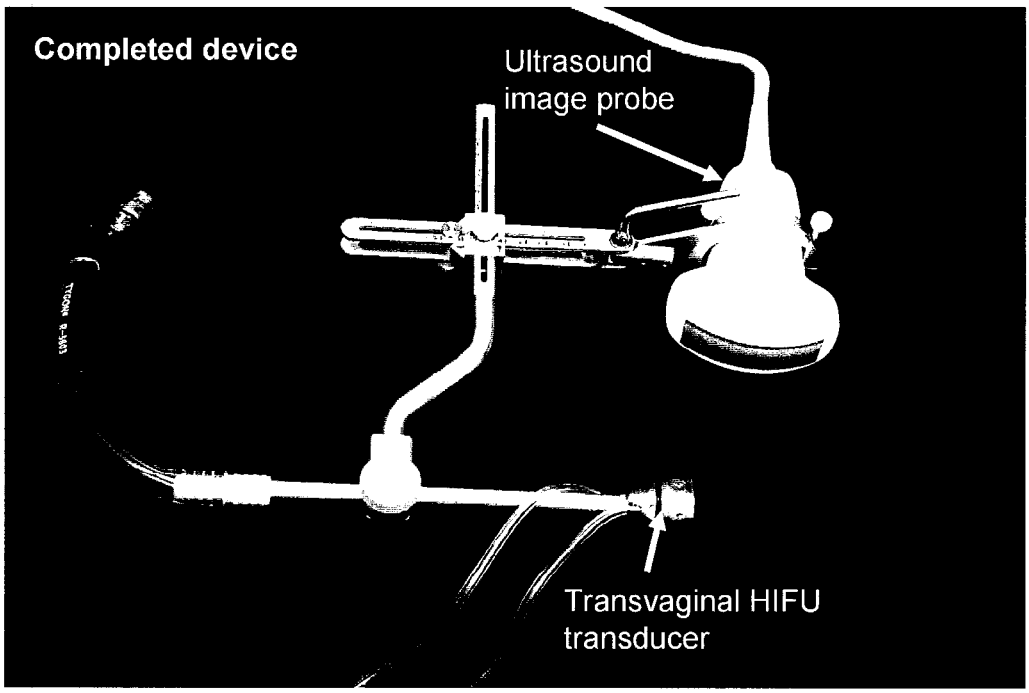

Figure 4.17 The completed device showing the transvaginal HIFU transducer and the Sonosite C60 4-2 MHz abdominal image probe.

4.3.5.5 Electrical impedance matching

As presented in section 2.12.4, the goal of electrical impedance matching is to maximize transmitted electrical power by tuning the impedance of the transducer to 50 Ω resulting in minimal reflected power to the 50 Ω equipment and cable. Since the impedance is a complex value, the matching network will be designed to tune the real part of the impedance to 50 Ω and cancel any imaginary part that may exist. A method devised and optimized by Dr. Roy Martin at the University of Washington was used. The matching network circuit, shown in Figure 4.18, consisted of a step-up transformer (with a ratio of turns T_2:T_1) to increase the real impedance of the transducer to within 5% of 50 ohms, and capacitances (C_1 and C_2) to eliminate the imaginary impedance. It was noticed that the piezoelectric crystal itself was capacitive or having a negative imaginary impedance (*32.05-j7.90* Ω). However, the coaxial cable attached to the transducer was inductive, and the pre-matched impedance of the transducer and cable was inductive (*8.014+j15.686* Ω) at a resonant frequency (f_c) of 3.607 MHz.

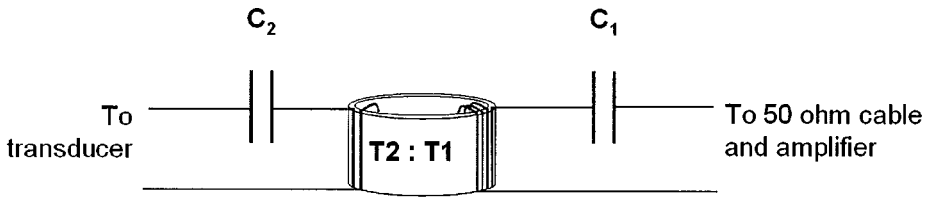

Figure 4.18 Electrical impedance matching network consisted of a transformer and two capacitors (C_2 and C_1) used to match the transducer impedance to 50 ohms.

The completed HIFU transducer was connected to an impedance analyzer (4914A, Hewlett Packard, Palo Alto, CA) and matched while placed in water to simulate the impedance conditions encountered when the device is used. The analyzer was initially calibrated, and the resonant frequency and the corresponding real and imaginary impedance of the transducer (shown in Eq. 4.13) were determined in water.

Eq. 4.13 $$Z_t = R_t + jX_t$$

The number of cores and the number of windings on the primary side of the transformer (T_1) were chosen so that the imaginary impedance was approximately 250 Ω (Roy Martin,

Terrance Myntti, personal communications). The transformer core ratio, and thus the number of windings on the secondary side of the transformer (T_2), was calculated based on the ratio shown in Eq. 4.14.

Eq. 4.14 $$\left(\frac{T_1}{T_2}\right)^2 = \frac{50}{R_t}$$

The capacitance values C_1 and C_2 were determined as:

Eq. 4.15 $$C_2 = \frac{1}{2\pi f_c X_t}$$

Eq. 4.16 $$C_1 = \frac{1}{2\pi f_c X_{t2}}$$

where X_{t2} was the imaginary impedance of the transducer with C_2 connected. These capacitive values cancel out any inductive component of the impedance. The post-matching impedance plot is shown in Figure 4.19. The center frequency, shown by the peak of the real impedance curve, was 3.6 MHz. At the center frequency, the impedance was 52.4-*j*5.6 Ω. The change in real impedance was approximately 3 Ω for a change in frequency of 0.03 MHz on either side of the center frequency.

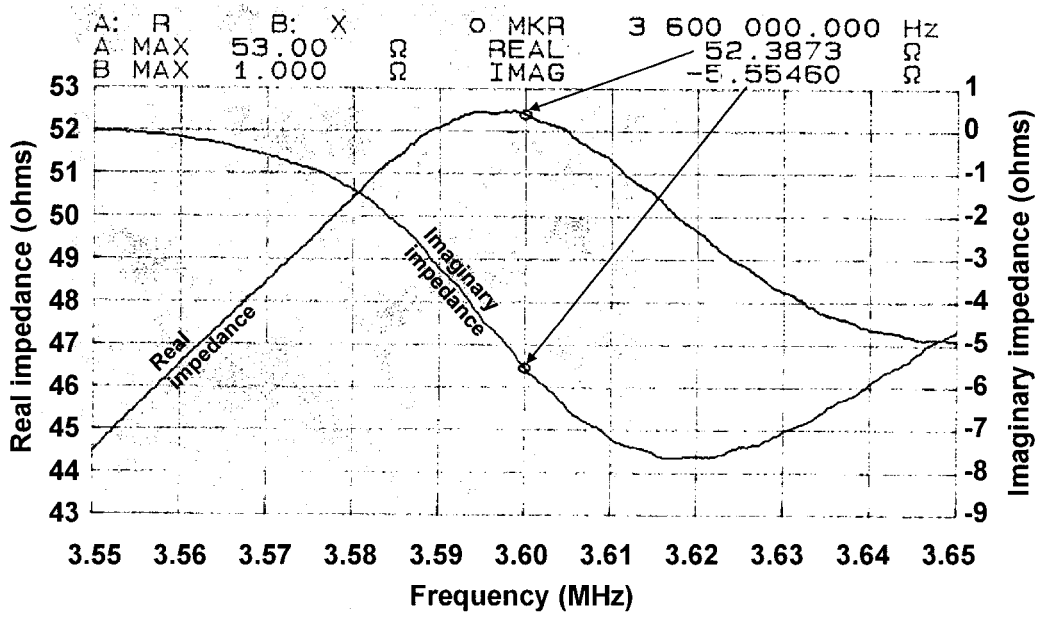

Figure 4.19 Transducer impedance with matching network showing a matched impedance of 52.4 ohms real and -5.6 ohms imaginary impedance at a center frequency of 3.6 MHz.

4.3.6 Device operation

4.3.6.1 HIFU Transducer operation

As shown in Figure 4.20, the HIFU transducer, when used alone (without the image probe) was driven with a RF power amplifier (150A100B, Amplifier Research, Souderton, PA). A waveform generator was used to control the source signal parameters of frequency and amplitude (33120A, Agilent Technologies, Palo Alto, CA). A RF power meter (4421, Bird Electronics, Cleveland, OH) was connected between the amplifier and the matching network to monitor electrical power output. A foot pedal connected between the waveform generator output and the amplifier was used as an on/off switch. A timer connected to the foot pedal measured HIFU exposure duration.

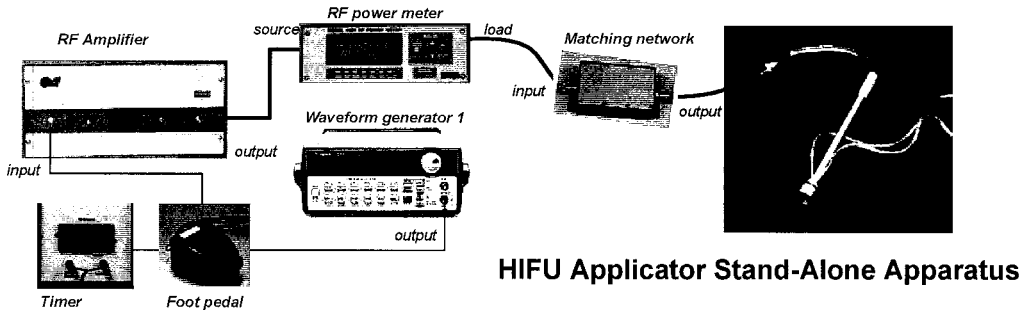

Figure 4.20 HIFU Transducer apparatus

4.3.6.2 Image-guided therapy system

The goal of having both the HIFU transducer and transabdominal image probe placed in the device was to allow real-time image-guided therapy. However, when HIFU was in operation, the high power levels saturated the receiver and circuitry of the ultrasound image probe resulting in interference band patterns on the ultrasound image. To ensure that the image was interference-free where the focus was to be visualized, a pulse gating method based on previous work in our group was used (Vaezy, Shi et al. 2001; Yuen 2001). The HIFU and the imaging ultrasound were synchronized so that the interference area, proportional to the duty cycle, was spatially stable and adjustable. With the Sonosite C60 image probe, a 50% HIFU duty cycle was adequate for visualization of HIFU, resulting in a 28-29° window of visualization (out of a total of 57° as per manufacturer's specifications, SonoSite Inc., Bothell, WA), as shown in Figure 4.21. Figure 4.21 also demonstrates that the window of visualization can be shifted to select the location of visualization (A: the window of visualization is 5° from the left edge, B: the window of visualization is 16° from the left edge). It should be noted that the parameters used to control the window of visualization is dependent upon the image probe used and its corresponding imaging depth and frame rate.

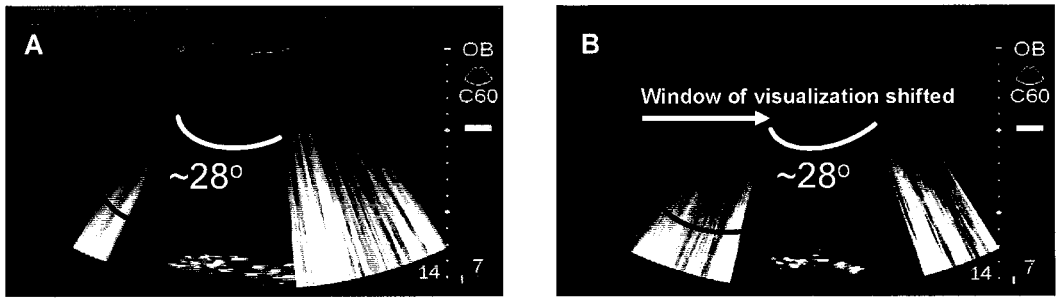

A 50% HIFU results in a 67° window of visualization

Location of spatially stable interference bands can be shifted

Figure 4.21 Screens captured from the SonoSite showing real-time image-guided therapy using synchronized HIFU and ultrasound imaging. The images show spatially stable moveable bands of interference using a HIFU duty cycle of 50 %.

The HIFU setup, described in Figure 4.20 was modified to provide synchronization of the HIFU with the image probe to provide an interference free window of visualization. A second function generator was required, and a computer using LabView software was used to control both function generators via a GPIB connection, as shown in Figure 4.22. Function generator 2 was used to generate a square wave excitation pulse. This excitation pulse triggered the output of Function generator 1 which operated in burst mode with a burst count corresponding to a 50% duty cycle. To ensure that the interference bands were spatially stable, the excitation pulse had to fall on the same image probe array element. The excitation pulse frequency (EPF) was the frame rate of the SonoSite, and varied with imaging depth. The EPF was determined experimentally by determining the frequency at which interference bands were spatially stable at each imaging depth. These values were entered into the LabView control program. The EPF for the range of depths of the Sonosite C60 are shown in Table 4.4. The LabView control program also allowed the interference area to be shifted by offsetting the phase of the EPF signal for one excitation pulse.

Table 4.4 Excitation pulse frequencies (EPF) for various depths of imaging (Sonosite C60)

Depth (cm)	EPF (Hz)	Depth (cm)	EPF (Hz)	Depth (cm)	EPF (Hz)
4	17.8670	12	20.3645	19	17.0345
7	17.7460	14	20.3645	22	15.3752
9	14.5688	17	18.9566		

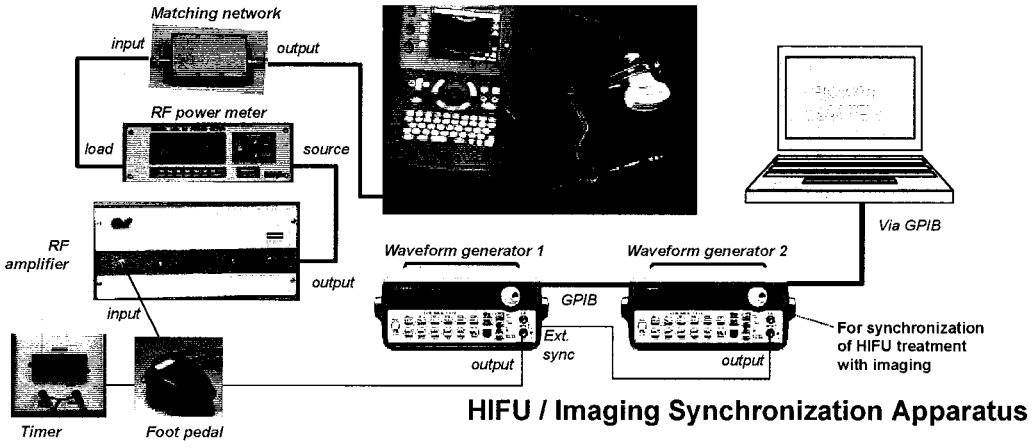

Figure 4.22 Apparatus for integrated HIFU and imaging required one waveform generator for generating an excitation pulse based on the frame rate of the SonoSite probe which, in turn, activated a second function generator that outputted the HIFU source wave at a 50 % duty cycle.

4.3.7 Water circulation system

The water-filled condom used for acoustic coupling and variable treatment standoff, as described in section 4.2.7, also has the potential to provide transducer cooling via convection when water is circulated through the condom, depicted in Figure 4.23. Transducer cooling is important to prevent tissue in contact with the transducer from thermal damage. Transducer cooling also prevents the transducer itself from excessive heating, which may lead to a shift in operating frequency. This shift in operating frequency may adversely affect transducer efficiency due to electrical impedance mismatch, especially for narrowband transducers. Impedance mismatch may lead to further transducer heating, and eventually all this heating may lead to transducer failure and unwanted tissue damage.

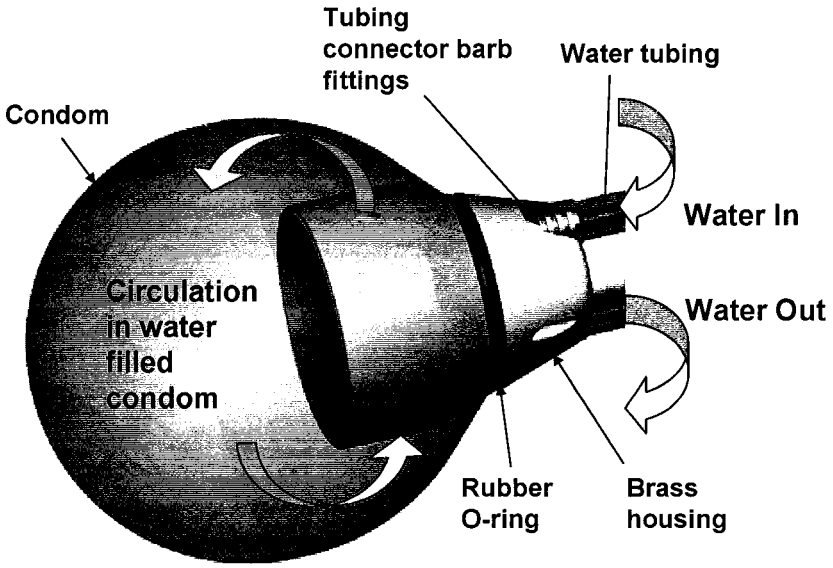

Figure 4.23 Water circulation within condom attached with an o-ring to the brass housing of the transducer. Water tubing connected to the brass housing via barb fittings carry water into and out of the condom.

4.3.7.1 Background and motivation

Other investigators have used a water filled membrane for acoustic coupling of the transducer to tissue (Bush, Rivens et al. 1993; Sanghvi, Foster et al. 1999; Hynynen, Pomeroy et al. 2001). It is uncertain whether the water in these membranes is circulated or if it simply acts to provide coupling and variable standoff. It is hypothesized that conduction and convection due to water circulation in front of the transducer may lower transducer operating temperatures.

4.3.7.2 Water circulation system design

A water circulation system (WCS) for use with the HIFU transducer was designed and constructed as shown in Figure 4.24. Tygon tubing (R3603, ¼" ID, Saint-Gorbain Performance Plastics, Wayne, NJ) was used for carrying flow between different components. Water was taken from a reservoir (Nalgene 1L plastic bottle, Nalge Nunc International Corporation, Rochester, NY) and pumped into the water filled condom using a magnetic micro-pump (TM92PMP2032, Herbach and Rademan, Moorestown, NJ). The rate of water influx into the water filled condom was controlled by a flow meter

(Cole Parmer Instrument Company, Vernon Hills, IL). Water was taken from the water filled condom back to the reservoir via a cooling radiator (Super radiator coils, Richmond, VA) using a second micro-pump, and flow rate was again controlled by a flow meter. To prevent over-pressuring of the pump and bursting of the tubing, the WCS incorporated a bypass (T-connection) to the reservoir after the outlet of pump 1. This allowed pump 1 to adequately operate even when flow to the transducer was turned off completely. To prevent dry suction from the transducer, a second bypass to the reservoir enabled water to be continually suctioned by pump 2 even when the flow from the transducer was turned off completely.

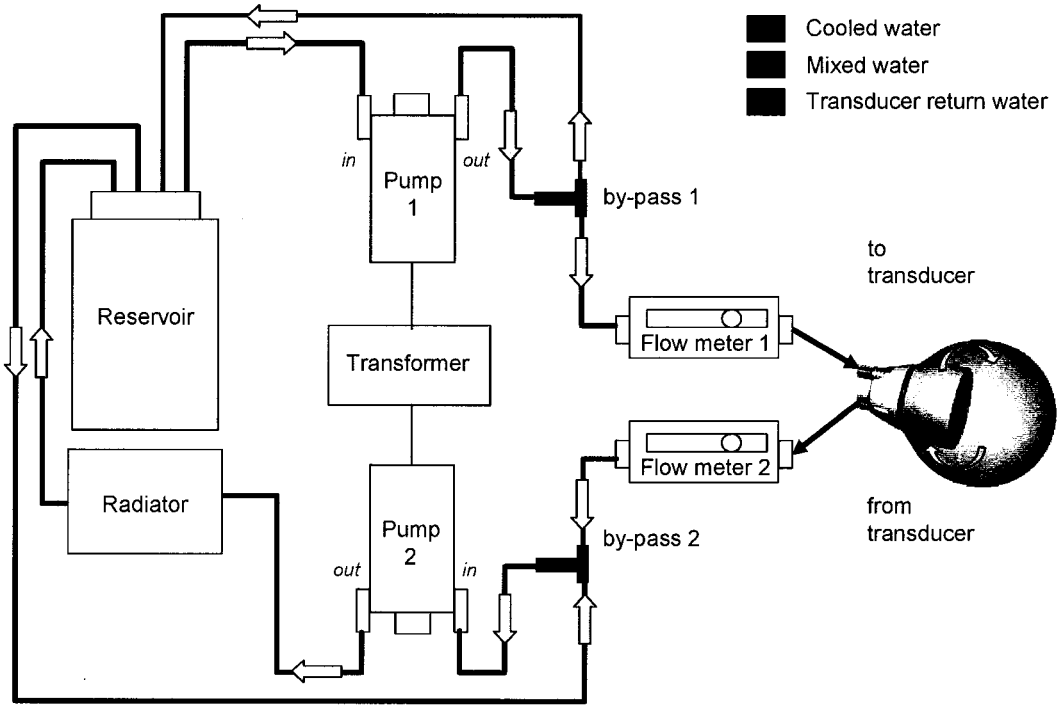

Figure 4.24 Water circulation system architecture.

Filling of the water filled condom was accomplished by increasing the flow using flow meter 1. Circulation of water was possible by setting both flow meters equal at a specified rate. Once the circulation rate was set, the water filled condom was inflated by increasing flow using flow meter 1, and reduced in size by decreasing flow using flow meter 1. Experimental testing of the water circulation system showed that the maximum flow rate achievable was 175 mL/min. Flow rates above this maximum increased the risk of water leakage where the tubing was connected to the bypasses and the flow meters due to high pressures at the connection points. The water circulation system was operated at 150 mL/min during experimentation.

4.4 ACOUSTIC MEASUREMENT TECHNIQUES

The completed HIFU transducer was characterized using three acoustic measurement techniques: Schlieren imaging, radiation force balance, and acoustic field mapping using a needle hydrophone. The theory behind these methods, the equipment and protocol used for testing, and the results specific to the HIFU transducer are discussed in this section.

4.4.1 Schlieren images

4.4.1.1 Theory

The Schlieren method originated in 1858 in France by Léon Foucault for use in testing lenses for astronomy. In 1887, Ernst Mach showed head waves of bullets using Schlieren photographs. Since then, Schlieren systems have provided an optical method for observing an ultrasonic field. Images can be acquired within a matter of seconds once the apparatus is set-up and calibrated. The Schlieren system was based on the idea that density gradient changes due to an ultrasound field in a fluid medium produced corresponding changes in the optical refractive index if the fluid medium, such as water, was transparent. The ultrasound beam pattern can be observed by viewing these changes in index of refraction.

In a Schlieren system, a collimated beam of light passes through a water tank in which the ultrasonic field is to be investigated. The light is then focused onto an obstruction so that none of the zero order light reaches the observer. When ultrasound changes the refractive index, light that passes through disturbed areas are not limited to passing through the occluded focal spot. As a result, the deviated light produces a corresponding variation in brightness, and can be projected onto a screen. Thus, the ultrasonic beam becomes visible as a light image against a dark background

4.4.1.2 Methods and materials

As shown in Figure 4.25, the Schlieren imaging system consisted of an incident laser beam that passed through two collimator lenses rendering the beam to be parallel and expanding it so that light filled up the area of mirror 1. This mirror directed the light through a water tank where the transducer was placed and activated, and onto a second mirror that projected the Schlieren image onto a screen. The Schlieren image was formed using a needle that blocked out the zero order of the incident light beam so that only the refracted light forming the beam pattern was visible. The laser and needle were adjusted to ensure a sharp and well defined image prior to testing. Schlieren images were observed at acoustic power levels between 0 and 75 W (continuous wave operation). Heat was generated by the transducer distorted the Schlieren images at higher power levels for exposure times of more than five seconds. Therefore the transducer was activated at each power level for approximately three seconds for a photograph to be taken using a digital SLR camera (D30, Canon Inc., Lake Success, NY) mounted to a tripod. The camera was set on a exposure time of 2 seconds, and an aperture setting of 8.0, parameters that were determined to ensure sufficient brightness and contrast.

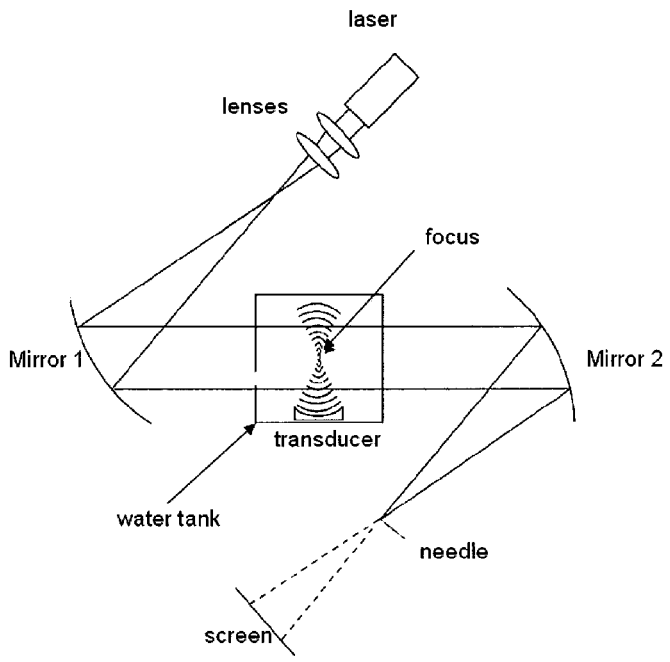

Figure 4.25 Schlieren imaging system apparatus (described in text)

4.4.1.3 Results

Figure 4.26 shows Schlieren images produced with the transvaginal HIFU transducer at acoustic powers of 10, 30, 45, 60 and 75 W. The focal region is clearly defined at 40 mm above the center of the lens. Sidelobes (shown by the "s" in Figure 4.26) were seen at continuous wave acoustic power levels above 60 W. Sidelobes may be a result of reflections, and shear wave conversion within the lens and at the crystal-epoxy-lens interfaces. Since Schlieren images are qualitative, an acoustic field map generated with a needle hydrophone, described in the following section, will provide more insight as to the relative intensity of the sidelobes compared to focal intensities.

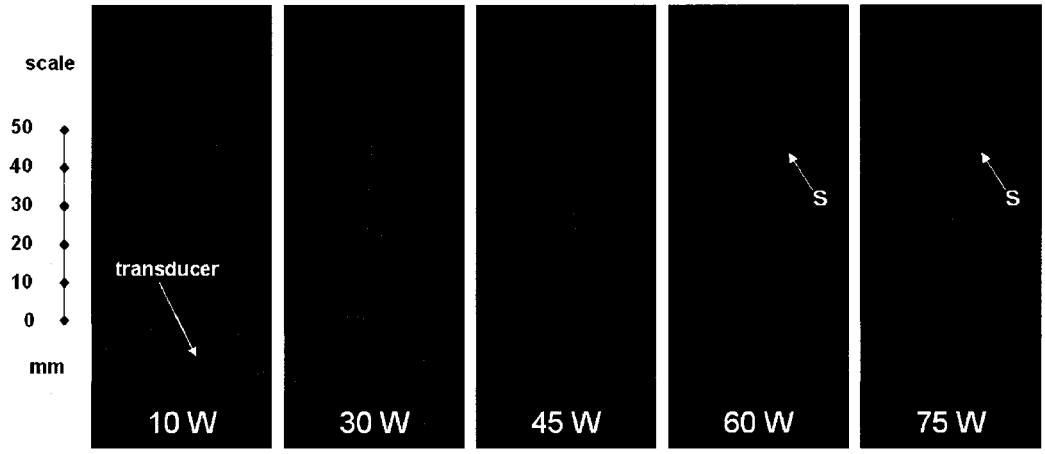

Figure 4.26 Schlieren images of the HIFU transducer in continuous wave operation at various acoustic power levels

4.4.2 Acoustic field map

4.4.2.1 Theory

Hydrophones are used to determine sound pressure measurements. A hydrophone measures pressure (p) based on a location in the acoustic field at a specific time (Ziskin and Lewan 1993)

Eq. 4.17 $$p = p(x, y, z, t)$$

The pressure signal waveform is commonly displayed on an oscilloscope as a voltage signal (U) related by

Eq. 4.18 $$U = pM$$

where M is the hydrophone sensitivity in volts per pascal. To obtain quantitative information about the acoustic beam, the acoustic field can be scanned using calibrated hydrophones resulting in a "field map". Information such as spatial peak values, focal dimensions, beam abnormalities and minima and maxima of the acoustic beam can be acquired.

The two main types of hydrophones are membrane and needle hydrophones. Membrane hydrophones consist of a suspended sheet of PVDF. They have a flat and weaker frequency response compared to needle hydrophones, and the sound field may be disturbed by reflections at the PVDF membrane. Needle hydrophones may be made of ceramic or PVDF. Ceramics have greater sensitivity for a given size compared to PVDF, but the frequency response is not smooth. The PVDF needle hydrophones have a smoother frequency response, but roughly 10 dB less sensitivity for a given size.

The field mapping system in this experiment used a PVDF (polyvinylidine fluoride) needle hydrophone. There are several factors that need to be considered when using a needle hydrophone to ensure a successful field map. First, the hydrophone chosen should be small relative to the wavelength of ultrasound signal received, sensitive, temporally stable and have a flat frequency response curve around the frequency of the HIFU transducer. Prior to performing a scan, the hydrophone position should be calibrated using measurements in 2 to 3 planes perpendicular to acoustic axis to ensure proper alignment. In the case of a needle hydrophone moving in stepwise intervals, the step size will depend on geometrical resolution or on the effective diameter of hydrophone. Finally, no matter how small, hydrophones should be regarded as finite-sized receivers. That is, they do not measure acoustic pressure at a point in the field but rather an average value over the "effective" hydrophone area (Smith 1989).

4.4.2.2 Materials and Methods

The field mapping apparatus was designed by engineer Bryan Cunitz at the Center for Industrial and Medical Ultrasound at the University of Washington. As shown in Figure 4.27, the measurement apparatus was composed of a PVDF needle hydrophone with a active diameter of 0.5 mm (TNU 001A, S/N 001 01 006, NTR Systems Inc., Seattle, WA) mounted onto a positioning system (Isel Automation, Germany) adjusted using 3 independently controlled stepper motors (minimum step size = 0.25 mm, Compumotor 6000, Parker Hannifin Corp., Rohnert, CA). Both needle hydrophone and HIFU transducer were suspended in a tank lined with acoustic absorber tiles to eliminate sound wave reflections and filled with degassed distilled water at room temperature. The received signal from the hydrophone was displayed with an oscilloscope. A LabVIEW

program controlled the positioning system and captured the oscilloscope data. To boost signal to noise ratio, an inline 30 dB preamplifier, powered by two 12 V batteries, was connected between the hydrophone and the oscilloscope. The hydrophone calibration curve, prepared by NTR Systems Inc. (Seattle, WA) with the 30 dB preamplifier, is shown in Figure 4.28. At 3.5 MHz, the sensitivity of the hydrophone was approximately 239 dBV/μPa.

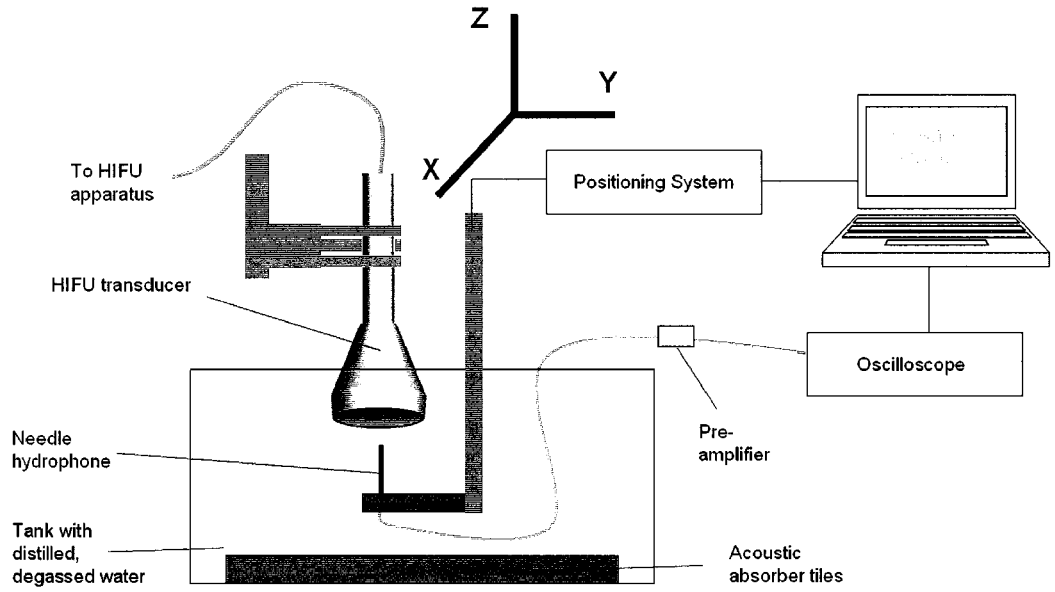

Figure 4.27 Field mapping apparatus (described in text)

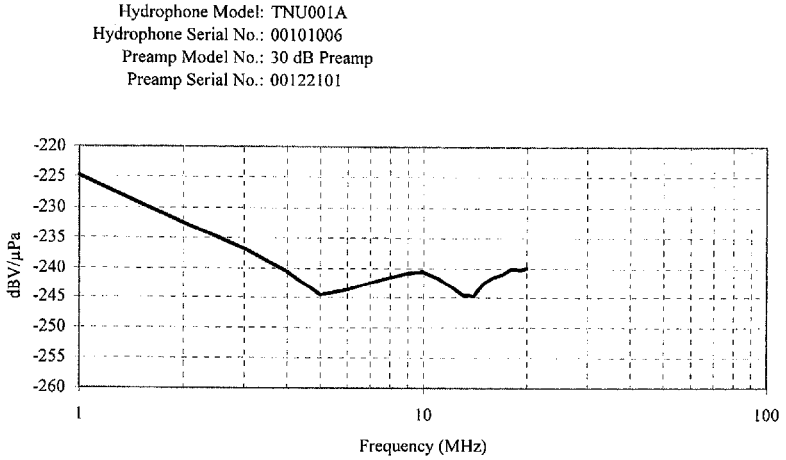

Figure 4.28 Hydrophone calibration curve showing the sensitivity of the hydrophone used in the field mapping apparatus, over a range of frequencies.

Assuming the beam pattern to be symmetrical about the Z axis, a 2D plot in the Z-Y plane was deemed sufficient to determine beam pattern and focal dimensions. The alignment of the needle hydrophone perpendicular to the transducer face was initially performed visually. The alignment was then fine tuned using the LabView software: the location of the focus was the location where peak voltages were obtained by the hydrophone, and a test scan determined the symmetry of the acoustic beam giving insight as to whether proper alignment was achieved. Once alignment was complete, a scan of the acoustic field was performed. The acoustic field was defined as an area between 5 and 55 mm away from the aluminum lens in the Z direction, and 12.5 mm on each side of the focal axis in the Y direction. This scan region covered the acoustic beam of the 25.4 mm aperture transducer with a 40 mm focal length. The hydrophone moved in increments of 0.5 mm until the entire acoustic field was covered. The transducer was connected to the HIFU apparatus (Figure 4.20), however, the RF power amplifier was not used. The waveform generator outputted an amplitude of 10 Vpp and operated in burst mode with a burst count of 50.

4.4.2.3 Results

The two-dimensional field map rendered using the needle hydrophone data is shown in Figure 4.29. The full width at half maximum (FWHM) focal dimensions were approximately 4.2 mm (length) by 1.2 mm (width), similar to values predicted by theory (section 4.3.1: 3.19 x 1.6 mm) and with the computer model (section 4.3.4: . This meant that HIFU treatment effects should be localized to an area represented by these focal dimensions. The lateral and axial HIFU beam profiles at the focal plane are shown in Figure 4.30 and Figure 4.31 respectively. There do not appear to be "hot spots" or areas of potential heating between the transducer and the focus greater than ~-10 dB of the peak pressure. The sidelobes appeared to be approximately -20 dB of peak focal intensities.

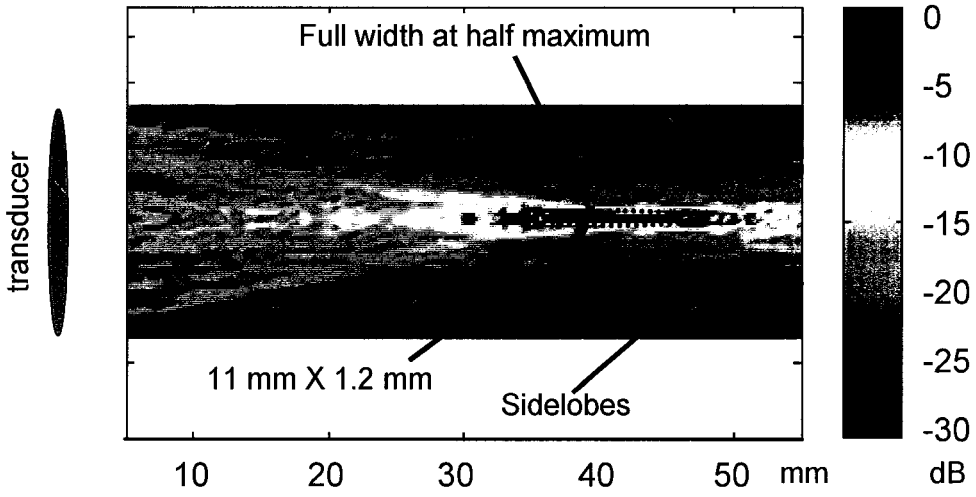

Figure 4.29 A field map showing the full width at half maximum focal dimensions as 11 mm by 1.2 mm.

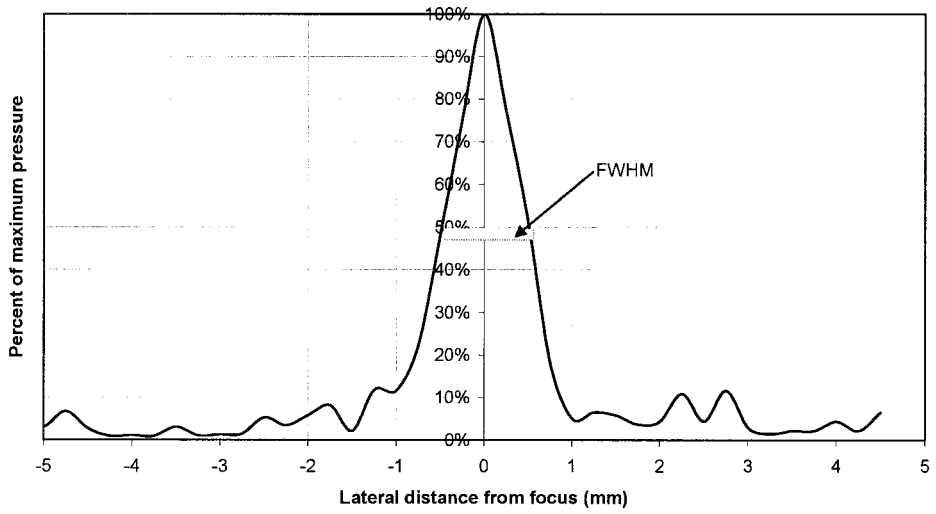

Figure 4.30 Lateral profile of the HIFU beam at the focal distance of 40 mm.

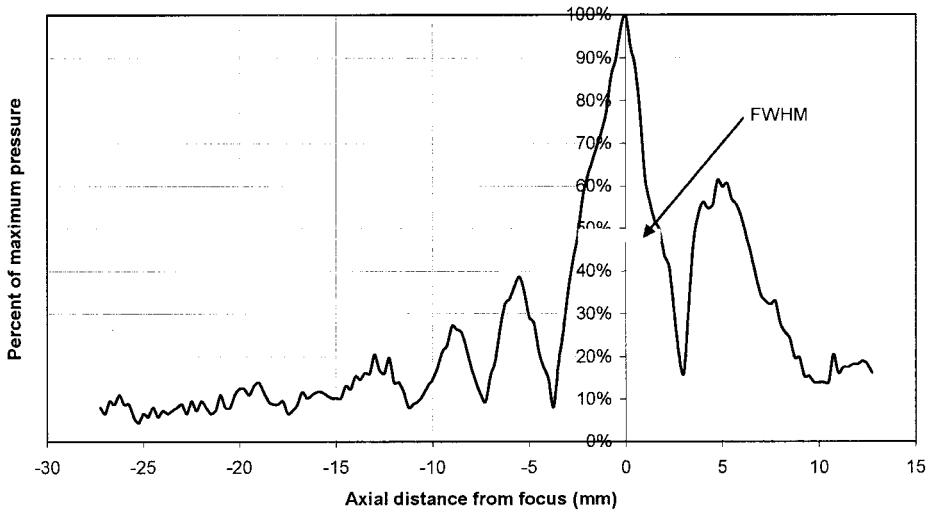

Figure 4.31 Axial profile of the HIFU beam at the focal distance of 40 mm.

4.4.3 Radiation force balance

4.4.3.1 Theory

A radiation force balance (RFB) may be used to measure the time-averaged total radiated power from an ultrasound transducer. In a RFB, an ultrasound beam is directed at and intercepted by a target that is attached to a scale, commonly an electronic microbalance. This target can be an absorber or a reflector. The ultrasound energy transfers momentum to this target that can be measured as a force integrated over the surface of the target. This force is directly proportional to the spatial average temporal average acoustic power. When an ultrasonic beam in water is directed normally to a plane surface that absorbs a majority of the acoustic energy, the total acoustic power (P_a) is equal to the force exerted on the target (F_{rad}) multiplied by the velocity of sound in water (c) (Ziskin and Lewan 1993):

Eq. 4.19 $$P_a = F_{rad} c$$

where F_{rad} is the mass reading obtained from the micro-balance (m) multiplied by the gravity constant g. Assuming g = 9.809 m/s^2 and c = 1483 m/s,

Eq. 4.20 $$P_a = \frac{m}{68.7 mg/Watt}$$

When an ultrasonic beam is directed towards an ideal reflector,

Eq. 4.21 $$P_a = \frac{F_{rad} c}{(2\cos^2 \varphi)}$$

where φ is the angle between the beam direction and the normal of the reflecting surface, as shown in Figure 4.34 using an aluminum cone reflector used in this experiment.

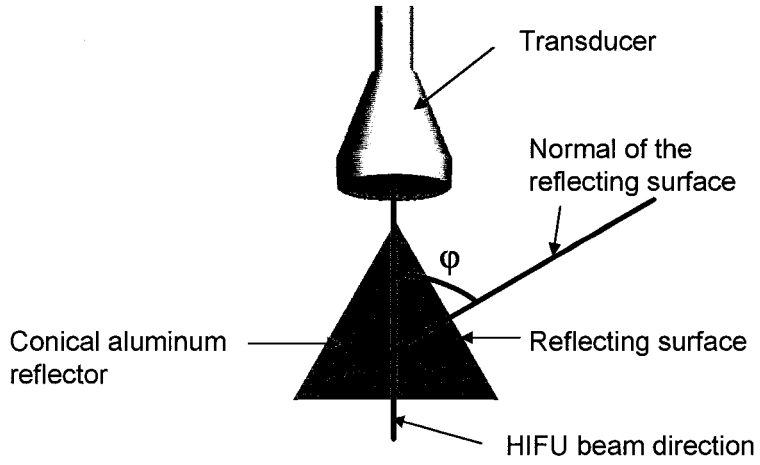

Figure 4.32 Schematic of the HIFU transducer and a typical aluminum conical reflector.

The above two equations assume a plane wave, and are generally a good approximation in unfocused fields (Ziskin and Lewan 1993). It has been stated that for focused fields, deviations from the plane wave approximation of ultrasonic fields differ, and thus Eq. 4.20 and Eq. 4.21 should be multiplied by a correction factor of

Eq. 4.22
$$\frac{2}{(1+\cos\beta)}$$

where β is the focus half angle (or half of the angle of divergence from the transducer to the focus) and is equal to

Eq. 4.23
$$\arctan\left(\frac{a}{l_f}\right)$$

where a is the transducer radius and l_f is the focal length (Ziskin and Lewan 1993). For the transvaginal HIFU transducer, $a/l_f = 0.3175$, $\beta = 17.6^{\circ}$ and the correction factor is 1.024 or close to 1. It should be noted that shielding membranes are often placed in front of targets to protect against acoustic streaming or heat convection flows since these are potential sources of RFB measurement uncertainty. The membrane should be positioned at a slightly oblique angle to prevent standing wave components (Ziskin and Lewan 1993).

4.4.3.2 Materials and methods

A reflective type RFB was used to determine the acoustic power output from the HIFU transducer. The RFB was a commercial unit (Ultrasound Power Meter UPM DT-10E, Ohmic Instruments, Easton, MD), shown in Figure 4.33. The transducer was suspended in a built-in distilled degassed water chamber on the force balance and directed towards an aluminum cone reflector secured onto the force balance. The transducer was secured using a metal clamp built into the unit, which also ensured proper alignment. Acoustic power measurements outputted by the RFB were recorded for three trials at each of nine electrical power levels ranging from 10 to 150 W. The transducer operated in continuous wave mode. The procedure was performed for frequencies of 3.4, 3.6 and 3.8 MHz to determine how broad of an operating frequency range the transducer had.

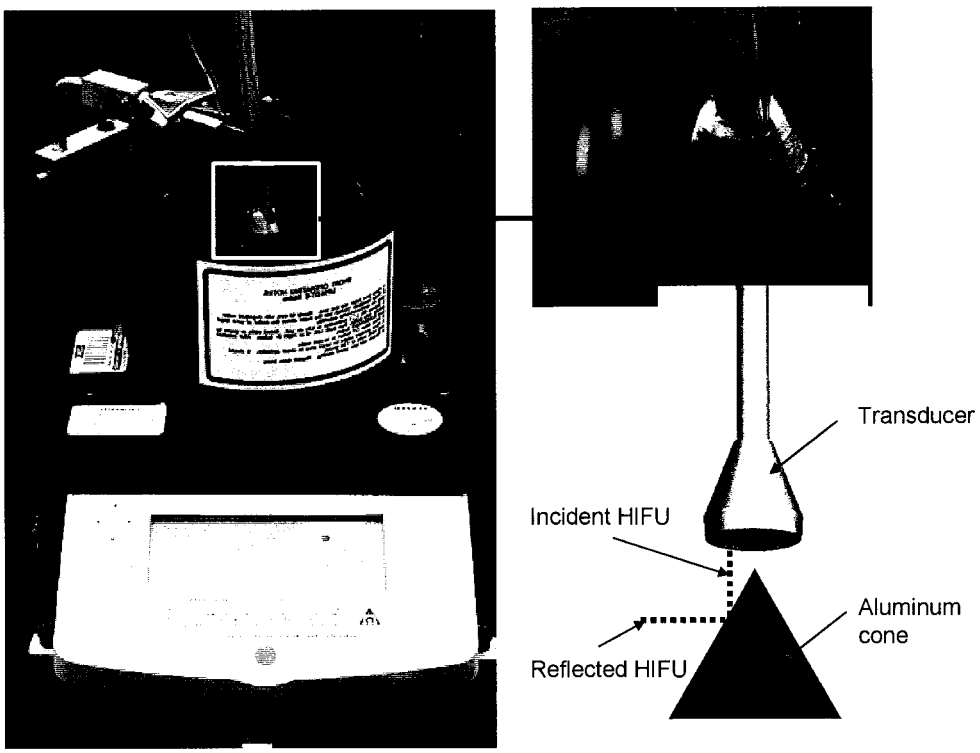

Figure 4.33 The HIFU transducer is placed in a water bath of an Ohmic Instruments reflecting radiation force balance. The HIFU energy radiates into the water bath onto a cone. The energy is quantified by the force balance as an acoustic power measurement in Watts.

4.4.3.3 Results

Results obtained from the RFB are shown in Figure 4.34. At the resonant frequency of 3.6 MHz, the average efficiency over the nine electrical power levels between 0 and 150 W was 56% ± 2%. When the transducer was operated 200 KHz off resonant frequency, the efficiency decreased by approximately 20-23%.

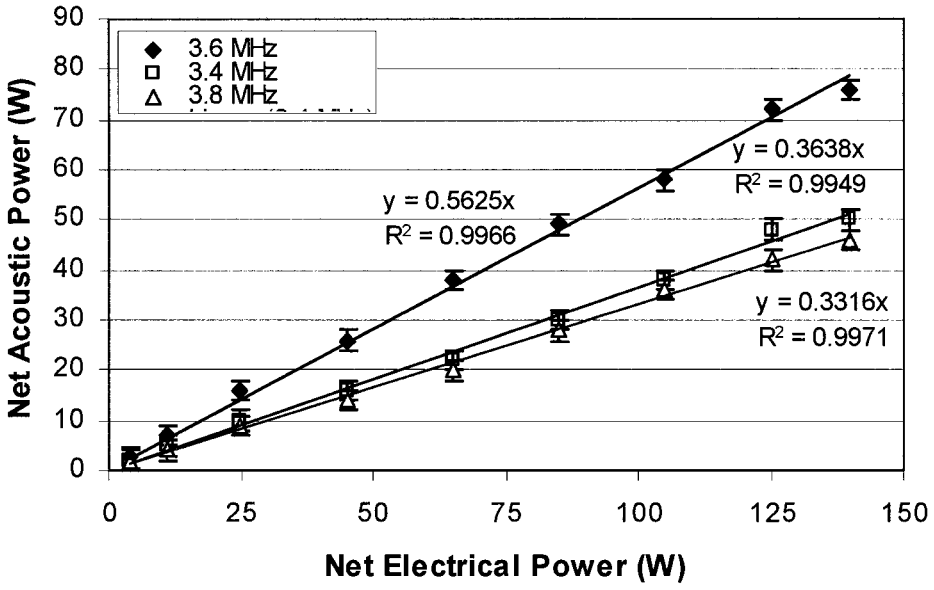

Figure 4.34 Acoustic power and efficiency determined using the radiation force balance shows the efficiency at 3.6 MHz as 56 % (based on the slope of the best fit line).

4.4.3.4 Transducer quality

The radiation force balance can be used to define the frequency response of the transducer. The frequency response is often defined as the quality factor (Q) of a transducer, which represents how broad the transducer's frequency response curve is, as shown in Figure 4.35 and defined by:

Eq. 4.24 $$Q = \frac{f_1}{\Delta f}$$

where f_1 is the center or fundamental frequency and Δf is the width of the frequency curve at half-power maximum.

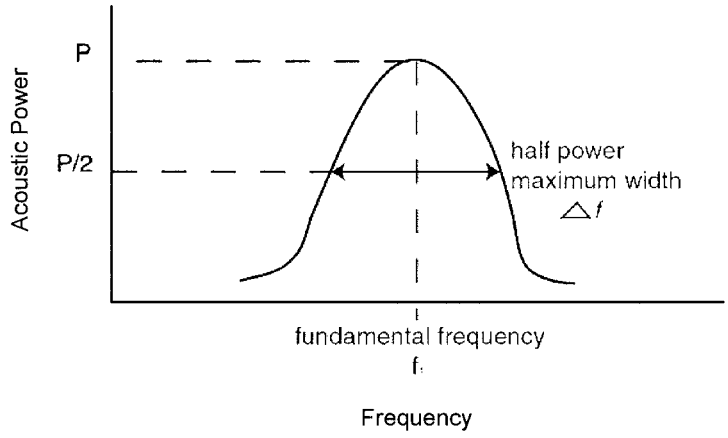

Figure 4.35 The quality factor is determined by the half power maximum frequency range, and the fundamental frequency.

The radiation force balance was used to measure the acoustic power output for a set electrical power input (100W) at various frequencies between 3.0 and 4.2 MHz, as shown in Figure 4.36. Three measurements were taken at each frequency. The acoustic power was normalized as a percentage of power at the center frequency (f_1) of 3.6 MHz. From Figure 4.36, Δf was found to be 0.57, and using Eq. 4.24, Q was calculated to be 6.32.

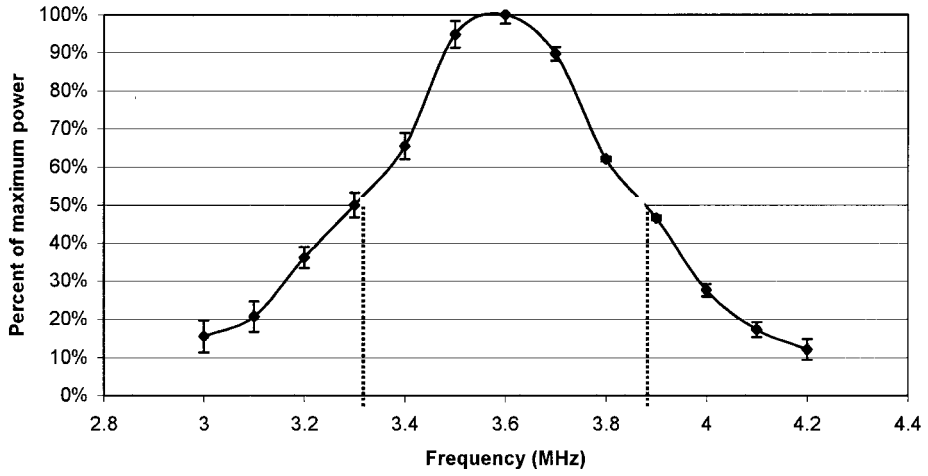

Figure 4.36 The acoustic power output as measured by the radiation force balance over a range of frequencies from 3.0 to 4.2 MHz. The electrical power input was kept constant at 100 W and three measurements were taken at each frequency. The error bars indicate one standard deviation.

4.5 INITIAL TRANSDUCER TEMPERATURE MEASUREMENTS

It was determined whether the water circulation system had the potential to provide adequate transducer cooling. A preliminary experiment was conducted measuring transducer and water temperature with and without water circulation in the condom. The transducer operated at 80 W electrical power. This corresponded to 47 W of acoustic power (from Figure 4.34) meaning there was approximately 33 W of power that was potentially converted to or lost as heat. The temperature during transducer operation was monitored for stagnant water and water circulated at 150 mL/min.

A thermocouple (type K, Omega Engineering Inc., Stamford, CT) was attached to the transducer brass housing using thermally conductive epoxy (Loctite 7387 and 384, Loctite Corporation, Rocky Hill, CT). The thermocouple was connected to a data acquisition unit (34970A, Agilent Technologies, Palo Alto, CA) via a 16-channel multiplexer module (34902A, Agilent Technologies, Palo Alto, CA), and data acquisition was automated using a program created in LabVIEW software (National Instruments). Temperature data was collected simultaneously from each thermocouple every 250 ms. Temperature data was collected over 20 seconds of transducer on time (at continuous

wave operation), and 40 seconds of off time for stagnant and circulated water in the water filled condom. The increases in temperature are shown in Figure 4.37. Three trials were performed and the temperatures recorded were accurate within 3% of the average value shown in the graph.

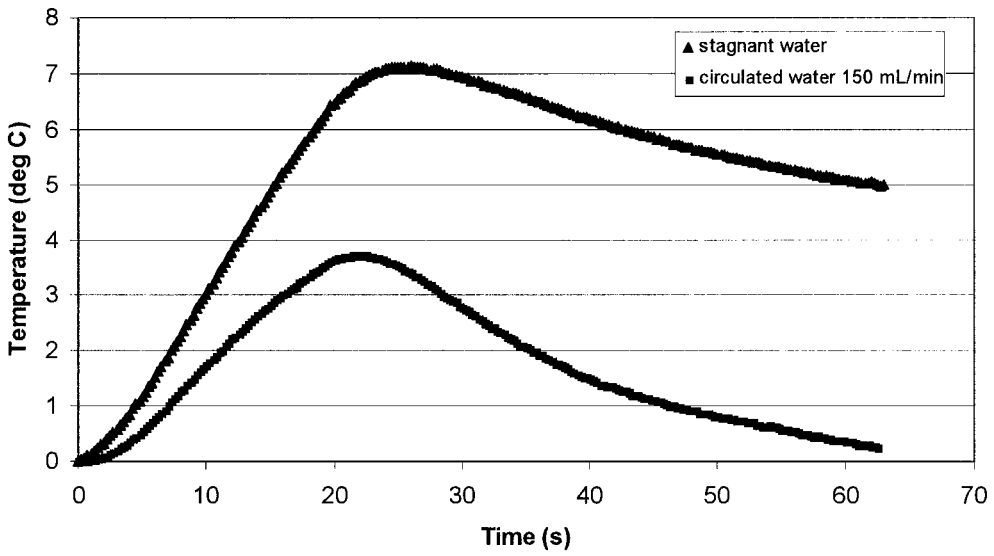

Figure 4.37 Transducer heating with stagnant and circulating water in the water filled condom shows that circulated water cools the HIFU transducer when the HIFU was on (the first 20 seconds) and when HIFU was turned off (between 20 and 60 seconds) more than stagnant water. 80 W of electrical power was used, 33 W of power was potentially converted to heat.

The rate of temperature increase without water circulation was much greater than with water circulation. The maximum temperature increase was 7.1°C with stagnant water and 3.8°C with circulated water. The maximum temperature increase occurred between 2-4 seconds after HIFU was turned off. This was because the thermocouple was mounted to the outside of the brass housing and therefore, the thermocouple response to transducer heating was delayed. The rate of cooling was also greater with water circulation. After 40 seconds of cooling, the temperatures returned to their original values with water circulation while they were still 5°C above original values without water circulation. Therefore, water circulation has the potential to provide adequate cooling during transducer operation.

5.0 CHAPTER 5 IMAGE-GUIDED HIFU DEVICE VERSION 1 *IN VITRO* TESTING, HUMAN ERGONOMICS STUDY, FEASIBILITY OF *IN VIVO* SHEEP MODEL

5.1 TESTING IN TISSUE MIMICKING PHANTOM

5.1.1 Purpose

A transparent tissue mimicking gel phantom, described in detail elsewhere (Lafon, Kaczkowski et al. 2001), was used to determine the repeatability of lesion formation at the focus, lesion visualization, and the effects of the water filled condom in lesion formation.

5.1.2 Materials and methods

Blocks of BSA/polyacrylamide tissue mimicking gel phantom (gel) were made according to a procedure developed at the Center for Industrial and Medical Ultrasound (Lafon, Kaczkowski et al. 2001). Each gel block measured 6.5 x 5.4 x 5.4 cm (~190 mL) and consisted of the ingredients listed in Table 5.1. The BSA concentration used in the tissue mimicking phantom was 7% by mass or 13.3 grams per block.

Table 5.1 Recipe for tissue mimicking phantom used to test HIFU transducer in vitro

Ingredient	% volume	Amount per block (mL)
40% Acrylamide	17.5	33.25
Distilled water	71.61	136.06
1M TRIS	10	19
10% APS (fresh)	0.84	1.60
TEMED	0.05	0.095
TOTAL	100	190

The attenuation of the gel was found to be 0.012 ± 0.002 NP/cm/MHz using the acoustic calipers method of measurement (Bloch 1998). The gel blocks were placed in a plastic holder, submerged, and anchored in a plastic tank filled with degassed distilled water at 25°C. The image-guided HIFU device was suspended in the water tank using a metal clamp, and connected to the HIFU and imaging apparatus, depicted in Figure 5.1. The device was positioned such that the focal region of the HIFU transducer was within the gel block, and the C60 imaging probe (Sonosite Inc., Bothell, WA) was capable of visualizing the treatment. The SonoSite (SonoSite Inc., Bothell, WA) was connected to a digital video recorder (GL1, Canon Inc., Lake Success, NY) that recorded ultrasound imaging during treatment. A digital camera was mounted on a tripod and aligned to photograph lesions formed in the gel. Lesion dimensions in these photos were measured using graphic analysis tools in Adobe Photoshop (Adobe Systems Incorporated, Seattle, WA). As shown in Figure 5.2, three treatment scenarios were performed, each with ten trials, to determine repeatability of lesion formation, visualization of treatment, and to determine if the water filled condom affected lesion formation. All trials were performed with 46W of acoustic power for 5 seconds at a duty cycle of 50%. This corresponded to *in situ* focal intensities of 1407 W/cm^2 with the transducer on the surface of the gel and 1587 W/cm^2 with the transducer and gel separated by 1.2 cm of water.

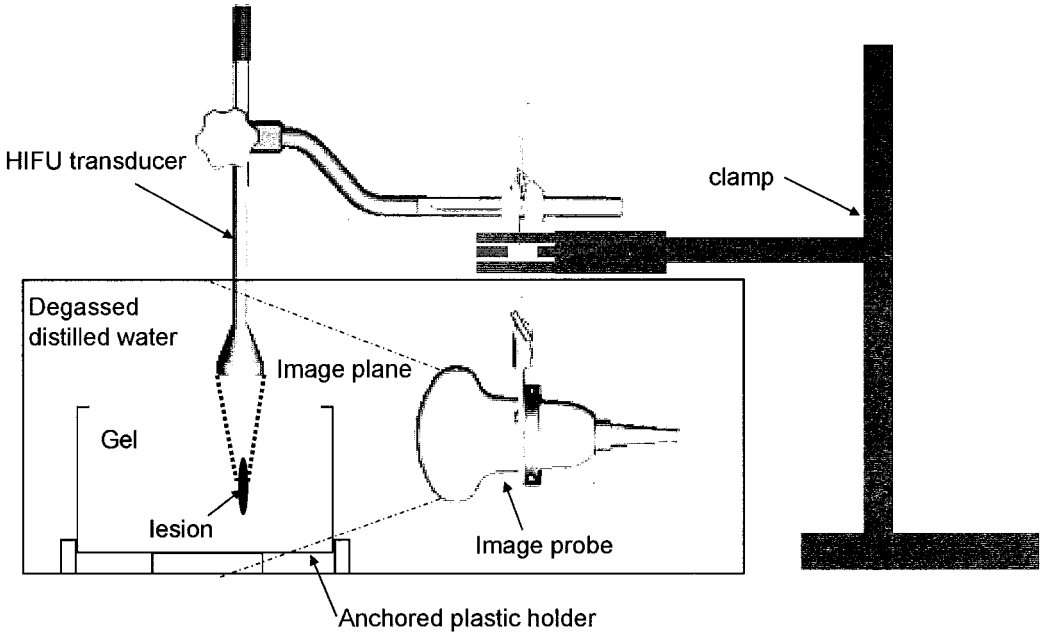

Figure 5.1 Tissue mimicking gel phantom experiment apparatus (described in text)

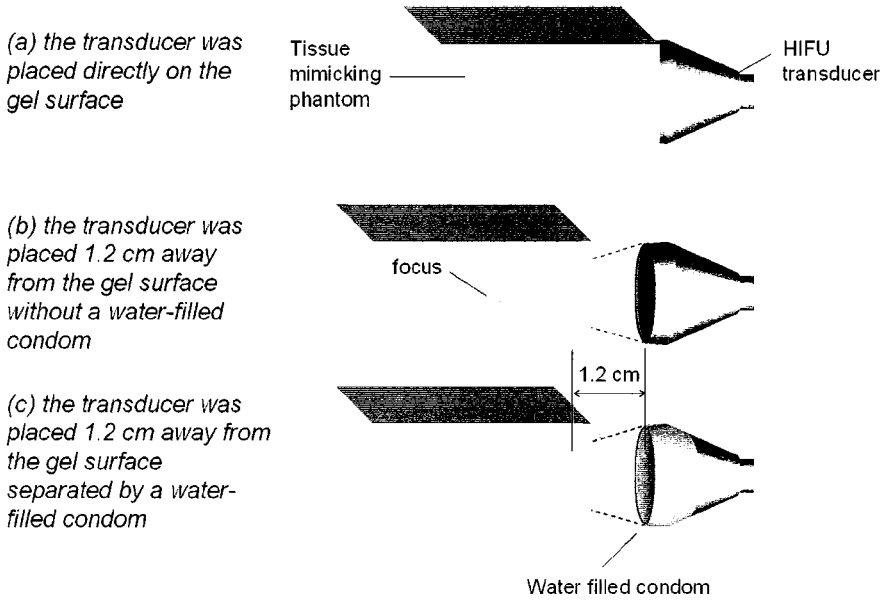

Figure 5.2 Three scenarios for the tissue mimicking phantom treatments

5.1.3 Results

A HIFU lesion produced in the gel and visualized with ultrasound is shown in Figure 5.3. This image depicts the treatment scenario where the transducer and gel were separated by 1.2 cm. The HIFU transducer and the water filled condom were clearly seen in the ultrasound image. The lesion formed by HIFU can be seen in Figure 5.3, characterized by the white opaque spot in the transparent gel, and the bright hyperechoic spot in the ultrasound image. All attempted lesions were visualized with ultrasound and were visible in the gel.

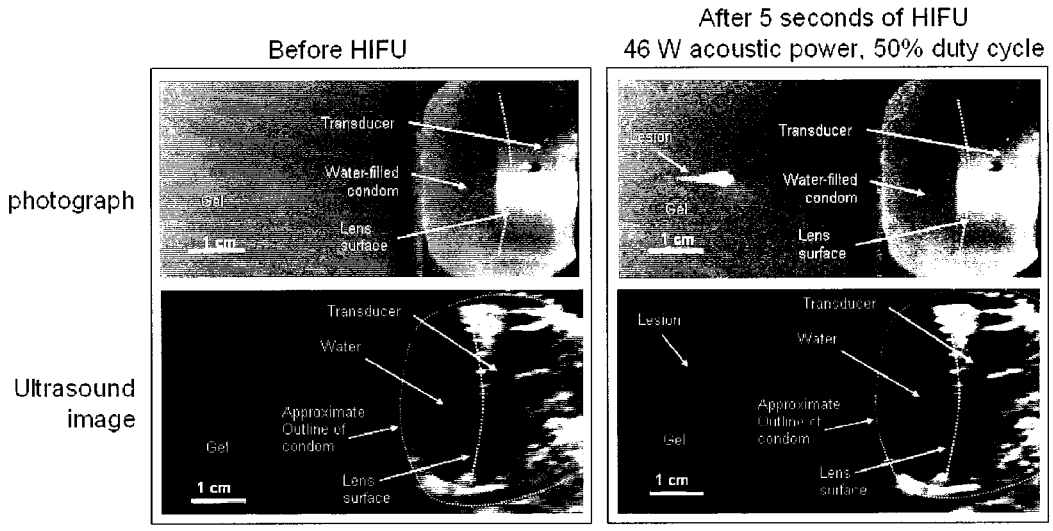

Figure 5.3 Photograph and ultrasound image of the HIFU transducer, water-filled condom and gel. A visible lesion in the gel and corresponding hyperechoic spot in the ultrasound image can be clearly seen.

The measured lesion dimensions for the three treatment scenarios are shown in Table 5.2. A two-sample two-tailed t-test indicated no statistically significant difference between lesions created with the water filled condom and without ($P<0.05$). There appeared to be correlation between lesion size and HIFU focal intensity. This finding will be explored in detail in section 5.2.

Table 5.2 Lesion dimensions in tissue mimicking phantom

Treatment scenario (n=10 for each)	**Focal Intensity (W/cm^2)**	**Lesion length (mm)**	**Lesion width (mm)**	**Ultrasound visualization (n=)**
Transducer directly on gel	1407	11.2 ± 0.8	2.2 ± 0.6	10
1.2 cm separation, no condom	1587	13.5 ± 1.1	2.6 ± 0.7	10
1.2 cm separation, with condom	1587[a]	13.3 ± 0.9	2.5 ± 0.8	10

a: attenuation of the 0.07 mm thin condom (Trojan Brand Non-Lubricated, CWI Carter Products Div., New York, NY) was assumed to be zero

5.2 TESTING IN TURKEY BREAST

5.2.1 Purpose

This study investigated the ability of the device to create lesions in turkey breast *in vitro*. The purpose of this study was to determine the effects of treatment time and intensity on lesion size. Although the transparent tissue mimicking phantom provided a method of visualizing lesion formation, its homogeneity and low attenuation coefficient meant that its acoustic properties were dissimilar to *in vivo* tissue. Turkey breast tissue ($\alpha = 0.835$ dB/cm/MHz, section 5.2.3), although not transparent, still enabled lesions to be clearly seen as white spots when dissected, and had similar properties to human muscle (α for myometrium was 0.713 dB/cm/MHz, Table 3.3).

5.2.2 Procedure

5.2.2.1 Turkey breast preparation and characterization

Six fresh, previously unfrozen turkey breasts (4-9 lbs each) were obtained (Plymouth Poultry, Seattle, WA). The turkey breast was separated into halves and the breast meat removed from the bone. The turkey breast halves were placed in 0.9% distilled degassed saline at 37°C. Each half will hereafter be referred to as a specimen. The density, attenuation, and acoustic velocities of each specimen, required for focal intensity calculations, were measured using the acoustic caliper method (Bloch 1998).

5.2.2.2 Lesion Creation

The parameters used for creating lesions in the turkey breast specimens are shown in Table 5.3. Three to five lesions were created at various depths between 0 and 4 cm in tissue for each acoustic power and treatment time combination in random order. The actual HIFU intensity at the focus for each treatment varied depending on the depth of tissue (affecting the attenuation of the incident ultrasound energy), and was calculated based on Eq. 2.20.

Table 5.3 Treatment parameters for turkey breast experiments

Parameter	Values to be tested (italics show default)
Acoustic power	46 W and 58 W (at a duty cycle of 50%)
Treatment time	5 seconds, 10 seconds
Depth of tissue	Between 0 cm and 4 cm

Each sample was pinned on a flat 20 cm by 10 cm sheet of high density foam (DuPont, Wilmington, DE) using pushpins. The foam was then submerged underwater and attached to a weighted fixture, as shown in Figure 5.4. The HIFU device was attached to a positioning system and aligned with the submerged sample, shown in Figure 5.4.

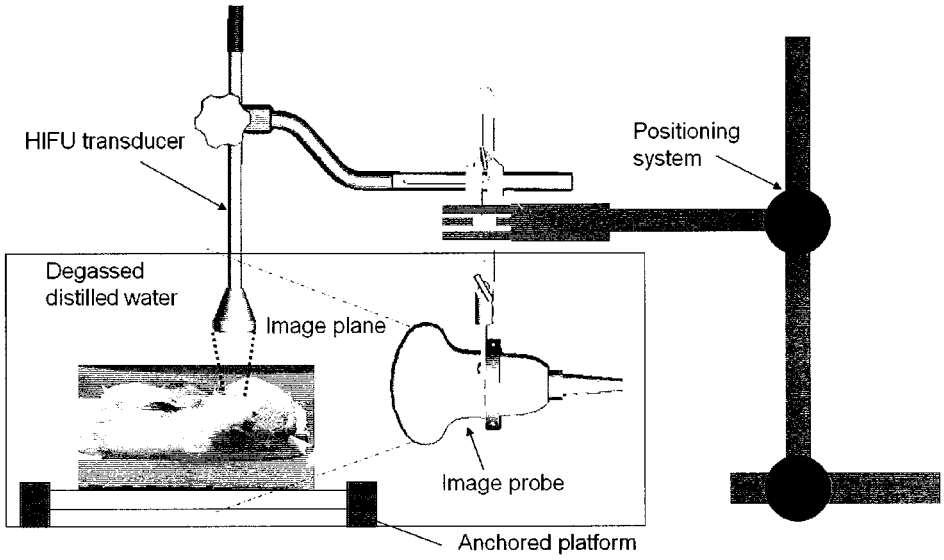

Figure 5.4 Apparatus and set-up for image-guided HIFU treatment of turkey breast (described in text)

The HIFU lesions were created in rows along the turkey breast, and the depth of each lesion was adjusted according to a randomization schedule. Lesions were created perpendicular to the muscle fibers of the tissue and were spaced approximately 1.5 cm apart. This spacing was determined by trial and error to be sufficient in preventing thermal and cavitation interactions between lesions. A marker lesion (a large lesion on the surface of the tissue) was created at the beginning and end of each row of lesions to allow for visualization and location of lesions during dissection of the sample. An example of a marker lesion is shown in Figure 5.5.

Figure 5.5 Examples of marker lesions in turkey breast tissue denoting the start and finish of a row of lesions

5.2.2.3 Lesion dissection and evaluation

After the lesions were created, the specimen on the foam pad was removed from the weighted fixture and was placed in a freezer for a duration of 20 minutes. This freezing time was determined optimal for the turkey breast to partially solidify facilitating dissection. Lesions were dissected using a size 10 scalpel. A slit was carefully cut through each lesion with the guidance of the marker lesions. Each lesion's maximum width and length, based on visually determined tissue discoloration, was measured using digital calipers (CD S6 CT, Mitutoyo Corp, Japan) with an accuracy of 0.01 mm. The ultrasound image from the SonoSite during HIFU treatment was recorded for each lesion using a digital video camera (GL1, Canon Inc., Lake Success, NY).

5.2.3 Results

This experiment provided means of understanding the relationship between focal intensities and lesion types and sizes. It was also of interest to note the minimum intensities required for lesion formation and ultrasound visualization of lesion formation. The turkey breast samples used in the experiment had a measured speed of sound of 1540 ± 11 m/s, an a measured attenuation of 0.096 ± 0.002 NP/cm/MHz (versus 0.082 NP/cm/MHz for uterus and 0.122 NP/cm MHz for fibroids, shown in Table 3.3). Upon dissection, two types of lesions were observed, as depicted in Figure 5.6. Lesions created at focal intensities (I_{SATA}) greater than ~1500 W/cm^2 were tadpole-shaped, indicative of cavitation activity at the focus (Yuen 2001). Lesions created at focal intensities (I_{SATA}) below ~1500 W/cm^2 were ellipsoidal and cigar-shaped, indicative of a thermally induced lesion (Yuen 2001). In comparison, Sanghvi et al. found that cavitation induced lesions occurred at intensities around 1700 W/cm^2 using a HIFU frequency of 4 MHz (Sanghvi, Foster et al. 1999). There was an intensity threshold for ultrasound visualization of lesion formation. HIFU lesions appeared immediately in the ultrasound image as bright hyperechoic spots 100% of the time at intensities above ~1250 W/cm^2. The minimum intensity required for consistent lesion formation in turkey breast was approximately 700 W/cm^2 meaning that there were physically produced lesions that were not visualized using ultrasound. The minimum intensity required for any lesion formation in turkey breast was dependant on exposure duration and approximately 400 W/cm^2 and 600

W/cm^2 for a 10 and 5 second exposure duration respectively. Previously, investigators have found that the following relationship approximated the threshold dose needed for forming a lesion:

Eq. 5.1 $$UE = \sqrt{It}$$

Where UE is "ultrasound energy" expressed in units of $W/cm^2sec^{0.5}$, I is the spatial average temporal average focal intensity (W/cm^2) and t is time (seconds). UE has been found to be 200 $W/cm^2sec^{0.5}$ in cat brain (Fry, Kossoff et al. 1970), 470 $W/cm^2sec^{0.5}$ in cat liver (Frizzell 1988) and 1150 $W/cm^2sec^{0.5}$ for dog prostate (Sanghvi, Foster et al. 1999). In comparison, our data showed that UE was approximately 1300 $W/cm^2sec^{0.5}$ based on the minimum intensity required for the onset of lesion formation at 5 and 10 seconds. The differences in these values show that the threshold ultrasound energy required for lesion formation varies greatly depending on tissue type.

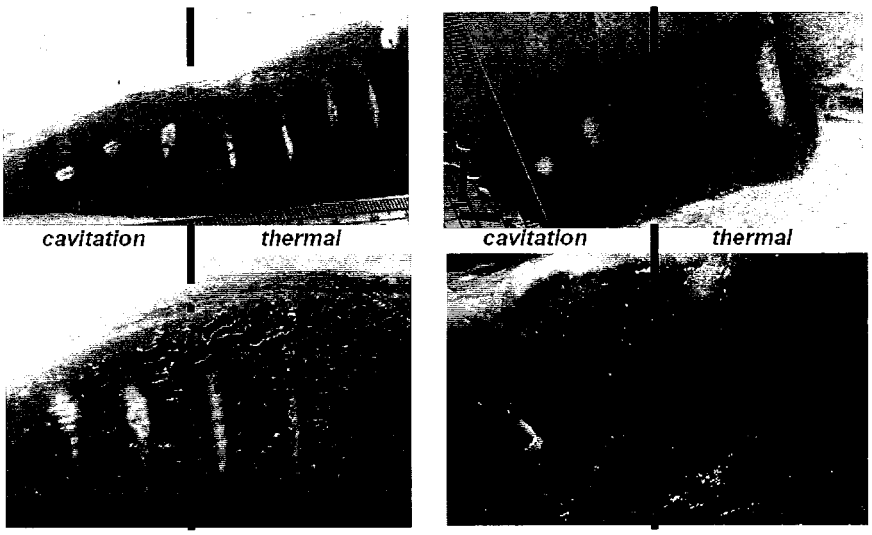

Figure 5.6 Comparison of thermal and cavitation induced lesions. Lesions primarily due to HIFU thermal effects are cigar shaped while lesions involving cavitation effects are tadpole shaped and show more tissue deformation.

Figure 5.7 and Figure 5.8 show a correlation between focal intensity and measured lesion width and length, respectively. Over an intensity range of 500 – 2500 W/cm^2, lesion widths ranged from 2 - 6 mm for a 10 second exposure time, and 1 - 4 mm for a 5 second exposure time. Over the same intensity range, lesion lengths ranged from 5 - 25 mm for

a 10 second expsoure time, and 5 - 18 mm for a 5 second exposure time. At intensities greater than 1500 W/cm^2, lesion widths were generally greater than the logarithmic best-fit line since cavitation induced lesions were formed.

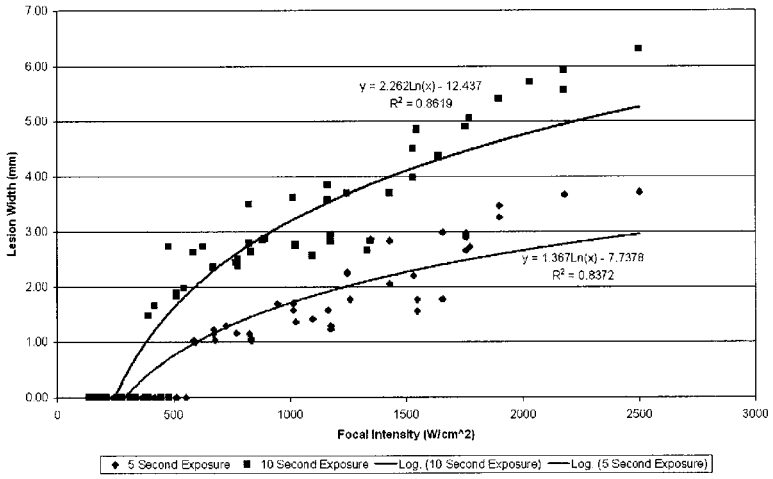

Figure 5.7 Measured lesion widths at various focal intensities

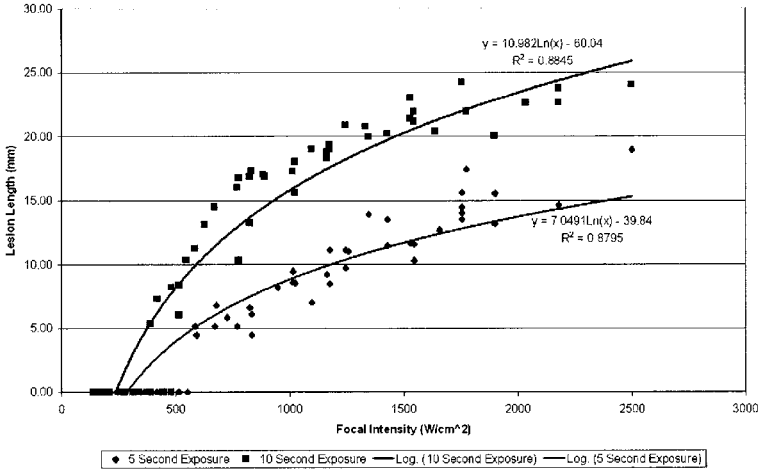

Figure 5.8 Measured lesion widths at various focal intensities

5.3 ERGONOMICS TESTING IN HUMANS

5.3.1 Purpose

Device ergonomics were tested in human volunteers in accordance with a human subjects research protocol approved at the University of Washington in accordance with guidelines set by the National Institutes of Health. This study also determined the areas of the uterus that could be visualized and potentially treated by the image-guided HIFU device.

5.3.2 Procedure

Six healthy female volunteers, age 23 to 49, not pregnant and with intact uteri, were recruited to participate in the study. The volunteers were asked to arrive with a full bladder – i.e. drink 750 mL of water at least a half hour before the study and not empty their bladders. The study involved a transvaginal ultrasound scan of the pelvic region, a transabdominal ultrasound scan of the pelvic region, and a transabdominal ultrasound scan with the sterilized transvaginal HIFU transducer inserted in the vagina (i.e. the device was positioned in the vaginal cavity as if treatment were to be administered although no treatment was administered). A sterile condom was secured to the HIFU transducer, lubricated, and filled with water prior to insertion into the vagina. Once the HIFU transducer was inside the vagina, the image probe was positioned to visualize pelvic structures and the HIFU transducer. The length and width of the uterus were measured, and the potential treatable region based on a fixed HIFU focal length of 4 cm was determined for various transducer positions. These positions corresponded to how the transducer would be placed for targeting the cervix, the mid-uterus region, and the fundus. Also, water was injected and removed from the condom to determine the feasibility of using a water-filled condom as a stand-off. After the study, each volunteer completed a survey regarding the comfort of the device during entrance into and exit from the vagina, and while the device was inside the vagina. Our sonographer, Marla Paun, also completed a survey regarding the ease of use of the device and any complications that arose during each study. These surveys are included in Appendix C.

5.3.3 Results

Placement of the device in human volunteers demonstrated successful visualization of the HIFU transducer and the uterus. The water filled condom and the transducer lens surface were easily seen in the ultrasound images, along with the uterus, vaginal wall, and bladder, as shown in Figure 5.9.

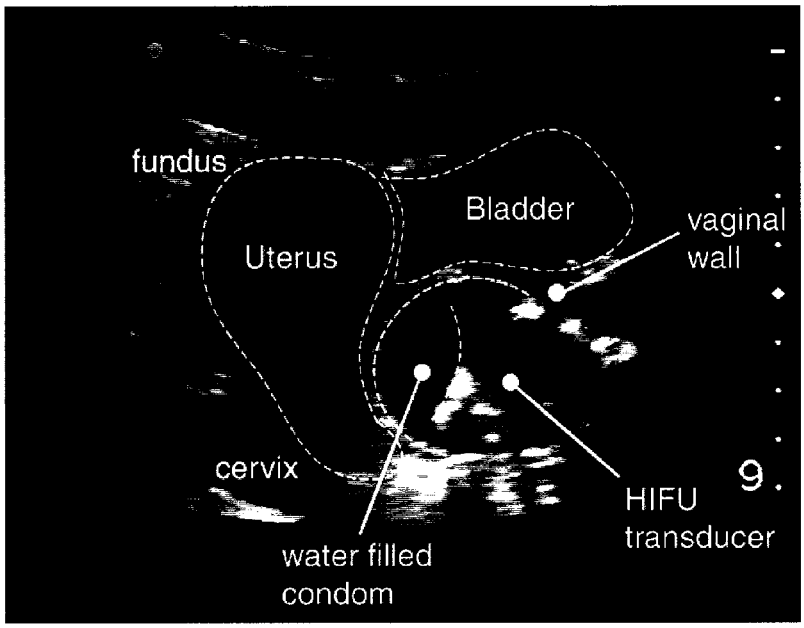

Figure 5.9 Ultrasound image of the HIFU transducer placed in a human vagina shows that the HIFU transducer can be seen along with the water filled condom and pelvic structures such as the uterus and the bladder.

Volunteer statistics and uteri measurements are shown in Table 5.4. The volunteers ranged in age between 23 and 49 years, and in body mass index (weight in kilograms divided by the square of height in meters) between 20.4 and 29.9. According to the US department of health and human services, the average female has a body mass index of 26.3 with a standard deviation of 5. Therefore, our sample population falls within one standard deviation of the average American female. One volunteer had previously given birth, and one volunteer had a fibroid located in the fundus. Four volunteers had aniflexed uteri (the uterus is pointed towards the abdomen) and two had midline uteri. Uteri length ranged between 5.90 and 8.49 cm and width ranged between 3.21 and 4.63 cm, excluding the volunteer with a fibroid located at the fundus whose total uterus length and width including fibroid were 11.7 cm and 8.03 cm, respectively. Volunteer 3 had previously given birth to two children and as a result had a larger uterus than others. No subjects had a retroflexed uterus (pointed towards the rectum). This may be a subject of future investigation. Also, all volunteers were white females. Therefore, any interracial differences were not studied.

Table 5.4 Volunteer statistics and uterus measurements

Subject	Age (years)	Body Mass Index	Uterus orient-tation[d]	Uterus length (cm)	Uterus width (cm)	Distance to cervix[e] (cm)	Distance to mid-uterus[e] (cm)	Distance to fundus[e] (cm)
1	26	20.4	A	6.15	3.42	1.88	2.69	3.92
2	27	22.0	A	5.90	3.21	1.83	2.52	3.87
3[a]	49	22.9	A	8.49	4.63	1.92	3.18	4.33
4	23	22.7	A	7.21	3.90	1.98	3.21	3.00
5	32	29.9	M	7.26	3.33	2.17	3.50	4.78
6[b]	42	24.6	M	11.7	8.03	3.61	5.64	5.44
Mean	33.17	23.75		7.79	4.42	2.23	3.46	4.22
St Dev[c]	10.23	3.31		2.13	1.84	0.69	1.13	0.84

a: volunteer had children b: volunteer had a fibroid located in the fundus
c: standard deviation d: A = aniflexed, M = midline
e: distance measured from the lens of the HIFU transducer

Table 5.4 also showed that if treatment was to be administered, a 4 cm focal length would be sufficient for treating fibroids located in the cervix and mid-uterus of all volunteers (average distance of 2.23 cm and 3.46 cm respectively). Since fibroids located in the fundus may exceed the 4 cm focal length for midline uteri and in subjects who have had children, the focal length may need to be increased or a transabdominal approach may be used for such cases. Figure 5.10 shows how the transducer can be positioned to target various areas of the uterus. By varying the amount of water in the condom, and the distance the transducer is in the vagina, different areas of the uterus can potentially be treated.

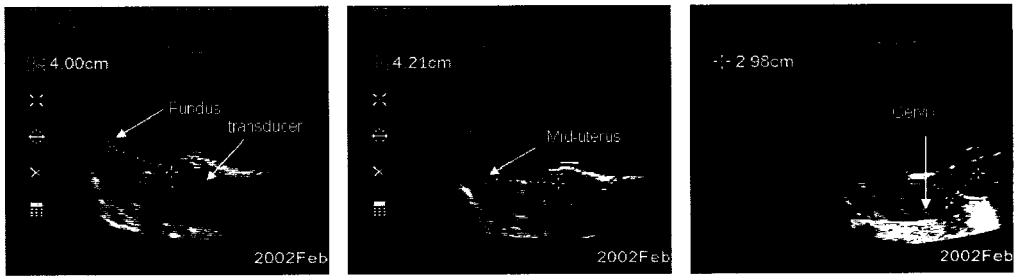

Figure 5.10 Transducer positioning for targeting various uterus locations

According to the survey completed by the volunteers after the study, entrance into the vagina was comfortable if lubrication was used and sufficient water was inside the condom to act as a cushion between the vaginal wall and the HIFU transducer. No discomfort was experienced while the applicator was in the vagina and when the applicator was removed from the vagina. The survey results are included in Appendix D.

The size of the water filled condom as it entered the vagina was approximately 4-5 cm in diameter. We noted that a larger transvaginal applicator (up to 4 cm in diameter) can potentially be used. This would result in a smaller focal region, and a concomitant increase in gain and HIFU intensity during treatment.

5.4 SHEEP MODEL FEASIBILITY TESTING

5.4.1 Purpose

It was proposed that sheep would be a good large animal model to use for *in vivo* studies. The purpose of this study was two-fold: First, the feasibility of using the sheep model and the acoustic properties of sheep uterine tissue was determined. Second, this experiment provided an opportunity for the device to be used *in vivo* in an animal model. The device was examined for its imaging and lesion forming capabilities, and the effects of HIFU treatment on uterus *in vivo* were studied. This experiment was conducted according to a protocol approved by the Animal Care Committee at the University of Washington following guidelines outlined by the National Institutes of Health.

5.4.2 Methods and materials

A female sheep, approximately 1 year of age weighing 40 – 50 kg, was ordered for this experiment. Two initial imaging, device positioning and protocol testing sessions with the sheep were performed four months prior to actual treatment. At the time of this experiment, the animal had gained weight to approximately 93 kg. The animal was sedated intramuscularly with xylazene (0.3 mg/kg) and atropine (1mL/9kg), transferred onto an operating table, connected to a ventilator, and placed under Isofluorane anesthesia. The abdominal region of the sheep was shaved and cleaned using water and Nair (Church & Dwight Co., Inc, Princeton, NJ) to allow ultrasound imaging.

A condom was attached to the HIFU transducer and filled with water. The HIFU transducer was placed in the vagina and the abdominal image probe was placed on the shaved abdomen, as shown in Figure 5.11. The abdominal region was initially scanned using the ultrasound image probe to determine the optimal imaging position, and to locate pelvic structures and the HIFU transducer. Ultrasound gel was used to ensure acoustic coupling between the abdominal skin and the abdominal image probe.

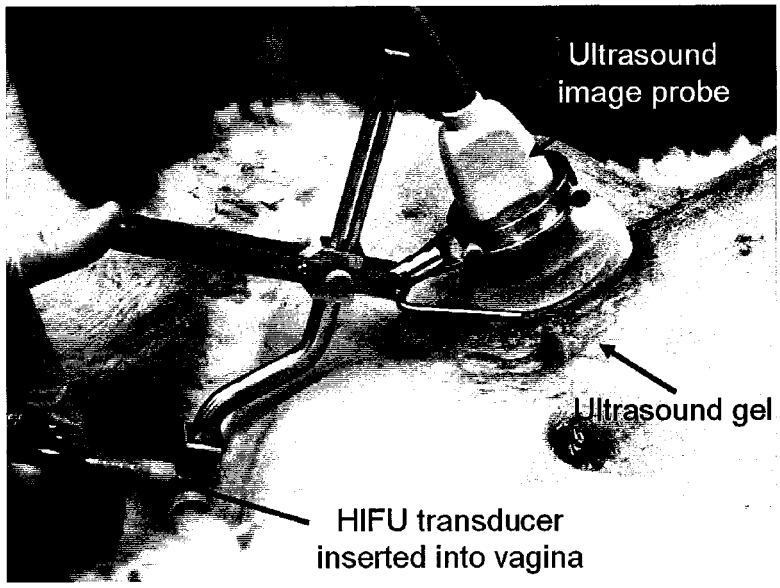

Figure 5.11 Placement of device in the sheep

The water filled condom was inflated and deflated to determine the boundaries of the treatment region using the HIFU transducer. HIFU was applied to various areas of the uterus and vaginal canal at focal intensities (I_{SATA}) between 500 and 1400 W/cm^2 at 7 seconds exposure duration per treatment. Two areas received ten consecutive treatments each with 20 seconds in between treatments. Ultrasound imaging was recorded using a digital video recorder (GL1, Canon Inc., Lake Success, NY).

At the completion of treatment, anesthetic was increased to 5% for 5 minutes and the animal was euthanized using an overdose of Pentasol. A surgical incision was made in the lower abdomen, and the vaginal canal and uterus were removed. Photographs were taken of the treated regions using a digital camera, a gross analysis to determine the appearance of HIFU treated area was performed, and selected sections of treated uterus were placed in a 10% neutral buffered formalin solution for fixation. These sections were sent to the histopathology laboratory for staining with hematoxylin and eosin and mounting on microscope slides. The completed slides were analyzed using bright field light microscopy (Leica DMLS, Leica Microsystems, Wetzlar, Germany). Six sections vaginal wall and uterus were also used (within 24 hours of dissection, preserved in saline solution) for acoustic property measurements using the acoustic calipers technique (Bloch 1998).

5.4.3 Results

5.4.3.1 Gross Examination

Macroscopic analysis of the treated areas revealed regions of necrosis surrounded by blood congestion inflammation. Figure 5.12 shows the two treated spots on the vaginal wall where ten consecutive treatments were given. These treated areas showed necrotic tissue as blanched tissue, and blood congestion as dark red borders surrounding the necrosis.

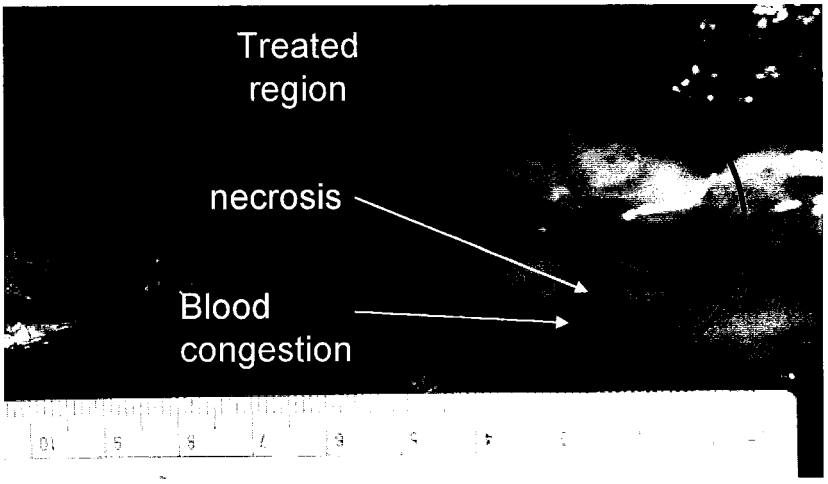

Figure 5.12 Repeated HIFU exposure to vaginal wall resulted in areas of necrosis surrounded by rings of blood congestion. Numbers on the ruler are in cm. The vaginal opening was to the left of the image, and the uterine horns were to the right of the image.

Figure 5.13 shows a treated area of the uterus, also showing a necrotic center surrounded by a ring of blood congestion. It can be seen in the cross section of the treated area that the coagulative necrosis extended through the depth of the tissue. Treatment effects appeared to be localized and well demarcated.

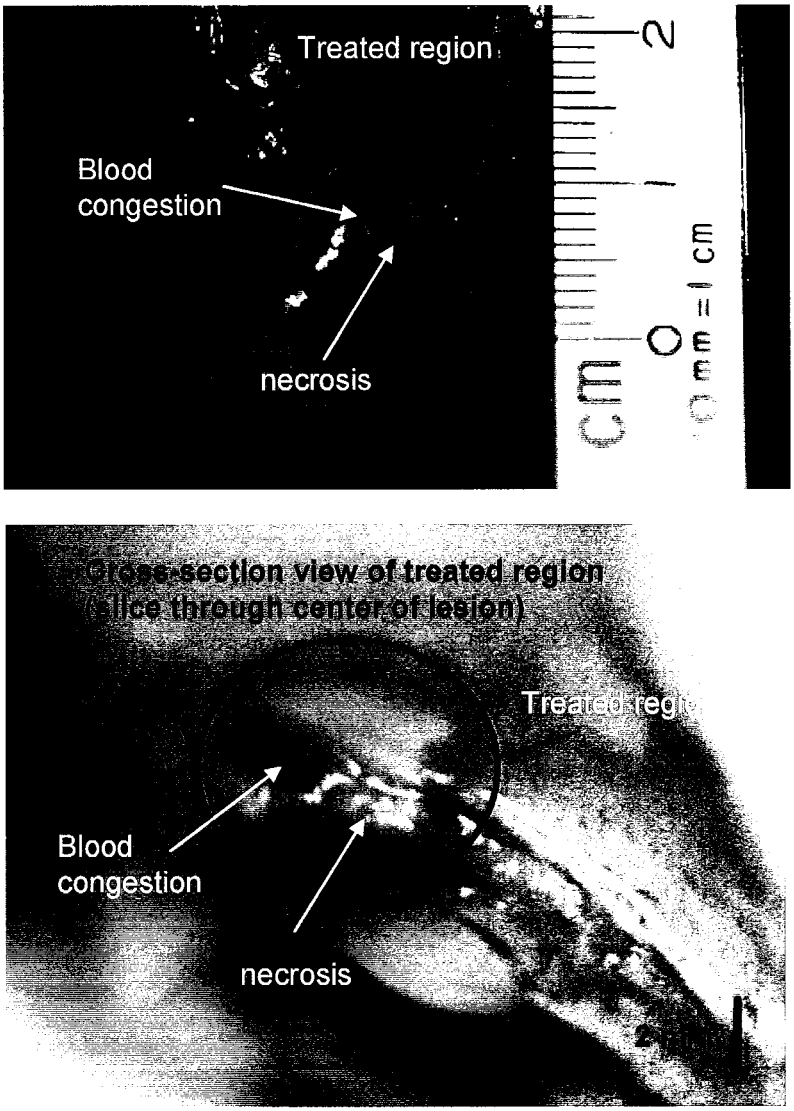

Figure 5.13 Treated sheep uterus showing coagulative necrosis, indicated by tissue necrosis (white region) surrounded by a ring of blood congestion

5.4.3.2 Histological analysis

Figure 5.14 shows a light microscopy image of non-treated sheep uterus at 10x magnification. Non treated areas are shown in Figure 5.14A. This image was taken at the border between the myometrium and the endometrium. The myometrium, or uterine wall, is comprised of densely packed smooth muscle fibers organized in interlacing bundles that are oriented randomly. The endometrium consisted of straight, tubular uterine glands embedded in endometrial stroma. This structural composition is similar to human uterus. Figure 5.14B and Figure 5.14C depict areas of HIFU treatment. A well demarcated region of HIFU induced gland shrinkage, glandular wall disruption and resulting fluid leakage, and separation of the glands from surrounding tissue can be seen in Figure 5.14b. Smooth muscle is disruption and separation can be observed in Figure 5.14c.

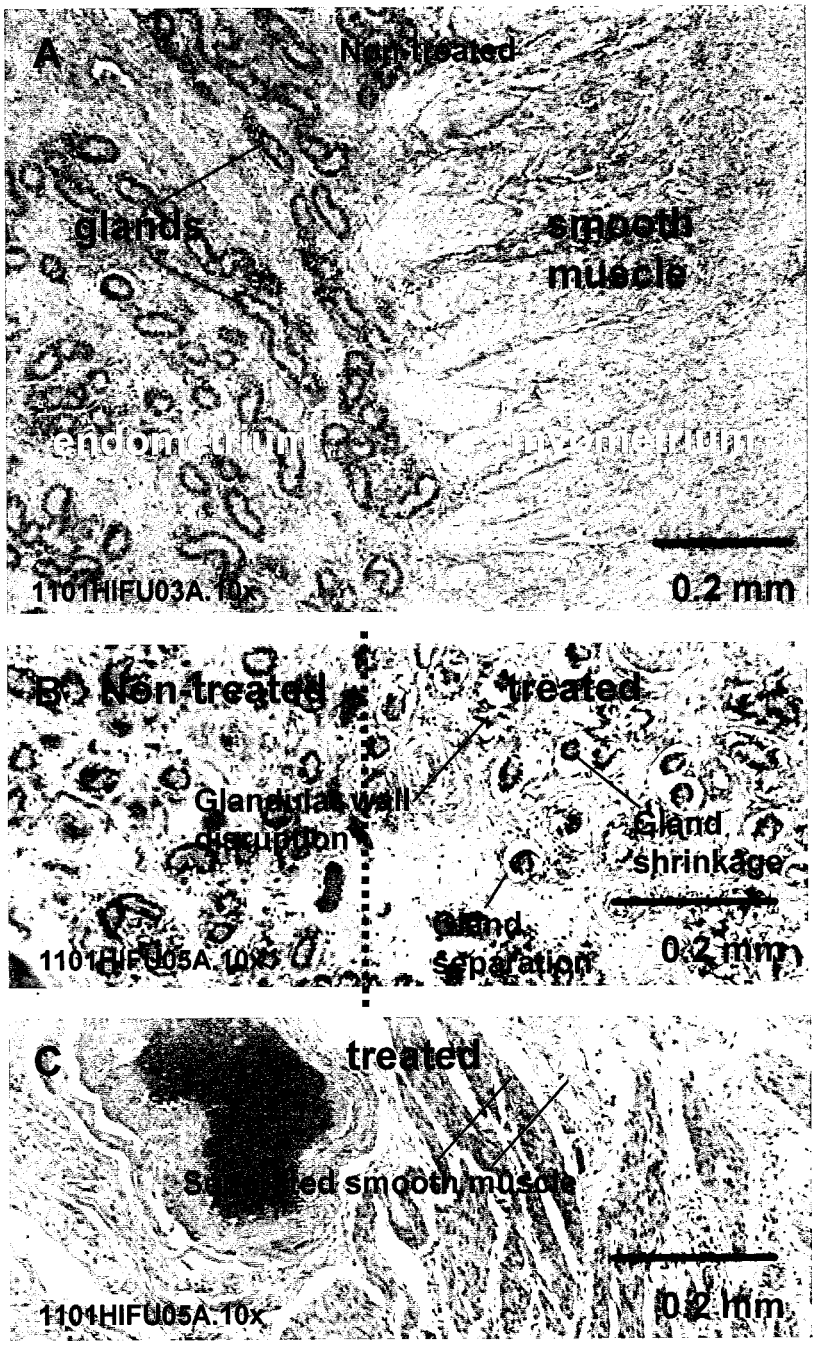

Figure 5.14 Light microscopy images of non-treated and treated sheep uterus. A shows normal, non-treated endometrium glands and smooth muscle (myometrium). B shows treated and non-treated endometrium. The treated myometrium exhibited damaged glands and fluid leakage. C shows treated smooth muscle that showed separated bundles.

5.4.3.3 Tissue properties

Both acoustic velocities and attenuation were measured using the acoustic calipers method within 7 hours of animal euthanasia (Bloch 1998; Keshavarzi, Vaezy et al. 2001). The tissue was stored in saline solution between euthanasia and measurement using the acoustic calipers. The measured acoustic velocities for the sheep vaginal wall and uterus were 1573 ± 20 m/s and 1559 ± 19 m/s respectively, similar to human uterus tissue as shown in Table 3.3. The attenuation curve for sheep vaginal wall and uterus between 1 and 5 MHz is shown in Figure 5.15. Attenuation values correlated well to a power fit using regression analysis ($R>0.99$). The mean attenuation values for human uterine fibroid and myometrium, taken from studies shown in Table 3.3, also shown on this graph for comparison. Standard deviations for the human attenuation values are not shown on this graph. The values for human uterus attenuation were greater than one standard deviation of the average value for sheep attenuation. At 3.5 MHz, the attenuation values for sheep and human uterus are 1.5 and 2.5 dB/cm respectively. The slope of the attenuation curve for sheep uterus was also less than that for human uterus. This difference may be due to the density of the smooth muscle in the myometrium. The sheep vaginal wall was much more attenuative than sheep uterus, even more so than human fibroid tissue. It is often useful to compare attenuation in dB/cm/MHz or NP/cm/MHz. Approximate linear relations for human fibroid and uterus, and sheep uterus and vaginal wall are presented in Table 5.5.

Table 5.5 Summary of attenuation measurements comparing sheep tissue to human tissue

Tissue	dB/cm/MHz	NP/cm/MHz
Human uterus	0.713	0.082
Human uterine fibroid	1.06	0.122
Sheep uterus	0.34	0.039
Sheep vaginal wall	1.2	0.138

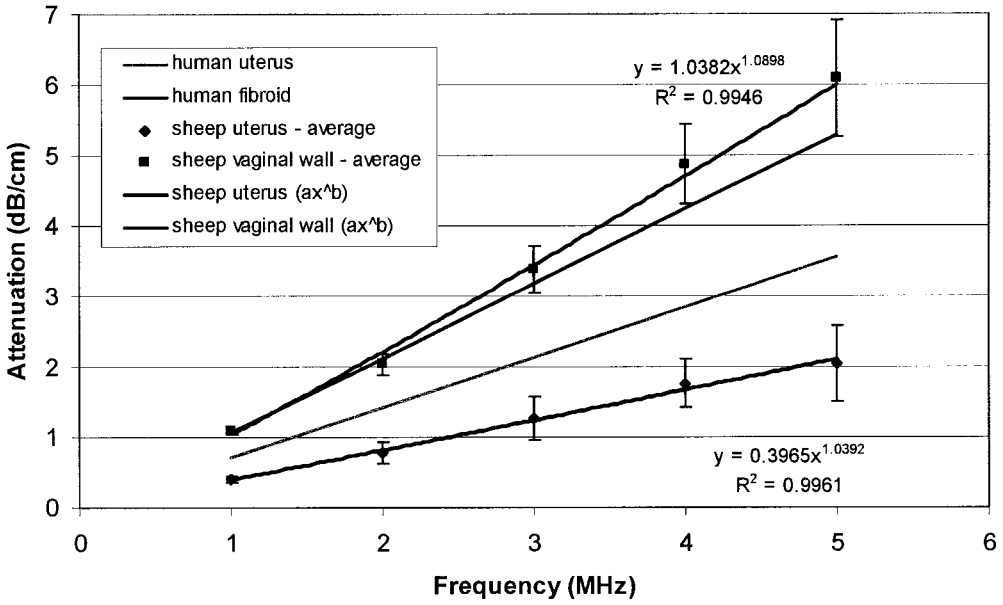

Figure 5.15 Sheep uterus and vaginal wall measured attenuation compared with human uterus and fibroid attenuation showed that sheep uterus had a lower attenuation than human uterus, and that human fibroid had a similar attenuation to sheep vaginal wall tissue.

5.4.4 Overall evaluation of the sheep model

The sheep provided an adequate means of *in vivo* testing of the device. Although the uterus of sheep was different than that of humans (sheep are bipartite meaning the uterus has two sides or "horns"), the tissue structure is similar, as revealed with microscopic analysis. Acoustic properties (taken at 3.5 MHz) of sheep uterus and vaginal wall were shown to be somewhat similar to that of human myometrium and fibroid tissue respectively. As a result, sheep uterus treatment may provide a feasible large animal model for future *in vivo* device testing.

The vaginal canal of the sheep is longer than in humans, and a larger depth of imaging was required to observe pelvic structures in sheep than in humans. However, the sheep, when treated, was also twice the size as originally expected. It is of interest to note that a study of the reproductive tract in an adult non-pregnant sheep revealed pelvic structure dimensions listed in Table 5.6. The sheep uterus body is similar in size to the human uterus (Table 5.4) while the vaginal length is longer than in humans (6-11 cm from Section 4.2.4).

Table 5.6 Sheep pelvic anatomy dimensions obtained from the Department of Agriculture at Montana State University

Parameter	Dimension
Oviduct length	15 - 19 cm
Uterine horn length	10 - 12 cm
Uterine body length	4 -10 cm
Uterine body width	3 - 6 cm
Cervix length	1 - 2 cm
Cervix outer diameter	2 - 3 cm
Anterior vagina length	10 - 14 cm

5.4.5 *Ultrasound Imaging Difficulties*

An ultrasound image captured during HIFU treatment of a sheep uterus is shown in Figure 5.16. The hyperechoic spot was dim and difficult to observe when it appeared. In Figure 5.16, image subtraction techniques were performed in Adobe Photoshop (Adobe Systems Inc., San Jose, CA) to visualize the hyperechoic spot better. For future *in vivo* sheep experiments, higher intensities may be used to ensure the hyperechoic spot is more pronounced.

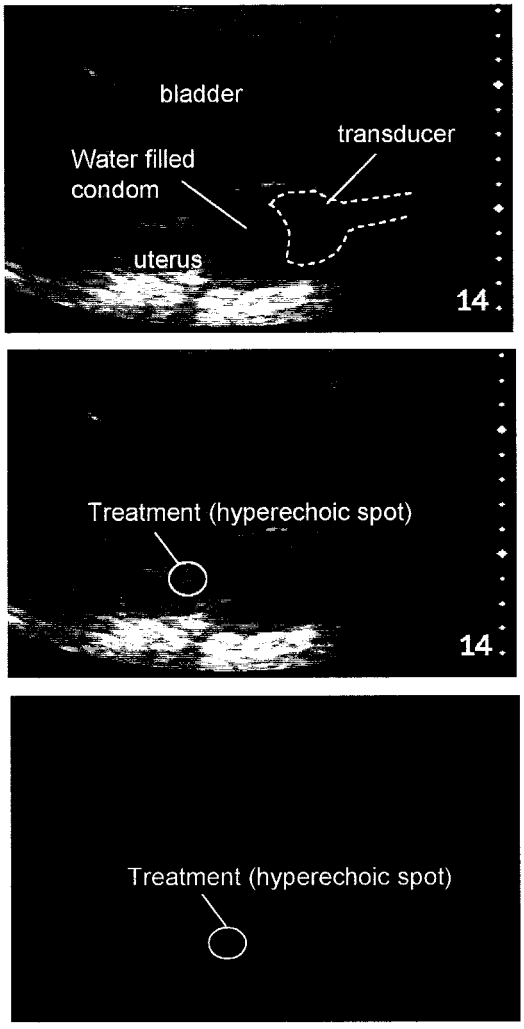

a. Ultrasound image before treatment, showing the HIFU transducer and pelvic structures can be seen.

b. Ultrasound image taken immediately after HIFU treatment shows a dim hyperechoic spot at the focus.

c. Image subtraction was performed, with image (b) subtracted from image (a). The hyperechoic spot can be more clearly seen. This hyperechoic spot has been superimposed on a darkened image (a) to show the relative location of the spot.

Figure 5.16 Ultrasound image of in vivo HIFU treatment of sheep uterus

5.5 EVALUATION OF VERSION 1 DEVICE

Several modifications to the device were recommended based on the studies discussed in this chapter. It was deemed necessary for these changes to be made prior to using the device in future *in vivo* safety and survival studies. These modifications are discussed in this section, the first two concerning the HIFU applicator, the third concerning the device.

5.5.1 *Increase HIFU intensity*

The sheep experiment demonstrated that the treated area was difficult to visualize using ultrasound imaging. This was inferred to be due to the lack of HIFU intensity at the focus, necessary to induce a hyperechoic spot. It was shown in the *in vitro* turkey and gel experiments that a threshold intensity ($I_{SATA} \sim 1250$ W/cm^2) was necessary for visualization of HIFU lesion. In sheep, this threshold may not have been met due to greater attenuation and tissue movement as a result of respiration. There are several methods in which the HIFU intensity can be increased: (a) a decrease in tissue attenuation between the HIFU applicator and the focus, (b) an increase in the duty cycle of the HIFU, (c) an increase in transducer focusing gain. The first two methods were impractical since (a) *in vivo* tissue properties and the path from the HIFU applicator to the treatment location cannot be altered (b) an increase in the HIFU duty cycle resulted in more of the ultrasound image being blocked by interference bands (section 4.3.6.2). Therefore, we attempted to increase the focusing gain of the HIFU applicator. Two approaches that will be investigated to increase the focusing gain were bringing the f-number closer to 1 (currently the f-number is 1.57), and increasing the transducer efficiency.

To bring the f-number closer to 1, the transducer diameter can be increased to ~4 cm, or the focal length can be decreased to ~2.5 cm. The ergonomic studies showed that a 4 cm focal length was necessary to treat various regions of the uterus. Also based on ergonomic study results, a slightly larger transducer (closer to 4 cm) can still be inserted comfortably into the vagina with the surrounding water filled condom and sufficient lubrication. Therefore, the transducer diameter was increased to 3.81 cm from 2.54 cm.

To increase the transducer efficiency, an acoustic impedance matching layer was placed in front of the aluminum lens. A matching layer decreases the impedance mismatch

between the transducer and the media that ultrasound is being radiated into, namely tissue. The next chapter will explore the matching layer selection and application in detail.

5.5.2 Transducer temperature monitoring

Since the transducer electro-acoustical efficiency was not 100%, there was potential for most of the electrical energy that is not converted into acoustical energy to be dissipated as heat. Therefore, the transducer temperature may reach levels capable of inducing thermal damage to tissue it comes in contact with. It was necessary to have some means of measuring applicator temperature at all times. An internally mounted thermocouple in the brass housing was used for this objective. The thermocouple also measured increases in transducer temperature if a leaking condom reduced the cooling potential.

5.5.3 Treatment targeting

It was necessary to have a means of accurately showing the HIFU focus for treatment planning and device positioning. The HIFU applicator was easily visualized in the ultrasound image and the fixed focus can be estimated by observing the position of the applicator. However, distortions in the image, inaccuracies in finding the center of the aluminum lens, and the time it would take to measure the focal distance every time the HIFU applicator was slightly moved would make this "visual focus estimation" technique impractical. It was shown that a hyperechoic spot appears at the focal region, but by the time this spot appears, the tissue at the spot would have already been treated. Thus, a method for showing focal position accurately prior to treatment will be developed. A mechanical method using position sensors that registered the device geometry was chosen due to its simplicity, compared to spatial recognition methods using infrared or electronic means. The targeting system is explored in Chapter 7.

6.0 CHAPTER 6 IMAGE-GUIDED HIFU DEVICE VERSION 2

6.1 MOTIVATION

A second generation of transvaginal HIFU transducers were designed and developed to prepare for *in vivo* experiments. Based on test results in Chapter 5, there were several modifications made to the transducer, namely an increase in size, the addition of an internal thermocouple, and the addition of an acoustic impedance matching layer. These changes, and the resulting improvements, are explored in this chapter.

6.2 RESIZING OF HIFU TRANSDUCER

First, the HIFU transducer was redesigned to be larger. The maximum diameter of the transducer was increased from 2.54 cm to 3.81 cm which would still fit inside the human vaginal canal. Since the focal distance will still remain at 4.0 cm, the f-number (section 2.12.2) will be 1.05. Compared to an f-number of 1.57 for the Version 1 transducer, the larger transducer will therefore have a smaller focal spot and thus have a higher focal gain. This higher focal gain will result in higher achievable intensities at the focus for the same applied power. As a result, lesion formation will be more localized and precise, and reduced transducer heating may result since less power is required to achieve the desired focal intensities for lesion formation. Also, visualization of the lesions as hyperechoic spots on the ultrasound will be more prevalent at a specified power level due to the increase in intensity when compared to the Version 1 transducer. We had specified the 3.81 cm diameter elements to have a center frequency of 3.5 MHz as per initial design specifications. However, when tested using an impedance analyzer (4194A, Hewlett Packard, Palo Alto, CA), their measured frequency was above 4.0 MHz (4.035 – 4.135 MHz). Figure 6.1 shows the difference in size between the version 1 and version 2 transducers.

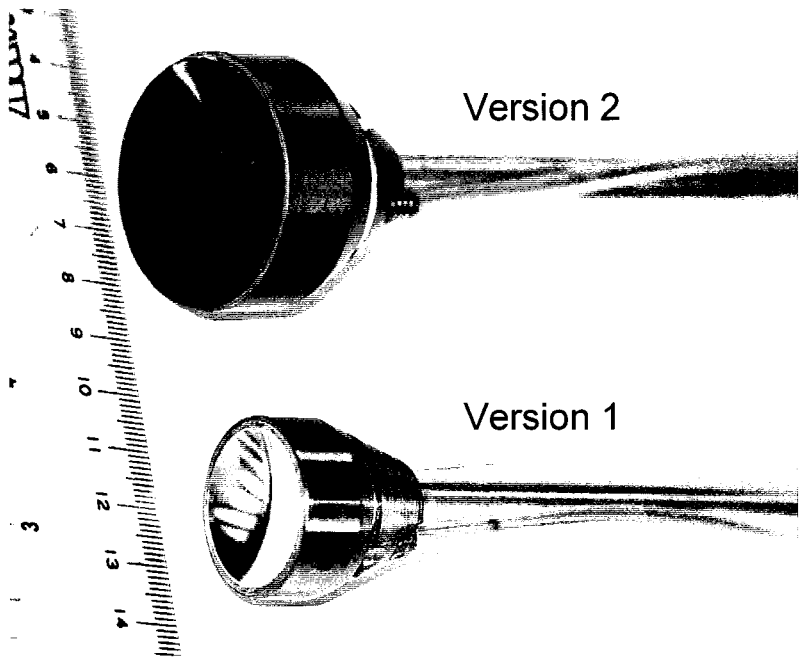

Figure 6.1 Comparison of version 1 and 2 transvaginal HIFU transducers. Numbers on the ruler are centimeters. The version 2 transducer has a graphite epoxy matching layer attached to the aluminum lens.

6.3 ATTACHMENT OF INTERNAL THERMOCOUPLE

It was important to be able to monitor transducer temperature during HIFU treatment, especially *in vivo*, when the transducer has the potential of damaging adjacent surrounding tissue. To perform this temperature monitoring, a type-K thermocouple (CH-AL, Omega Engineering Inc., Stamford, CT) was attached to the inner surface of the brass housing using thermally conductive epoxy (Loctite 7387 and 384, Loctite Corporation, Rocky Hill, CT) as shown in Figure 6.2. This location was chosen since the brass housing was the part of the transducer that was most likely to be in contact with surrounding tissue (next to the water filled condom), and also to prevent interference between the thermocouple and the electrical circuit connecting the PZT element. The thermocouple wire was fed through the transducer handle along with the coaxial cable supplying power to the transducer. A connector pin was attached to the open end of the thermocouple wire for connectivity to a data acquisition unit.

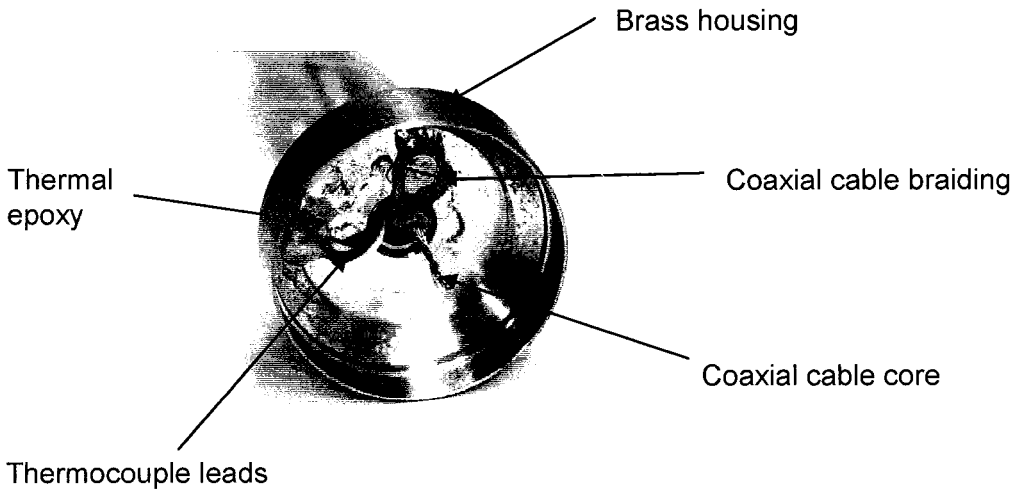

Figure 6.2 Thermocouple leads were attached to the inside of the brass housing using thermal epoxy, away from the coaxial cable braiding and core. This image shows the transducer prior to the aluminum lens and piezoceramic crystal being mounted into the brass housing.

6.4 GRAPHITE-EPOXY ACOUSTIC MATCHING LAYER

Because of the limited aperture size of the transvaginal HIFU transducer, it was desirable to have a high transducer efficiency to maximize the energy delivered to the treatment site. A matching layer (discussed in Section 2.12.3) made of epoxy embedded with graphite powder, has the potential to reduce the impedance mismatch between the acoustic lens made of aluminum and the surrounding water. This concept was hypothesized to increase transducer efficiency, and tested.

6.4.1 Background and motivation

In section 2.12.3, it was stated that a matching layer increases the transmission of acoustic waves from a transducer, and thus increases transducer efficiency. Single matching layers of epoxy resins loaded with dense powders such as tungsten or alumina have been tried. However, it was difficult to achieve a high enough density of the embedded substance to produce the acoustic impedances required (~7 Mrayl) to match the piezoceramic material (~32 Mrayl) to water (1.5 Mrayl) based on Eq. 2.32. Solid materials such as glass and graphite have been considered as matching layers, but there

was the problem of bonding pre-fabricated matching layers to the transducer without the bond layer destroying the effectiveness of the matching layer (Ziskin and Lewan 1993).

For the transvaginal HIFU transducer, the matching requirements differ because an acoustic lens made of aluminum was already placed in front of the PZT. Therefore, the goal was to match the impedance of aluminum (~ 17.1 Mrayl) with that of water (1.5 Mrayl). Using equation Eq. 2.33 and Eq. 2.34, a quarter wavelength thick matching layer with an impedance of approximately 5 Mrayl should therefore improve transducer efficiency. The reduced matching layer impedance needed (5 vs 7 Mrayl) made the use of powder embedded epoxy more feasible.

The theoretical increase in transducer transmission was determined using equation 2.10. If the piezoceramic material had an impedance of 34.65 MRayl (as with APC 880 used in our transducer), and ultrasound was transmitted into water (Z=1.5 MRayl), the transmission coefficient would be 0.16. With an aluminum lens (Z=17.1 MRayl), the transmission coefficients were 0.88 and 0.30 from piezoceramic to aluminum and aluminum to water respectively resulting in an overall transmission coefficient of 0.26. With the addition of a matching layer, the transmission coefficient will be increased based on the acoustic impedance of the matching layer, as shown in Figure 6.3. Therefore, if a matching layer with an acoustic impedance of 5 MRayl was used, the transmission coefficient would be 0.44 meaning a transmission increase of 0.18.

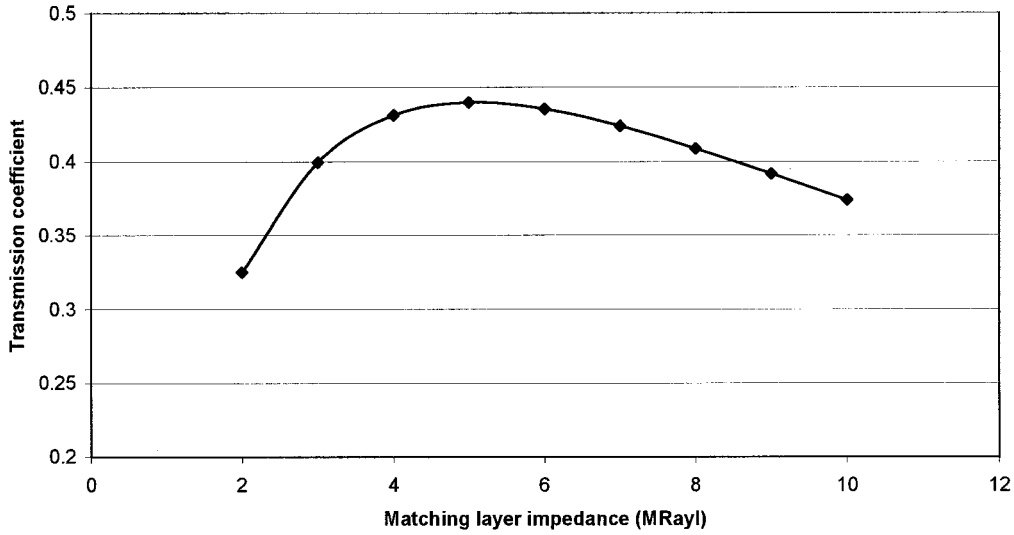

Figure 6.3 Relationship between matching layer impedance and transmission coefficient of HIFU transducer. This plot assumes that the matching layer is attached to an aluminum lens (Z=17.1 MRayl) and that ultrasound is emitted from a APC 880 (Z=34.65 MRayl) piezoceramic crystal.

We chose to experiment making a matching layer by embedding a two-part epoxy (Hysol 2039 and 3561, Loctite Corporation, Rocky Hill, CT) with powdered graphite (Graphite 96%, 325 Mesh, JT Baker Inc., Phillipsburg, NJ) since graphite is a dense and readily available substance. The powdered graphite had a maximum particle size of 45 microns. The acoustic impedance of graphite epoxy depended on the concentration of graphite. Hardened epoxy has an acoustic velocity and impedance of approximately 2530 m/s and 2.98 Mrayl respectively (Selfridge 1985). Since solid graphite has an acoustic velocity and impedance of approximately 3600 m/s and 6.48 Mrayl respectively (Specialty Engineering Associates, Santa Clara, CA), the theoretical impedance and velocity of graphite epoxy can be estimated as:

Eq. 6.1 $$\mathbf{Z_{grep} = m_{epoxy} Z_{epoxy} + m_{graphite} Z_{graphite}}$$

Eq. 6.2 $$\mathbf{c_{grep} = m_{epoxy} c_{epoxy} + m_{graphite} c_{graphite}}$$

Where m_{epoxy} and $m_{graphite}$ are the mass fractions of epoxy and graphite respectively. This theoretical impedance will be compared to experimental data in the following section.

6.4.2 *Characterizing graphite epoxy*

To determine the validity of equations Eq. 6.1 and Eq. 6.2, blocks measuring 2.5 x 2.5 x 2.0 cm made of degassed graphite epoxy of various graphite concentrations were made and acoustic properties (speed of sound and attenuation) measured using the acoustic calipers method described elsewhere (Bloch 1998). The density of these blocks was also measured to determine the acoustic impedance. In Figure 6.4, the acoustic impedance and velocity of graphite epoxy with graphite concentrations ranging from 0 to 40 % are shown. As expected, a higher concentration of graphite resulted in greater velocities and impedances. The velocities ranged from 2690 m/s to 2925 m/s for 0 to 40 % graphite respectively, and were within 50 m/s of the theoretical velocity determined from Eq. 6.2. The impedances ranged from 3.1 to 4.0 Mrayl, and were within 0.3 Mrayl of the theoretical impedance determined from Eq. 6.1. Error bars showed one standard deviation among three trials taken at each of the following frequencies: 3.0, 3.5, and 4.0 MHz. These frequencies were chosen due to the desired operating frequency of the HIFU transducer (3.5 MHz to 4.0 MHz) and to provide a range for which to compare the trend between frequency, impedances, and attenuation.

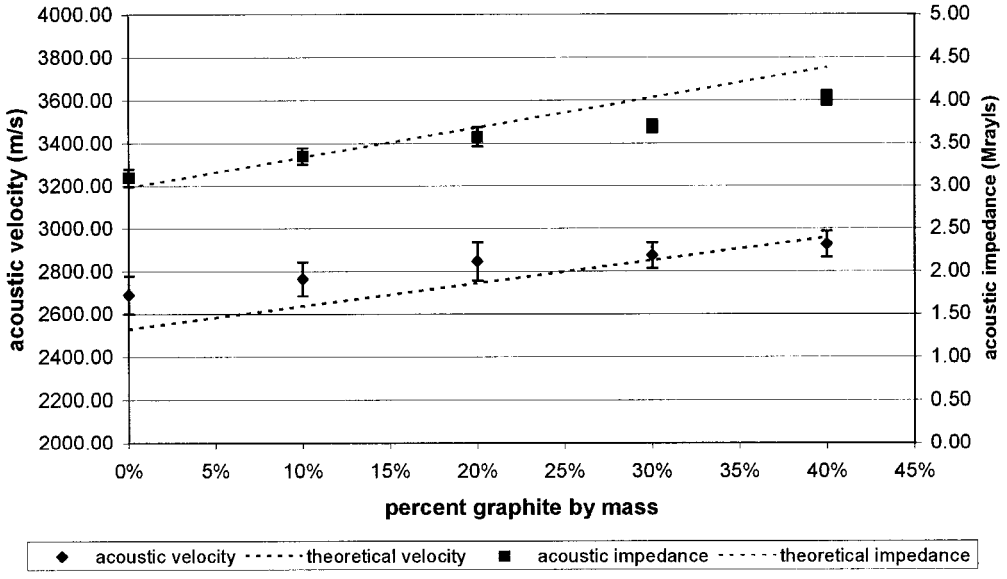

Figure 6.4 Acoustic impedance and velocity of graphite epoxy (mean ± standard deviation) show that acoustic experimentally measured values at various % graphite were close to the theoretically calculated values although not always within one standard deviation.

Figure 6.5 shows the attenuation of graphite epoxy ranging from 0 to 40 % epoxy, with error bars indicating one standard deviation.

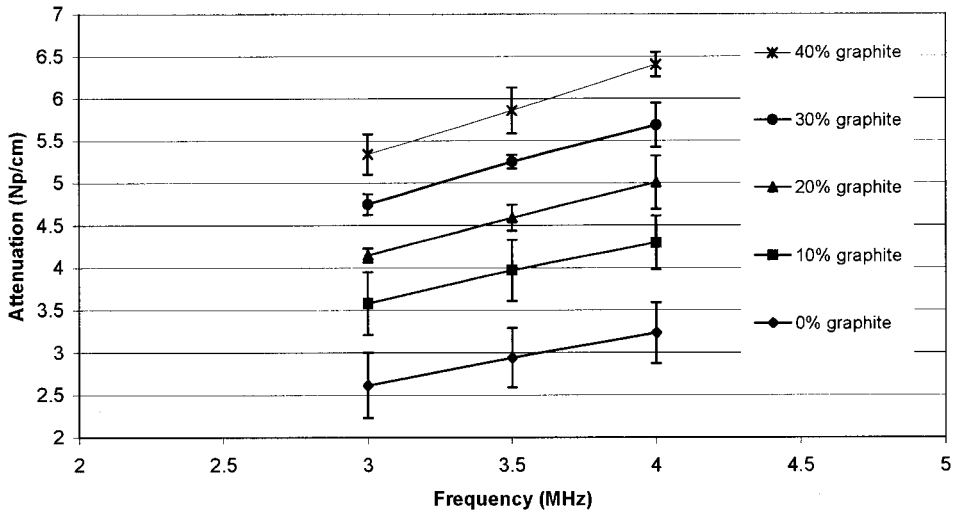

Figure 6.5 Attenuation of graphite epoxy at various graphite concentrations (mean ± standard deviation) show statistical significance in attenuation at each frequency between the various graphite concentrations.

When creating the graphite epoxy samples, it was found that although a 40% graphite concentration resulted in an impedance (4 Mrayl) closest to the desired matching impedance of 5 Mrayl, it resulted in a mixture that was thick and difficult to apply and bond to an aluminum surface. Also, as the percentage of graphite increases, the time for degassing the mixture also increased.

Next, it was found that the acoustic impedance between 20 and 30% graphite concentration was not significantly greater ($p>0.05$) and the attenuation was significantly less for a 20% graphite concentration at 4.0 MHz ($p<0.05$). Therefore, a 20% graphite concentration will be used for the matching layer material. At 4.0 MHz, the matching layer quarter wavelength thickness corresponded to 0.18 mm for 20% graphite epoxy ($c=2846$ m/s), resulting in a total attenuation of 0.09 NP or 0.01 dB (using a value of α = 5 NP/cm) across the matching layer. The impedance of a matching layer using a 20% graphite concentration was 3.6 Mrayl.

From Figure 6.3, the corresponding transmission is 0.42 using a matching layer with an impedance of 3.6 MRayl. Compared to a transducer without a matching layer, the increase in ultrasound transmitted is 16%. The attenuation in the matching layer can be neglected since a 0.01 dB loss is equivalent to a 99.7% transmission.

6.5 VERSION 2 TRANSDUCER CONSTRUCTION

The transducer construction procedure outlined in section 4.3.5 was modified to account for the addition of the matching layer. The matching layer was placed onto the curved surface of the lens prior to affixing the PZT element to the flat surface of the lens. Two transducers were constructed: one with the graphite epoxy matching layer and one without. This allowed us to determine the effectiveness of the matching layer in transducer efficiency measurements and transducer cooling studies discussed in sections 6.6.3 and 6.6.5 respectively.

6.5.1 Matching layer application

A custom mold was developed to ensure that the matching layer had a uniform thickness throughout the entire layer and prevented any air bubbles and debris from being introduced into the matching layer by sealing and isolating the matching layer and aluminum lens. A cross-section of this mold is shown in Figure 6.6. The mold was made of delrin plastic and a silicone rubber mixture (RTV 630 A and B, 10:1 by mass, GE Silicones, Waterford, NY). The mold consisted of a base, a central cylinder, and a cover. The top and base fitted onto the cylinder. The top piece consisted of a plastic cap attaching a rubber mold that was an exact negative of the lens shape, molded using the lens itself. The central cylinder was cut so that the lens and top would be centered while the graphite epoxy matching layer set in the mold. A piece of hollowed out aluminum shimstock with a thickness of 0.18 mm (corresponding to a quarter wavelength thickness for the matching layer), was custom made to fit on the plastic cap ensuring the matching layer would be of correct thickness. Small 0.5 mm slits that extended the length of the cylinder were cut on the perimeter of the rubber mold attached to the top cap. These slits allowed excess graphite epoxy mixture to leak out and prevented any air from being trapped during the lowering of the top piece of the mold by allowing air to escape.

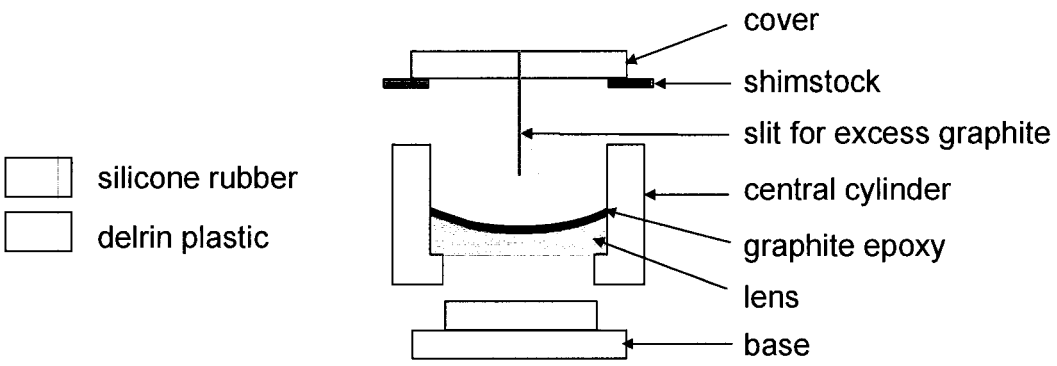

Figure 6.6 Custom mold apparatus for matching layer application

The following method for application of the matching layer was developed via trial and error.

1. The surface of the lens was lightly sanded with fine grain sand paper to eliminate any dimples or small metal particles that may remain from machining the lens. The lens surface was also brushed over with a fiberglass brush. A rough surface provided a better bonding surface for the graphite epoxy. It was hypothesized that as long as the grooves induced by the sandpaper and fiberglass brush were less than a quarter wavelength deep, they would not affect the ultrasound beam pattern.

2. The sanded lens was cleaned with acetone in an ultrasonic cleaner and dried using compressed air.

3. A very thin layer of wax was used to cover the inner surfaces of the mold to allow the lens and matching layer to be extracted easily.

4. The base was placed into the cylinder and the lens was placed on top of the base.

5. Graphite was mixed with the thicker (resin) component of the epoxy (Hysol RE2039, Loctite Corporation, Rocky Hill, CT) at a ratio of 13:40 (graphite:resin) by mass for an overall graphite concentration of 20%. The mixing was performed in a plastic mixing tray with an aluminum stir rod.

6. Prior to use, the graphite and resin mixture was degassed under a vacuum at 30 mmHg pressure until air bubbles stopped rising to the surface and popping.

7. The hardener (HD3561, Loctite Corporation, Rocky Hill, CT) was added to the graphite-resin mixture at a ratio of 12:43 (hardener:graphite-resin mixture) and mixed thoroughly using the metal stir rod.

8. The three part mixture was degassed again under a vacuum at 30 mmHg pressure until air bubbles stopped rising to the surface and popping.

9. A 5 mL syringe was used to extract the graphite epoxy mixture from the bottom of the plastic mixing tray with caution taken to prevent induction of air bubbles into the syringe. Air bubbles in the syringe were allowed to rise to the piston end of the syringe prior to the next step.

10. The mixture was carefully injected from the syringe onto the center of the lens using an amount greater than necessary to cover the entire surface of the lens with the appropriate quarter wavelength thickness (Figure 6.7).

11. The top cap and mold were carefully centered on the cylinder and lowered with the assistance of a vice clamp until the shimstock touched the top surface of the cylinder (Figure 6.7). Excess graphite epoxy mixture leaked out of the slits cut in the mold.

12. The graphite epoxy was allowed to dry and set onto the lens surface over a 24 hour period at 25°C. The lens and matching layer were carefully extracted out of the mold.

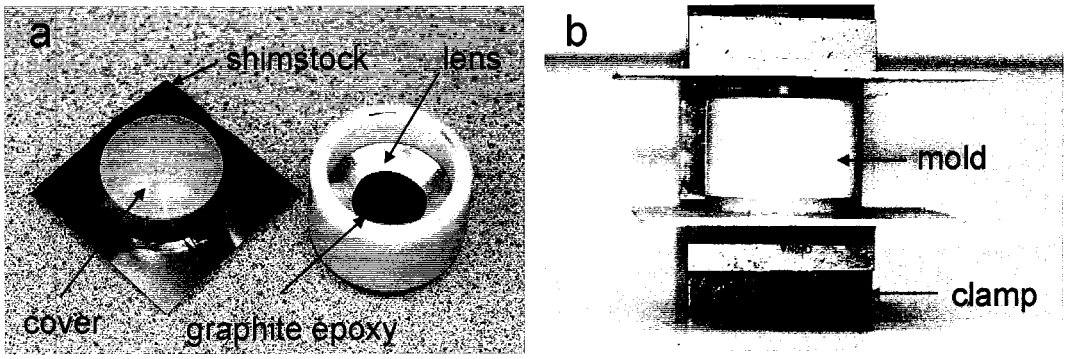

Figure 6.7 Photographs of matching layer application

Through trial and error, it was deemed important to mix the graphite and resin first rather than adding graphite powder to already mixed two part epoxy. This was because the epoxy had a pot life of 35 minutes meaning the chemical reaction causing hardening took effect 35 minutes after mixing. Due to the large amount of air trapped in powdered graphite, it would take much longer than 35 minutes to degass the quantity of graphite epoxy used for a matching layer. By degassing the graphite mixed with the thicker part of the epoxy (resin), the majority of the degassing occurred without hardening. When the degassed graphite-resin mixture was mixed with the hardener and degassed a second time, less than 35 minutes was required for complete air bubble removal.

The procedure in section 4.3.5 was used to construct two transducers, one with a matching layer and one without. A photograph of the completed transducers is shown in Figure 6.8.

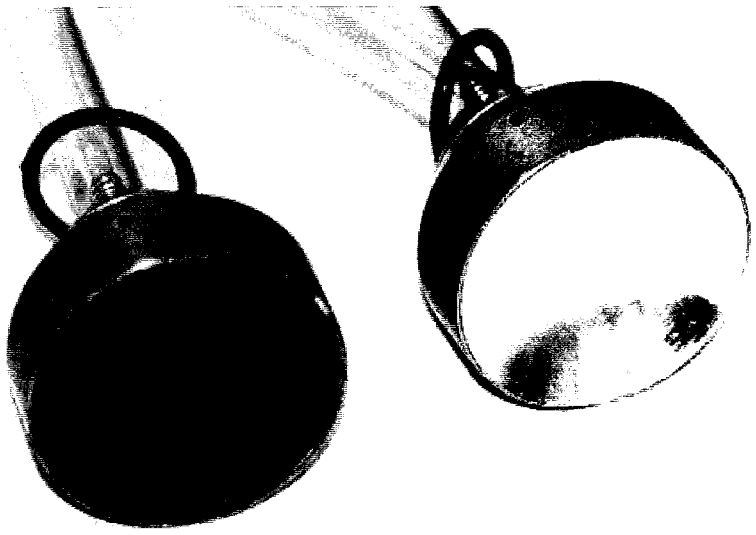

Figure 6.8 Two completed transducers, one with matching layer (left) and one without (right)

6.5.2 Impedance measurements and frequency temperature response

An electrical impedance matching network was made for each of the transducers (with and without matching layer) using the procedure outlined in section 4.3.5.5. The real impedances of the transducers were tuned to be between 45 and 50 Ω, and the imaginary impedances tuned to be between -5 and 5 Ω. The impedance plot for the transducer with the matching layer is shown in Figure 6.9. The center frequency of the transducer was 4.035 MHz, and the impedance was 50.32-*j*3.18 Ω at the center frequency. The version 2 transducers appeared to be of narrower bandwidth than the version 1 transducer upon initial comparison impedance plots. The change in real impedance for an increase or decrease of 0.03 MHz was 3 Ω for the version 2 transducers versus 4 Ω for the version 1 transducer. The true bandwidth of the version 2 transducer was determined in section 6.6.3.

The temperature dependent variation in the center frequency of the transducer (determined by the peak real impedance as shown by the impedance analyzer) was studied. This provided insight as to the effects of transducer heating on center frequency variation and potential power output. The power output is dependant on the difference between the operating frequency and center frequency. The impedance of the version 2

transducer with matching layer was measured and center frequency determined in degassed distilled water of different temperatures. Three center frequency measurements were taken at each 2 degree temperature increment from 20 to 80°C. As shown in Figure 6.10, there was good linear correlation (R^2>0.99) showing the change in frequency to be -1583 Hz/°C.

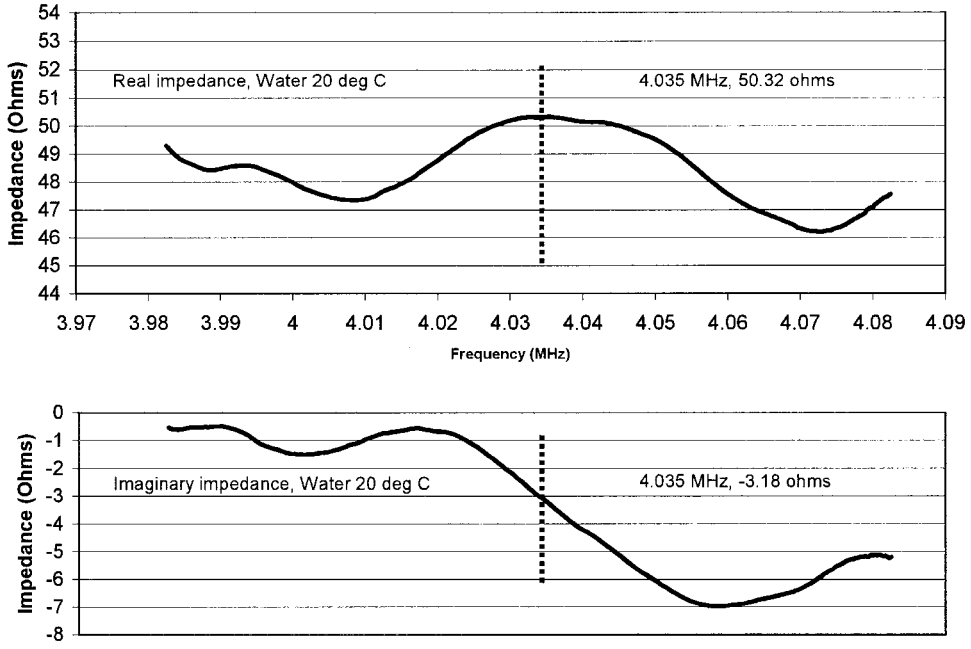

Figure 6.9 Impedance plot for version 2 transducer with matching layer. The center frequency was determined by the peak of the real impedance curve as 4.035 MHz. The impedance at the center frequency was 50.3 ohms real and -3.18 ohms imaginary.

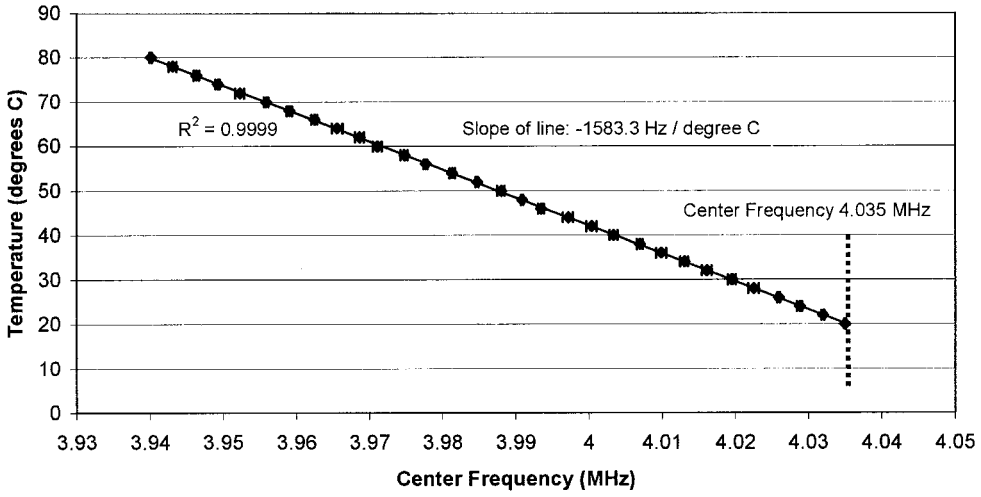

Figure 6.10 The shift in center frequency over a range of temperatures (20 to 80 degrees C) is shown. The frequency drops approximately 1583 Hz for each degree increase in temperature. (N=3 for each temperature).

6.6 DEVICE CHARACTERIZATION

6.6.1 Thermocouple calibration

Once the version 2 transducer was completed, the thermocouple was compared against a previously calibrated thermocouple (for clarification I will name this "thermocouple 2"). This calibration enabled differences between the internal thermocouple and the actual temperature of the outside of the brass housing to be determined. The calibration was performed as follows. First, the transducer was suspended in a glass tank. Thermocouple 2 was then attached to the outside of the brass housing using thermally conductive epoxy (Loctite 7387 and 384, Loctite Corporation, Rocky Hill, CT). The glass tank was filled with water, and a water heater / circulator (Model 1112, VWR Scientific, West Chester, PA) was affixed to the side of the tank to heat the water. The internal thermocouple was connected to a data acquisition unit and data acquisition was automated using LabVIEW software (National Instruments). The water temperature was increased using the water heater, from 21°C to 86°C, and back to 21°C three times. The temperature was allowed to settle approximately every 3°C for data recording. Temperature data was collected from each thermocouple at each temperature interval. The temperature measured with the

internal thermocouple stabilized within one second of the external temperature measurement stabilization. This is important as a fast response in measuring change in transducer temperature is desired. For safety reasons, this would be useful if there was a sudden increase in transducer temperature during *in vivo* treatment. The temperature reading from thermocouple 2 was plotted against the internally measured temperature and shown in Figure 6.11 (for transducer with a matching layer). The temperature calibration was defined by the slope and intercept value determined from linear regression. The slopes were 0.989 and 0.992 and offset values were 4.527 and 4.509 for the transducer with and without matching layers respectively. These values were determined from linear fits with correlations R^2>0.99. The slopes and temperature offsets were taken into account during the programming of the HIFU software, described in section 7.7.4.

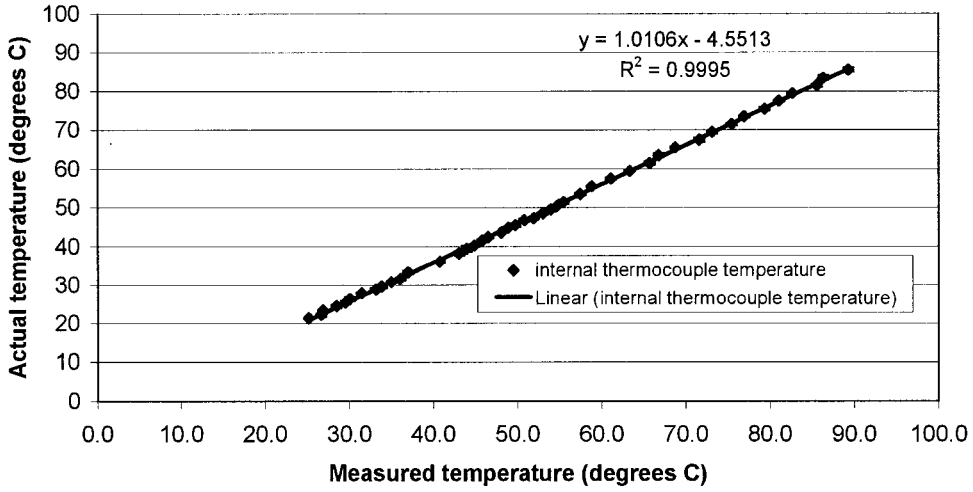

Figure 6.11 Thermocouple calibration curve for transducer with matching layer.

Both internal thermocouples showed a higher temperature and a slope greater than 1 when plotted against the actual temperature. This may be due to heat absorption by the thermal epoxy and brass housing, or the fact that the transducer housing may act as an insulator to heat. If the latter two facts were true, the internal thermocouple-measured transducer temperature may be higher than the actual temperature if the heat were to be generated by the transducer, as during HIFU treatment. This would actually be beneficial by providing a small safety margin.

6.6.2 *Acoustic field map*

A needle hydrophone was used to determine the acoustic pressure field for both version 2 transducers as described in Section 4.4.2. Figure 6.12 shows the field maps in both linear scale and dB scale and the -3dB and -6dB pressure contours. Although the scan range was different for the two transducers, the focal shape and sizes were similar. Cross section scans, shown by Figure 6.13, were used to determine the -6dB pressure (full width half maximum) focal widths. The average full width half maximum focal widths for the transducer with and without matching layer were 1.11±0.3 and 1.13±0.5 mm respectively. This corresponds to focal areas of 0.0097 cm^2 and 0.01 cm^2, and focal gains of 1175 and 1140 for the transducer with and without matching layer respectively. This is smaller than the 1.2 mm focal width of the version 1 transducer and was expected due to a smaller f-number. The theoretical focal width was calculated as 0.96 mm using the lateral resolution equation (Eq. 2.30).

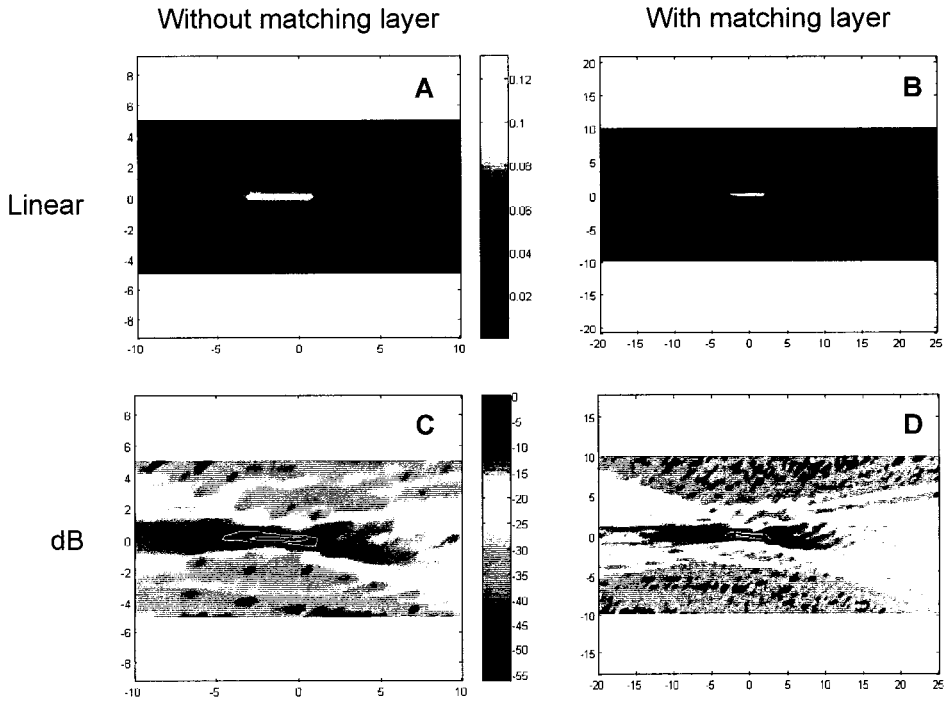

Figure 6.12 Linear and dB scale field maps. (A) linear scale, without matching layer; (B) linear scale, with matching layer; (C) dB scale, without matching layer; (D) dB scale, with matching layer. All dimensions in mm. The inner and outer contour in figure C and D show a -3dB and -6dB contour respectively.

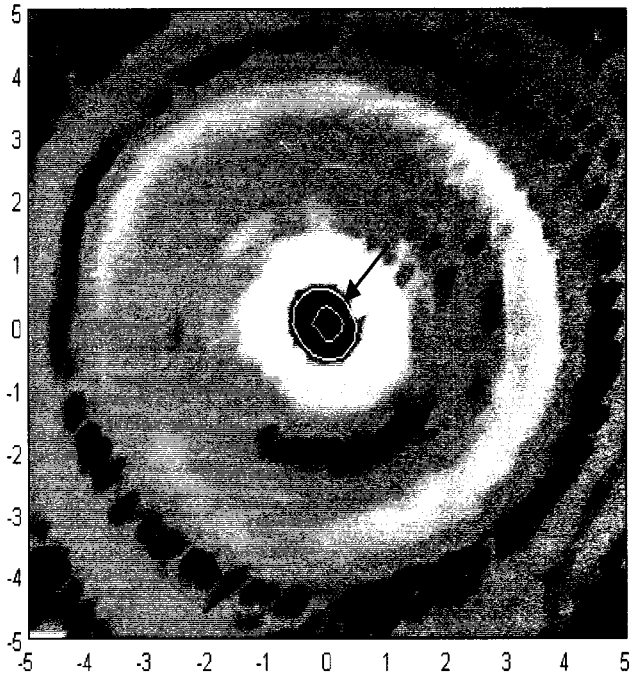

Figure 6.13 Cross section scan of focus for transducer with matching layer. The arrow points to the -6dB pressure contour defined as full width at half maximum. Dimensions in mm. The average width of the contour was 1.11 mm.

6.6.3 *Radiation force balance*

Acoustic power and efficiency for both transducers were measured using the reflective radiation force balance technique described in Section 4.4.3. Figure 6.14 shows the acoustic power emitted for a given electrical power input. The slope of the best-fit line represents the average efficiency over the 0 to 150 W of electrical power input. Linear correlation coefficients were greater than 0.999 for both transducers. The transducer with matching layer has a higher average efficiency (62.2%) compared to the transducer without matching layer (57.0%). In fact, the transducer without matching layer had an efficiency similar to the version 1 transducer (58.0%), also without matching layer. The percent increase in transmitted acoustic power was calculated as 9% based on Eq. 6.3, lower than the theoretically predicted increase in transmitted acoustic power of 16% (Section 6.4.2).

Eq. 6.3 $\%\ \text{increase in transmission} = (\eta_{\text{matching}} - \eta_{\text{no matching}}) / (\eta_{\text{no matching}})$

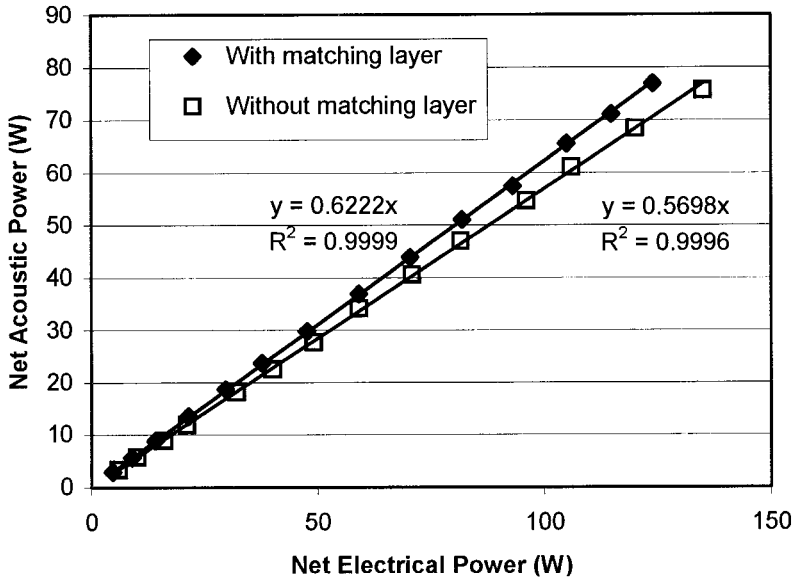

Figure 6.14 Electrical power plotted against acoustic power shows the acoustic efficiency of both version 2 transducers. The efficiency, represented by the slope of the best fit line, is approximately 5-6% greater for the transducer with a matching layer.

Similar to section 4.4.3.4, the quality of the transducer was determined by measuring the acoustic power of the transducer (with matching layer) at different frequencies. The results are shown in Figure 6.15. The bandwidth of this transducer (0.46 MHz) was less than that of the version 1 transducer (0.57 MHz). The center frequency was also greater (4.035 MHz versus 3.6 MHz), resulting in the quality of the transducer being higher (8.77).

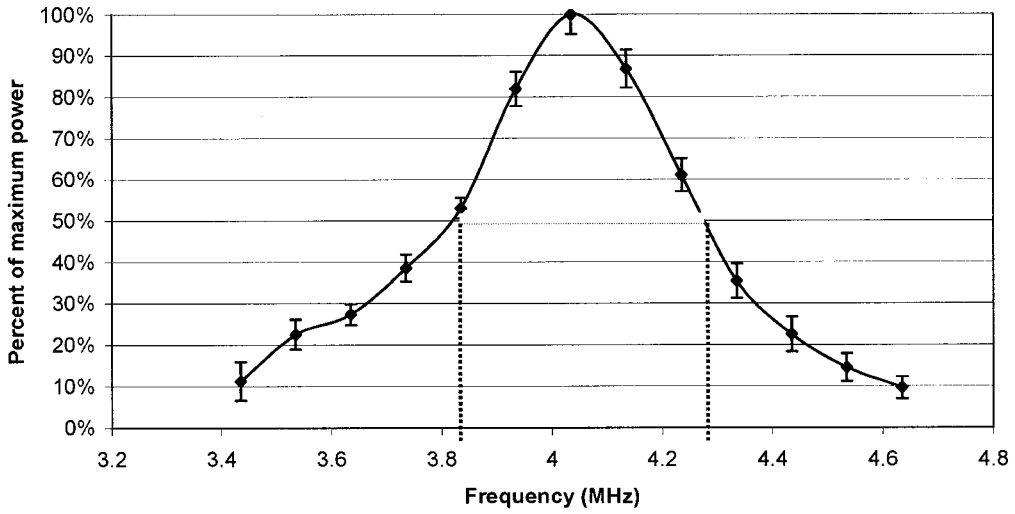

Figure 6.15 The acoustic power output as measured by the radiation force balance over a range of frequencies from 3.4 to 4.6 MHz. The electrical power input was kept constant at 100 W and three measurements were taken at each frequency. The error bars indicate one standard deviation.

6.6.4 *Focal intensity estimates*

What is more important than the acoustic power output is the intensity at the focus. This is dependent on not only acoustic power output but also on tissue attenuation and the size of the HIFU focus, as discussed in section 2.14. The tissue attenuation coefficient used for estimating focal intensity was 1.76 dB/cm or 0.2 NP/cm, determined as the value for sheep uterus attenuation at 4 MHz (section 5.4.3.3). Intensity estimates are presented here for the transducer with matching layer. The average full width half maximum (-6dB) focal area (section 6.6.2) was 0.0097 cm^2. The intensity is plotted as a function of acoustic power output in Figure 6.16. Since the attenuation is depth dependant, various depths into tissue are plotted.

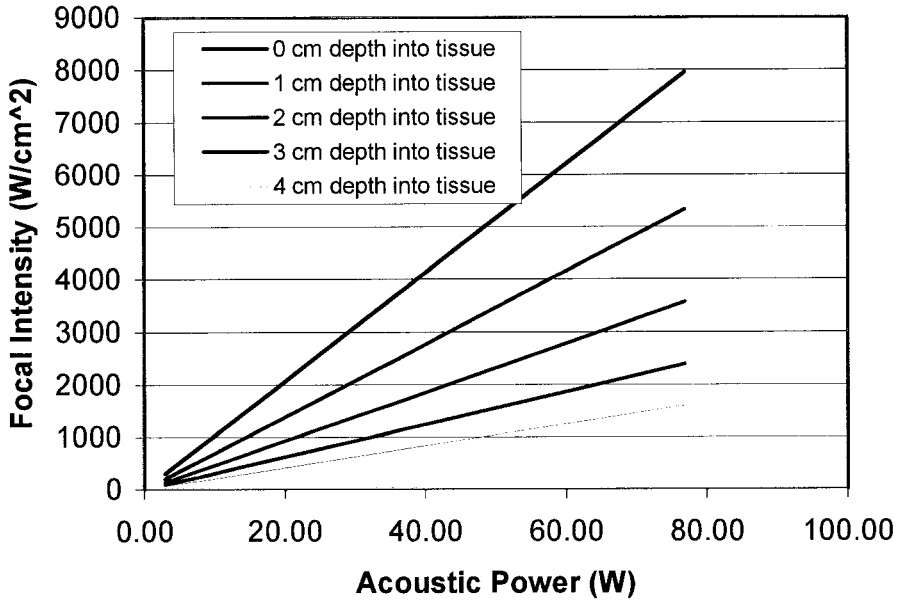

Figure 6.16 Estimates of focal intensity for different depths into sheep uterus tissue at various acoustic power levels

6.6.5 *Transducer temperature measurements*

Two temperature measurement experiments were performed. The first experiment measured the transducer temperature change for several transducer on-off cycles at a fixed acoustic power. The second experiment determined the temperature increase after a 10 second treatment at various acoustic powers. For both experiments, the HIFU transducer was operated in a simulated *in vivo* environment to determine what the increase in temperature would be for various treatment scenarios. The transducer was placed in a piece of beef muscle measuring approximately 15 x 12 x 12 cm. The transducer and beef muscle were placed in a plastic tank filled with distilled water heated to 37°C using a water circulator (Model 1112, VWR Scientific, West Chester, PA). The internal thermocouple was connected to a data acquisition unit and data acquisition was automated using a program created with LabVIEW software (National Instruments). A condom was attached to the transducer, and the transducer water tubing was connected to the water circulation system. Water was circulated at 150 mL/min inside the condom. The following two experiments were performed that simulated actual treatment scenarios.

6.6.5.1 *Measuring temperature change for constant acoustic power*

During treatment, a typical acoustic power that would be used is 50 W. This required an excitation voltage of 225 mV-pp (with matching layer) and 240 mV-pp (without matching layer). This typical value for acoustic power was limited by the RF power amplifier capability. From trial and error, the voltage amplitude input into the power amplifier was kept below 300 mV-pp to prevent the amplifier from being overdriven. Using an acoustic power of 50W, the HIFU transducer was operated in two burst modes with the total cycle length of 10 seconds. The first mode was 3 seconds on, 7 seconds off (30% on-time), and the second mode was 5 seconds on and 5 seconds off (50% on-time). Ten cycles were used for this experiment. The temperatures measured are shown in Figure 6.17. A shorter on-time and the presence of a matching layer resulted in lower operating temperatures. Comparing the two extremes, the maximum temperature increase over ten cycles was approximately 1.7°C for the transducer with matching layer using a 30% on-time, about half of the temperature reached (3.4°C) for the transducer without matching layer operating at a 50% on-time. The on-time for a particular

treatment would have to be empirically optimized for the tissue type to ensure that the desired lesion formation occurs. As shown in Figure 6.17, the temperature leveled off with repeated on/off cycles indicating that the cooling rate and time was sufficient to counteract the heating produced at every treatment. The initial temperature increase for the first two cycles was at a higher rate than subsequent cycles in all cases. This was due to the fact that the equilibrium temperature of the brass housing was initially lower (approximately 25°C) since the circulated water temperature was less than 37°C.

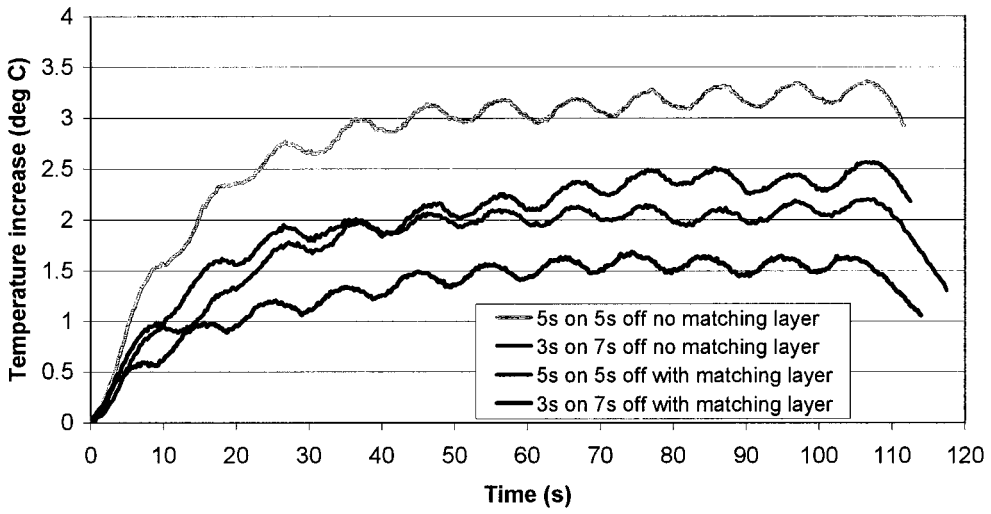

Figure 6.17 Temperature increase for different treatment cycle times for transducer with and without matching layer

6.6.5.2 Measuring temperature change at various acoustic powers

The next experiment was aimed at determining maximum temperature increases for various acoustic power levels. It was unlikely that a single lesion formation would last longer than 10 seconds, thus the maximum temperature reached after 10 seconds of on-time, at various acoustic powers for both transducers, was measured. The results are shown in Figure 6.18. The difference in temperature increase after 10 seconds was lower with a matching layer for all power levels, and this difference increases for higher power levels. This was due to the difference in efficiency between the transducers, meaning there was more electrical power converted to heat for the transducer with a lower

efficiency (without matching layer). From Figure 6.14 it was observed that the efficiencies were 62% and 57% for the transducer with and without matching layer respectively. Therefore, at 40 W of acoustic power, the transducer with matching layer would have 15.1 W of electrical power potentially converted to heat, while the transducer without the matching layer would have 17.2 W. This experiment shows that the increase in efficiency due to the matching layer resulted in a desirable decrease in transducer operating temperature.

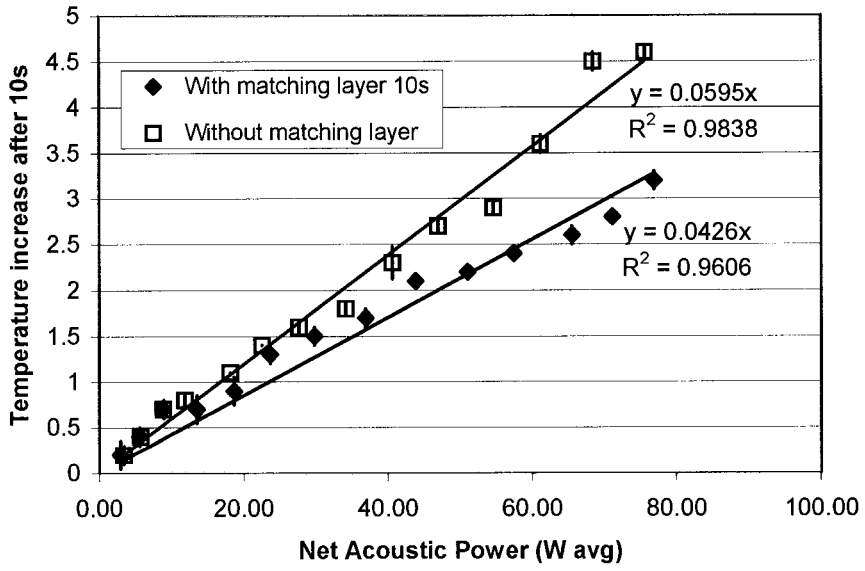

Figure 6.18 Transducer housing temperature after 10 seconds of on-time at various acoustic power levels showed that temperatures were higher for the transducer without a matching layer.

6.6.5.3 Theoretical temperature increase

The theoretical increase in temperature at various acoustic powers was determined. This increase in temperature can be derived from the calorimetry equation:

Eq. 6.4 $Q = mc\Delta T$

Where Q is the electrical energy lost as heat (Joules), m is the mass of the component heated (grams), c is the specific heat capacity of the component heated (J/g°C), and ΔT is the temperature change (°C). Q can be calculated given the acoustic power (P_A) in watts:

Eq. 6.5 $Q = (\frac{P_A}{\eta} - P_A)t$

Where η is the transducer efficiency, and t is the exposure time (in seconds).

The component that was assumed to be primarily heated was the brass housing. The mass of the brass housing was 279 g and the specific heat capacity of brass was 0.380 J/g°C. Using Eq. 6.4 and Eq. 6.5, and an exposure time of 10 seconds, the theoretical increase in temperature was found over a range of acoustic powers from 0 to 80 W for the transducer with matching layer (η=0.62) and without matching layer (η=0.57), and shown in Figure 6.19.

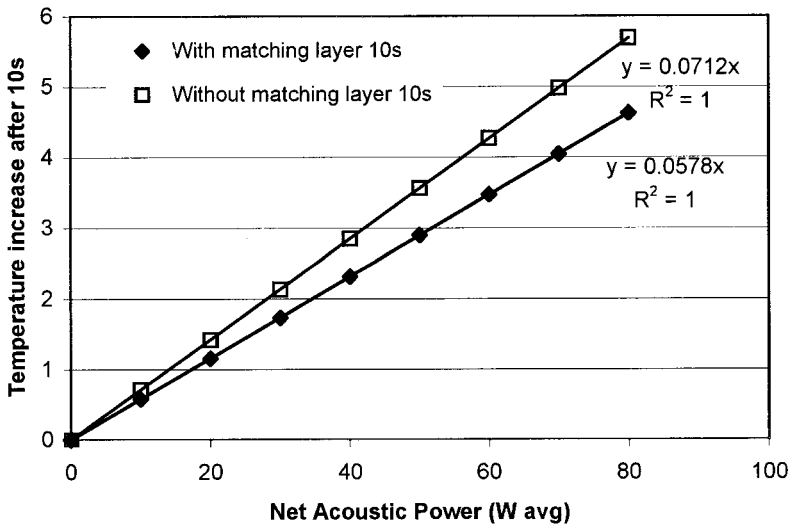

Figure 6.19 Theoretical temperature increase at various acoustic power levels for transducer with and without matching layer.

The theoretical increases in temperature were greater than the experimental increases in temperature (section 6.6.5.2). This can be seen by comparing the slope of the best fit line, which represented the expected increase in transducer temperature at a given acoustic power. The slope for the transducer without matching layer was 0.712°C/W (theory) versus 0.595 °C/W (experiment). The slope for the transducer with matching layer was 0.578 °C/W (theory) versus 0.426 °C/W (experiment). Neglecting convection effects due to water circulation, and conduction of heat away from the brass housing to other parts of the transducer (such as the aluminum handle) accounted for the higher increase in temperatures calculated using the calorimetry equations.

6.7 VERSION 2 TRANSDUCER: CONCLUSIONS AND NEXT STEPS

A larger transducer was built and a matching layer made of epoxy embedded with graphite (20% by mass) was applied to the aluminum lens. The larger transducer resulted in an f-number closer to one reducing the focal spot size as shown by a hydrophone field map. The matching layer resulted in higher transducer efficiencies as measured with a radiation force balance. The smaller focal dimensions and increased efficiencies meant greater intensities at the focus for a given acoustic power. An internal thermocouple attached to the brass housing of the transducer was calibrated and capable of measuring the transducer temperature. This temperature data will be valuable to detect potential for tissue damage adjacent to the transducer or abnormal transducer heating indicating failure. The completed transducer with the matching layer was used to create lesions in gel and in turkey breast tissue *in vitro*, and in sheep uterus *in vivo*. The studies were performed after the HIFU integrated targeting system, discussed in Chapter 7, was completed. Thus, experimental protocols and results from these experiments will be discussed in the following chapters.

7.0 CHAPTER 7 HIFU INTEGRATED TARGETING SYSTEM

7.1 INTRODUCTION

A crucial feature of any image-guided therapy system is the ability to accurately target the tissue to be treated prior to actual treatment. A computer aided targeting system has been developed for the HIFU device. This chapter explores the concept, hardware, software, implementation and testing of the HIFU integrated targeting system, or HITS.

7.2 BACKGROUND AND MOTIVATION

Prior to development of HITS, HIFU treatment was targeted using two methods. First, the location of the treatment was estimated based on the lens and focal location on the B-mode ultrasound image if the transducer had a fixed focal length. Second, the treatment location was determined by observing the hyperechoic spot formation during lesion formation once the HIFU was applied. Unfortunately, both of these methods were insufficiently reliable for clinical use. The former method was inaccurate since the location of the focus was subject to observer interpretation of the ultrasound image, and reflections and scattering in the 2-D B-mode image may obscure precise visualization of the exact lens location. Furthermore the angle of the HIFU transducer and the center of the lens, both necessary to determine focal location, were difficult to determine using the B-mode image. The latter method would not be acceptable clinically since it involves commencing treatment to determine treatment location.

HITS was implemented taking into account the following characteristics of the device:

- the transvaginal HIFU transducer had one degree of motion
- the relative position of the HIFU transducer to the imaging probe can be determined via geometry
- the HIFU transducer had a fixed focal length

Therefore, a targeting system that used the relative position of the HIFU transducer and image probe to determine the focal location was designed and developed. The existing

device was modified to include targeting system components consisting of two linear displacement sensors and a rotary encoder, shown in Figure 7.1. The data from the targeting system components were collected using a data acquisition unit (SCB 68, National Instruments Corporation, Austin, TX) connected to a laptop computer. A photograph of the completed device is shown in Figure 7.2.

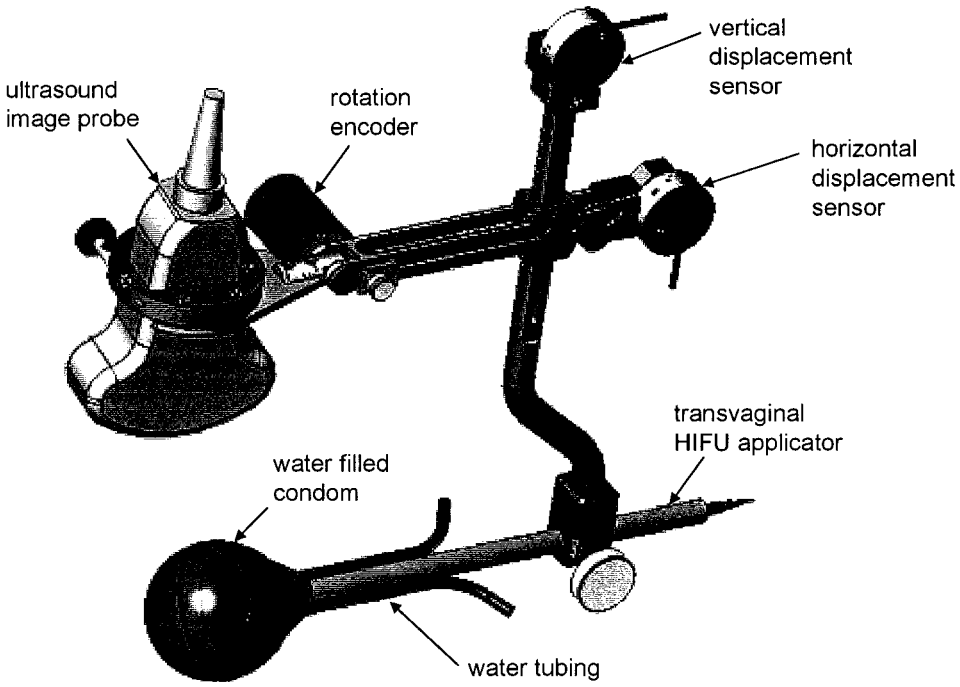

Figure 7.1 Modified device with linear displacement sensors and rotary encoder that were used to track the position of the HIFU focus relative to the image plane

Figure 7.2 Photograph of completed device with position sensors and version 2 transducer, connected to SonoSite portable ultrasound.

7.3 GEOMETRICAL RELATIONSHIPS

A simplified drawing of the device is shown in Figure 7.3. The fixed focus is shown as point C. The pin about which the image probe rotates is at point O. Point A represents the point where the vertical rod meets the horizontal rod connecting the image probe on the device. Point B represents a point on the HIFU transducer directly below point A. As shown in Figure 7.3, when there was no rotation of the image probe, the focus (point C), can be determined by knowing r_1 (horizontal position of the image probe), r_2 (vertical position of the image probe), and r_3 (horizontal position of the HIFU transducer), as shown in Eq. 7.1 and Eq. 7.2.

Eq. 7.1 $$Y_1 = Y_0 - r_2$$

Eq. 7.2 $$X_1 = X_0 - r_1 + r_3$$

With rotation of the image probe, the rotation angle θ must also be taken into consideration when determining the position of the focus. As shown in Figure 7.3, the location of the focus when there was rotation, relative to the non-rotated state of the device, can be calculated via superposition. Thus, the cumulative change in the position of C is a combined contribution of the motion of points A, B, and C, and is still based on the lengths of segments r_1, r_2, and r_3. This cumulative change in position C is expressed in Eq. 7.3 and Eq. 7.4.

Eq. 7.3 $$Y_2 = Y_1 + r_1 \sin\theta + r_2(1 - \cos\theta) - r_3 \sin\theta$$

Eq. 7.4 $$X_2 = X_1 + r_1(1 - \cos\theta) - r_2 \sin\theta - r_3(1 + \cos\theta)$$

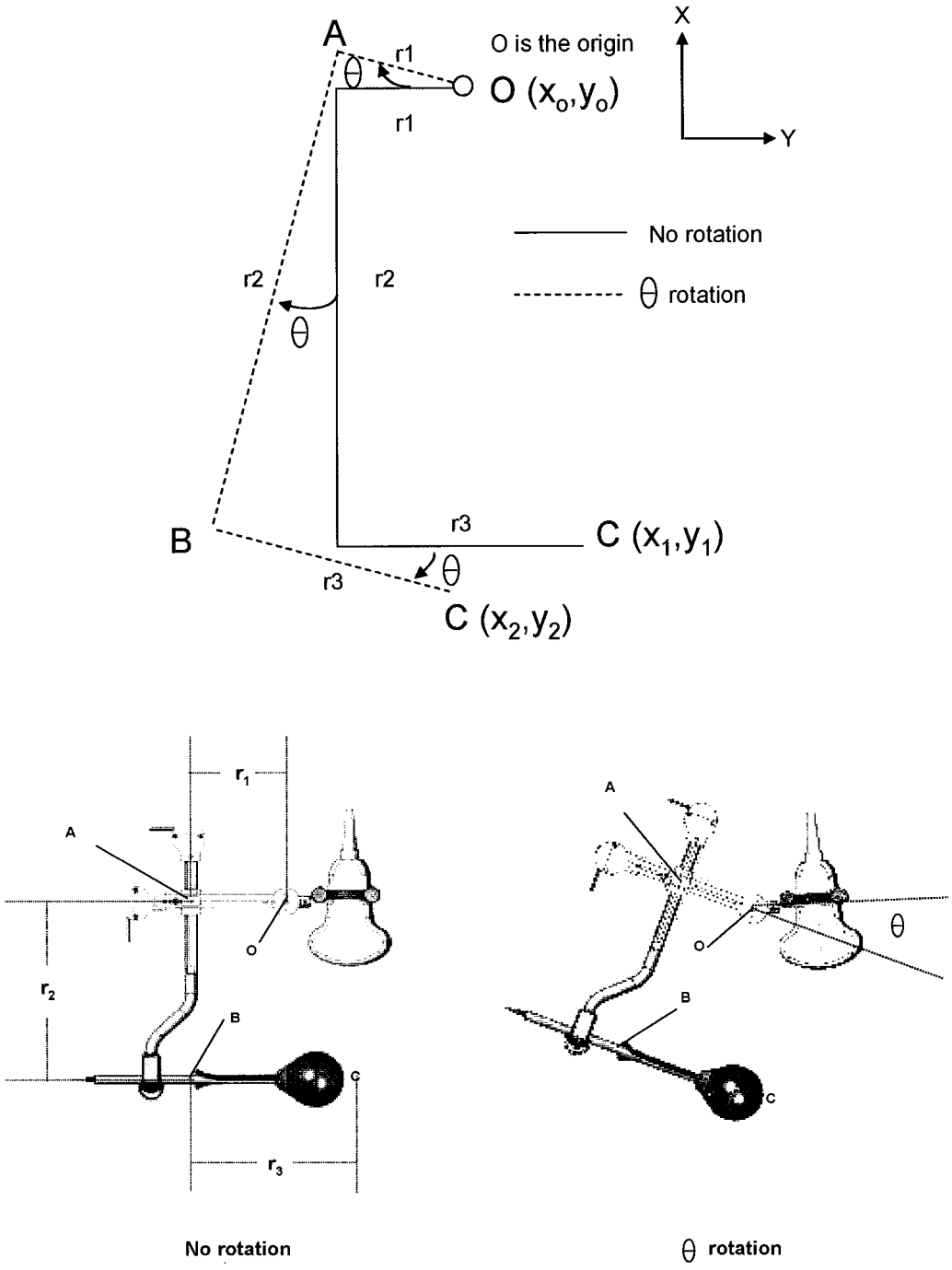

Figure 7.3 Simplified drawing of device used in determining the location of the focus, and corresponding device positions for rotation and no rotation states

7.4 POSITION SENSORS

7.4.1 Linear displacement sensors

It was necessary to develop a method for tracking the vertical and horizontal motion of the image probe. Linear displacement sensors were used to perform this task. The following requirements were used to select a sensor:

- Sensors must be robust enough to be able to withstand *in vivo* experimentation operating conditions (exposure to water, blood, ultrasound gel, body fluids)
- Sensors needed to be able to measure a distance of 75 mm (this was the maximum distance of travel for horizontal and vertical displacement of image probe)
- Sensors should be small enough to be mounted on the device without disrupting operation
- Sensors with fewer connection wires were preferable
- Sensors needed to be able to measure millimeter displacements accurately and consistently
- Sensors needed to be compatible with the SCB 68 data acquisition unit (National Instruments Corporation, Austin, TX) for data collection (i.e. have a voltage, impedance, or current output, and require no more than 5V input voltage)

Miniature linear displacement sensors (173-0241, Space Age Control, Palmdale, CA) were selected. These sensors are shown in Figure 7.4 (specifications included in Appendix D). Each sensor consisted of a stainless steel extension cable that was wound onto a threaded drum. As the cable was extended, the drum rotated. The rotating drum was coupled to a rotary sensor to measure displacement.

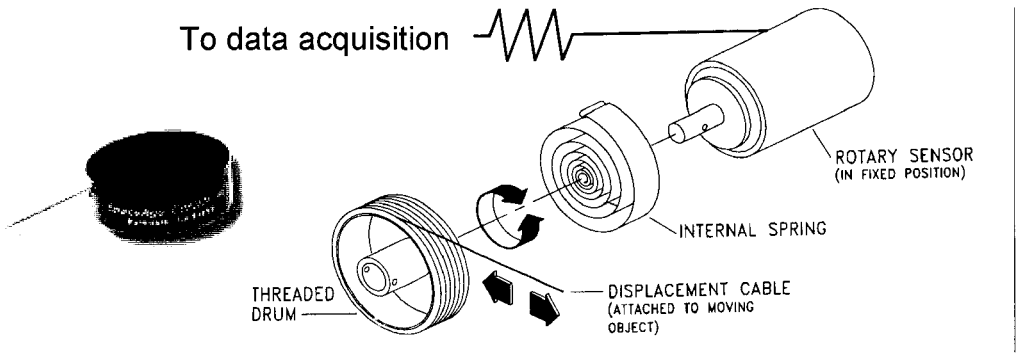

Figure 7.4 Cable pull displacement sensor (courtesy Space Age Control, Palmdale, CA), used to determine the horizontal and vertical position of the image probe, converted the displacement of a cable to an electrical signal. The displacement cable was wound onto a threaded drum which rotated a rotary sensor. An internal spring retracts the displacement cable when not extended.

7.4.1.1 Theory of operation

The rotary sensor (rotary variable inductance transducer) converted the rotary motion induced by cable pull into a potential difference. While in use, the position sensor was mounted in a fixed position and the extension cable was attached to a moving object. In the case of the device, the moving object was the moveable link that joined the horizontal and vertical rods of the device, as depicted in Figure 7.5. Position sensor mounts secured the position sensors onto the device. The cables were connected onto the moveable link using set screws. Cables were positioned in a machined groove on the moveable link such that the axis of movement for the cable and the moveable link were aligned. As horizontal and vertical motion of the image probe occurred, the cable extracted and retracted, resulting in the threaded drum and rotary sensor rotation. A voltage output proportional to the cable travel was obtained indicating the position of the imaging probe. This voltage output was processed by the HITS software, described in section 7.7.2.

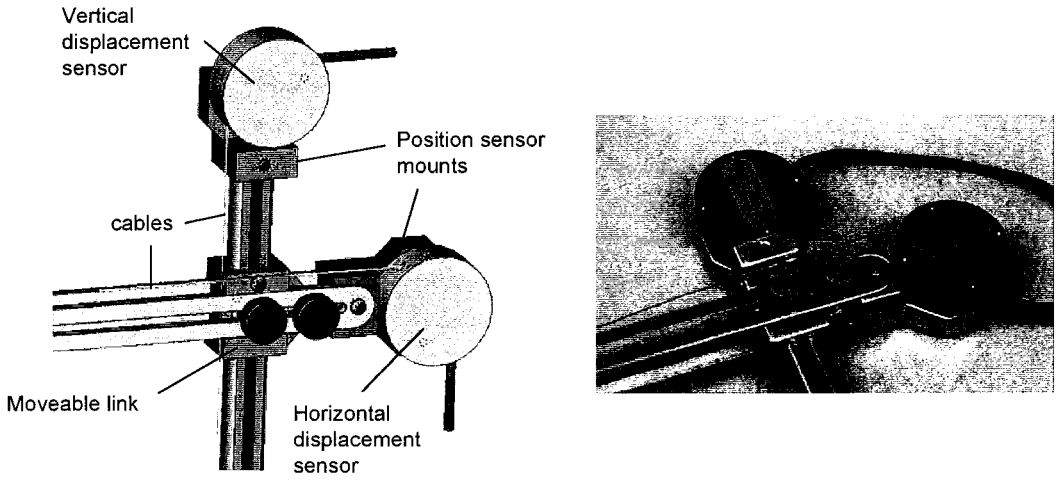

Figure 7.5 Linear displacement sensors were mounted onto the device with position sensor mounts. The cables were attached to the moveable link on the device with set screws. A photo of the mounted displacement sensors is shown.

7.4.1.2 Linear displacement sensor calibration

The position sensors were characterized prior to use on the device. Each position sensor was connected to a 5 V voltage source and a ground terminal. The output signal was connected to an oscilloscope and was shown to be a constant voltage output. The relationship between cable pull distance, as measured with digital calipers, and output voltage in mV is shown in Figure 7.6. These measurements were performed at intervals of 1 cm until the cable was pulled to its maximum extent and the test was performed 3 times per sensor. The sensitivity of the position sensors was 65.5 mV/mm determined from the slope of the line in Figure 7.6. There was no hysteresis or change in zero pull voltage in either sensor. Also, exposure of the cable to water did not result in any measurement anomalies.

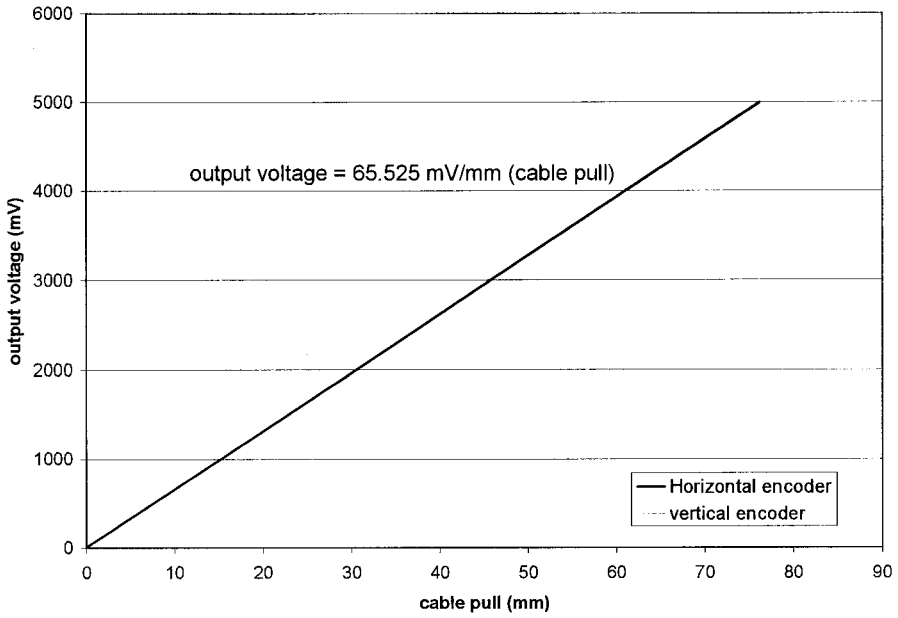

Figure 7.6 Relationship between displacement sensor cable pull and output voltage shows a sensitivity of approximately 65.5 mV/mm.

7.4.2 Rotary encoder

The rotation of the image probe was measured to determine the focal location using HITS. Criteria similar to that used for selecting displacement sensors, as described in Section 2.3.1, were used to choose a rotation sensors for this application. The range of measurement required for the rotary encoder was 90 degrees in each direction, or 180 degrees total. Although rotary motion can be converted to linear motion and measured using the cable pull sensors (section 7.4.1), a device designed for rotary measurements was preferred for simplicity. An optical-rotary encoder (HEDR-5420, Agilent Technologies, Palo Alto, CA) was selected (specifications included in Appendix F). This encoder, shown in Figure 7.7, consisted of an LED light source, a photodetector integrated circuit, and a code wheel. A cap was built to cover the rotary encoder to shield it from moisture and other substances that may be encountered during *in vivo* experimentation.

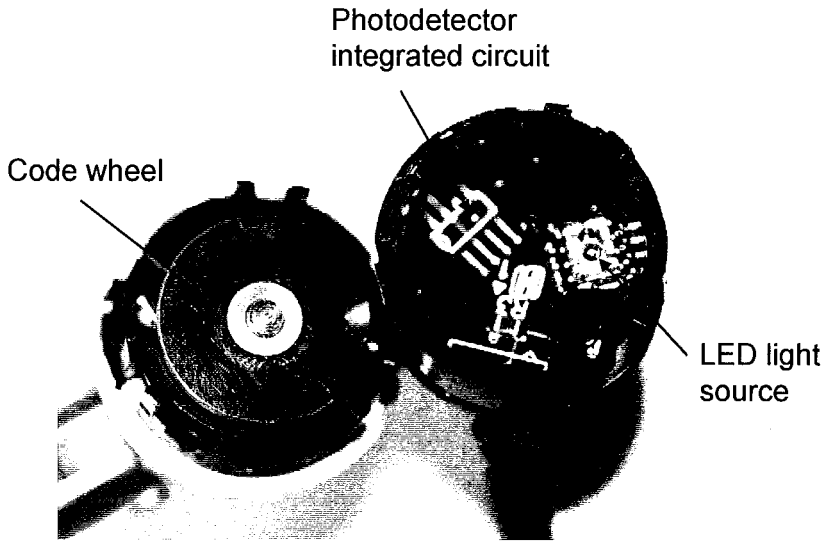

Figure 7.7 HEDR-5420 rotary encoder consisted of an LED light source, a photodetector integrated circuit, and a code wheel.

7.4.2.1 Theory of operation

The HEDR-5420 translated rotary motion of a shaft into a two channel (A and B) voltage output with high and low states. As shown in Figure 7.8, the codewheel was mounted onto a shaft connected to the image probe holder on the device.

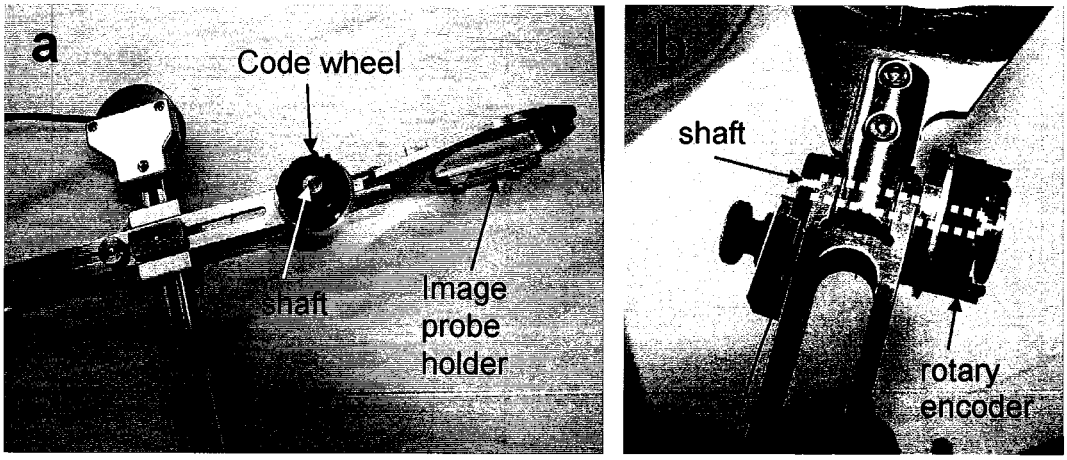

Figure 7.8 Codewheel and rotary encoder mounted onto the device. A shaft connects the code wheel to the image probe holder allowing rotation of the probe holder to be measured. (a) shows the side view of the device and (b) shows the top view of where the rotary encoder is mounted.

As the image probe rotated, the shaft and codewheel rotated also. The codewheel consisted of alternating reflective and non-reflective stripes. Figure 7.9 shows that a lens over the LED focused light onto the codewheel. Light is either reflected or not reflected back to the photodetector circuit via a second lens, depending on whether the LED shines on a reflective or non-reflective area respectively. Therefore, as the codewheel rotated, an alternating pattern of light and dark corresponding to the pattern of the code wheel was detected by the photodiodes.

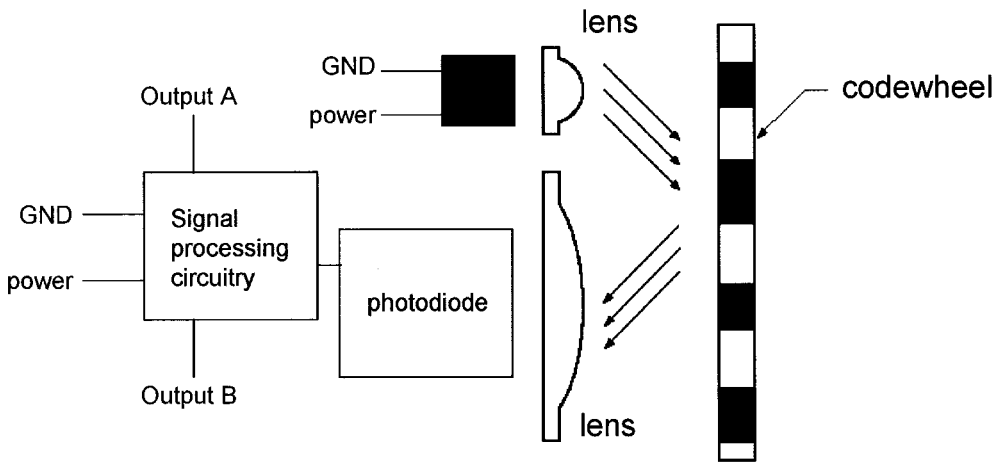

Figure 7.9 The rotary encoder consists of an LED, a codewheel, and photodiodes with signal processing circuitry

The light was used to produce internal signals which, when fed through comparators, produce the final outputs for channels A and B, as shown in Figure 7.10. The direction of codewheel rotation can be deciphered by determining which channel output leads the other by 90 degrees.

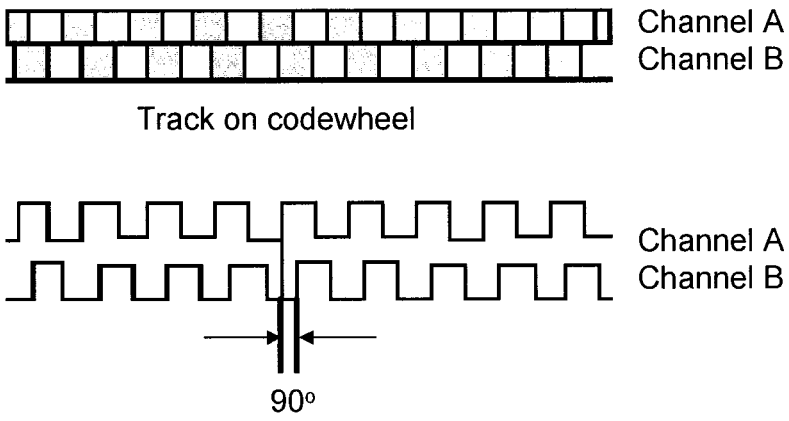

Figure 7.10 Output channels A and B from rotary encoder are 90° apart from each other. The direction of rotation was determined based on which channel led the other.

The channel A and B outputs of the rotary encoder were initially connected directly to the data acquisition board (SCB 68, National Instruments): channel A was connected to the source input of the SCB 68 (pin 37) and channel B was connected to the UP_DOWN input of the SCB 68 (pin 16). In this configuration, the counter will increment on state transitions (from low-to-high) on channel A. When a channel A low-to-high transition occurs, the state of channel B will be high or low, depending directly on the direction of rotation. Therefore, the DAQ counter will increment when the encoder rotates in one direction, and decrement when the encoder rotates in the opposite direction.

7.4.2.2 Rotary encoder initial testing

Upon initial testing, the counting was very inaccurate. Counts were skipped and did not return to zero when the probe rotation returned to its original position. Counts sometimes moved in the wrong direction. Although directly connecting the rotation encoder to the DAQ was simple to implement, this method had drawbacks. First, if the encoder disk was not rotating, but was instead vibrating sufficiently enough back and forth to cause active transitions on channel A, then each movement was incorrectly counted. The effect of this vibration is illustrated in Figure 7.11. As the encoder disk moved back and forth across A2, channel B remains low but the DAQ counter continued to increment the count, resulting in an incorrect position reading. A quadrature clock converter device, described

in section 7.4.2.3, was able to solve this problem. Another problem resulted when encoder outputs included noise or jitter that was large enough to be erroneously counted as a valid state transition. This problem was solved with lowpass filters on the A and B signal outputs.

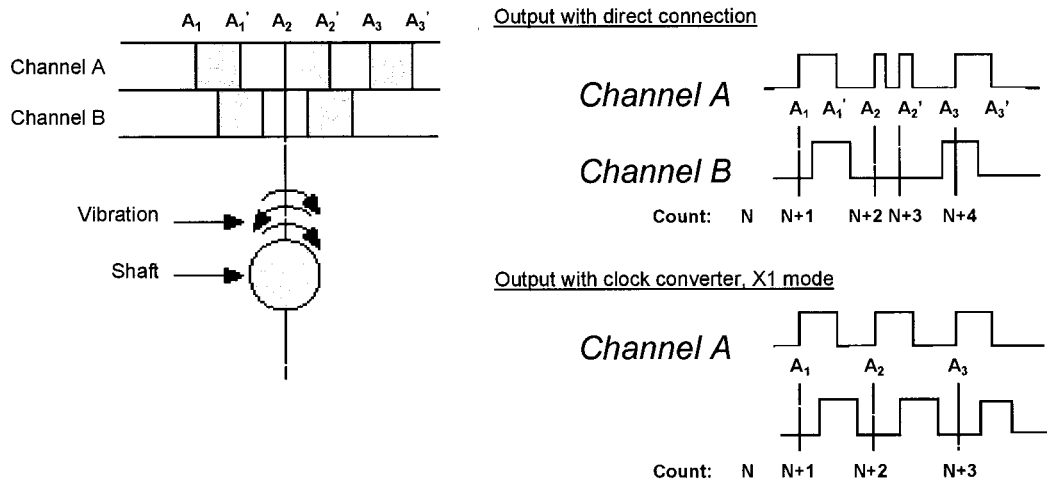

Figure 7.11 Effect of shaft vibration on counting with and without the clock converter. The clock converter prevents vibration from incrementing count values. (Picture obtained from National Instruments, Austin, TX).

7.4.2.3 Quadrature clock converter

A clock converter chip prevented errors due to rotational encoder vibration, noise, and jitter. A quadrature clock converter (LS7084, LSI Computer Systems, Inc., Melville, NY) was used to convert the A and B signals from an encoder into a clock and up/down signal that was connected directly to the DAQ. The LS7084 included a lowpass filters to prevent miscounts due to noise and jitter. In addition, the LS7084 used dual one-shots (monostable multivibrators) to prevent the miscounting produced by vibration, or dither, as described in the previous section. A one-shot is an integrated circuit device that produces an output pulse width independent of the input pulse width, and can be programmed by an external resistor-capacitor network.

The clock converter was connected between the rotation encoder and the DAQ as shown in section 7.5. The LS7084 chip shared the ground and 5V input with the other position sensors. The chip was mounted onto an 8-pin mount, and the mount was placed onto a

breadboard and placed into the DAQ unit. The LS7084 was operated in X1 mode, as shown in Figure 7.12. This meant that one pulse was generated on every rising edge on channel A when channel A was leading, and on every falling edge on channel B when channel B was leading. The chip could also operate in X4 mode where one pulse would be generated on every transition of either the A or B signals. The pulse width emitted by the LS7084 was adjusted by connecting a resistor to the chip. A 100 kΩ resistor in parallel with a 1μF capacitor yielded a 4μs pulse that worked well with the DAQ. With the clock converter connected, the encoder was not affected by jitters or vibration, and counted accurately.

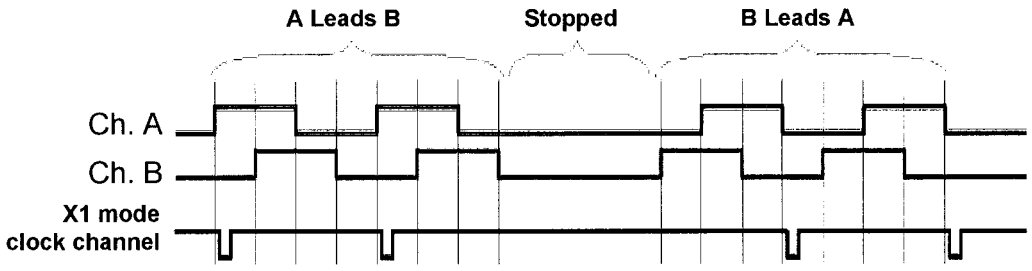

Figure 7.12 LS7084 X1 mode clock output signal based on A and B outputs from rotation encoder

7.4.3 HIFU transducer position markings

The HIFU transducer was designed to be removable from the device. The transducer was also not intended to be moved relative to the device during treatment. Its position would be set based on pelvic anatomy and treatment area. Any device movement necessary for image adjustment during treatment would be made by adjusting the image probe rather than the HIFU transducer and a position sensor for the transducer was not necessary. However, as shown in Figure 7.3, it was still necessary to determine the distance that the transducer protrudes from the device in order to determine the focal location. Therefore, centimeter markings were made onto the shaft of the HIFU transducer.

7.5 CONNECTIONS AND DATA ACQUISTION (DAQ) UNIT

A wiring of the displacement sensors and rotary encoders connected to the SCB 68 (National Instruments Corporation, Austin, TX) data acquisition unit is shown in Figure 7.13. The 5 V source and ground were shared between the sensors, encoder and clock converter. The leads from each component were connected to the data acquisition unit via a DB9 connector.

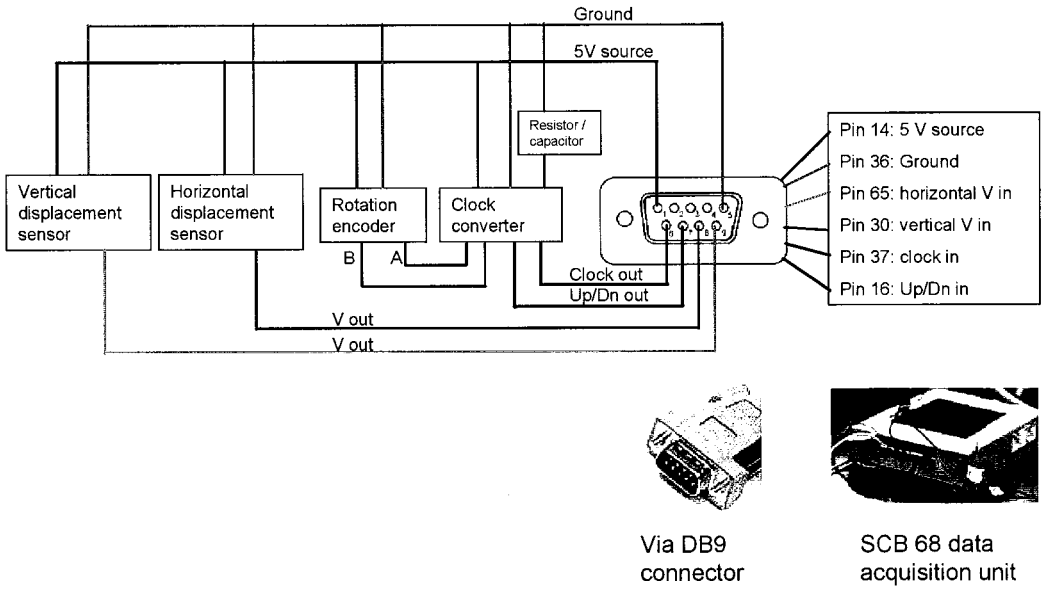

Figure 7.13 Wiring diagram for HITS components

7.6 ULTRASOUND IMAGE ACQUISITION HARDWARE

In order for a target to be superimposed on the ultrasound image, the ultrasound image had to first be acquired from the SonoSite into the computer. The simplest method to accomplish this acquisition was to convert the analog video output signal from the SonoSite (via an RCA plug) to a digital image using a universal serial bus (USB) analog to digital video converter. The Dazzle 80 (Dazzle Incorporated, Fremont, CA) USB video converter was chosen for this application. The Dazzle 80 was capable of capturing analog video images with a 320 by 240 pixel resolution.

7.7 HITS SOFTWARE

7.7.1 Overview

The HITS software was designed to provide real-time position monitoring based on feedback from the three position sensors. The feedback was translated into a visual target that was superimposed on an ultrasound image and displayed on a computer screen. The HITS software also controlled HIFU operating parameters and monitored the transducer temperature. The HITS control panel and screen display is shown in Figure 7.14 and a conceptual diagram of HITS is presented in Figure 7.15. This diagram shows the four interdependent sections of HITS: (i) user provided inputs (controlling HIFU operating parameters, HIFU transducer position, and phase angle), (ii) automated inputs (sensing position data), (iii) processing subroutines (calculating target position and phase interference location), and (iv) outputs (function generator control, positioning target on ultrasound image, transducer temperature and time display). Each section of the program will be explored in detail below. The complete LabView code is shown in Appendix E.

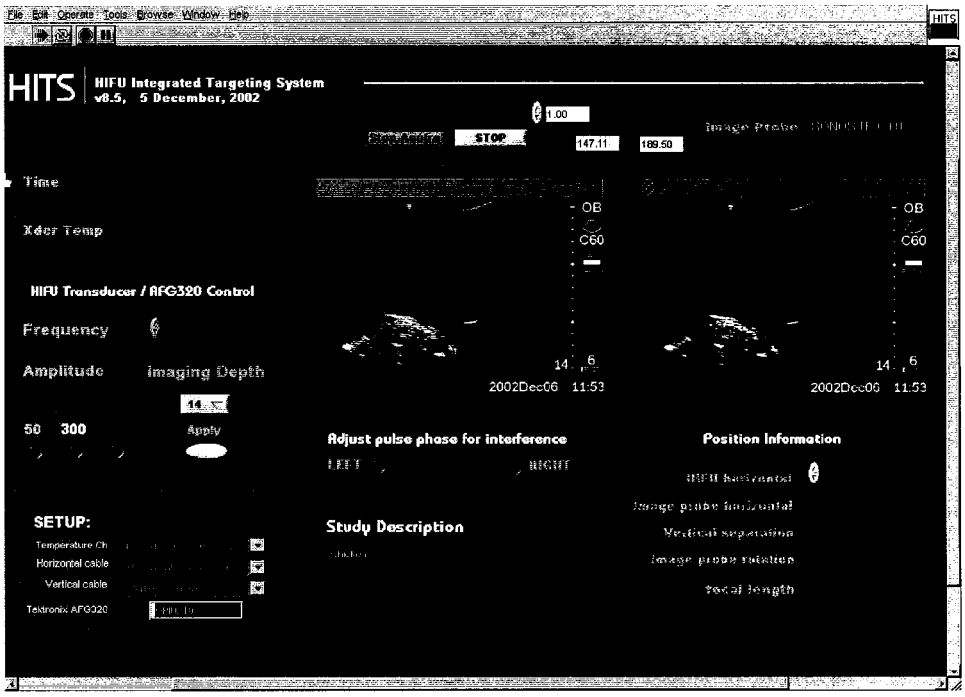

Figure 7.14 HIFU Integrated Targeting System and HIFU control screen display

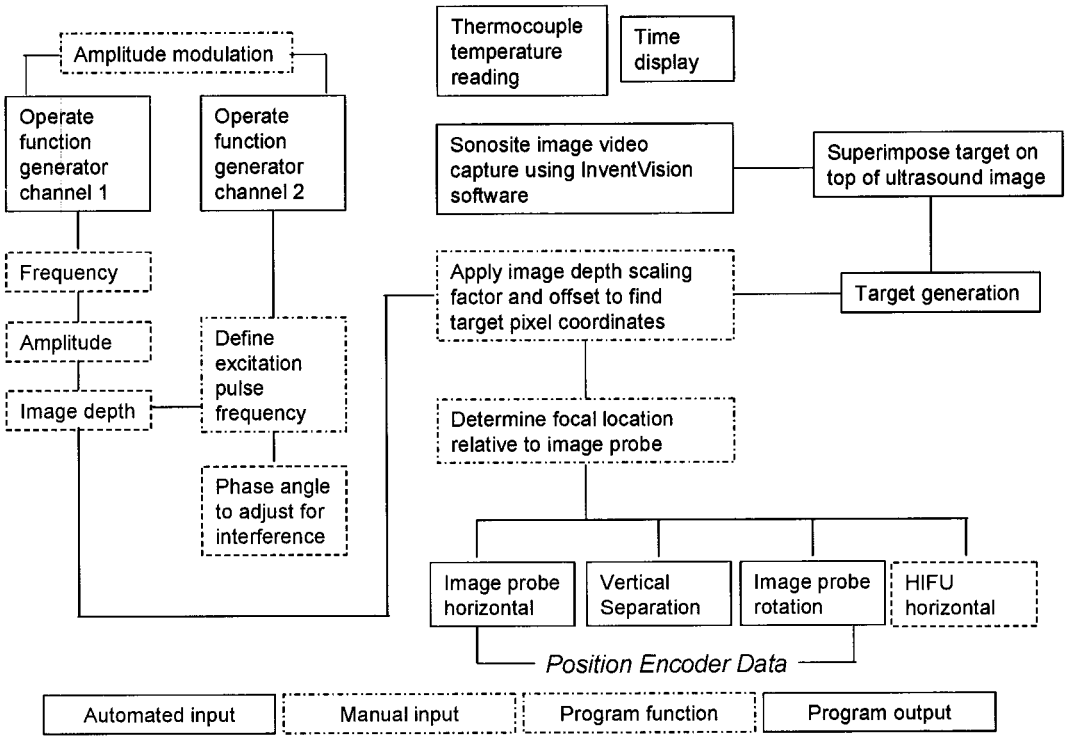

Figure 7.15 The HITS and HIFU control system software concept

7.7.2 Processing of linear displacement sensor data

The voltage output from each of the two linear displacement sensors was acquired via the DAQ board every 100 ms. Since the cables in both displacement sensors have a maximum cable extension of 76 mm, and the maximum input voltage to each sensor was 5 V, the voltage acquired was multiplied by 15.20 mm / V to obtain the vertical and horizontal position in millimeters. The voltage signal was acquired using the LabVIEW "analog input sample channels VI" (filename: AIonept.vi) that allowed data from a defined analog input channel on the DAQ board to be fed into LabVIEW. The subroutines ran until the "stop acquisition" button is pushed on the control panel. This button prevents further inputs of voltage data from the displacement sensors.

7.7.3 Time display

During treatment, elapsed time was visualized to determine exposure duration and off-times. The time readout on the computer screen also assisted in data recording. The time data was obtained from the computer's internal clock via the LabView "get time/date" string function.

7.7.4 Thermocouple data acquisition

The data from the thermocouple inside the transducer was acquired using the LabView built in VI "AI one pt" and displayed on the computer screen. The acquired value was offset by a temperature calibration value. The temperature calibration value was determined by comparing the temperature data of the thermocouple inside the HIFU transducer against a calibrated thermocouple, as described in section 6.6.1. The wait timer function in LabView limited the temperature acquisition to every 100 ms. Due to computer memory limitations, the acquisition was limited to a specific time interval.

7.7.5 Rotary encoder data acquisition

The rotation of the image probe was determined using an existing LabView VIs for optical encoders connected to a quadrature clock converter. These VIs can acquire data from several encoders. For our application, the VI was used in simple event counting mode, and kept track of how many pulses (code strips) were encountered by the LED in the encoder. The number of counts acquired by the DAQ was processed in LabView and converted to an angular displacement (AD) value in degrees based on Eq. 7.5 where N is the resolution of the encoder in codestrips per resolution (CPR).

Eq. 7.5 $$AD = \frac{counts}{N}(360^{o})$$

Since the encoder used has a resolution of 200 CPR, the count value was multiplied by 360/200 or 1.8 degrees per count. The rotation position was sampled every 200 ms. This optimal time sampling rate was empirically determined for the computer to prevent delays in image acquisition and target repositioning.

7.7.6 Rotary encoder calibration subroutine

For testing and experimental purposes, the "zero" position of the rotary encoder was determined each time the VI was run. A calibration button was incorporated into the program to determine the true location of the hyperechoic spot on the screen. The calibration button temporarily disconnected the data acquisition of the rotation encoder. To calibrate the transducer, the rotation was brought to a zero position and the VI was started. A lesion was created in gel or another calibration medium so that a hyperechoic spot was visible. The calibration button was pressed and the transducer was rotated until the hyperechoic spot was in the center of the target. The calibration button was then released and the position sensing of the rotation encoder was once again active.

7.7.7 Ultrasound image acquisition

The video signal acquired by the Dazzle 80 video capture device was imported into LabView using Inventvision software (Inventeering, San Diego, CA). This software was an ActiveX control that allowed different video sources, compatible with video for windows (VFW interface), to work within a LabView VI. Two identical images were generated on the display screen: one on which the target was superimposed on top of, and one without the target. Both were performed in real time in 320 x 240 pixel resolution.

7.7.8 Target location

Several steps were required to process the values obtained by the displacement sensors and rotary encoder into coordinates for generating the target on the screen. These steps are outlined in this section and shown in Figure 7.16.

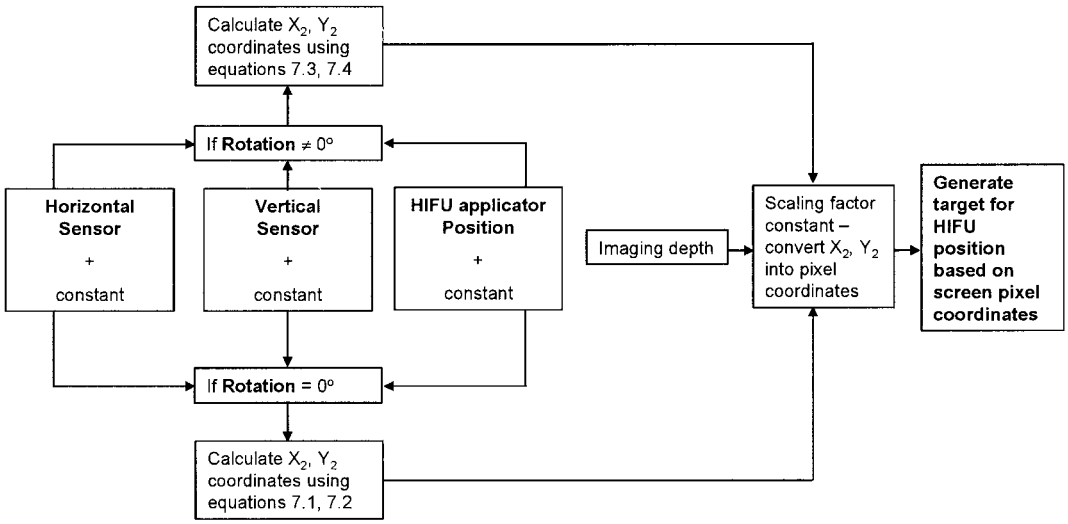

Figure 7.16 Flowchart showing how sensor position data is manipulated into target coordinates based on imaging depth scaling factor and whether or not there is rotation of the image probe

First, the lengths r_1, r_2, and r_3, as discussed in section 7.3, were determined. As shown in Figure 7.3, these lengths were calculated based on the distance from the displacement sensors to points A and B, and the HIFU horizontal distance (described in section 7.4.3) to the focus or point c (Eq. 7.6(a) – (c)).

Eq. 7.6 **(a)** $r_1 = HS + 28$ **(b)** $r_2 = VS + 125$ **(c)** $r_3 = HH + 99.5$

In the above equations, HS and VS are the values obtained from the horizontal and vertical displacement sensors, and HH is the HIFU horizontal distance. The constants (28, 125 and 99.5) in millimeters necessary for determining r_1, r_2, and r_3, added onto the above equations, were determined by digital caliper measurement of the device. All numbers are in millimeters.

Next, the software determined if there was a rotation of the image probe by determining if the angular displacement value from the rotation encoder was 0. Eq. 7.1 and Eq. 7.2 were used to calculate the X_2 and Y_2 coordinates corresponding to the focus when no rotation was present. Eq. 7.3 and Eq. 7.4 were used to calculate the X_2 and Y_2 coordinates corresponding to the focus when rotation was present.

These X_2 and Y_2 values were then converted into pixel values and positioned the focus accurately on the ultrasound image. Because various ultrasound imaging depths were used and because each imaging depth had a different scale (pixel-distance correlation), the X_2 and Y_2 values were first multiplied by a scaling factor and then added to an offset. The scaling factors and offset values were empirically determined by observing how the location of a point on the screen changes (in pixels) compared to the amount of movement (in millimeters) of the device while imaging was performed in water. The X and Y scaling factors and offsets were different for each imaging depth.

Figure 7.17 and Figure 7.18 show the relationship between the screen position (in pixels) and image probe horizontal and vertical separation respectively, for imaging depths ranging from 9 to 22 cm. Different points of measurement were plotted and a best fit line was drawn with the slope being the scaling factor and the intercept being the offset value. Linear regression yielded $R^2 > 0.99$ at all depths. Graphs comparing the differences in slope (scaling factor) and intercept (offset value) for horizontal and vertical movement are shown in Figure 7.19 for various imaging depths. The slope and intercepts for vertical movement both decreased with increased imaging depth. The slope decreased while the intercept values increased for horizontal movement with increased imaging depth.

It was noted while performing pixel position correlations that the pixel aspect ratio (pixels/mm in y divided by pixels/mm in x) was not always 1:1. As a result, the image aspect ratio changed with the imaging depth applied, as listed in Table 7.1. However, since the HITS software calculated the pixels/mm in x and y independently, the change in aspect ratio does not affect the target positioning.

Table 7.1 Image aspect ratio for different imaging depths with SonoSite C60 image probe

Imaging depth (cm)	Aspect ratio (Y:X)
9	1.04
12	0.96
14	0.91
17	0.96
19	0.99
22	0.99
Average ± SD	0.97 ± 0.04

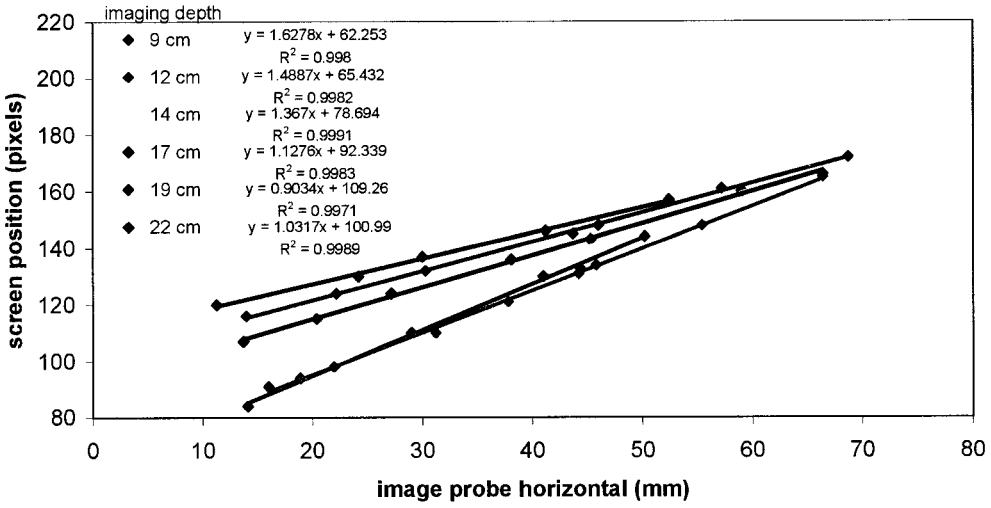

Figure 7.17 Relationship between image probe horizontal and screen pixel position

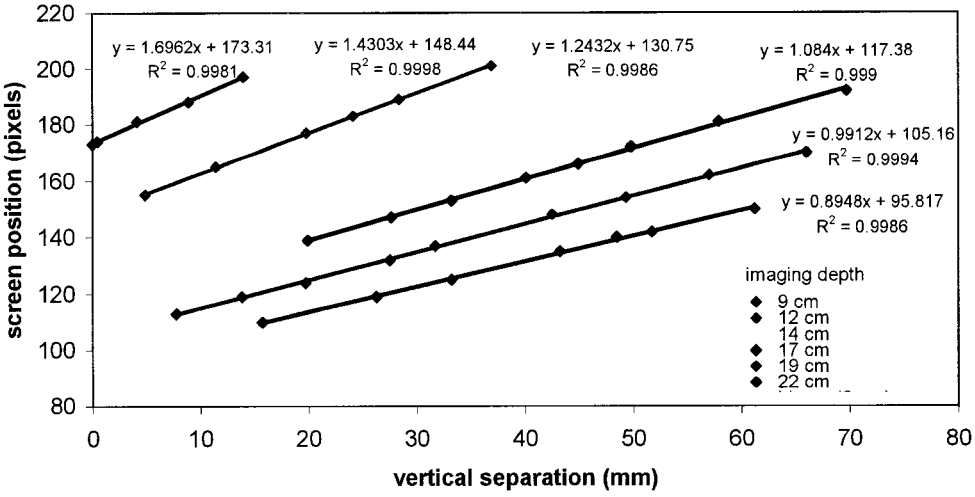

Figure 7.18 Relationship between vertical separation of image probe and HIFU and screen pixel position

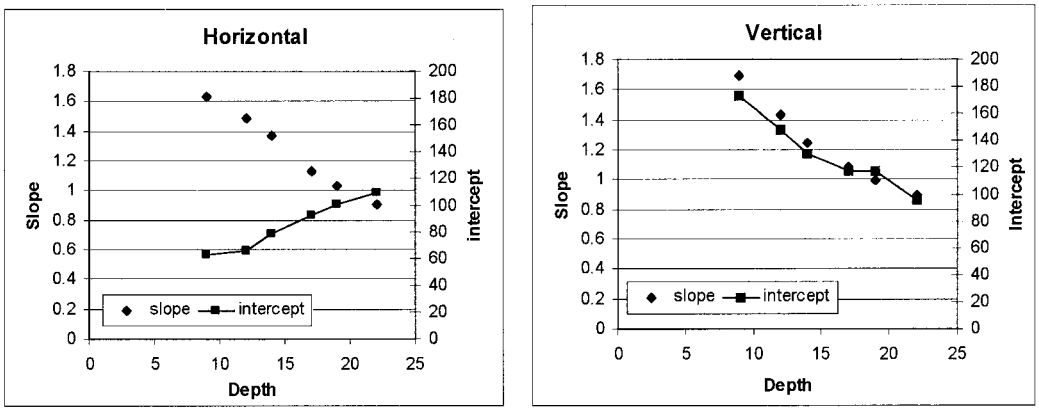

Figure 7.19 Comparison of image probe horizontal and vertical separation slope and intercepts for various depths

Finally, the pixel values were imported into the target generation subroutine described in the following section (7.7.9).

7.7.9 Target generation

A subroutine generated a graphical target based on the determined pixel coordinates of the HIFU focus on the ultrasound image as described in the previous section. The target image was drawn as either crosshairs or a circle 1 cm in radius, scaled according to image depth, both with centers on the HIFU focus coordinates. The target was then superimposed on an ultrasound image obtained by the Inventvision software (Inventeering, San Diego, CA).

7.8 HIFU CONTROL SOFTWARE

7.8.1 Function generator control

A Sony/Tektronix AFG320 2-channel function generator was controlled via a laptop computer using existing National Instruments Labview VIs (afg310wave, afg3xxoutput, afg310waveparam). These existing VIs allowed various wave parameters to be set: frequency, amplitude, offset and phase. The frequency, amplitude and phase were set as controls on the panel while the offset was set to zero. This output wave was assigned to Channel 1 on the function generator.

7.8.1.1 Amplitude buttons

Three amplitude settings were implemented as buttons on the control panel: 50 mV (low power to check for phase interference), 300 mV (medium power), and 500 mV (full / treatment power). The actual acoustic power emitted at each of these settings was determined as per the radiation force balance results in Section 6.6.3 with a duty cycle of 50%. Thus, 50 mV corresponded to 2 W, 300 mV corresponded to 22 W, and 500 mV corresponded to 56 W. Once an amplitude button was pressed, the amplitude setting in the function generator control subroutine was altered correspondingly. When an amplitude button was pressed, the signal to change the power setting was applied to the function generator for 200 ms. This timing consistently changed the amplitude setting on the function generator.

7.8.2 Phase interference stabilization and control

A subroutine was written to stabilize the HIFU induced interference bands on the ultrasound image as described in Section 4.3.6.2. The excitation pulse frequency (EPF) values based on imaging depth (from Table 4.4) were used to define the square wave frequency on channel 2 of the function generator. The square wave corresponded to a 50% duty cycle allowing half of the ultrasound image to be interference free. The amplitude of this square wave was set at 0.9V to control the output of channel 1 using amplitude modulation. Therefore, if the square wave on channel 2 was on a "high" position, the waveform on channel 1 (HIFU parameters) would be activated. If the

square wave on channel 2 was on a "low" position, no output would be generated from channel 1. This technique is illustrated in Figure 7.20.

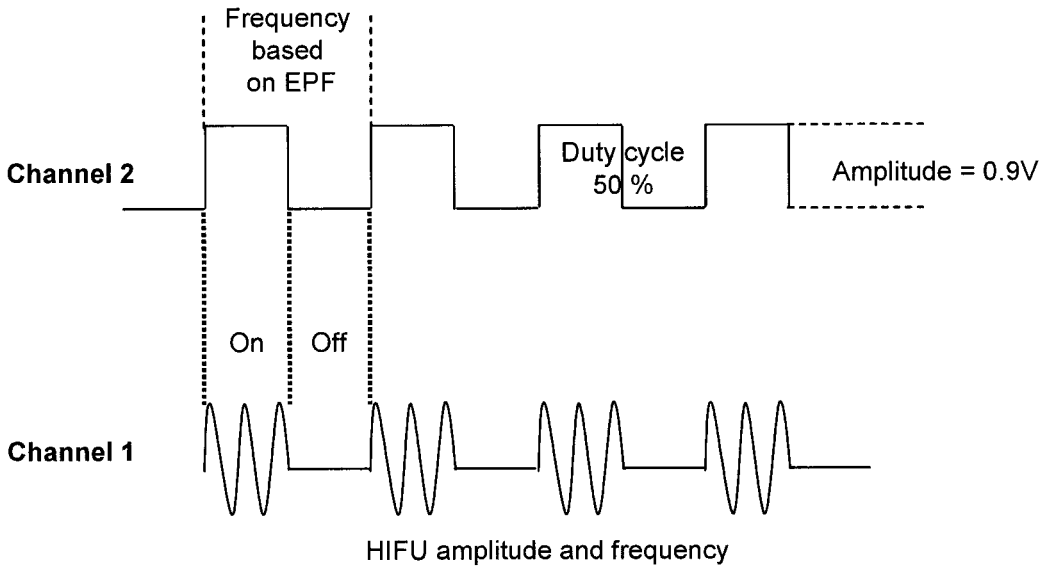

Figure 7.20 Theory of 2-channel function generator operation. Channel 2 generated a square wave at 50% duty cycle corresponding to the excitation pulse frequency or frame rate of the image probe. Channel 2 modulates channel 1, which is the waveform output to the HIFU transducer

Two subroutines were programmed into the VI corresponding to two buttons labeled "left" and "right". These buttons allowed the interference bands to be moved to the left and right respectively, and then stabilized at their new location. Upon pressing the button, the phase angle of the channel 2 square waveform was either increased (left) or decreased (right) by increments of 30 degrees. Upon release of the button, the phase angle remained at its new value. These slight phase changes temporarily offset the EPF causing the spatially stable interference bands to be moveable.

7.9 SOFTWARE OPERATION

A protocol was developed for the operation of HITS to ensure the software functioned consistently and problem free. The HITS software was generally set-up and used as follows. When the software was initially loaded, the video capture device had to be selected. Upon selecting the "WDM (Windows Driver Module) image capture" option (corresponding to the Windows driver for image acquisition using the Dazzle 80), the ultrasound image from the SonoSite was shown on the computer screen twice: one with the superimposed target, and one without. If the device was connected, the program automatically determined the position of the position encoders and since the rotation encoder had not been moved, it assumed the rotation of the image probe to be zero. Therefore, the image probe needed to be brought to a zero rotation position prior to running the software. This zero position was marked on the device during its construction for reference. The HIFU horizontal position and imaging depth were then selected to place the target in the correct position on top of the ultrasound image. Next, the HIFU frequency was selected, and the amplitude defaulted to 50 mV-pp. This is the lowest amplitude setting on the amplifier corresponding to 2 W of acoustic power or a maximum focal intensity without attenuation in water of 207 W/cm^2 for our transducer. The device was positioned for treatment and then operated at this low amplitude for a very short duration (less than 1 second) to determine the location of the phase interference bands on the ultrasound image. If the phase interference bands obstructed the focal location intended for treatment, the bands were moved using the phase control buttons. Once the interference was in its desired location and the device was positioned and ready, the amplitude was changed to an intensity appropriate for treatment, and HIFU was applied.

7.10 SYSTEM TESTING

The HITS was tested for functionality, reliability and repeatability. The first two tests are described in this section, and the repeatability of targeting lesion formation is described in Section 7.11.

7.10.1 Testing HITS for functionality

First, the location of the target on the captured ultrasound image was verified to be correct by placing a pin exactly 4 cm in front of the HIFU transducer at the location of the HIFU focus, with the transducer placed in a water bath. The target location was compared to the location of the pin (which appeared as a small hyperechoic spot on the ultrasound image) for all imaging depths. Device components were moved (horizontally, vertically, and the image probe was rotated) to determine if the system target followed the pin location. Qualitative results from this test indicated that HITS was able to accurately track the theoretical focal location 4 cm from the HIFU transducer. Next, a lesion was created in a block of gel, a piece of turkey breast, and a piece of turkey breast placed inside a piece of beef, shown in Figure 7.21. The latter was to determine if speed of sound variations in the HIFU and imaging path (significance to be discussed in Section 7.11.2.3) affected targeting. The speed of sound was 1540 m/s in turkey breast (measured) and 1580 m/s in beef muscle (Duck 1990). After the lesion was created and the hyperechoic spot was visualized, the device components were moved to random locations to determine if the targeting system could follow the spot. Qualitative analysis indicated that HITS tracked the lesion successfully in all media tested, as exemplified in Figure 7.22 in turkey breast.

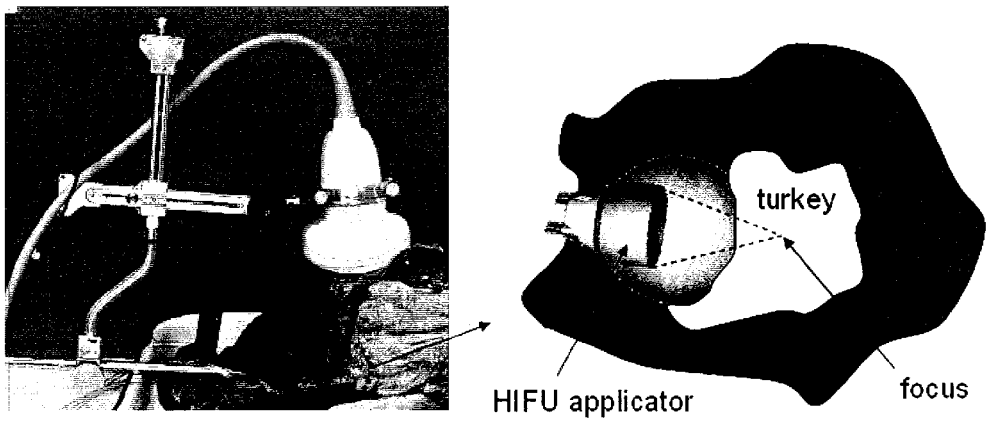

Figure 7.21 Testing the device with targeting system by creating lesions in a piece of turkey inside a piece of beef.

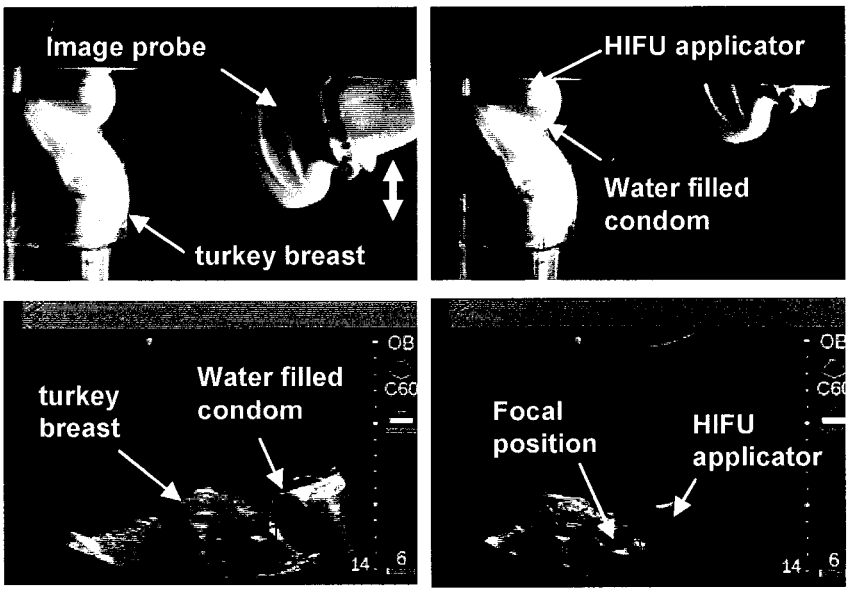

Image probe linear movement

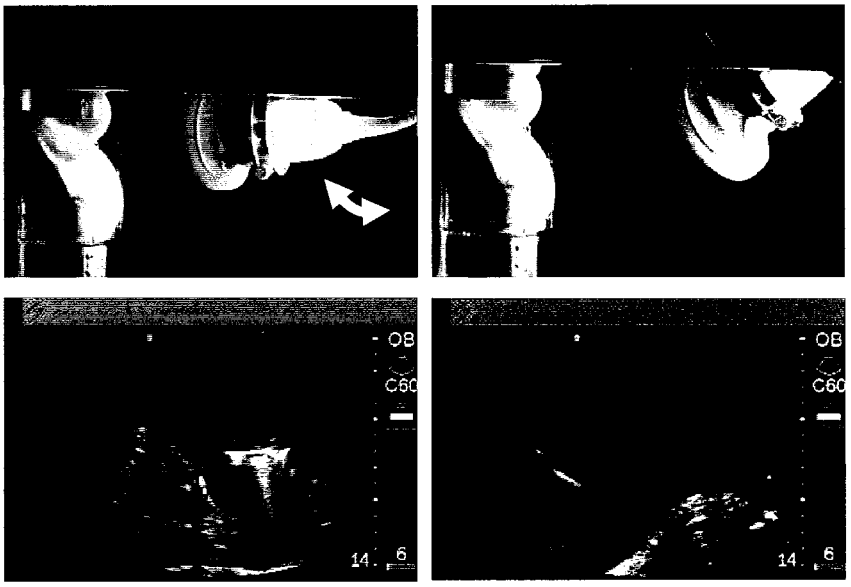

Image probe rotation

Figure 7.22 Tracking of HIFU lesion (hyperechoic spot) using HITS. The image probe is moved horizontally (top four images) and rotated (bottom four images) in a treatment of turkey breast tissue.

7.10.2 Testing HITS for reliability

For the system to be used in an *in vivo* setting, it the software and system must be able to withstand mishaps during treatment. As a result, devices connected to the computer were randomly unplugged or turned off, and wires were randomly disconnected and reconnected to determine if HITS was able to continue operation despite these disruptions. No conflicts or software crashes were noticed. The power to the computer was turned off to simulate a power failure scenario and the software booted successfully subsequently on the first try. Finally, the SonoSite system had a self-timer meaning it would automatically turn off after 15 minutes of no activity. The software's reaction to the SonoSite automatically turning off was tested. Although the software kept functioning once the SonoSite was off, there was obviously no captured image displayed on the computer screen. When the SonoSite was turned on again, the program continued to function and images instantly displayed on the computer screen. However, the program had a tendency to freeze when there is no video signal connected to the USB port before the program is loaded. This video input requirement was not a fault of the HITS program but a property of the image capture software (detailed in Section 7.7.7) as it continuously searches for the video signal. A subroutine allowing the user to specify whether a video signal was present or not may remedy this problem.

7.11 Error Analysis

To determine the potential for discrepancy between the HITS indicated treatment location and the actual treatment location, an error analysis was performed. The predicted theoretical error was compared to the error incurred upon testing the device.

7.11.1 External error estimate

The first part of this error analysis encompassed the errors from the displacement sensors and rotary encoders. The cumulative error due to position sensors was calculated as an external error estimate (an error measurement that can be derived from a set of equations) based on equations Eq. 7.3 and Eq. 7.4. The error values used to compute the cumulative error are listed in Eq. 7.5. All errors were assumed random and uncorrelated.

Table 7.2 External sources of error

Error source	Error type and description	Maximum error value
Horizontal displacement sensor	Resolution + maximum independent linearity error: the accuracy of the displacement sensor was based on the minimum resolvable cable travel and the manufacturer's specified maximum linearity error.	ε_{r1} = 0.01+0.5%(76.2) = 0.391 mm
Vertical displacement sensor	Resolution + maximum independent linearity error: the accuracy of the displacement sensor was based on the minimum resolvable cable travel and the manufacturer's specified maximum linearity error.	ε_{r2} = 0.01+0.5%(76.2) = 0.391 mm
Rotation encoder	Resolution: the accuracy of the rotation encoder was based on the degree of rotation needed to produce one count.	ε_{r3} @ 200 lines/rotation = 0.0157 radians
HIFU transducer position	The accuracy of the HIFU transducer position was based on how accurately the transducer was locked into the device based on the engraved markings (section 7.4.3), and how accurate the markings were.	Negligible error due to locking position, 0.03 mm caliper error.

The mean square error for statistically independent errors can be calculated using the partial derivatives of the equation that defines the measurement in question and its individual error contributions:

Eq. 7.7
$$\varepsilon_m^{\,2} = \sum_{i=1}^{n} \left(\frac{\partial m}{\partial r_i} \right)^2 \varepsilon_{ri}^{\,2}$$

The variable m is the measurement in question and ε_m is the cumulative error in that measurement. ε_{ri} is the individual contribution of each measurement (r) to the cumulative error. Note that the caliper error in HIFU transducer position was two orders of magnitude less than the error due to displacement sensor and can be ignored. The total position error was a combination of error in X (ε_X) and in Y (ε_Y), and can be calculated as

Eq. 7.8
$$\varepsilon_Z^{\,2} = \varepsilon_X^{\,2} + \varepsilon_Y^{\,2}$$

The error in X and in Y can be calculated as follows, based on Eq. 7.7, Eq. 7.3 and Eq. 7.4,

Eq. 7.9

$$\varepsilon_{Y2}{}^2 = \left(\frac{\partial Y_2}{\partial Y_1}\right)^2 \varepsilon_{Y1}{}^2 + \left(\frac{\partial Y_2}{\partial r_1}\right)^2 \varepsilon_{r1}{}^2 + \left(\frac{\partial Y_2}{\partial r_2}\right)^2 \varepsilon_{r2}{}^2 + \left(\frac{\partial Y_2}{\partial r_3}\right)^2 \varepsilon_{r3}{}^2 + \left(\frac{\partial Y_2}{\partial \theta}\right)^2 \varepsilon_{\theta}{}^2$$

Eq. 7.10

$$\varepsilon_{X2}{}^2 = \left(\frac{\partial X_2}{\partial X_1}\right)^2 \varepsilon_{X1}{}^2 + \left(\frac{\partial X_2}{\partial r_1}\right)^2 \varepsilon_{r1}{}^2 + \left(\frac{\partial X_2}{\partial r_2}\right)^2 \varepsilon_{r2}{}^2 + \left(\frac{\partial X_2}{\partial r_3}\right)^2 \varepsilon_{r3}{}^2 + \left(\frac{\partial X_2}{\partial \theta}\right)^2 \varepsilon_{\theta}{}^2$$

Solving Eq. 7.9 yields

$$\varepsilon_{Y2}{}^2 = (\varepsilon_{Y1})^2 + (\sin\theta)^2(\varepsilon_{r1})^2 + (1-\cos\theta)^2(\varepsilon_{r2})^2 + (-\sin\theta)^2(\varepsilon_{r3})^2 + (r_1\cos\theta + r_2\sin\theta - r_3\cos\theta)^2(\varepsilon_{\theta})^2$$

and solving Eq. 7.10 yields

$$\varepsilon_{X2}{}^2 = (\varepsilon_{X1})^2 + (1-\cos\theta)^2(\varepsilon_{r1})^2 + (-\sin\theta)^2(\varepsilon_{r2})^2 + (\cos\theta-1)^2(\varepsilon_{r3})^2 + (r_1\sin\theta - r_2\cos\theta + r_3\sin\theta)^2(\varepsilon_{\theta})^2$$

The error was dependent on the contributions of the rotation amplified errors in r_1, r_2, and r_3, as well as the error in rotation itself. The error in position was determined for three cases, shown in Figure 7.23 and quantified in

Table 7.3:

- Maximum: (the horizontal displacement sensor was fully extended, the vertical displacement sensor was fully retracted, and the HIFU transducer was also fully extended (13 cm);
- Minimum: (the horizontal displacement sensor was fully retracted, the vertical displacement sensor was fully extended and the HIFU transducer was at a minimal extension (5 cm));
- Typical: (the device was set to a position used for *in vitro and in vivo* treatments, and the HIFU transducer was extended 8 cm).

Table 7.3 Device position cases for error determination

Case Length	Maximum	Minimum	Typical
r1	104 mm	28 mm	75 mm
r2	204 mm	125 mm	190 mm
r3	230 mm	150 mm	180 mm

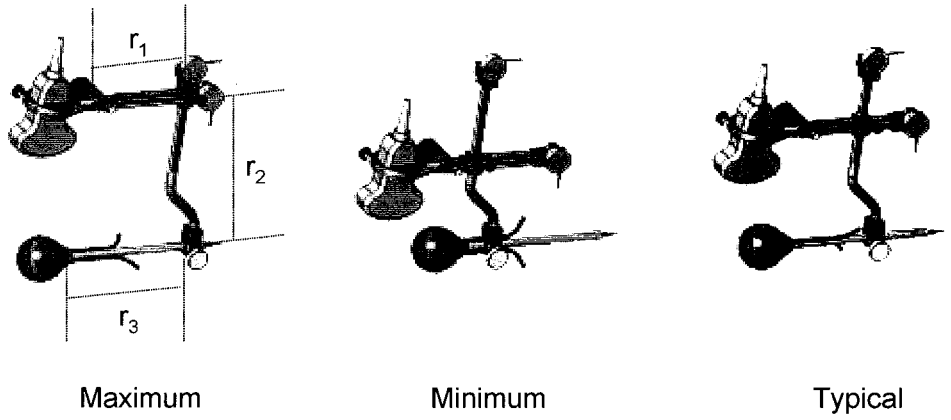

Figure 7.23 Three device position cases used in determining error

The errors are plotted in Figure 7.24 for the limits of rotation of the image probe (-60 to 60°). As expected, the error was minimized for each case when the image probe was not rotated. As the probe rotates, the error in horizontal position (ε_X) and the error in vertical position (ε_Y) were affected differently. However, the cumulative position error, ε_Z increased with rotation, and increased symmetrically about the zero rotation position. Since the image probe was not normally rotated past 20° during *in vivo* treatment and *in vitro* testing, the maximum error in position that can be expected during treatment, estimated from these external error estimates, was ±4.45 mm. The error increased as the device components were extended. Error due to the rotation encoder resolution was amplified more with greater extension, analogous to an increase in moment arm providing greater leverage in generating torque.

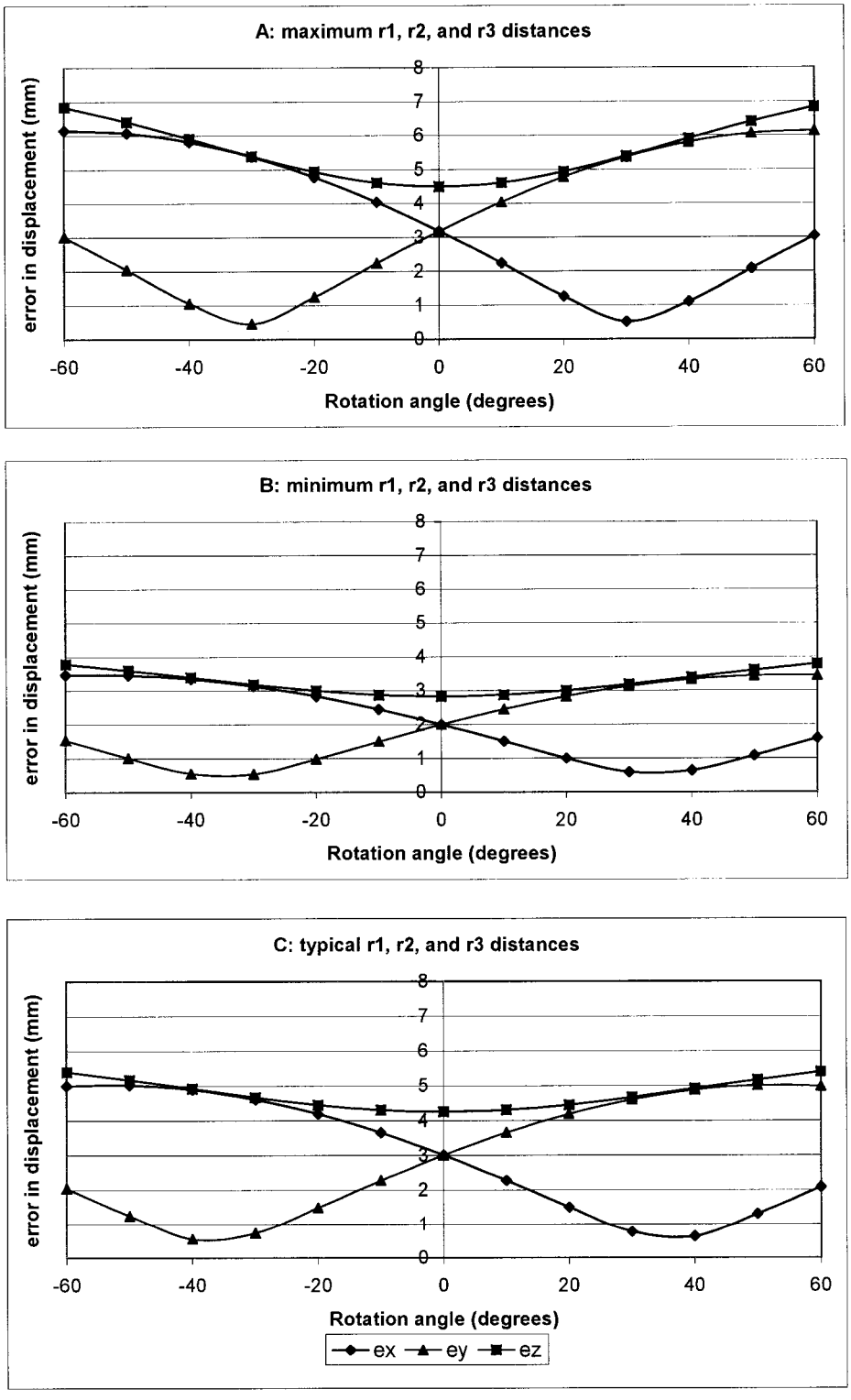

Figure 7.24 Position errors as a function of image probe rotation for maximum, minimum, and typical device position cases

7.11.2 Internal error contributions

Internal errors are those that are due to inaccuracies during the operation of the device, experimental calibration, and imaging inaccuracies. The three errors that are investigated here are motion in device components, errors in pixel-distance correlation, and errors due to imaging media with dissimilar speeds of sound.

7.11.2.1 Motion in device components

When the horizontal arm of the device connecting the image probe was not locked in place, there was potential for slight movement of the arm. This motion was due to the tolerance needed to allow the arms to slide. The motion was determined using digital calipers to be 0.4 mm, an order of magnitude less than the error due to position sensor resolution.

7.11.2.2 Errors in pixel-distance correlation

There was concern that inaccuracies in determining the image scale or the number of pixels per millimeter, for each imaging depth (refer to Figure 7.17 and Figure 7.18), would lead to an inaccurate target position. The target would be further than the focus if the scale was too large, or located between the transducer and the focus if the scale was too small. However, with linear correlations between pixel location and physical location greater than 0.99 for all imaging depths, this inaccuracy was deemed negligible.

7.11.2.3 Errors due to dissimilar speeds of sound

Another reason why the pixel-distance correlation may be inaccurate is due to variations of the sound speed in heterogeneous media. The ultrasound machine assumed a speed of sound (c_o) in performing imaging, and assumed this speed of sound to be consistent throughout the imaged medium. If the speed of sound varied within this media, then the sound travel time to a particular location will be different than that predicted using c_o. As a result, the number of pixels traversed in that time will be different, as shown in Figure 7.25. However, since the physical distance is still the same, the pixel-distance correlation would now be different and the target location may be inaccurate. As an example, if the speed of sound varies greatly in the image path, but is consistent in the HIFU path, the

target location shown on the screen, calibrated in Section 7.7.8 using homogeneous media (water), may not be indicative of the actual treatment location in the heterogeneous media.

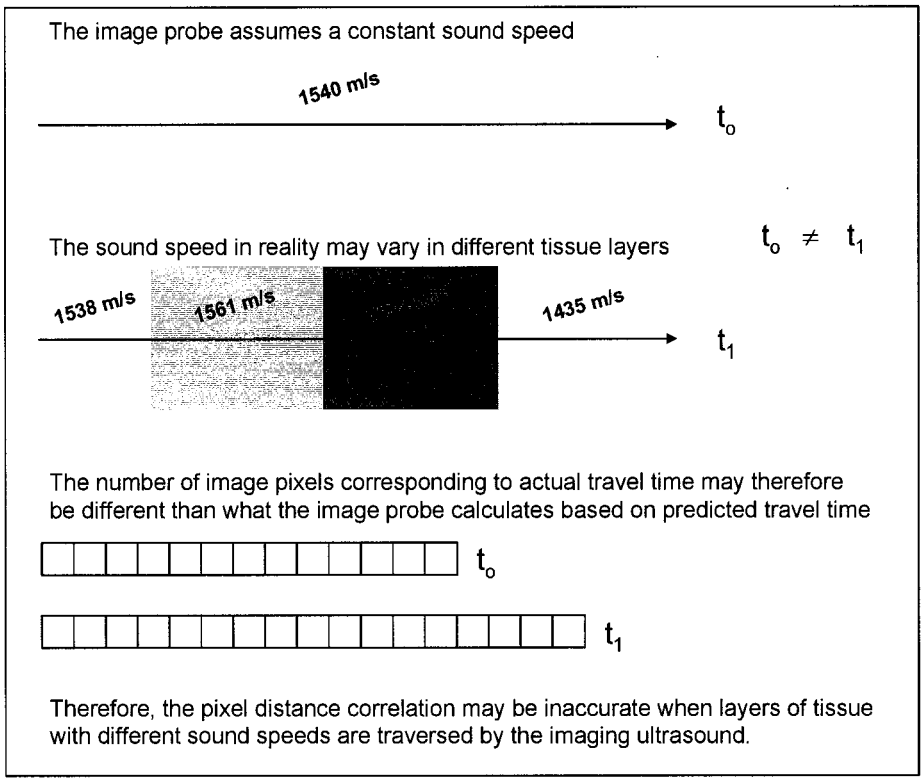

Figure 7.25 The pixel distance correlation may be inaccurate if the imaging ultrasound traverses layers of tissue with sound speeds different from the assumed constant sound speed

To determine the sensitivity of the target system to changes in sound speed, the following calculations were performed. The imaging device assumed that speed of sound c_o was 1540 m/s and the sound speeds of various media that the device may encounter is listed in Table 7.4. It can be assumed from Table 7.4 that a suitable range to determine the effects of varied speed of sound is 1483 to 1600 m/s.

Table 7.4 Sound speeds of different in vitro and in vivo test media

Media	Speed of sound (reference)
Water (25°C)	1483 m/s
Turkey breast	1540 ± 11 m/s (section 5.2.3)
Polyacrylamide/BSA gel phantom	1544 ± 4 m/s (Lafon, Kaczkowski et al. 2001)
Sheep uterus	1559 ± 19 m/s (section 5.4.3.3)
Sheep vaginal wall	1573 ± 20 m/s (section 5.4.3.3)
Human myometrium	1584 m/s (section 3.6)
Human uterine fibroid	1584 m/s (section 3.6)

The discrepancies in target location based on this chosen range of sound speeds were determined for two cases:

- Typical imaging scenario: an image depth of 14 cm was used to observe a treatment target located at a depth of 10 cm.
- Maximum imaging depth: an image depth of 22 cm was used to observe a treatment target located at a depth of 20 cm.

First, time of travel was determined, as shown in Figure 7.26, for image depths of 14 cm and 20 cm, at sound speeds from 1483 to 1600 m/s.

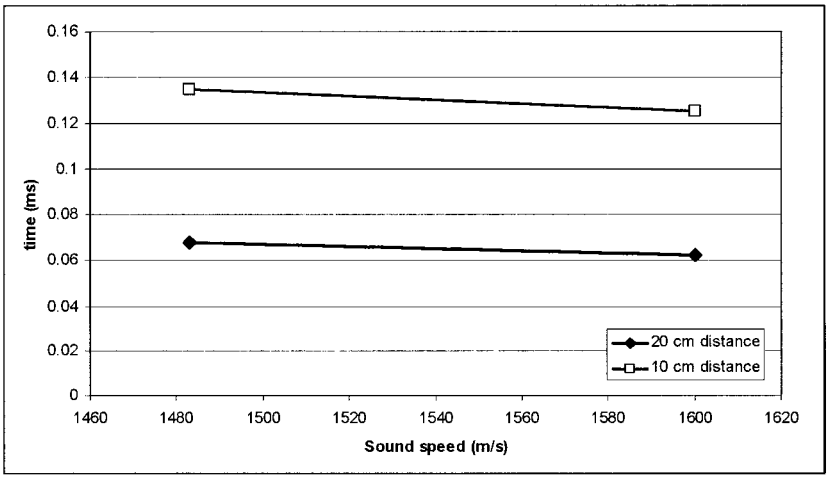

Figure 7.26 differences in travel time at various speeds of sound for two imaging depths

Next, the time difference between 1483 m/s and 1600 m/s were used to determine the difference in distance that may be encountered based on the assumed sound speed of 1540 m/s for imaging depths of 10 and 20 cm. These differences in distance were calculated as follows:

First, the time of flight corresponding to velocities of 1483 and 1600 m/s (t_v) for distances (d) of 10 cm and 20 cm were calculated as:

Eq. 7.11 $$t_v = \frac{d}{v}$$

The difference in distance encountered assuming a sound speed of 1540 m/s was then determined, for a specific image depth, as:

Eq. 7.12 $$\Delta d_{1540} = 1540(t_{1483} - t_{1600})$$

The difference in distance was calculated as 7.59 and 15.18 mm for a 10 cm and 20 cm imaging depth respectively, and can be assumed as the maximum error due to differences in sound speed. Although these errors seem very large, larger than errors due to position sensor resolution, these errors would only be encountered in very heterogeneous tissue with a wide range of sound speeds. In addition, these errors would only be encountered if the sound speeds were very different between the image path and the treatment path. In a typical treatment scenario with tissue sound speeds ranging from 1540 to 1580 m/s, the maximum error due to variations in speed of sound (assuming image path and treatment path sound speeds to be on opposite ends of the range) is 2.58 mm at a 10 cm image depth in one direction. Using Eq. 7.8, the estimated total maximum error in position is 3.65 mm (although it is unlikely that the maximum error will be experienced in both x and y directions). This study also indicated that the larger the imaging depth, the more chance for tissue sound speeds to vary, and the greater the potential error due to variances in speed of sound in heterogeneous tissue.

7.11.3 Combined error contributions

The total potential error in targeting took into account the external estimates of error (section 7.11.1) and the potential error due to speed of sound variances in heterogeneous tissue between imaging and treatment paths (7.11.2.3). The potential error ignored the insignificant contributions due to motion in device components (section 7.11.2.1), and errors in pixel distance correlation (7.11.2.2). The maximum anticipated error for a typical in vitro or in vivo treatment (typical device position in

Table 7.3, image depth of 14 cm and target depth of 10 cm, image probe rotation at 20o) was estimated to be the summation of the external estimates of error and potential error due to speed of sound variances: 4.45 + 3.65 mm. This means that at any given target location, the actual center of the HIFU focus may be off by a radius of ± 8.1 mm. At first, this value seemed problematic because it is in the order of the size of the hyperechoic spot. However, this calculation assumes that the errors all affect the target location in the same direction. In reality, components of these errors may end up canceling out if their magnitudes are similar but directions are opposite. The next section describes tests showing actual experimental error.

7.11.4 Experimental error measurements

A series of lesions were created in a gel phantom using the "typical" device configuration to determine the accuracy of the targeting system and to test the validity of the theoretical limits of error determined in section 7.11.3. The lesions were imaged with the image probe rotating up to 20° in each direction. The location of the brightest pixel of the lesion (presumed to be the center of lesion formation) was compared to the location of the center of the target circle using ImageJ software (NIH). The difference in the number of pixels was converted to a distance in millimeters, recorded, and compared to the theoretical limits of error. Ten lesions were created with the following image probe rotation settings: -20, -15, -10, -5, 0, 5, 10, 15, and 20 degrees. For all lesions, HIFU was operated at 40 W of acoustic power, at a frequency of 4.035 MHz, a duty cycle of 50%, and for 10 seconds of exposure time. During treatment, water was circulated in the condom at a rate of 150 mL/min to simulate an *in vivo* treatment scenario. The focal intensity for each treatment was 3590 W/cm^2 determined using the methods described in

section 2.14 with a HIFU transducer focal area of 0.00968 cm^2, gel attenuation of 0.0496 NP/cm (at 4.035 MHz) and the depth of treatment into the gel of 1.5 cm.

The results comparing experimental to theoretical error are shown in Figure 7.27a and b. Every error measurement was within the theoretical limits of error throughout the entire -20° to 20° rotation. The error was proportional to the amount of rotation in both theoretical predictions and in the experiment. However, the differences in mean error between rotation amounts were not significant in the experiment ($p>0.05$). For the same magnitude of rotation, the mean error was generally greater for positive rotation than for negative rotation. However, this was also not statistically significant ($p>0.05$) and may be due to slight hysteresis in the mechanical pin joint during rotation. Furthermore, more variation was observed in the error values for greater image probe rotation, shown in Figure 7.27a. Finally, when comparing the percent difference in error (ε_D), calculated as Eq. 7.13, and shown in Figure 7.27b, the experimental error (ε_E) was closer to the theoretical predictions (ε_T) for larger degrees of rotation.

Eq. 7.13 $$\varepsilon_D = \frac{\varepsilon_T - \varepsilon_E}{\varepsilon_T}$$

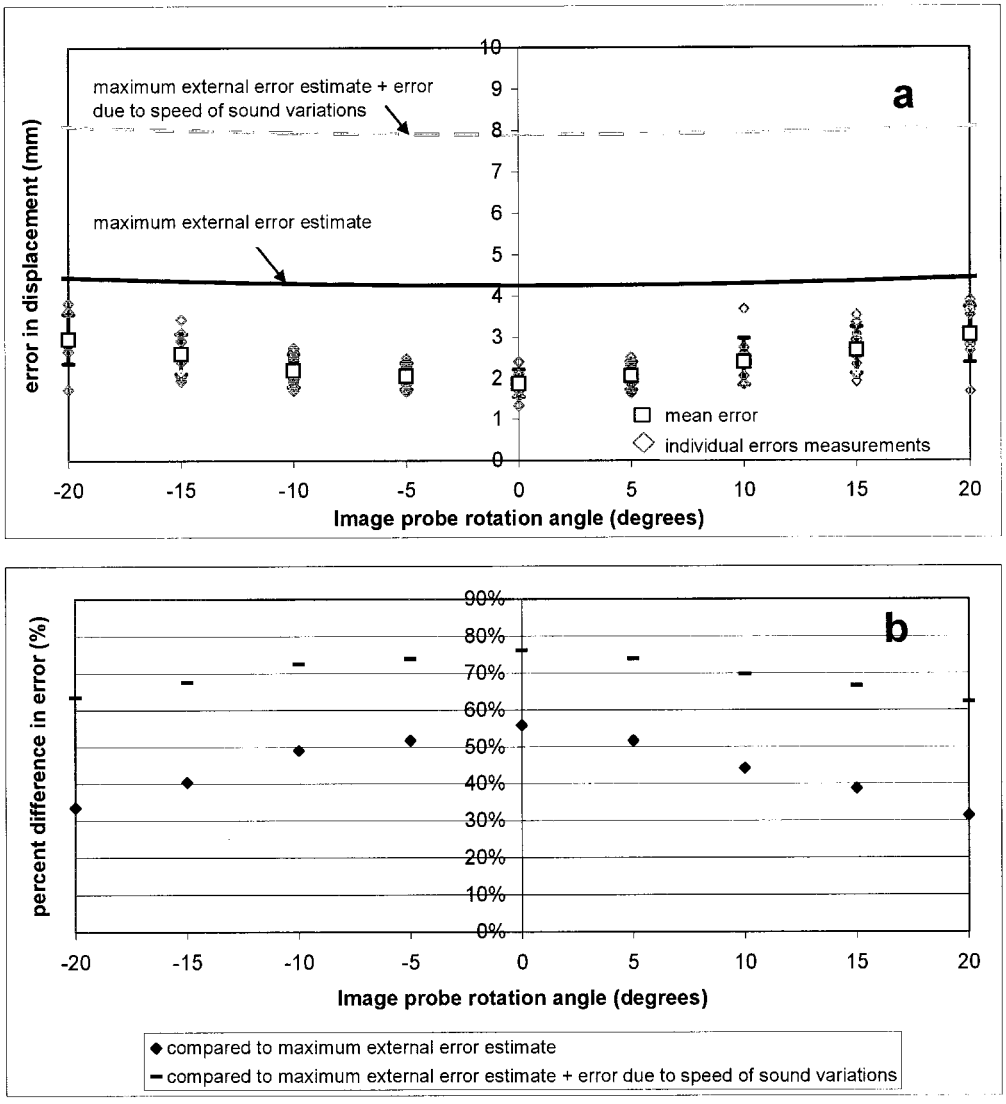

Figure 7.27 Comparison of experimental to theoretical error. (a) shows the theoretical error limit (solid line) along with experimentally determined points of error, and their mean ± 1 SD for image probe rotation angles from -20 to 20 degrees. (b) shows the percent difference in error between theoretical and experimental results.

7.12 DISCUSSION

The experimental errors were considerably lower than the theoretically predicted errors. The actual errors were over 75% lower than the predicted errors without rotation, and over 60% lower than predicted errors at 20° of rotation. Several assumptions used in deriving the theoretical limits of error may have contributed to this discrepancy. First, the error limits were maximum errors that may be encountered. Second, the error in horizontal and vertical position due to displacement sensor was based on the manufacturer's specified maximum linearity error. The sensors that were used in this device likely had linearity error less than the specified maximum. Upon initial calibration of the sensors (section 7.4.1.2), negligible linearity error was noticed. Next, the theoretical error limits assumed that speed of sound variation errors and external error estimates both increased the error in the system. However, in reality, these errors may cancel since they were both independent and random.

The error in displacement of 2 to 3 mm noted during experimentation was deemed acceptable. In perspective, this represented only 2-6 pixels depending on the image depth. Hyperechoic spots are usually 5-7 times larger than the error. Furthermore, the target generated by HITS was to be used as an indication of the area that may be affected by a lesion. Due to thermal spreading of the treatment, the affected area *in vivo* may be larger than the treated area that appears as a hyperechoic spot. Therefore, the error becomes less significant. The target circle, 1 cm in radius, described in section 7.7.9, encompassed a treated "region", more than just the center of treatment.

The largest contributor of error in the targeting system was the resolution of the rotational encoder. A higher resolution rotation encoder would improve the accuracy of the target. For example, doubling the resolution of the rotation encoder would halve the external error estimate.

7.13 HITS: CONCLUSIONS

The work presented in this chapter demonstrated the feasibility and practicality of using externally mounted positions sensors on the device to determine the location of the HIFU focus on the ultrasound image. The position sensors were robust and withstood exposure to water and damp conditions that may be present in an *in vivo* environment. Computer software, written in LabView, accurately monitored the position of the sensors in real-time and generated a visual target that was superimposed on the ultrasound image captured onto the computer screen corresponding to the HIFU focus. The software also controlled HIFU operating parameters and monitored transducer temperature. An error analysis indicated that the inaccuracies due to displacement sensor precision were much smaller than the HIFU treated area. This meant that the system operator could be confident that the targeted region for treatment on the ultrasound image will be a good representation of the treated area in tissue. However, this system only provides targeting in two-dimensions, and a three-dimensional targeting system would improve the accuracy of HIFU treatment targeting. HITS was tested *in vivo* in the sheep experiments explored in Chapter 8.

8.0 CHAPTER 8 IN VIVO TREATMENT OF SHEEP UTERUS

8.1 INTRODUCTION

In vivo experimentation prepares a medical device for human use. Although bench top experiments and laboratory tests are crucial in determining device performance characteristics, an in vivo setting presents additional challenges which may affect the device performance. Factors such as respiration, tissue perfusion, tissue inhomogeneities, reflections at tissue interfaces, blood circulation, acoustic streaming, and limited acoustic window may affect in vivo treatment.

8.2 BACKGROUND AND MOTIVATION

The completed image-guided transvaginal HIFU device was tested in vivo. The sheep model was used for image-guided transvaginal HIFU device testing, as discussed in section 5.4. Although the sheep pelvic anatomy was somewhat different from that of humans, the vaginal canal size and access to the uterus makes it a feasible model for device testing. Uterine fibroid tumors were not present in the sheep, but it should be noted that the goal was to prove that the device can be used to visualize, target, and ablate a designated area in the uterus. The second goal was to observe effects of HIFU at several post-treatment intervals using the sheep model. This will provide insight into how uterine tissue will react to HIFU treatment.

8.3 METHODS AND MATERIALS

8.3.1 Animal Preparation

Eight domestic female sheep aged 2 - 3 years and weighing between 52 and 71 kg were used for this study. The animals were obtained from the University of Idaho and the experiment was performed according to a protocol approved by the Animal Care Committee at the University of Washington according to guidelines set by the National Institutes of Health. The 8 sheep were randomly assigned into four groups of two animals each, with each group was randomly assigned a time point for euthanization: immediately after treatment, 2-days, 7-days and 30-days. The sheep were fasted 12 hours prior to treatment and relocated from a vivarium to an operating room prior to the treatment procedure. The animals were given intramuscular sedation consisting of 0.3

mg/kg xylazene, masked, and placed under isofluorine anesthesia with their abdomen facing upwards on an operating table. The abdominal region was shaved using a shearer and the remaining hair removed using Nair (Church & Dwight Co., Inc, Princeton, NJ). Since a full bladder was necessary to obtain clear visualization of the uterus, a balloon catheter was inserted into the urethra. This balloon catheter was used to fill the bladder with saline (0.9% NaCl) and to prevent fluid leakage from the bladder. Sterile acoustic coupling gel (Aquasonic 100, Parker Laboratories Inc., Fairfield, NJ) was applied onto the sheep abdomen prior to ultrasound imaging.

8.3.2 *Ultrasound imaging and HIFU treatment*

The protocol used for HIFU treatment of sheep uterus is described here. The SonoSite C60 abdominal imaging probe was used to scan the sheep abdomen to locate pelvic structures: urethra (and balloon catheter), bladder, bowel, vaginal canal, ovaries and uterus. Once the pelvic structures were located, three different sized vaginal dilators made of delrin plastic (15 mm, 25 mm and 40 mm in diameter) were used in sequence to prepare the vaginal canal for the insertion of the HIFU transducer. A removable plastic tube, (45 mm OD, 42 mm ID), was placed concentrically over the largest vaginal dilator. After this dilator was removed, the tube remained inside the vagina aiding the insertion of the transvaginal HIFU transducer.

Prior to vaginal insertion, a sterile condom was secured onto the HIFU transducer with an o-ring (as described in section 4.2.7). The water tubes connecting the transducer to the water circulation system were purged free of air, the condom was filled with 40 mL of water, and water was circulated until all visible air bubbles were forced out of the condom. The initial 40 mL of water in the condom also provided a "cushion" between the HIFU transducer brass housing and the vaginal wall during insertion.

The HIFU transducer was connected to the driving circuitry. The HITS software was activated and the image probe position was calibrated as described in section 7.7.6. The HIFU transducer was inserted through the plastic tube and into the vaginal canal with ultrasound image-guidance. Once the transducer was inside the vaginal canal, the plastic tube was removed and the condom was filled with an additional 60 mL of water for a total of 100 mL.

The transducer was then positioned for treatment in an area of the uterus body within 3 cm of the cervix. The treatment area was then identified using the targeting system (HITS). With the aid of ultrasound image-guidance and HITS, the water in the condom was adjusted so that the transducer was properly positioned for treatment. Water was circulated during treatment to keep the transducer temperature under 37°C. This guideline was used in all but the first animal treated. Thermal damage was noted in that animal when higher transducer temperatures were used (described in section 8.5). The volume of water in the condom during treatment was kept between 80 and 120 mL. Five treatments, 10 seconds in duration, at 40 W of acoustic power were applied, guided by the ultrasound image and HITS. The HITS display for each treatment, including the superimposed target, was recorded using video capture software (SnagIt Video Capture, TechSmith Corporation, East Lansing, MI). The ultrasound image from the SonoSite (without superimposed target) was recorded with a Super VHS recorder (Panasonic AG-1960, Matsushita Electric Co. Ltd, Japan). Approximately 60 seconds elapsed between each treatment allowing for the hyperechoic spot to be recorded and the transducer to be repositioned for the subsequent treatment. After all five lesions were formed, the water in the condom was reduced to 40 mL and the transducer was removed. After treatment, the animals were allowed to recover from anesthesia and were returned to the vivarium. The total time the sheep was under anesthesia was approximately 45 minutes. The sheep were monitored for abnormal behavior and vaginal abnormalities until euthanasia. For euthanasia, the animals were sedated, anesthetized, and euthanized using an injection of KCl to the heart.

8.3.3 Gross and microscopic analysis

Upon euthanasia, a midline incision was made in the animal and the uterus and vaginal canal were removed. The vagina, colon, bladder, ureters, and blood vessels surrounding the uterus were examined for damage and abnormalities. The colon and remaining tissue in the body adjacent to the uterus were also examined. All treated regions were photographed using a digital camera (D-30, Canon Inc., Lake Success, NY).

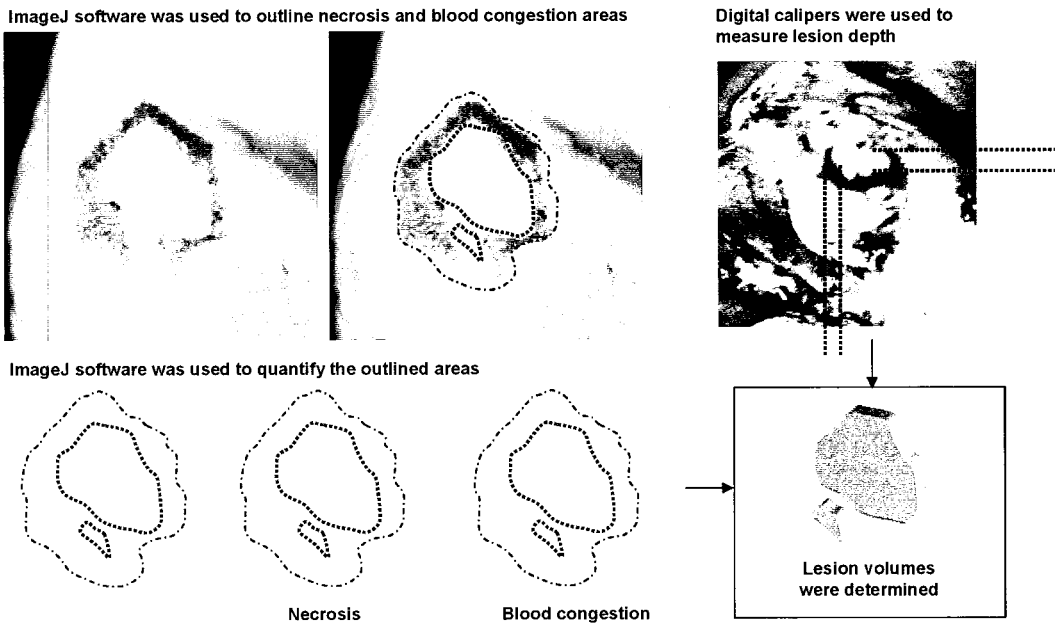

Figure 8.1 Image quantification techniques used to determine volumes of necrotic tissue and regions of blood congestion

Lesion volume was determined as depicted in Figure 8.1. Lesions due to HIFU treatment were characteristic of coagulative necrosis. As explored in section 2.7.7.1, these lesions consist of a white necrotic center surrounded by a ring of red blood congestion and inflammation. To quantify these lesions, the depth of the lesion into the tissue was first measured using digital calipers (CD S6 CT, Mitutoyo Corp, Japan) at six different locations: three within the necrotic tissue and three within surrounding inflammatory tissue. Next, necrotic and blood congestion areas in the digital photographs were distinguished using pixel intensity analysis. Since necrotic tissue is of an off-white cream color, and blood congested tissue is a reddish maroon color, distinguishing the two tissue types by color was possible. To determine the color corresponding to normal tissue, and regions of necrosis and blood congestion, approximately 2500 points from photographs from all animals were sampled using image analysis software (ImageJ, National Institutes of Health) for three categories of tissue: treated necrotic areas, treated blood congestion areas, and untreated tissue. The RGB value was determined for each sampled point and plotted on histograms as shown in Figure 8.2. This RGB value can be represented as a value on a 256 shade grayscale spectrum, with 255 being white and 0 being black. A student's t-test indicated statistical significance between the three categories ($p<0.05$),

and thus the size of the necrotic and hemorrhagic areas were determined by calculating the number of pixels of a particular range of RGB values within the entire lesion.

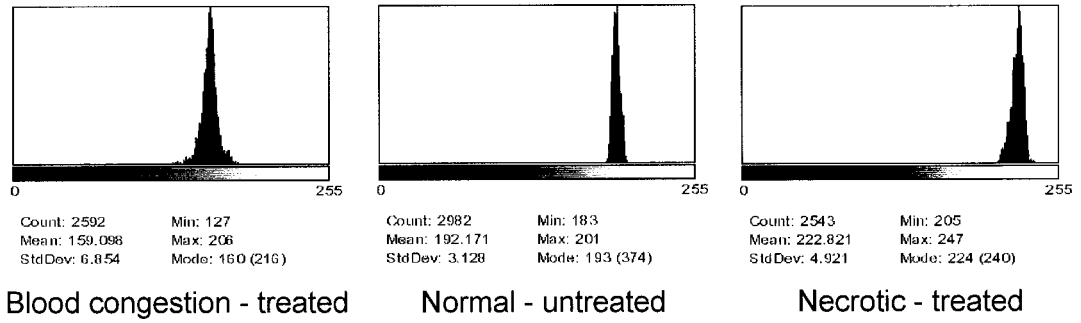

Figure 8.2 Histograms showing RGB values of treated (hemorrhagic and necrotic) and normal untreated tissue. The mean values for blood congested areas, normal areas, and necrotic areas were 159, 192, and 223 respectively, all significantly different from each other. These values were used to distinguish tissue types.

The necrotic and hemorrhagic area of each lesion was measured three times electronically using ImageJ software. A different RGB cutoff value was used each time to compensate for differences in lighting when the photograph was taken. The RGB criteria for samples taken in each trial are shown in Table 8.1.

Table 8.1 RGB values for inclusion of necrotic and hemorrhagic tissue

Tissue type	Sample 1	Sample 2	Sample 3
Necrosis	212 < RGB < 255	210 < RGB < 255	208 < RGB < 255
Blood congestion	0 < RGB < 172	0 < RGB < 174	0 < RGB < 176

The treated volumes were determined by multiplying the average of these area measurements and the average of the caliper measured depths (Eq. 8.1).

Eq. 8.1 Treated volume = (software determined area) (caliper measured depth)

Samples from treated and non-treated areas on the uterus were fixed with formalin (10%), embedded in paraffin wax, then sectioned and stained using hematoxylin and eosin. The samples were mounted on microscope slides for histopathological analysis at the Histopathology Laboratory at the University of Washington. Light microscopy images were obtained from the samples. These microscopic images were used to compare HIFU

affected tissue at various euthanasia times. These images were also used to compare the effects of varying degrees of HIFU treatment.

8.4 RESULTS: PROTOCOL SUMMARY

A summary of the animals treated, target depths, and focal intensities generated are listed in Table 8.2. The 8 animals used in this experiment had an average mass of 58 ± 6 kg. The average HIFU treatment of all 40 lesions attempted was at a spatial average temporal average intensity[e] of 1909 ± 295 W/cm^2. Although the acoustic power was kept at 40 W, the different locations of treatment into the uterus resulted in different intensity values generated. The location of treatment was at 2.0 ± 0.4 cm into the uterus body[f]. Figure 8.3 shows that there was no statistically significant difference in the average intensity between animals. This was important for comparing lesion sizes since it shows that although the treatment location varied between animals, the HIFU dosage (intensity multiplied by time) between animals was similar. Figure 8.3 also shows that there was no statistically significant difference in the maximum HIFU transducer temperature during treatment (as measured by the internal thermocouple) between animals, except for sheep A. Since this was the first animal treated, acceptable temperature ranges had not yet been ascertained. During the treatment of sheep A, it was observed that the temperatures reached by the HIFU transducer caused thermal damage, as described in Section 8.5. Therefore, the maximum transducer temperature was limited to 37°C.

---

[e] The intensity refers to the derated intensity at the focus taking into account the attenuation of the tissue between the HIFU transducer and the focus. The attenuation coefficient of sheep uterus tissue was 1.67 dB/cm based on measurements in section 5.4.3.3.

[f] The location of treatment (depth into tissue for intensity calculations) was based on the ultrasound images recorded during treatment.

Table 8.2 Summary of animals treated and treatment intensities

Subject	Evaluation Period[a] Days	Mass kg	Treatment depth in uterus[b] cm	Average focal intensity[c] W/cm^2
			Average ± standard deviation (N=5)	
A	0	55	2.0 ± 0.7	1966 ± 572
B	7	62	1.7 ± 0.4	2097 ± 309
C	2	58	1.8 ± 0.5	2031 ± 403
D	2	52	1.8 ± 0.1	2014 ± 104
E	30	53	2.0 ± 0.1	1829 ± 83
F	30	59	2.2 ± 0.4	1744 ± 268
G	0	56	2.0 ± 0.1	1843 ± 67
H	7	71	2.2 ± 0.1	1744 ± 102
Average		58	2.0	1909
Standard Deviation		6	0.4	295
N=		8	40	40

a. the evaluation period is the number of days (24 hour periods) elapsed from treatment to euthanasia
b. the treatment depth in uterus is the distance that the HIFU travels through tissue proximal to the focus
c. spatial average temporal average

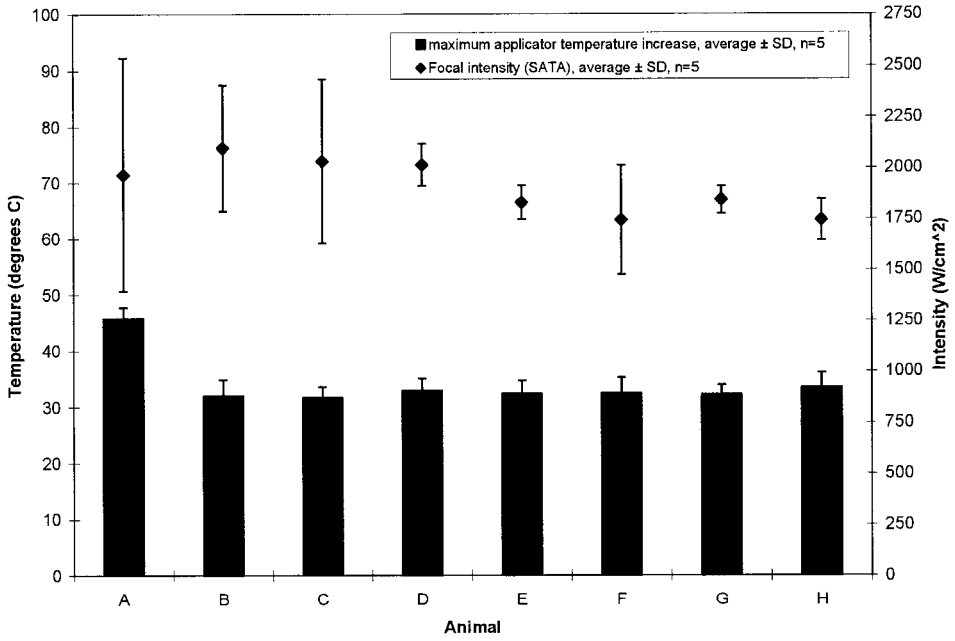

Figure 8.3 Treatment intensities and maximum HIFU transducer temperature for all 8 animals. Animal A experienced significantly higher temperatures due to a leaky condom (described in Section 8.5). There was no statistically significant difference between the intensities used in all animals.

8.5 RESULTS: COMPLICATIONS ENCOUNTERED

As indicated in Table 8.3, there were treatment complications in 3 of the 8 treated animals. These three animals also had undesired effects of thermal damage to the vaginal tissue, and HIFU treated colon, noted upon dissection.

Table 8.3 Sheep uterus treatment complications

Subject	Complications during treatment	Complications noted during dissection
A	Water condom leakage, not catheterized, poor visualization of uterus due to empty bladder	Thermal damage to vaginal tissue
B	None	None
C	None	None
D	Not catheterized due to swollen urethra, poor visualization of uterus due to empty bladder	Treated spots on the colon adjacent to intentionally treated uterus
E	None	None
F	None	None
G	None	None
H	Not catheterized due to swollen urethra, poor visualization of uterus due to empty bladder	Treated spots on the colon adjacent to intentionally treated uterus

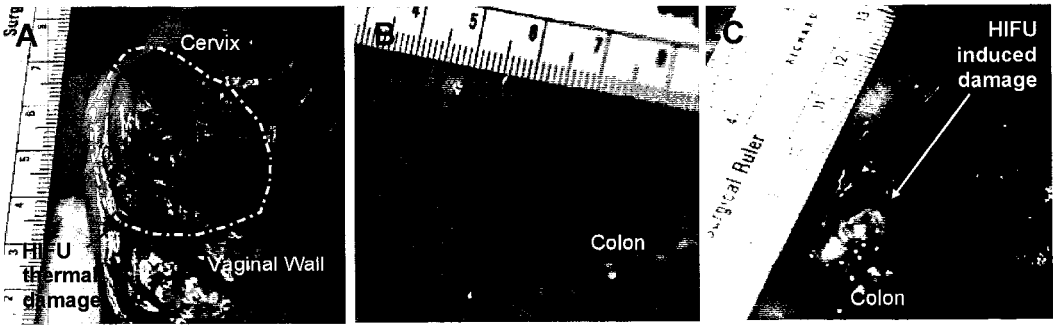

Figure 8.4 Adverse effects due to HIFU treatment discovered during dissection. A: sheep A vaginal wall thermal damage, B: sheep D colon surface lesions, C: sheep H deep colon lesion

During the treatment of sheep A, a large amount of water was leaking from the vaginal cavity. When the HIFU transducer was removed after treatment, it was discovered that the condom had a leak and that there was no water remaining in the condom. The fact that this animal had not been catheterized also resulted in poor visualization of the HIFU transducer and uterus. This lack of visualization precluded observation of any condom leakage. Upon dissection of sheep A, thermal damage to the vaginal wall was seen, as shown in Figure 8.4a. Since this animal was immediately euthanized after the treatment, healing of the vaginal wall burns could not be studied. It was inferred that the thermal damage was a direct result of the lack of water in the condom. First, the lack of water meant that water cooling was less effective in cooling the vaginal wall tissue immediately surrounding the HIFU transducer. Second, the lack of water meant reduced acoustic coupling, or less efficient transfer of HIFU energy into the tissue, especially if the deflated water condom enabled air pockets to be formed. Finally, both of these factors would result in the HIFU transducer temperature during treatment being higher than desired. As shown in section 5.4.3.3, the attenuation, and thus absorption of HIFU energy, was greater in vaginal wall tissue than in uterus tissue. This high absorption could potentially have resulted in pre-focal damage, especially with poor acoustic coupling, analogous to previously reported pre-focal skin burns (Fry and Johnson 1978; Moore, Lopez et al. 1989; Visioli, Rivens et al. 1999). In hindsight, the elevated temperature and water leakage should have resulted in the termination of treatment. However, since this was the first animal in the protocol, there was no basis for judgment of what was considered anomalies. This particular case emphasized the importance of good visualization, effective water circulation, acoustic coupling, and temperature monitoring.

Balloon catheters were not inserted into the urethra of Sheep D and Sheep H because both animals had very swollen and reddened openings to the urethra, possible due to uterine tract infection. As a result, the bladders of these animals were not full during treatment. The lack of fluid in the bladder may have allowed bowel tissue to encroach areas adjacent to the treated region. With a full bladder, the bowel would have been pushed out of the way of HIFU treated regions. The interfering bowel also obstructed clear ultrasound visualization of the uterus. During treatment, hyperechoic spots were seen in the targeted region, confirming treatment in tissue. However, what was treated

could not be visualized as well as those animals that were catheterized. Upon dissection, treated areas were noticed on the colon in both sheep D and sheep H, along with intended lesions in the uterus. The colon lesions, shown in Figure 8.4 b and c, were indicative of coagulative necrosis. The two lesions in the colon of sheep D were very superficial. However, the treated area in sheep H extended the entire depth of the colon and felt very stiff to touch. Sheep H was a one week survival animal, and during that week, there were no abnormal bowel movements or bleeding. These undesired colon lesions again demonstrate the importance of good visualization of the uterus prior to treatment. As a result, it was imperative to ensure that the bladder is full enabling a clear image of the HIFU transducer and uterus prior to treatment.

8.6 RESULTS: HIFU LESION ANALYSIS, QUALITATIVE: GROSS EXAMINATION

This section explores the qualitative changes in lesion appearance over a 30 day period from a gross examination standpoint. The lesions formed in each animal and discovered upon dissection are discussed in detail in sections 8.6.1 through 8.6.4. HIFU lesions were discovered in the uterine body of all 8 animals at the targeted treatment locations. The majority of lesions found were indicative of coagulative necrosis, consisting of white necrotic tissue in the center surrounded by a red ring of blood congestion. There were differences in lesion appearance between the 4 time points of euthanasia (immediate, 2, 7, and 30 days). Lesions in uteri dissected immediately after treatment consisted of a dark red ring surrounding an area of necrosis. Two days after treatment, the red ring appeared lighter in color, spread over a larger area, and appeared more inflamed. By day 7, only a very small red ring was present and the majority of the lesion was necrotic. It appeared that the previously inflamed area and area of blood congestion had become necrotic. Some of the area surrounding the coagulative necrosis lesion had also necrosed, probably due to the ablation of vasculature, namely capillaries, leading to the lesion area. By day 30, only a small red spot of blood congestion was observed, with no necrotic tissue observed. Characteristic lesions at each time point are shown in Figure 8.5.

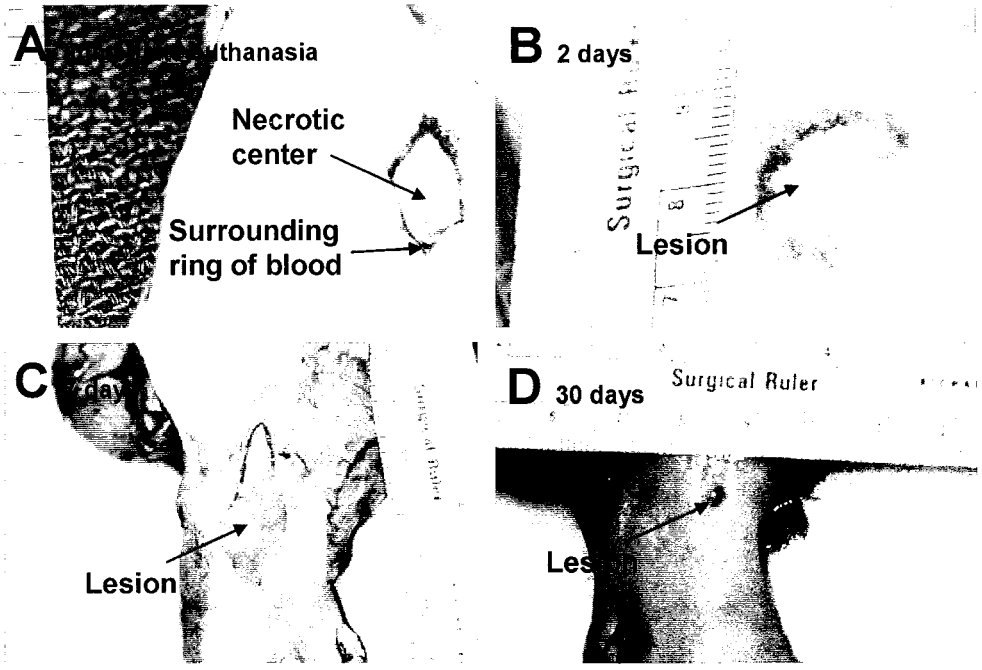

Figure 8.5 Characteristic HIFU lesions in uterus body at various time points. A: immediately after treatment showing a white necrotic center surrounded by a red ring of congested blood, B: 2 days after treatment showing an enlarged blood congestion region and inflammation, C: 7 days after treatment showing the majority of the affected area becoming necrosed, D: 30 days after treatment showing the treated area had reduced to a small red spot.

Smaller lesions in the uterine horn (UH) and uterine body (UB) (areas not intended for treatment) were found, as shown in Figure 8.7A and B. These unintended lesions were found in sheep B. The lesion in the uterine horn was due folding of the uterine horns over the uterine body during the treatments and the proximity to the HIFU focus may have resulted in treatment effects spreading to the uterine horn, as depicted in Figure 8.6. The small lesions (1) and (2) in the uterine body away from the intended area of treatment may have been due to reflections from gas in the bowel.

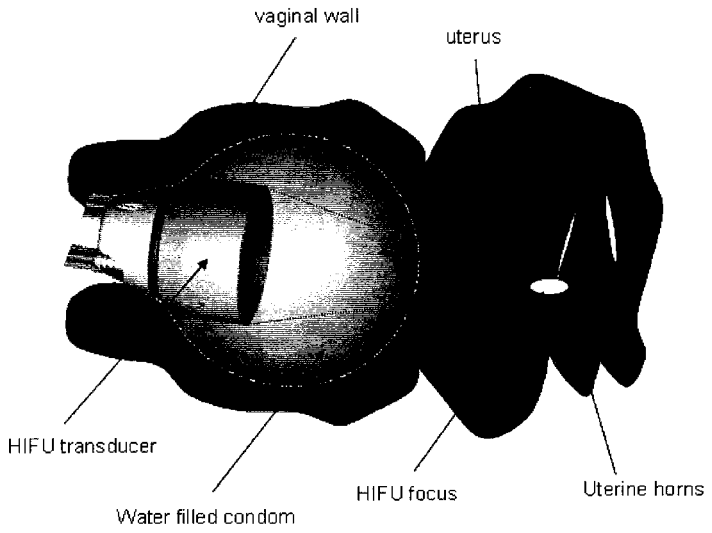

Figure 8.6 Uterine horns folded over during HIFU treatment of the uterus may have resulted in unintended treatment of the horns due to their proximity to the HIFU focus.

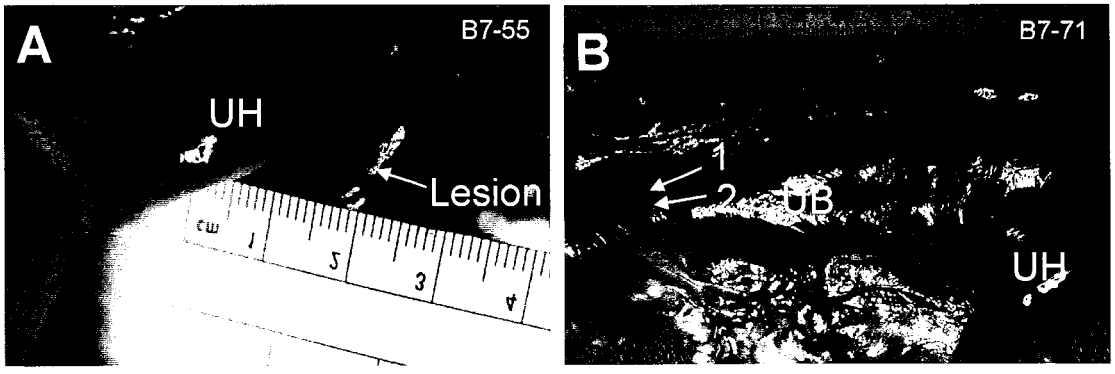

Figure 8.7 Unintended lesions formed in (A) the uterine horn (UH) and (B) the uterine body (UB), shown as 1 and 2. Numbers on the ruler are in cm.

8.6.1 *Sheep A and G: immediate euthanasia*

Images from the sheep A and sheep G dissections are shown in Figure 8.8 and Figure 8.9 respectively.

In Figure 8.8A, the dissected uterus showed a surface lesion on the uterine body (UB). The lesion (1) showed coagulative necrosis characteristics. The small white center was necrotic tissue while the surrounding red area was congested blood. (V) indicates the vaginal canal and (UH) indicates the location of the uterine horns. Figure 8.8B shows another lesion found on the opposite side of the uterus body. This lesion (2) was also comprised of a ring of congested blood surrounding an area of necrosis. Upon dissection of the uterus, two lesions deep in tissue (3) and (4) were found in an intended treatment area in the uterine body near the cervix (CX), as shown in Figure 8.8C.

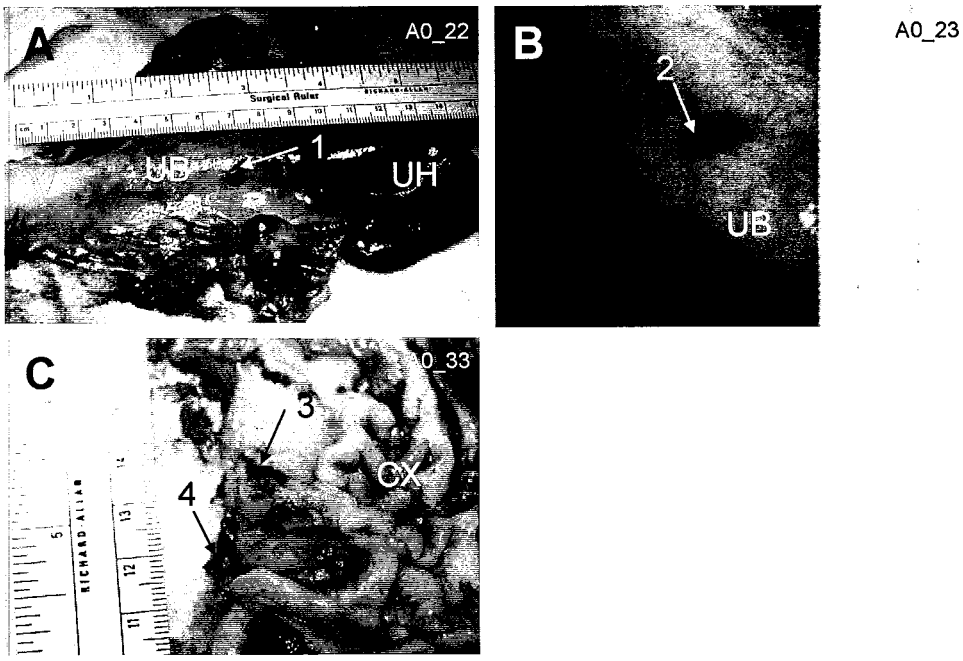

Figure 8.8 Sheep A dissection photographs

Figure 8.9A shows an intended lesion (1) found on the uterus body distal to the cervix. There was no damage to the uterine horns (UH), bladder (BL) or ovaries (OV). Figure 8.9b shows there was also no damage to the colon (CO). The lesion (1) was examined upon opening the uterine body. The treated area shows a coagulative necrosis lesion with a necrosed center (white) surrounded by blood congestion (Figure 8.9C). This lesion (1) penetrated the uterine body is shown from the back of the uterine body (Figure 8.9D).

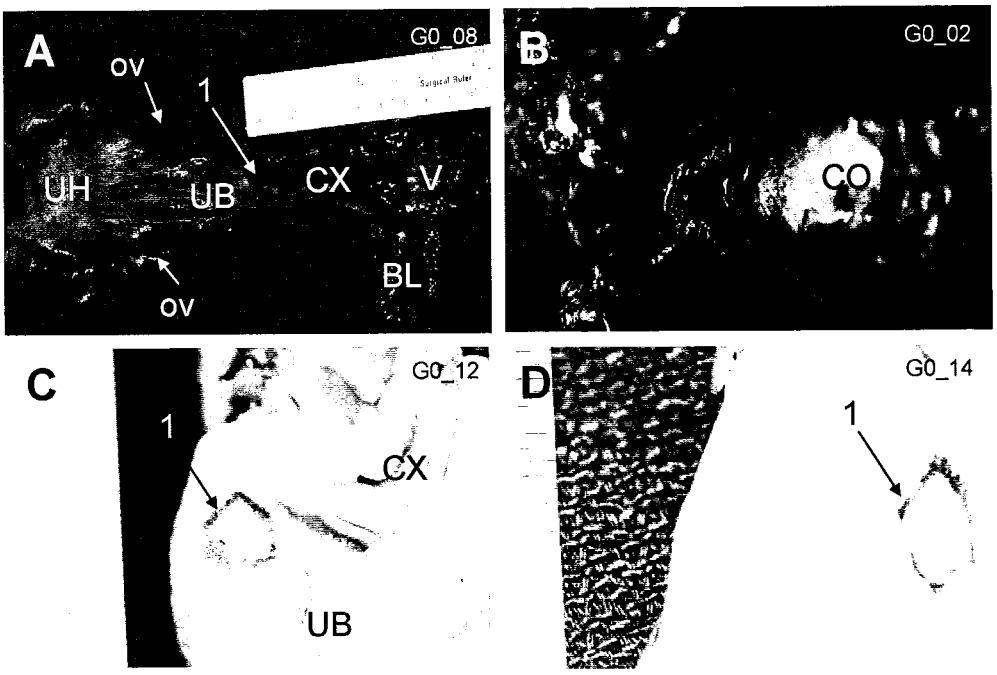

Figure 8.9 Sheep G dissection photographs

8.6.2 Sheep C and D: 2 day survival

Images from the sheep C and sheep D dissections are shown in Figure 8.10 and Figure 8.11 respectively.

Figure 8.10A exposes the vaginal cavity and uterus after midline incision. The HIFU transducer is placed in treatment position to provide orientation of the transducer to the uterus. Landmarks on the vagina and uterus are shown: (V) vagina, (CX) cervix, (UB) uterine body, (UH) uterine horns. Lesions in the cervical region, as well as in the middle of the uterine body in shown in Figure 8.10B. During treatment, the uterine horns were folded over the uterine body as shown by the dashed line. The smaller lesion in the mid-upper portion of the uterine body may have developed as a part of the larger lesion formed closer to the cervix. A close-up view of the lesions formed in the uterine body is shown in Figure 8.10C. Areas of necrosis appeared as white spots. Lesions were ellipsoidal in shape (dotted lines). A ring of congested blood in the tissue surrounding the necrotic regions can be seen (dot-dash line). Areas (2) and (3) were lesions formed by two 10 second treatments and three 10 second treatments respectively. It was inferred that area (1) developed during the formation of area (3) since the uterus was folded over during treatment. Figure 8.10D shows the vaginal canal and uterus cut open. The cervix, consisting of very tough tissue, can be seen, along with the lesions in the uterine body. The lesions extend deep into uterine tissue outwards to the surface of the uterus (4).

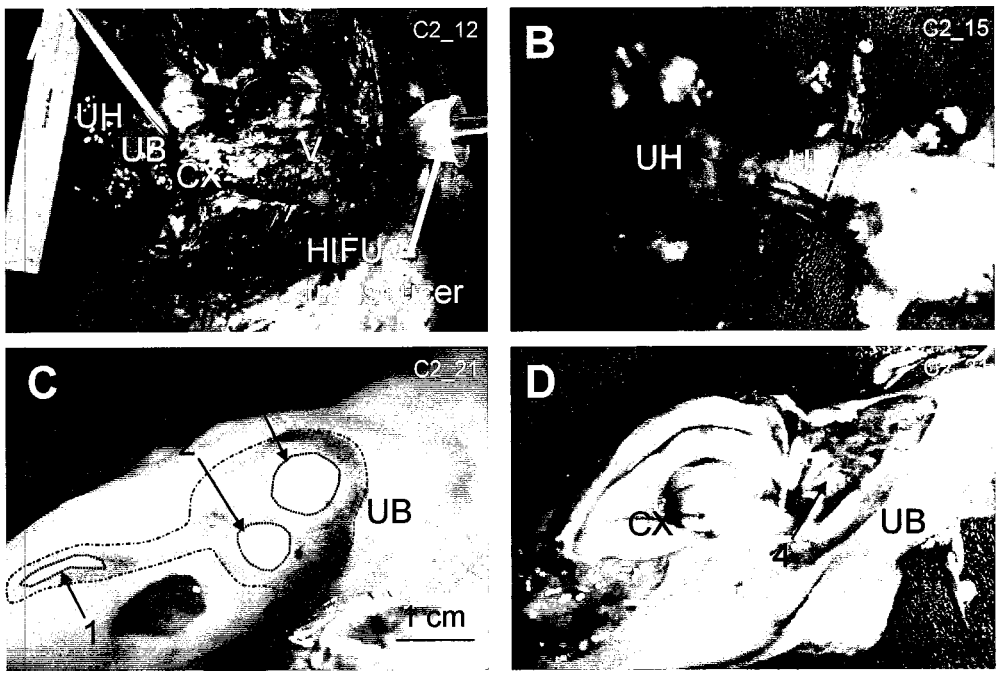

Figure 8.10 Sheep C dissection photographs

In Sheep D, five lesions were intentionally formed adjacent to one another to determine the ability for a hand-held instrument to treat a localized area. Upon dissection, five lesions (1) through (5), were observed on the uterine body (UB) in a circular pattern, depicted in Figure 8.11A. The colon (CO) adjacent to this large area of treatment was not affected. The lesions were characteristic of coagulative necrosis. The necrotic (white) region had a slightly darkened center. Figure 8.11B shows that once the uterine body was opened, the lesion extended through the depth of the myometrium. The back of the lesion (Lb) is shown. Figure 8.11C shows that a smaller sized lesion (R) was located next to the treated area (L) between the uterine body (UB) and the uterine horn (UH). To put the location into perspective, the vaginal canal is marked with a (V). This smaller lesion was considered a reflected lesion. Figure 8.11D illustrates the concept of this reflected lesion. During treatment, the uterine horn (UH) was folded over the uterine body (UB) as shown by the dashed line. As the ultrasound transducer was placed in the vagina (V) the treated region on the uterine body (L) extended onto a section of the uterine horn (R). It can also be seen from this photograph that the bladder (BL) was not damaged during the treatment.

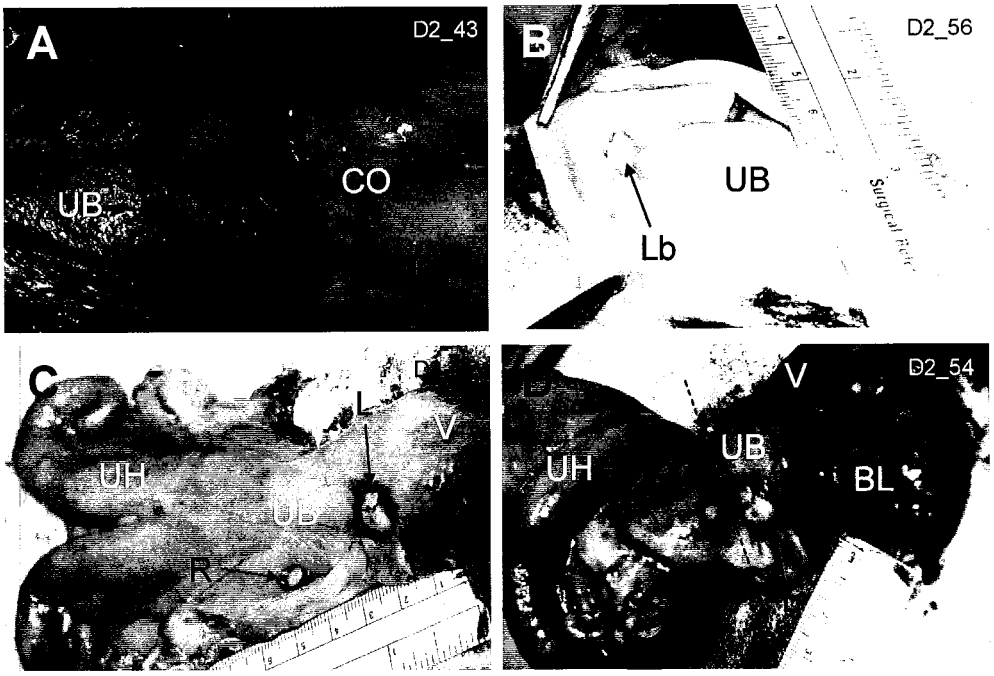

Figure 8.11 Sheep D dissection photographs

8.6.3 Sheep B and H: 7 day survival

Images from sheep B and sheep H dissection are shown in Figure 8.12 and Figure 8.13 respectively.

During treatment, the uterus body (UB) was folded over the bladder (BL). Although coagulative necrosis lesions can be seen on the uterine body adjacent to the bladder, (1) and (2), there was no damage to the bladder as seen in Figure 8.12A. The region of the uterus body adjacent to the colon (COL) was also treated, as shown in Figure 8.12B. Coagulative necrosis lesions (3) and (4) are clearly visible. There was no damage to the colon showing or other structures adjacent to the uterus showing that localized treatment to the uterus was possible. The uterus is shown in Figure 8.12C, extracted from the body and displaying the location of lesions (1) and (2) relative to the uterine body (UB) and uterine horns (UH). The uterus is shown in Figure 8.12D, extracted from the body and displaying the location of lesions (3) and (4) relative to the vagina (V), cervix (CX), and uterine horns (UH). Figure 8.12E shows that upon inspection of the cross sections of lesions 3 and 4, the HIFU lesions penetrate deep into the tissue.

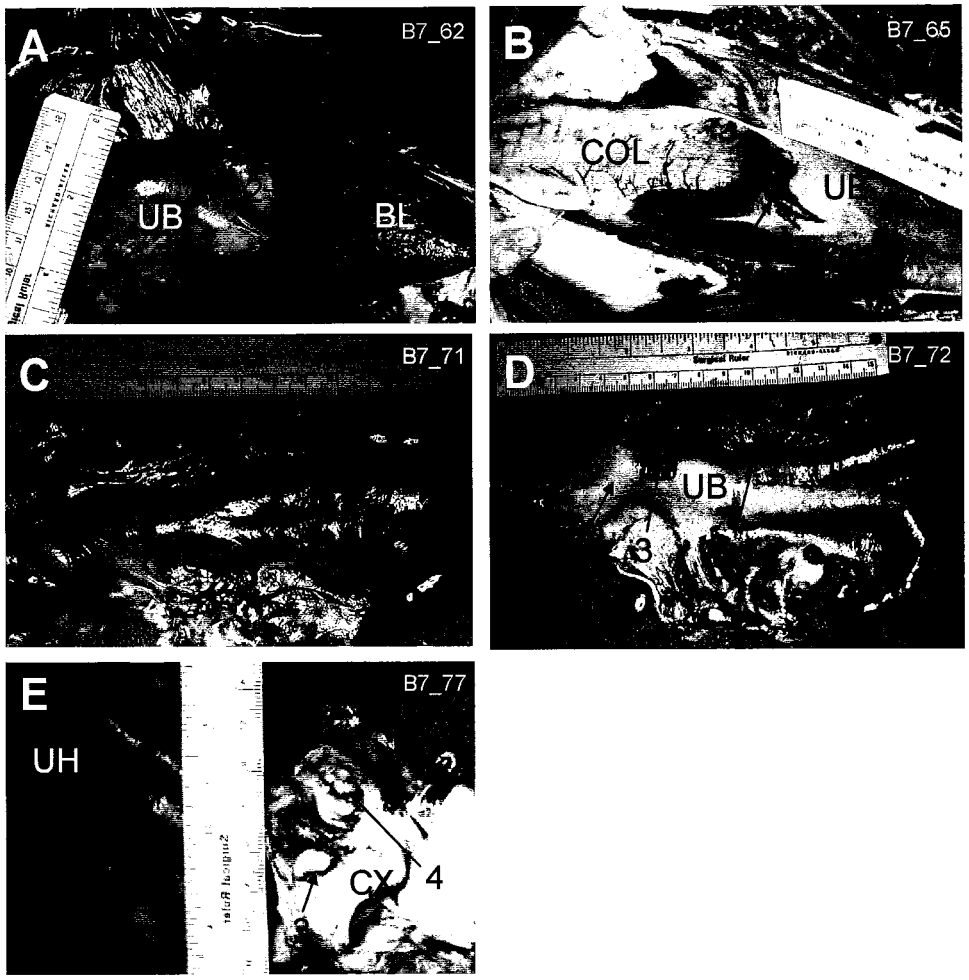

Figure 8.12 Sheep B dissection photographs

Figure 8.13A shows a region intended for treatment (2) discovered on the uterine body (UB). There was no damage to the vaginal wall (V), ovaries (OV), bladder (BL) or uterine horn (UH). The treated area was characteristic of coagulative necrosis, with a white necrotic area surrounded by a ring of red. A close up view of the treated region (2) is depicted in Figure 8.13B. Upon cutting open the uterine body, the treated region (2) varied in depth, and part of the lesion extended through the myometrium into the inner surface of the uterine body (Figure 8.13C). Figure 8.13D shows there was no other damage to the uterine body, cervix (CX) or uterine horns (UH).

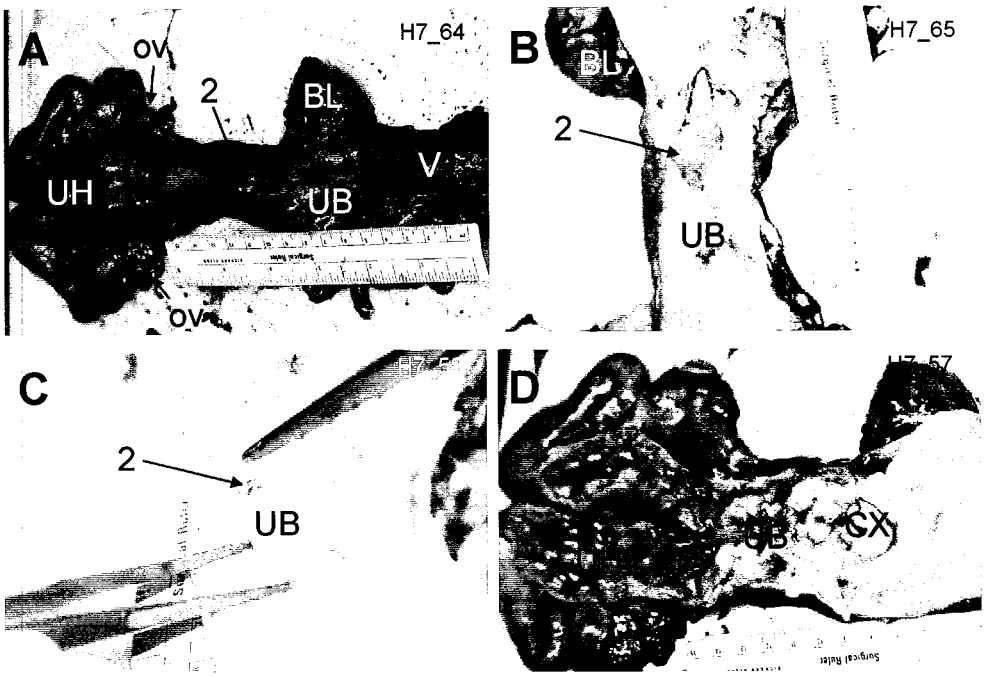

Figure 8.13 Sheep H dissection photographs

8.6.4 Sheep E and F: 30 day survival

Images from sheep E and sheep F dissection are shown in Figure 8.14 and Figure 8.15, respectively.

Figure 8.14A shows that upon dissection of the vaginal canal and uterus, there were no signs of adverse effects due to treatment. The uterine horns (UH), uterine body (UB), vaginal canal (V), ovaries (OV) and bladder (BL) all appeared normal when the uterus was opened. No damage or adverse effects internally to these structures were revealed (Figure 8.14B). Figure 8.14C shows an enlarged and hardened lymph node that was found. The lymph node measured approximately 20 mm in length and 10 mm in diameter. It was uncertain whether the HIFU treatment and/or the healing process of the treated region caused the enlarged lymphnode. Figure 8.14D shows that there was no damage to the colon (CO). The only indication of treatment is shown in Figure 8.14E. A small spot of blood congestion (1) approximately 1.5 mm in diameter was discovered on the inner surface of the uterine body (UB) near the cervix (CX). This was a remnant of a

HIFU treated area and was red in color. There was no sign of necrotic white tissue as shown in fresh lesions. Finally, upon closer examination of the cervix (CX), it was noted that one lobe (L) of the cervix was smaller and more red in color compared to other lobes on this cervix and other cervices (Figure 8.14F). It was uncertain whether this was due to HIFU or simply a natural occurrence in this particular animal.

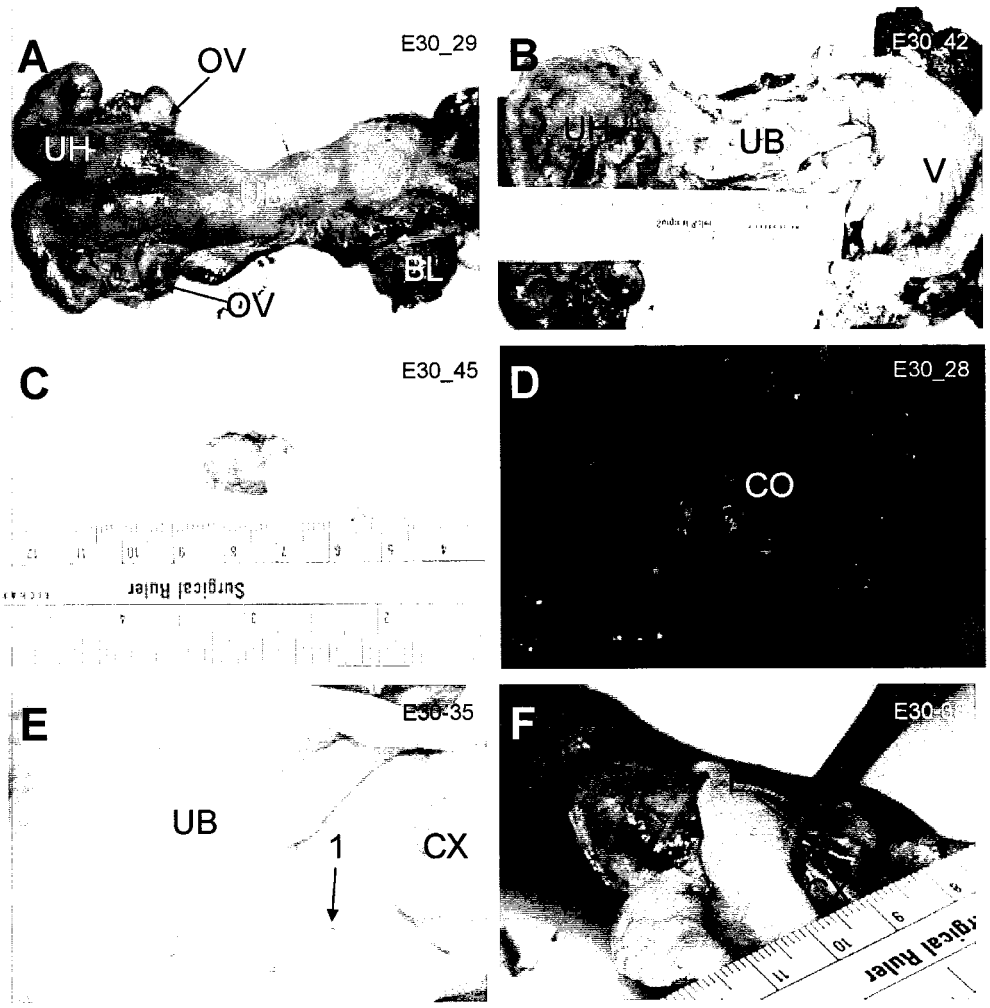

Figure 8.14 Sheep E dissection photographs

Figure 8.15A shows a small surface lesion (1) seen on the uterus body. This lesion was a small red dot approximately 3 mm in diameter. There was again no white necrosed area observed in the lesion. There was no damage to the vagina (V), bladder (B), ovaries (OV) or uterine horns (UH). A close-up view of the lesion on the uterine body is shown in Figure 8.15B. Upon opening the uterine body (UB), there was no damage in the cervical region (CX) (Figure 8.15C). Finally, Figure 8.15D shows that there was no damage to the colon (CO).

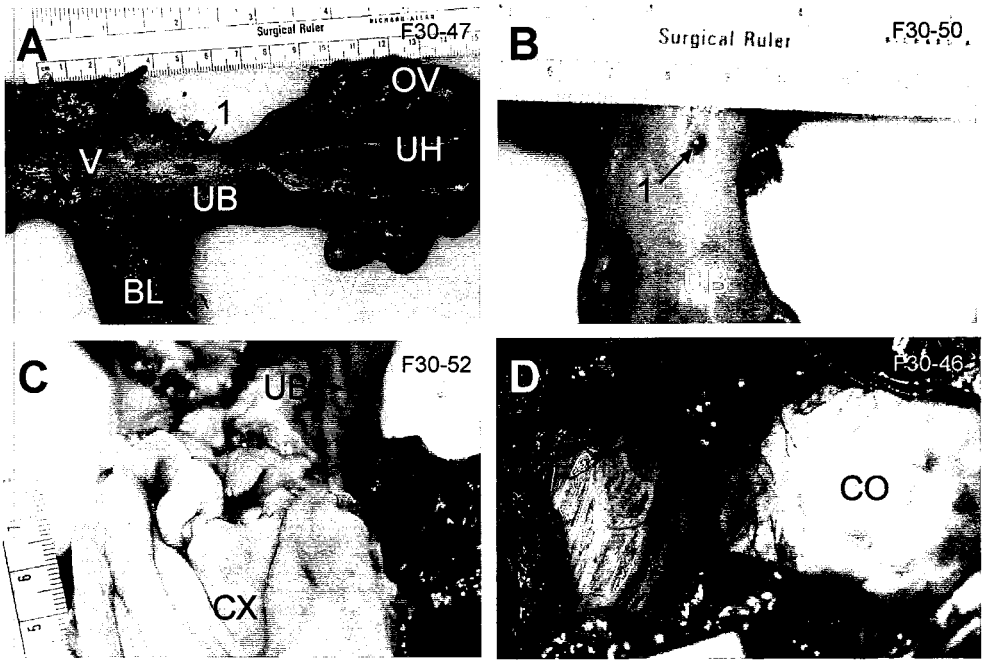

Figure 8.15 Sheep F dissection photographs

8.7 RESULTS: QUANTITATIVE LESION ANALYSIS, GROSS EXAMINATION

8.7.1 Lesion volumes at various post-treatment times

From the measurement methods described in section 8.3.3, lesion volumes are listed in Table 8.4 and graphed in Figure 8.16. The affected volume was the sum of the necrosed and congestion volumes. The percent necrosis was calculated using Eq. 8.2.

Eq. 8.2 $$\%necrosis = \frac{necrotic\_volume}{affected\_volume}(100\%)$$

The necrotic and blood congestion volumes were very similar (within 6 %) between animals at each time point since the treatment dosages were statistically similar as discussed in section 8.4. Furthermore, the percent of the lesion that was necrotic was similar between animals at each time point.

Table 8.4 Sheep uterus HIFU treated lesion volumes

Euthanasia time	Subject	Necrosed volume mm^3	Congestion volume mm^3	Affected volume mm^3	Percent necrosis
0 day	A	27.87	75.70	103.57	27
	G	48.54	100.13	148.67	33
2 days	C	85.61	330.52	416.13	21
	D (col*)	93.35	427.21	520.55	18
7 days	B	931.94	442.52	1374.46	68
	H (col*)	841.36	467.06	1308.42	64
30 days	E	0.00	2.04	2.04	0
	F	0.00	2.24	2.24	0

(col) measurement included the treated colon.*

The data in Table 8.4 is graphed in Figure 8.16a. The necrotic volume increased in size from day 1 to 7. Within the first two days, the rate of blood congestion volume increase appeared to be greater than the necrotic area. However, congestion growth appeared to decline after day 2, while necrotic growth increased. This was inferred to being a result of the inflamed area becoming necrosed, along with areas of capillary and vasculature ablation surrounding the lesion also becoming necrosed. By day 30, there was no necrotic tissue left, only a small spot of blood congestion. Figure 8.16b shows volumes of necrotic, blood congestion, and total affected tissue in the first 7 days. Figure 8.16c shows how the ratio of necrotic tissue to total affected area varied at each time point. These results suggest that the blood surrounding the treatment area became more congested within the first two days post-treatment, and then the entire affected area becomes necrotic.

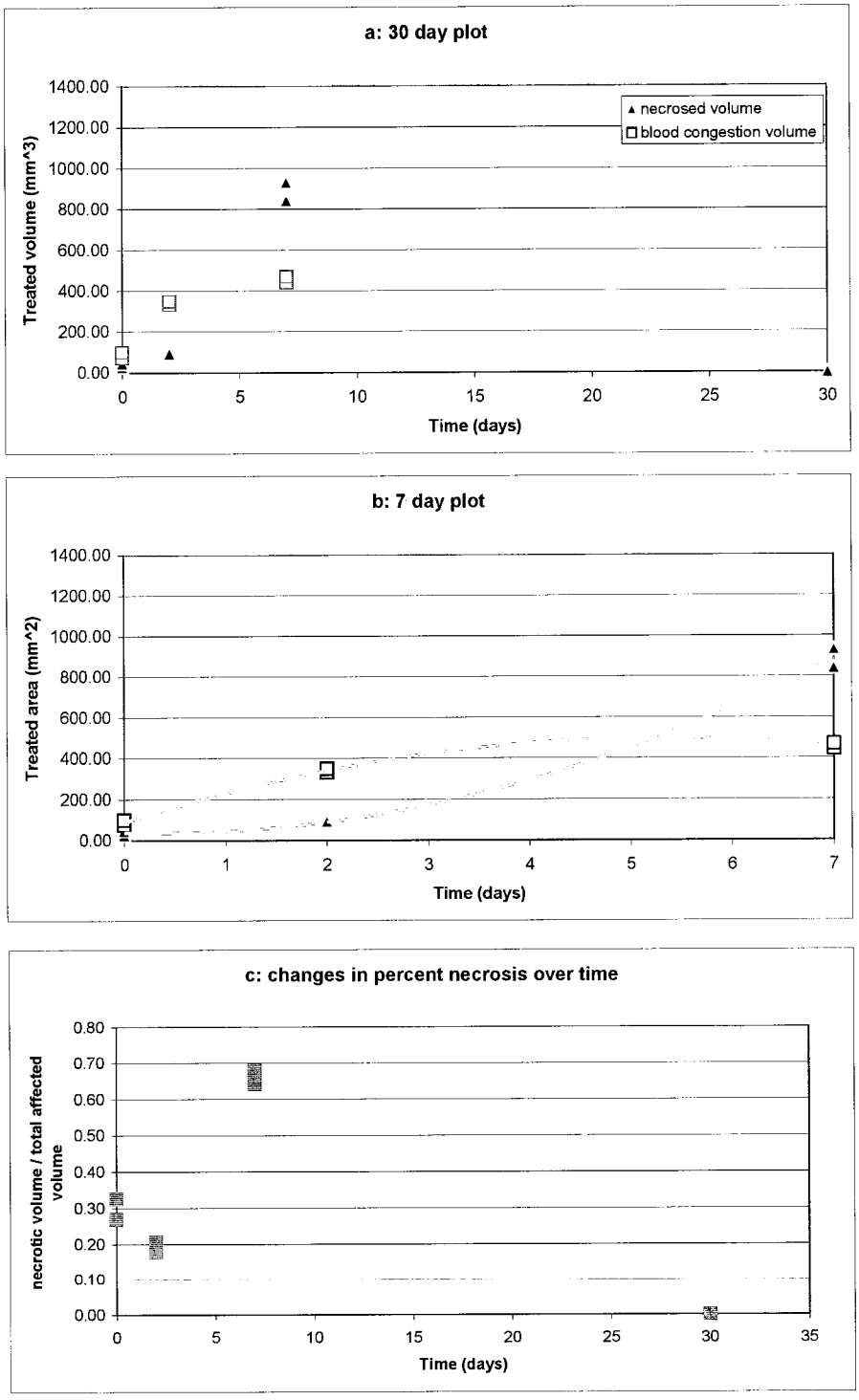

Figure 8.16 Lesion volume quantification. A: changes in lesion volume over 30 day study period, B: changes in lesion volume over first 7 days, C: changes in percent necrosis over 30 days.

8.7.2 Comparison to other studies

HIFU lesions formed in the uterus were similar to HIFU lesions formed *in vivo* in other tissue types. Similar to the findings in this study, HIFU treated testis, liver, kidney and solid malignancies have also displayed lesions with necrotic centers surrounded by blood congestion, and histological analysis has revealed nuclei disappearance, blood vessel wall disruption and blood congestion (Madersbacher, Pedevilla et al. 1995; Madersbacher, Kratzik et al. 1998; Daum, Smith et al. 1999; Wu, Chen et al. 2001). In these studies, there were also sharp demarcations between treated and untreated areas, as noted in our lesions. In a study of *in vivo* treatment of rat and rabbit liver and kidney, Linke et al. showed a similar trend to our study in the lesion size over time. The size of the affected volume more than doubled three days after treatment, and then diminished (Linke, Carstensen et al. 1973). Scar tissue formation as a result of HIFU lesion healing has also been noted in previous studies (Linke, Carstensen et al. 1973; Sibille, Prat et al. 1993).

8.7.3 Insight into fibroids treatment

The intended application for the image-guided transvaginal HIFU device is the treatment of submucosal fibroids. Although these are less common than intramural fibroids (Stewart 2001), they are the smallest (usually pea sized, 0.5 to 2 cm in diameter, not exceeding 4 to 5 cm) and most symptomatic. This study has shown that five 10 second treatments (or a total time of 350 seconds including 60 seconds of "off-time" between treatments) resulted in an average treated volume of 126.1 mm^3. Therefore, the rate of treatment was 0.36 mm^3 per second and the volume treated per ten-second lesion was 25.2 mm^3. The total number of lesions required for a 1 cm diameter fibroid (524 mm^3) would be 21 lesions, resulting in a treatment time of approximately 24 minutes. However, the majority of this time would consist of "off-time" used for repositioning the HIFU focus and transducer cooling. The total treatment time could be decreased by reducing "off-time". This reduction in "off-time" can be accomplished by using a mechanical or computer controlled positioning device as well as by enhancing cooling. Cooling may be enhanced using circulated water at higher rates or lower temperatures, although the latter may result in patient discomfort. Finding novel methods of increasing the transducer efficiency will also result in less heat generated during treatment resulting in a decrease

in "off-time". Furthermore, fibroid tissue has a higher acoustic absorption coefficient (Keshavarzi et al., 2001) meaning more HIFU energy would be absorbed by the fibroids than by the sheep uterus uterus treated in this study. Therefore, the treatment time required for fibroids should be less than sheep uterus. For comparison, Hynynen et al. showed that treating a 2 cm lesion in breast fibroadenoma took approximately 2 hours using 10 second treatment times and 50 second off-times between treatments at 28-50 W of acoustic power (Hynynen, Pomeroy et al. 2001). As shown by Wu et al., it may often be desirable to treat a volume that includes tissue adjacent to the fibroid to ensure that all tumor cells are eliminated, which would actually increase treatment time (Wu, Chen et al. 2001). The treatment of a volume beyond the fibroids should therefore be considered when estimating treatment times.

Researchers have shown that a tumor volume can be treated by applying a series of overlapping lesions, with appropriate delay times between sonications, to avoid heating between the transducer and the focus (near-field heating) (Damianou and Hynynen 1993; Hill, Rivens et al. 1994; Fan and Hynynen 1996; Arefiev, Prat et al. 1998; McDannold, Jolesz et al. 1999). In one study, it was shown that significant delays (>20s) between sonications must be introduced to avoid unwanted tissue damage in front of the focal zone (Damianou and Hynynen 1993). Also, a decreased pulse duration and F-number close to 1 reduced temperature build-up in front of the focus (Damianou and Hynynen 1993). In another study, burst pulses shorter than 20 ms and repetition periods shorter than 0.5 s resulted in lesions in intermediate tissues and at the surface of the tissue sample (Barkman, Almquist et al. 1999). For burst signals with duration and repetition period longer than above mentioned values, localized lesions resulted at focus (Barkman, Almquist et al. 1999). However, the exposure duration of each lesion (to ensure sufficient heating, and determine lesion size) and the cooling time required between treatments are transducer and tissue-specific, and need to be optimized for each treatment. It would be of interest to develop treatment planning software that allows the number of lesions, optimal treatment times and HIFU intensities to be calculated based on fibroid shape and size.

Treating larger fibroids will take a longer period of time, but the reduced risk of surgical complications may still make this procedure appealing. HIFU has also been shown effective in occluding blood vessels (Vaezy, Martin et al. 1998). Therefore, larger fibroids may be more effectively ablated via HIFU treatment of fibroid vessels, similar to the uterine artery embolisation concept. By ablating the vasculature feeding the fibroid with HIFU, the fibroid may eventually shrink due to lack of blood flow and nutrients.

8.8 HISTOPATHOLOGY ANALYSIS

8.8.1 Introduction

A goal of the survival study was to evaluate the pathological changes of HIFU treated sheep uterus tissue over time. This section provides an analysis of the hematoxlin and eosin stained slides from different areas of the dissected uteri used in this study. First, an overview of the sheep uterine structure and a comparison to a human uterus from a microscopic perspective will be presented. Second, tissue samples that received varying amounts of HIFU treatment will be compared. Next, the morphology of the HIFU treated tissue over time will be explored. Finally, the accidentally damaged vaginal cavity (sheep A) and colon (sheep D and H) will be investigated.

8.8.2 Sheep and human uterine tissue

The structure of sheep and human uterus is very similar, as shown in Figure 8.17 from a microscopic viewpoint. The uterus is composed of two main layers: (1) the endometrium (a mucus membrane) and (2) the myometrium (smooth muscle layer). The endometrium consists of a columnar epithelial lining, from which numerous uterine glands (G) extend. The glands secrete mucus, glycogen, proteins, and lipids. The lining itself is comprised of endometrial stroma. The remainder of the endometrial tissue is loose connective tissue. The myometrium is comprised of smooth muscle fibers which appear as interlacing bundles. These bundles are mostly parallel, but may be oriented randomly to allow the uterus to stretch in different directions. Coiled arteries located throughout the uterus (A) have lumens surrounded by a boundary of smooth muscle cells. The thickness of the endometrium and myometrium in humans is approximately 0.15 cm and 3 cm respectively (source: Virtual Hospital, University of Iowa). In sheep, the thickness of the

endometrium and myometrium was measured in our samples (n=5) to have a mean value of 0.04 cm and 0.7 cm respectively.

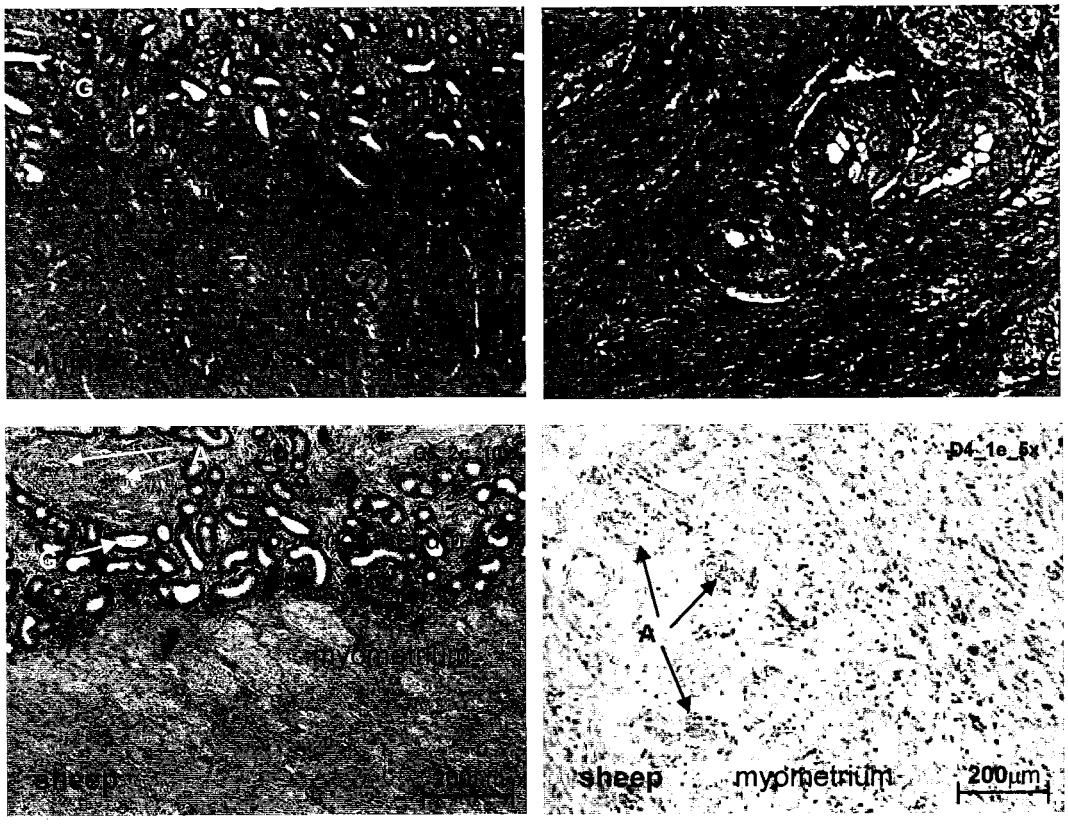

Figure 8.17 Comparison of normal, untreated human and sheep uterus tissue, normal. Human uterus images obtained from the College of Medicine, University of Illinois at Urbana-Champaign. A: coiled arteries have lumens surrounded by smooth muscle cells.

8.8.3 Levels of HIFU effects

The degree of HIFU induced damage on a microscopic scale varied corresponding to the HIFU intensity at a particular location. These differences were distinguished using the following classifications:

- Class 1 - Normal and viable. Smooth muscle cells were neatly bundled and nuclei were abundant. Blood vessels and glandular structures were intact with vessel and gland walls visible and distinguishable.

- Class 2 - Primarily thermal. Areas that received primary HIFU thermal damage appear structurally organized and intact. However, missing nuclei was indicative of necrotic tissue. Thermal effects lead to an inflammatory response and damaged blood vessels.

- Class 3 - Thermal and minor cavitation. Areas that received minor effects of cavitation showed more spacing between smooth muscle bundles in addition to lack of nuclei. Damaged blood vessels leading to blood congestion were apparent.

- Class 4 - Major cavitation. Areas that were subjected to a higher degree of cavitation showed pronounced smooth muscle bundle separation, large areas of blood congestion, and no nuclei.

The four classes of HIFU disruption are illustrated in Figure 8.18. Figure 8.18a shows normal untreated tissue. Glands (G) and blood vessels (B) were well defined and protective membranes were distinguishable. Smooth muscle (SM) was organized in bundles, and nuclei was seen throughout the region. Figure 8.18b shows a class 2 region. Nuclei were noticeably absent from the tissue. The smooth muscle still appeared in bundles although the tissue appeared inflamed between the muscle bundles. Figure 8.18c shows a transition from class 2 to class 3. The class 2 region has blood vessels that were still intact (A). The surrounding smooth muscle in this region was lacking nuclei. The Class 3 region shows blood vessel walls (comprised of endothelial cells) damaged and thus vessels less defined (B). There was an onset of smooth muscle bundle disruption and separation. Figure 8.18d shows the transition between classes 2, 3 and 4. The smooth muscle became more and more separated, and blood vessels were less defined (B). Figure 8.18e shows a class 4 region. The smooth muscle was highly separated, and blood congestion (C) was visible throughout the region. Figure 8.18f shows a close up view of the highly disrupted smooth muscle in a severely affected class 4 region.

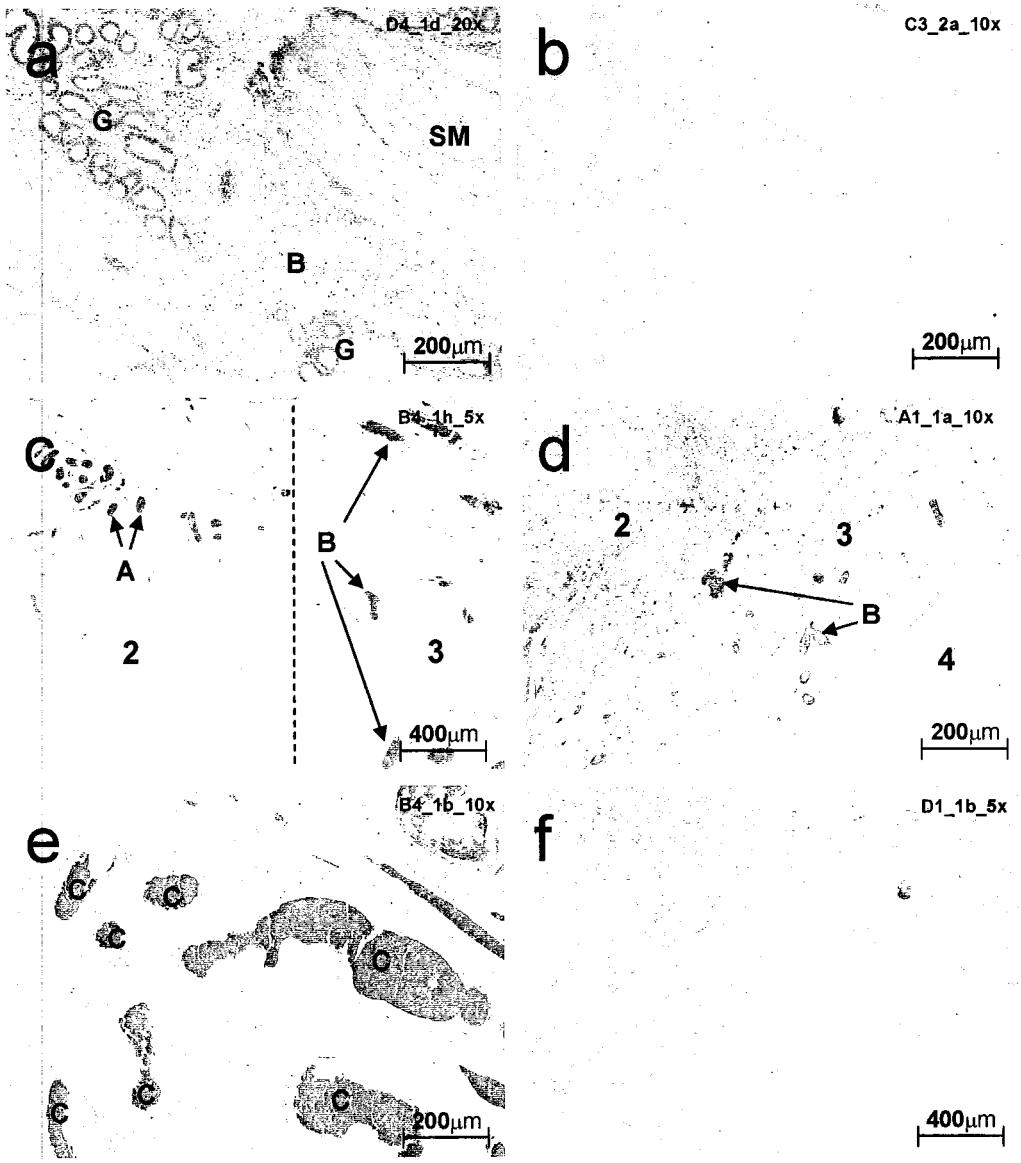

Figure 8.18 Different degrees of HIFU affected uterus tissue. (a) normal untreated tissue (b) primarily thermal effects (c) transition from thermal to minor cavitation effects (d) transition from thermal to minor and major cavitation effects (e) major cavitation effects (f) major cavitation effects at higher magnification

8.8.4 *Progression of HIFU treated area*

The microscopic changes observed over time are presented in this section. The progression of histological changes, from initial treatment to tissue healing, are shown in Figure 8.19. Initially, thermal and cavitation effects (described in the previous section) were present and the tissue affected by HIFU was necrotic. By day 2, inflammatory cells infiltrated the affected region, and perivascular cuffing was apparent. The inflammatory cells were most likely neutrophils which migrate into the affected region shortly after treatment. Perivascular cuffing is a common pattern of lymphocytic infiltration in chronic inflammmatory reactions. Lymphocytes emerged from the circulating blood mostly through the walls of small venules and tended to aggregate around the vessels. By day 7, some neutrophils were still present although the majority underwent apoptosis. Macrophages, another type of inflammatory cell, were seen phagocytosing necrotic tissue. Smooth muscle began to generate in small bundles. At day 30, many smooth muscle bundles were restored and surrounded by scar tissue. Scar tissue, primarily composed of collagen, was less cellularized and had fewer nuclei than smooth muscle.

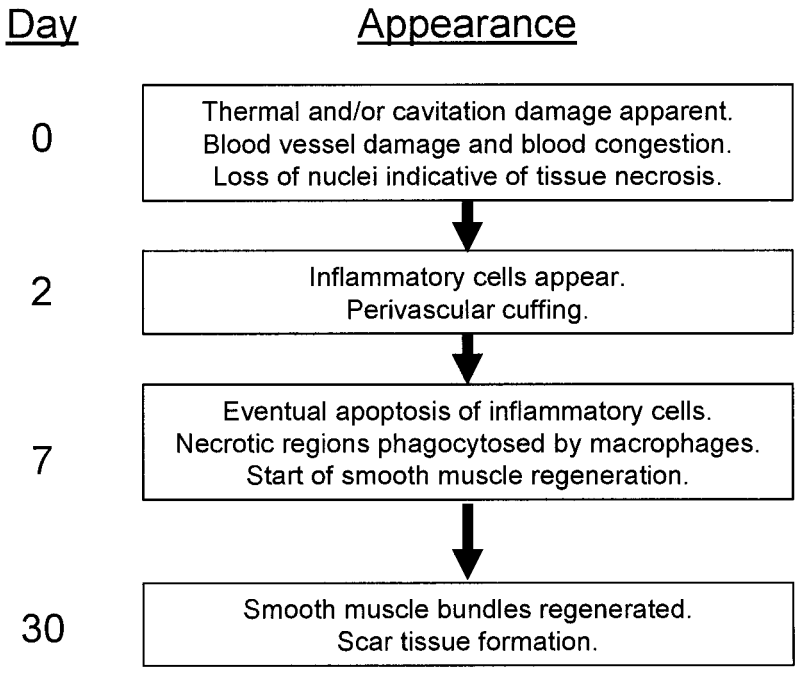

Figure 8.19 Progression of HIFU affected area

Figure 8.20a and b are images from dissected sheep uterus extracted immediately after treatment. Both images show cavitation and thermally affected areas lacking nuclei, indicative of necrosis. In Figure 8.20a, a transition zone between normal and HIFU treatment can be seen. Normal organized bundles of smooth muscle fibers and viable cells can be seen in the primarily normal region (1). Pockets of blood congestion and separated smooth muscle bundles are shown in region (2). Finally, gross smooth muscle disruption, cell death (indicated by the absence of nuclei) and scattered cellular fragments are seen in areas most affected by HIFU (3). Figure 8.20 b shows disrupted and separated smooth muscle due to HIFU induced cavitation along with the absence of nuclei.

Figure 8.20c and d are images from dissected uterus 2 days after treatment. In Figure 8.20c, the infiltration of inflammatory cells (neutrophils) and perivascular cuffing (p) surrounding damaged blood vessels and areas of blood congestion can be seen. The region affected by cavitation shows smooth muscle disruption (2) whereas the region affected primarily by HIFU thermal effects has relatively intact smooth muscle bundles (1). Figure 8.20d shows a close up view of neutrophils (arrows) in an area affected by HIFU treatment, which are characterized by the lopsided clump-like nuclei.

Figure 8.21a and b are images from sheep uterus dissected 7 days after treatment. Figure 8.21a shows a large quantity and macrophages scattered throughout the region and smooth muscle fiber bundles starting to be repaired (r). Macrophages, which appeared as dark dots on the image (arrows) phagocytosed necrotic smooth muscle fibers. Perivascular cuffing was still seen at times (p). Remnants of blood vessels (b) were seen as shriveled and collapsed structures. The tissue in Figure 8.21b was primarily affected by thermal effects. As a result, there was less smooth muscle separation, and tissue repair was at a further stage than the sample in Figure 8.21a.

Figure 8.21c and d show dissected uterus 30 days after treatment. Both figures show smooth muscle fibers repaired within scar tissue. One such bundle is outlined to differentiate from the surrounding scar tissue. The scar tissue was primarily composed of collagen and has fewer nuclei than the smooth muscle bundles. The ratio of smooth muscle to scar tissue appeared to be inversely proportional to the extent of HIFU damage to the region. Blood vessel walls also appeared to have been repaired, although the vessel lumens still appear collapsed (b).

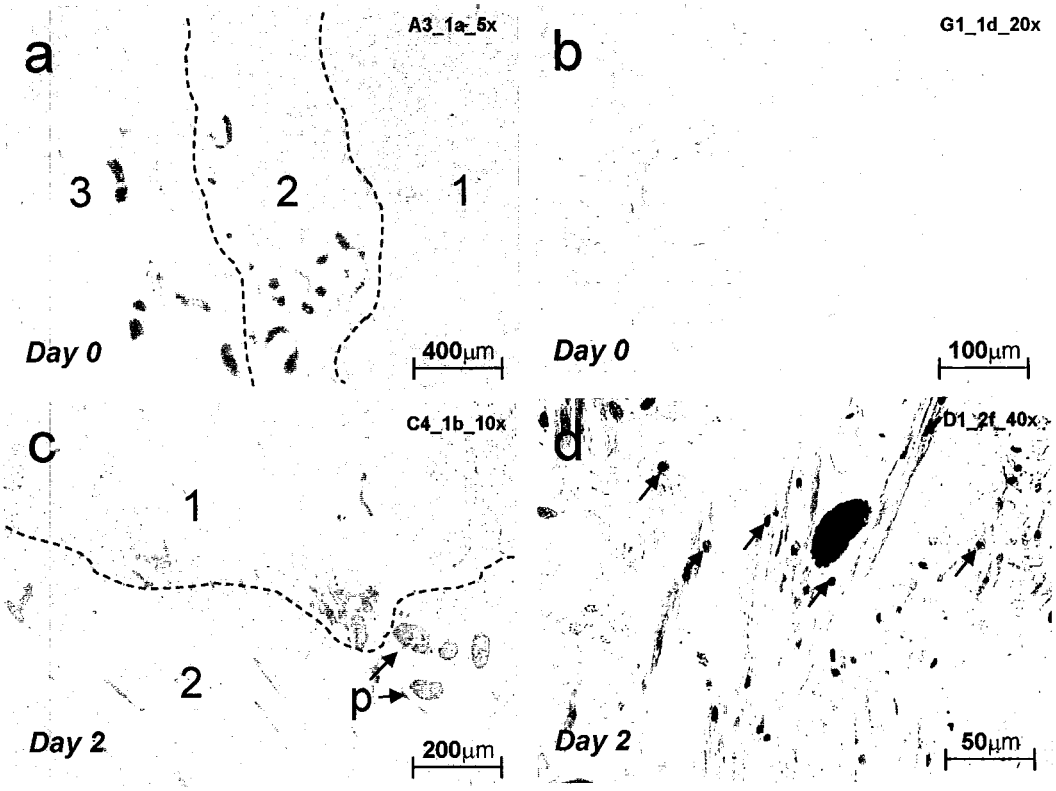

Figure 8.20 Images taken from post treatment uterus immediately after treatment (a and b) and 2 days after treatment (c and d)

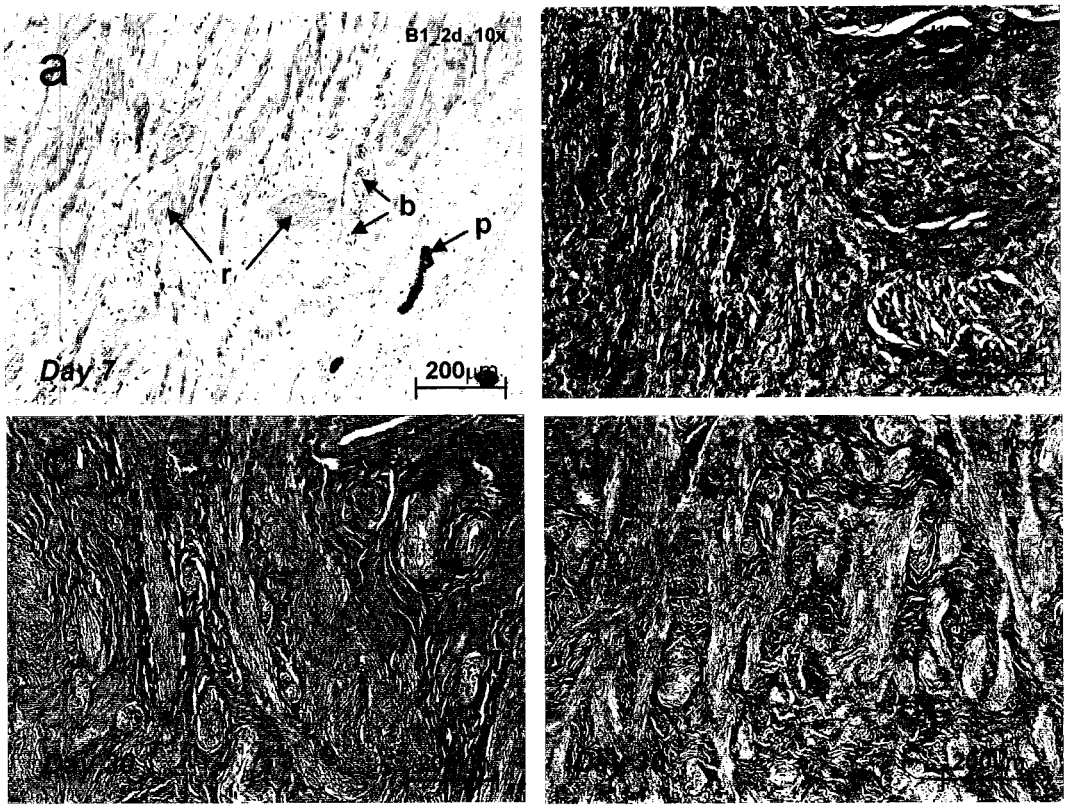

Figure 8.21 Images taken from post treatment uterus 7 days after treatment (a and b) and 30 days after treatment (c and d)

8.8.5 *Evaluation of treatment complications*

The histology of thermally damaged vaginal cavity tissue and treated colon was performed. The affected area of the vaginal cavity was primary in the submucosal layer, the second most superficial layer of the vagina. The submucosa contained an abundance of connective tissue and a few capillaries. Figure 8.22a shows normal vaginal submucosa tissue, and Figure 8.22b shows treated submucosa tissue. The treated submucosa lacked nuclei, indicative of thermally induced tissue necrosis.

Figure 8.23a shows normal colon tissue. The transition between normal colon and HIFU damaged colon after 2 days is shown in Figure 8.23b. The normal colon was comprised of organized bundles of tissue. The treated colon was highly disrupted with few nuclei, and inflammatory cells were present. Figure 8.23c represents HIFU induced colon damage as shown by capillary and tissue disruption, as well as pools of congested blood. This damage indicates that the colon may have experienced cavitation induced damage. Nuclei were considerably less abundant in the treated region and damage to the epithelial layer can be seen. Glands were constricted and blood congestion and pooling was frequent. Figure 8.23d shows treated colon tissue with primarily cavitation effects. HIFU induced cavitation damage was shown again by capillary and tissue disruption, and pools of congested blood. There were a lot fewer nuclei in the treated region, and inflammatory cells can be seen.

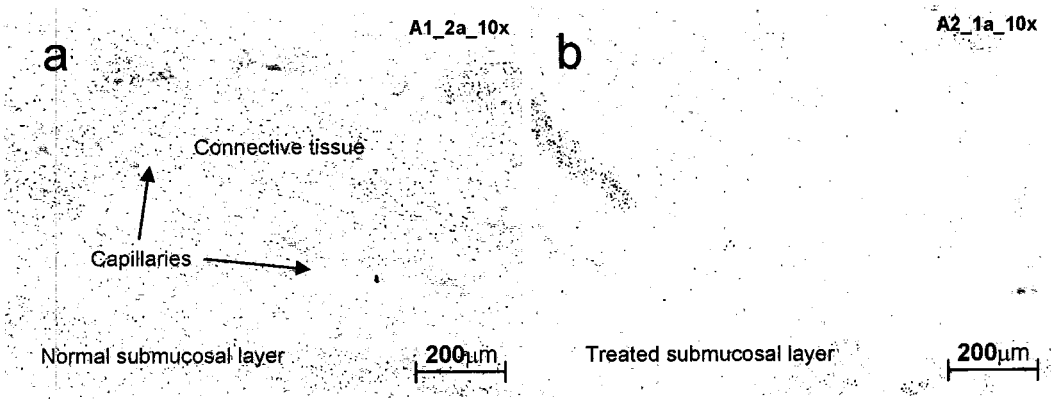

Figure 8.22 (a) Normal vaginal wall tissue shows abundant nuclei (b) Vaginal wall that experienced HIFU induced thermal damage shows fewer nuclei.

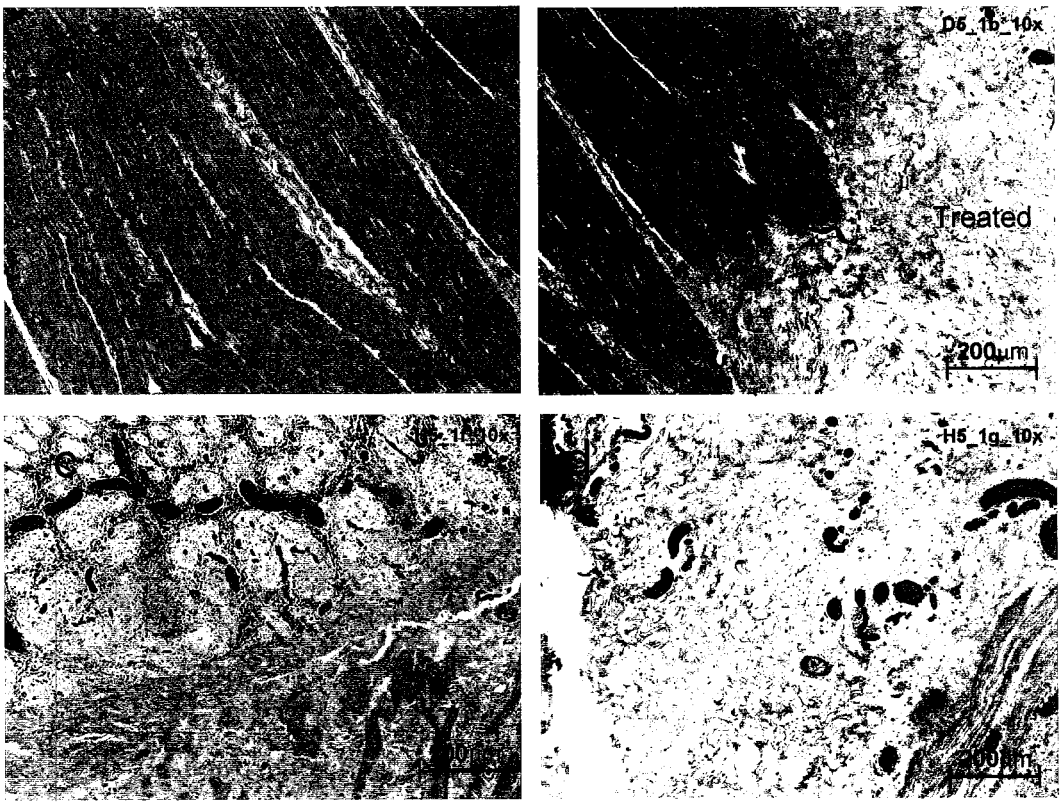

Figure 8.23 (a) Normal colon tissue shows organized bundles of tissue (b) HIFU treated colon shows disrupted tissue bundles and the presence of inflammatory cells (c) Blood pooling in HIFU treated colon (d) Blood pooling and tissue disruption was prominent in cavitation affected region of the HIFU treated colon.

8.8.6 Conclusions

A microscopic analysis of the uterus examined the histology of HIFU treated tissue. Tissue affected by varying degrees of HIFU showed differences in morphology. Tissue affected primarily by thermal effects showed cellular necrosis indicated by the lack of nuclei. Areas subjected to cavitation effects showed vessel wall endothelial cell damage resulting in blood congestion, along with smooth muscle disruption. The normally organized smooth muscle bundles became disorganized and separated. Over time, changes in the HIFU treated area were observed. After 2 days, there was an infiltration of neutrophils, which were inflammatory cells with lopsided nuclei. The appearance of neutrophils was an expected event following the acute injury to the tissue caused by HIFU. By day 7, the neutrophils underwent apoptosis, and macrophages became more apparent. The macrophages phagocytosed apoptotic neutrophils and necrotic smooth muscle tissues. At this time, smooth muscle regeneration was also seen. By day 30, the treated area had healed and collagenous scar tissue and regenerated smooth muscle bundles were visible.

For future histological analyses of HIFU treated uteri, various stains should be used to render tissue changes more visible. For example, vessel disruption would be more visible using a C31 or pecam-1 stain which marks the endothelial cells surrounding blood vessels. This would be useful for determining which vessels were intact, and which were damaged due to HIFU. The presence of macrophages could be confirmed by using macrophage specific stains such as BM8 (generally for mature macrophages), and anti-mac-3. Finally, a trichrome stain would allow the contrast between collagen (scar) tissue and smooth muscle to be more distinguishable.

9.0 CHAPTER 9 ANALYSIS OF LESION VISUALIZATION WITH ULTRASOUND

9.1 INTRODUCTION

The device presented in this thesis used ultrasound image-guidance for treatment planning, targeting, and verification. The merits of ultrasound image-guidance are outlined in section 2.9.1. Treatment planning and targeting have been successful as discussed in Chapter 7. The ability to visualize the formation of a lesion in the presence of HIFU is important for ultrasound image-guidance. In this chapter, the repeatability of hyperechoic spot formation, visibility of HIFU lesions, and consistency of lesion appearance on the ultrasound image will be investigated.

9.2 LESION VISUALIZATION STUDY

9.2.1 Methods and Materials

Lesions formed *in vitro* in a gel phantom and in turkey breast tissue (during testing of HITS), along with lesions formed *in vivo* during the sheep experiment, were recorded using a screen capture utility (SnagIt Video Capture, Techsmith, Okemos, MI) and evaluated in three separate studies to determine the following:

- The probability that the lesion will appear as a hyperechoic spot on the ultrasound image.
- Whether the brightness of the hyperechoic spot was related to the focal intensity applied during treatment.
- How the hyperechoic spot changes over time during and after the treatment.

9.2.1.1 In vitro apparatus

For the *in vitro* studies, a block of gel or a piece of turkey breast was suspended in a custom built holder submerged in a 20 x 20 x 40 cm glass tank filled with degassed distilled water at 37°C, exemplified in Figure 9.1. The device was also suspended in the tank and the image probe was set to a rotation of 0. The vertical separation between the image probe and the HIFU applicator was kept constant at 6 cm.

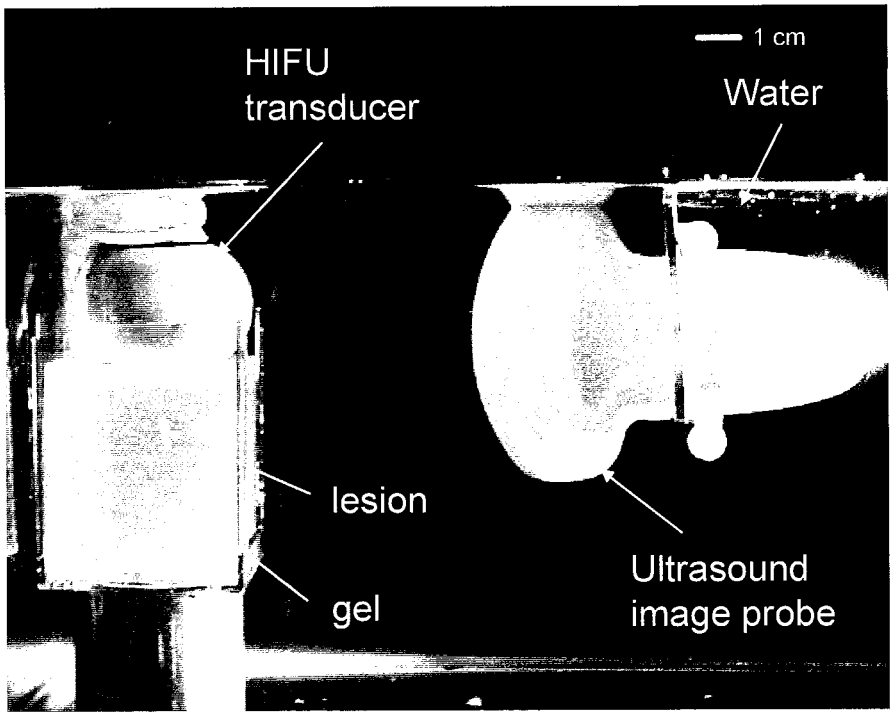

Figure 9.1 Apparatus for visualizing HIFU lesions formed in gel. The gel and the device were suspended in degassed distilled water such that the ultrasound image probe was 6 cm from the HIFU transducer and the HIFU transducer created lesions approximately 1-2 cm into the gel.

9.2.1.2 Lesion formation parameters: In vitro

Lesions were formed at four different depths in both gel and in turkey breast. The different depths were used to obtain different HIFU focal intensities as the HIFU applicator parameters were kept constant for the entire experiment. For all lesions, HIFU was operated at a frequency of 4.035 MHz using 40 W of acoustic power at a 50% duty cycle for 10 seconds. During treatment, water was circulated in the condom at a rate of 150 mL/min to simulate an *in vivo* treatment scenario. The focal intensity for each treatment was determined as described in section 2.14, using a HIFU applicator focal area of 0.00968 cm^2, the attenuation of gel as 0.0496 NP/cm (at 4.035 MHz), and the attenuation of turkey breast as 0.397 NP/cm (at 4.035 MHz). Ten lesions were created at each of the depths shown in Table 9.1 and Table 9.2. Since image analysis was performed on the captured images, the ultrasound imaging parameters were kept constant. The depth was kept constant at 14 cm, gain controls were kept at their factory set default settings, and the resolution setting on the SonoSite was set to "general" mode (for general purpose imaging versus "resolution" or "penetration"). The "resolution" mode optimizes the image area closest to the image probe, the "penetration" mode optimizes the deepest image area furthest from the image probe, and the "general" mode provides a resolution that is not optimized, but is suitable for all depths of imaging.

Table 9.1 Intensities at various depths in gel

Depth (cm)	Intensity (W/cm^2)	N=
0.5	3964	10
1.5	3590	10
2.5	3251	10
3.5	2943	10

Table 9.2 Intensities at various depths in turkey breast tissue

Depth (cm)	Intensity (W/cm^2)	N=
0.5	2801	10
1.5	1884	10
2.5	1266	10
3.5	852	10

9.2.1.3 Lesion formation parameters: In vivo

Due to the variations in anatomy and the difficulty of treating sheep uterus in the exact location, the treatment depths (and therefore intensities) varied between animals and lesions. The captured ultrasound images, were used to determine the depth into sheep uterus of each treatment attempted *in vivo*. Using a value of 0.2 NP/cm for the attenuation of sheep uterus (section 5.4.3.3) at 4.035 MHz, the focal intensities *in vivo* were determined. Table 9.3 shows the depths and intensities of all 40 lesions formed in the 8 sheep used in this study. The SonoSite gain controls were not kept constant during *in vivo* treatment since it was necessary for our sonographer to adjust the contrast and brightness in order to obtain a clear, well-defined ultrasound image of the pelvic structures and transducer..

Table 9.3 Intensities for in vivo lesions in sheep uterus

Depth (cm)	Intensity (W/cm^2)	Number of lesions
1.3	2477	3
1.4	2380	1
1.5	2287	2
1.6	2197	1
1.7	2111	3
1.8	2028	3
1.9	1949	5
2.0	1872	4
2.1	1799	6
2.2	1728	3
2.3	1660	1
2.4	1595	4
2.5	1532	2
2.7	1415	2

9.2.1.4 Characterizing lesion brightness

The method for obtaining and analyzing images from the ultrasound video capture is described here. First, the video capture from each treatment, from the time the HIFU was turned on (indicated by the interference on the screen) until 10 seconds after the HIFU was turned off, was imported into Adobe Premiere (Adobe Systems, San Jose, CA) for a total of 20 seconds. A frame was exported as a TIFF file every second of the video capture, from time 0 seconds until 20 seconds as exemplified in Figure 9.2. These 21 TIFF files, corresponding to one complete treatment, were then opened using ImageJ software (National Institutes of Health). The image showing the hyperechoic spot at its brightest was used to determine the location in pixel coordinates of the brightest pixel. The grayscale value of this brightest pixel was recorded at 1 second increments from time 0 seconds until 20 seconds.

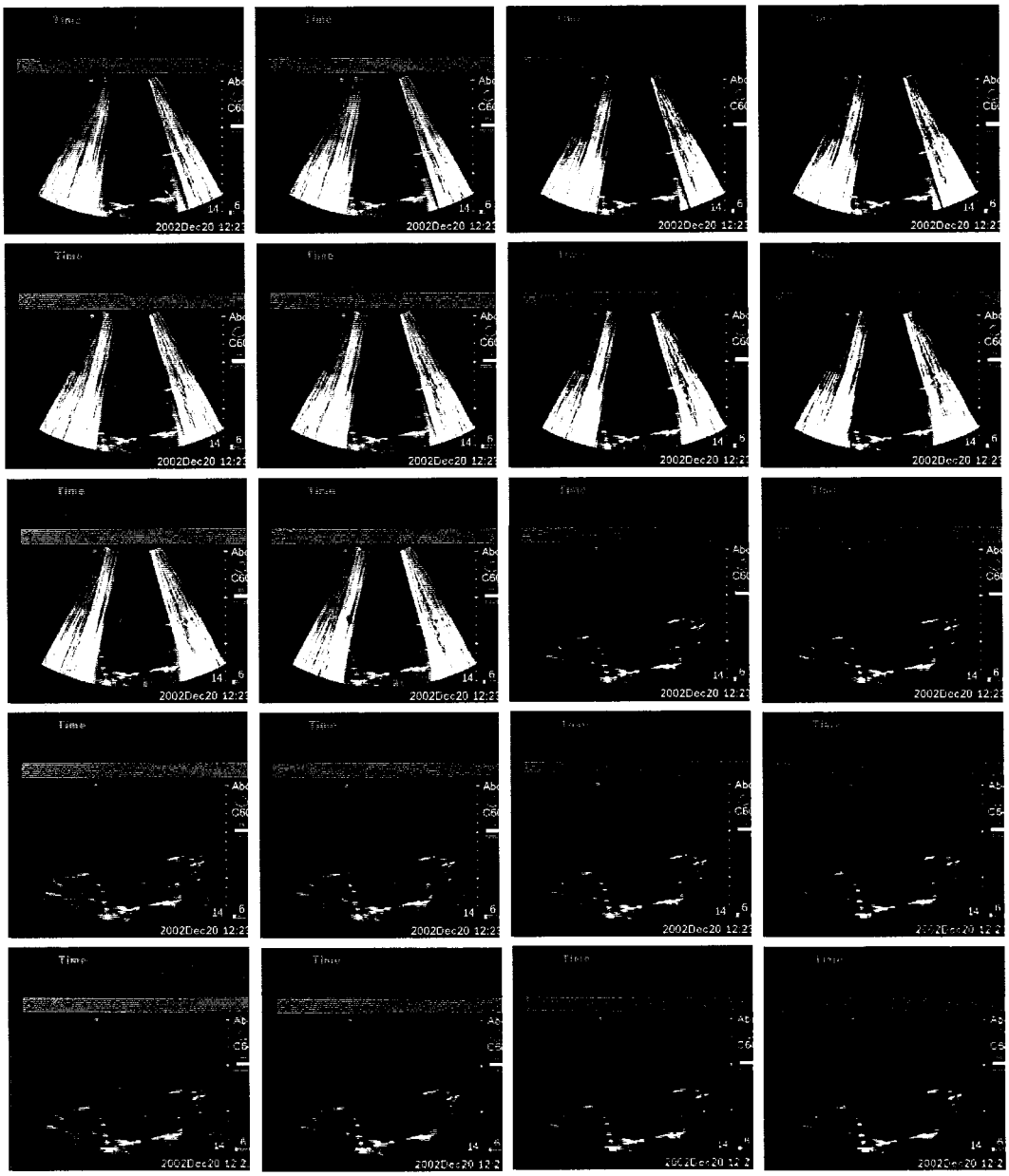

Figure 9.2 Images from each second of the video capture were obtained and the brightness of the hyperechoic spot in each image was determined

To account for the brightness of the entire hyperechoic spot, Adobe Photoshop (Adobe Systems Inc., San Jose, CA) was used to perform image subtraction between the image showing the hyperechoic spot at its brightest, usually immediately after HIFU treatment, and the image taken at time 0 seconds before HIFU was applied. The image showing the difference was used to determine the hyperechoic spot area (HSA), as shown in Figure 9.3. The average grayscale value of the HSA was recorded from 0 seconds until 20 seconds for every single lesion.

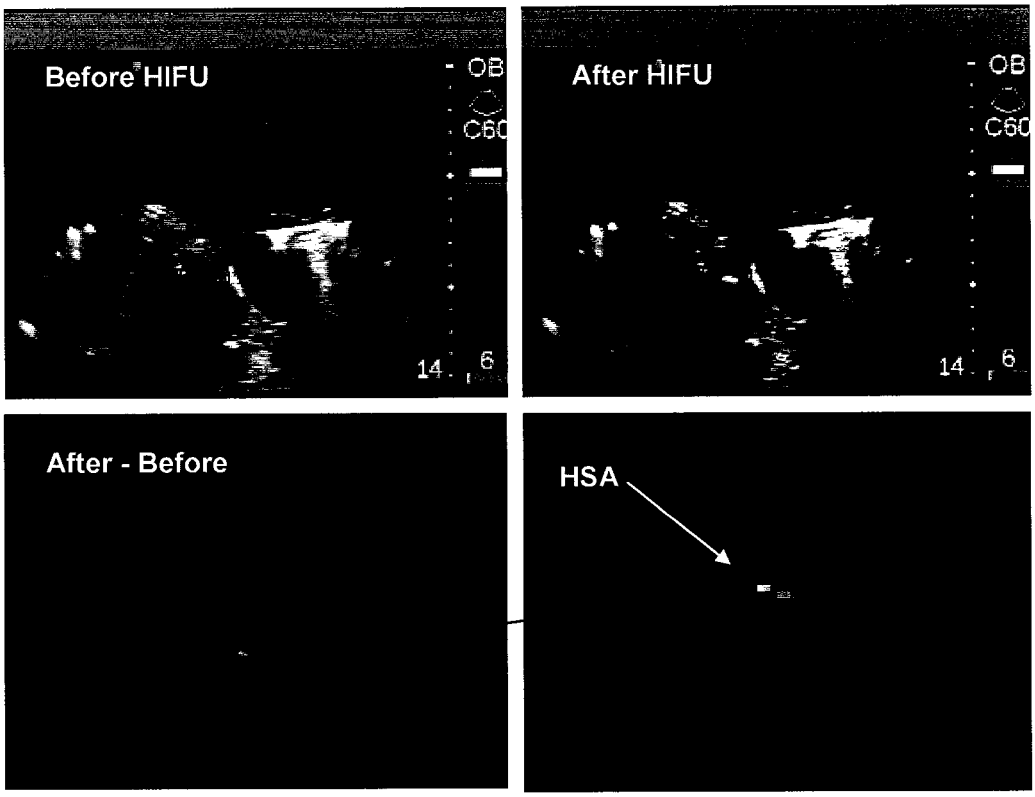

Figure 9.3 Defining the hyperechoic spot area (HSA) using image subtraction technique. The images show the formation of a hyperechoic spot in turkey breast tissue.

9.2.2 Results

9.2.2.1 Lesion visualization

Figure 9.4a shows the number of lesions attempted *in vitro*, in gel and in turkey breast, and the number of lesions that were visualized by ultrasound imaging. All the gel lesions were visible on the ultrasound image as hyperechoic spots. All the turkey breast lesions created using the two higher intensities were visualized also as hyperechoic spots. At 1266 W/cm^2, 80% of lesions were visualized and at 852 W/cm^2, only 40% were appeared as hyperechoic spots. This confirms the study in section 5.2.3 showing that there was a threshold intensity above which hyperechoic spots will appear consistently. These results also indicate that as the intensity falls below this threshold, the probability of visualizing treatment as a hyperechoic spot declines.

All the lesions attempted *in vivo* in sheep uterus were sorted into 6 intensity ranges, as shown in Figure 9.4b. This histogram shows the number of lesions attempted at each intensity range, and the number of lesions visualized as hyperechoic spots. Above 2200 W/cm^2, all lesions were visualized using ultrasound. As shown *in vitro*, the probability of visualizing the lesion decreases as the focal intensity decreases. It should be noted that for the *in vivo* case, it appears that the threshold intensity above which lesions will be visualized is higher than for the *in vitro* case. This is due to factors present *in vivo* that may affect the formation of a hyperechoic spot that is visible, including respiratory motion, perfusion, and tissue inhomogeneities.

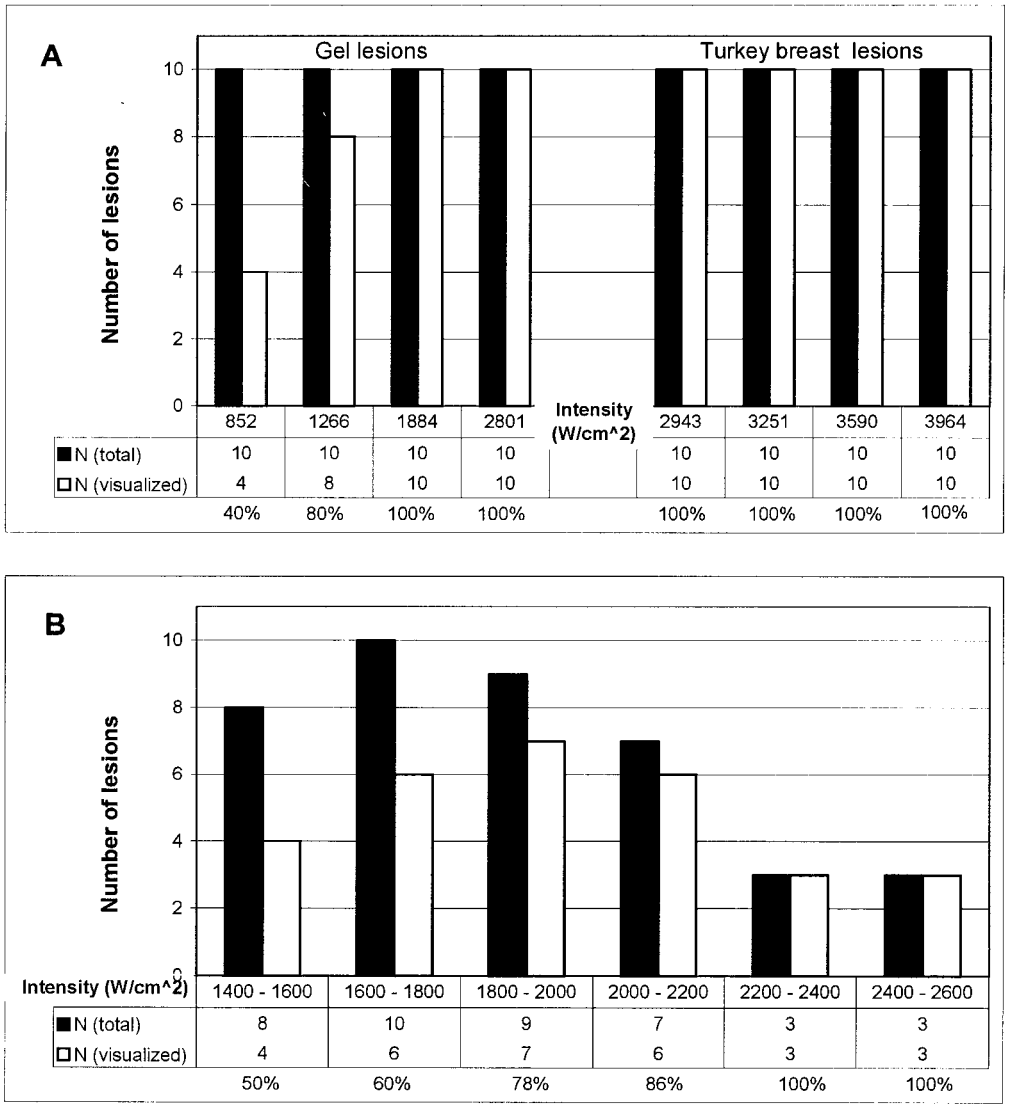

Figure 9.4 Number of lesions formed and visualized (A) in gel and turkey breast and (B) in sheep uterus

9.2.2.2 Hyperechoic spot brightness – spatial analysis

It was of interest to determine if the brightness of the hyperechoic spot was related to the treatment intensity. This study was intended to observe if hyperechoic spot brightness can be used as an indicator of HIFU dosimetry, along with size and shape, which were studied by Yuen et al. (Yuen 2001).

It was observed that the baseline grayscale value, or the brightness of the tissue without any HIFU treatment, was different between media. The baseline value was approximately 54 in gel and 63 in turkey breast. The baseline value was between 78-85 in sheep uterus (average of 81.5) since the gain controls on the SonoSite were not kept constant during sheep treatment. The visibility of a hyperechoic spot was not solely due to its brightness value, but also dependant on its contrast with surrounding tissue (difference between maximum brightness and baseline value). Therefore, lesions would be more visible in gel than they would be in sheep uterus given the same brightness value. To compensate for the difference in baseline values, the grayscale values of the hyperechoic spots were normalized by subtracting the baseline value from its brightness values.

Figure 9.5a shows the normalized grayscale value for the pixel with the maximum brightness for lesions formed in gel and turkey breast, as well as the average grayscale value over the HSA for each lesion, at the time of maximum brightness, for various intensities. These data points were averaged, as shown in Figure 9.5b, and linear regression was performed to determine the relationship between intensity and brightness.

The data indicated that there was a correlation between HIFU intensity and hyperechoic spot brightness. In gel, the normalized maximum brightness was 167 $\pm$ 4.5 and 187 $\pm$ 5.6 for spatial average temporal average focal intensities of 2943 and 3964 W/cm^2 respectively, with a linear correlation between intensity and brightness (R^2>0.99). There was a similar correlation between HSA average brightness values and focal intensities (R^2>0.99). However, the differences in brightness values were only significant ($p<0.05$) for a change in intensity of about 1000 W/cm^2, as shown by the error bars. These correlations were also present in the turkey breast lesions. In turkey breast, the normalized maximum brightness ranged from 129 $\pm$ 18.1 to 157 $\pm$ 13.0 for focal

intensities of 852 to 2801 W/cm^2 respectively. The variance between brightness values of lesions formed at the same intensity was much greater in turkey breast tissue than in gel. This may be due to tissue inhomogeneities and the presence of air bubbles in the tissue. The linear correlations were less than gel (R^2=0.9783, R^2=0.8964) for maximum and average brightness respectively, and the differences in brightness values were not statistically significant ($p>0.05$) over the intensity range (852 to 2801 W/cm^2) studied.

Figure 9.6 shows that *in vivo*, there was a greater variance in the brightness values for lesions created at a particular intensity range. This can be mainly attributed to the fact that the gain controls on the SonoSite were not kept constant for every treatment. Changes in gain control will affect the brightness and contrast of the ultrasound image. Although there appeared to be a slight increase in maximum brightness as intensity increased, this was not statistically significant ($p>0.05$) and the relationship did not hold true for the average brightness.

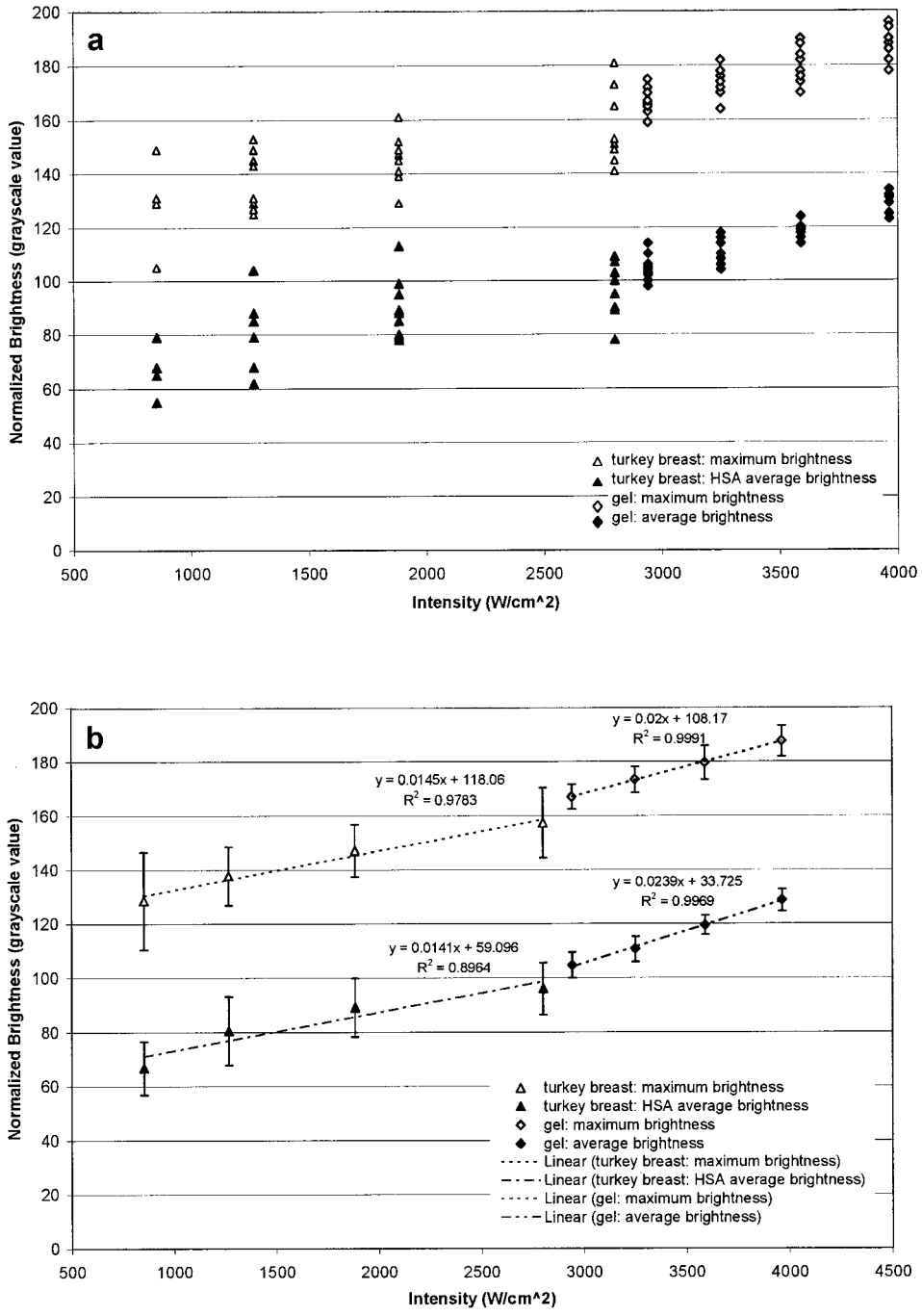

Figure 9.5 Maximum and average normalized brightness of the hyperechoic spot area at various treatment intensities: in vitro gel and turkey breast. (a) shows individual data points (b) shows the average of each data set, the standard deviation (error bars) and linear regression fits.

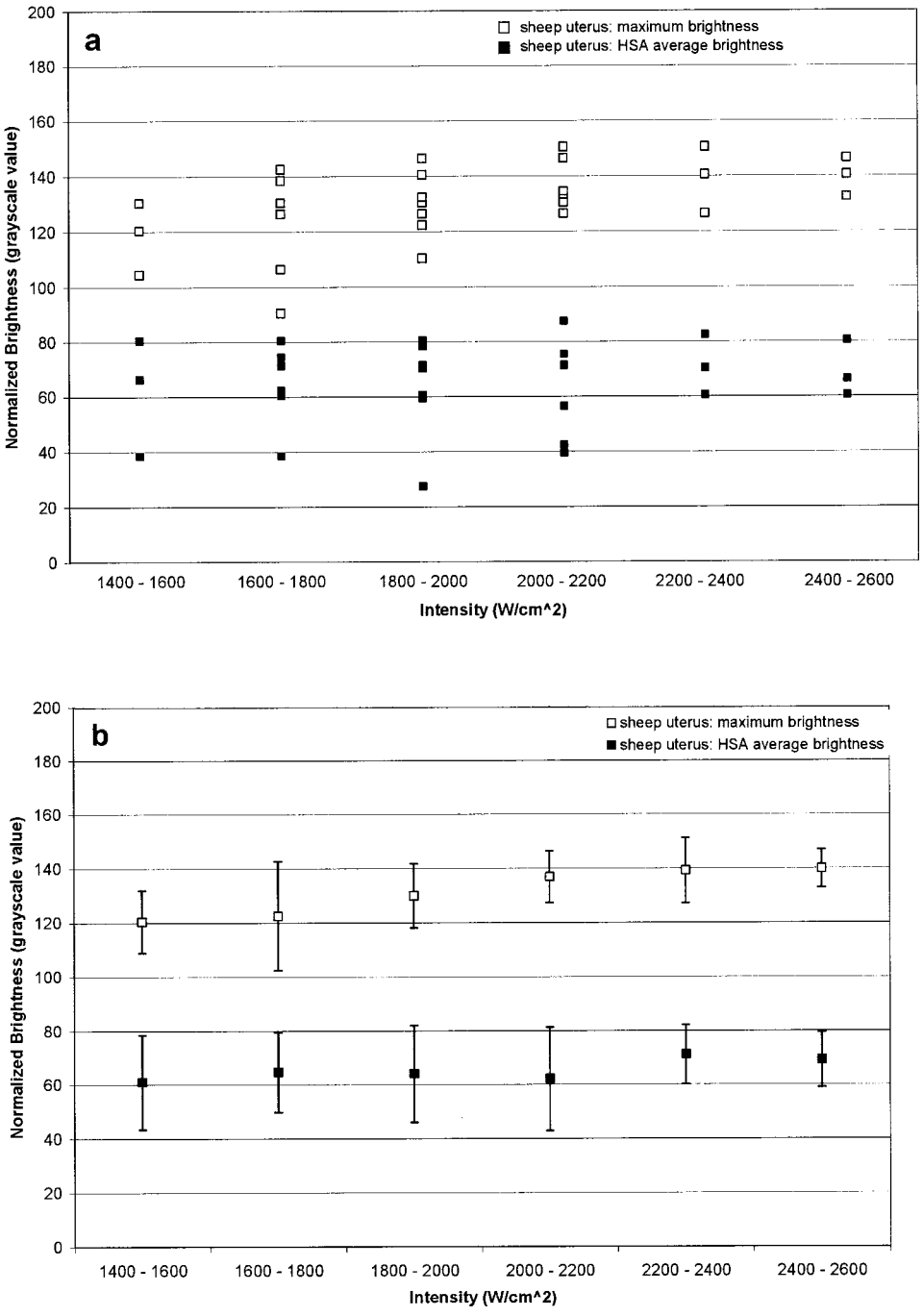

Figure 9.6 Maximum and average normalized brightness of the hyperechoic spot area at various treatment intensities: sheep uterus. (a) shows individual data points (b) shows the average of each data set and the standard deviation (error bars)

9.2.2.3 Hyperechoic spot brightness – temporal analysis

The appearance of the hyperechoic spot over time was studied *in vitro* during testing of HITS and *in vivo* during sheep uterus treatment. It was of interest to determine how the brightness of the lesion varied as a function of not only treatment intensity but treatment time as well, from the onset of HIFU until 20 seconds after HIFU began.

Figure 9.7, Figure 9.8, and Figure 9.9 show the brightness time-dependence for lesions created at various intensities in gel, turkey breast, and sheep uterus respectively. The points show the average normalized brightness value ± one standard deviation (n=10 *in vitro* and n=5 *in vivo*) over the hyperechoic spot area (HSA). In all media, the lesions formed at higher intensities appeared as hyperechoic spots with higher grayscale values. This was true for both the brightest pixel and the grayscale value averaged over the HSA. Hyperechoic spots of treatments at higher intensities also reached higher pixel grayscale values more quickly. This can be inferred as a result of more rapid cavitation activity and vaporization at higher intensities (Hynynen 1991), resulting in a brighter hyperechoic spot. The rise in brightness is rapid once cavitation or vaporization activity begins. After just 1 to 2 seconds of HIFU, the pixel brightness changes allowing lesion formation to be visualized. Thus, changes in tissue properties were noticed which may be independent of cavitation.

After the HIFU was turned off at 10 seconds, the lesions faded (reflected by a decrease in normalized brightness values). Eventually, the amount of fading leveled off and the lesions remained visible but less bright. When the data for all the intensity levels were normalized, (values plotted as percentage of maximum brighteness), the lesion brightness leveled off at approximately 60% (gel), 50% (turkey) and 30-60% (sheep uterus) of the maximum brightness after HIFU was turned off. In comparing the hyperechoic spot brightness in different media, it was observed that gel, which was very homogeneous, resulted in fewer variations in brightness (standard deviations of 4-6 grayscale values). In comparison, there was much greater variance in less homogeneous turkey and sheep uterus (standard deviations of 8-11 and 8-15 grayscale values for turkey and sheep uterus respectively). The variances in grayscale values may also be due to air bubbles that may

have existed in the tissue and not in the degassed gel. Also, the gain controls on the SonoSite was not kept constant during sheep uterus treatment.

Since the brightness of the hyperechoic spot after HIFU was turned off was a lot closer to the baseline brightness in sheep uterus (Figure 9.9) compared with gel and turkey breast tissue, it was difficult at times to distinguish the treated area with the surrounding tissue *in vivo*.

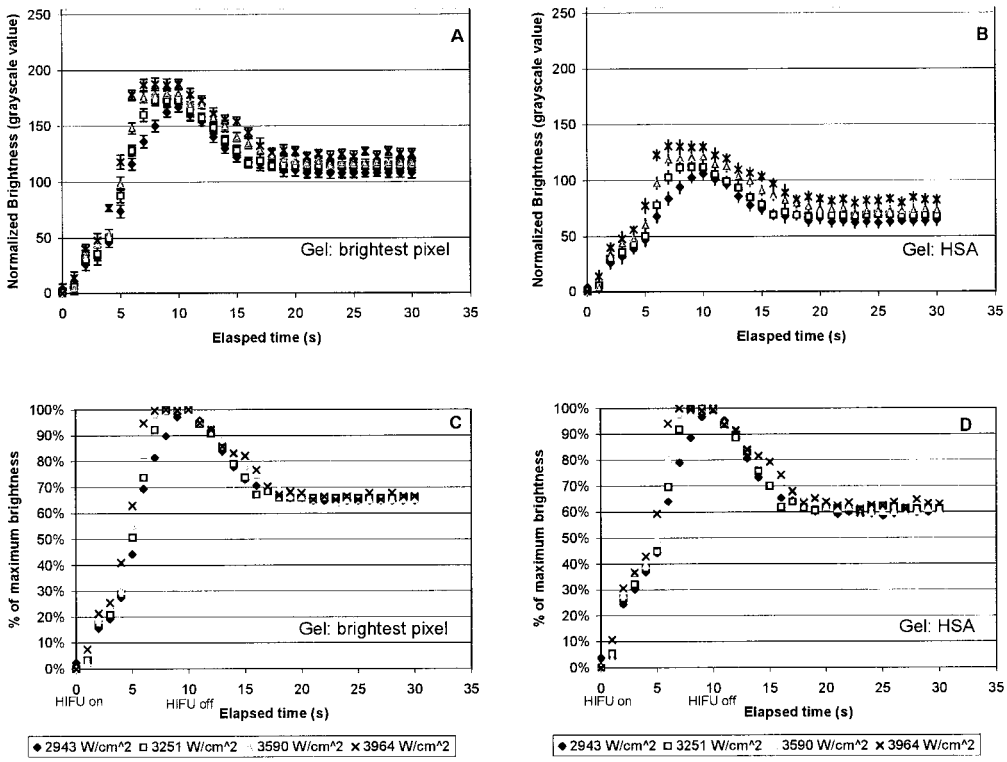

Figure 9.7 Hyperechoic spot normalized brightness over time: gel lesions. A and B show the normalized brightness of the brightest pixel and average over the hyperechoic spot area (HSA) respectively. C and D show the data as a percent of maximum brightness.

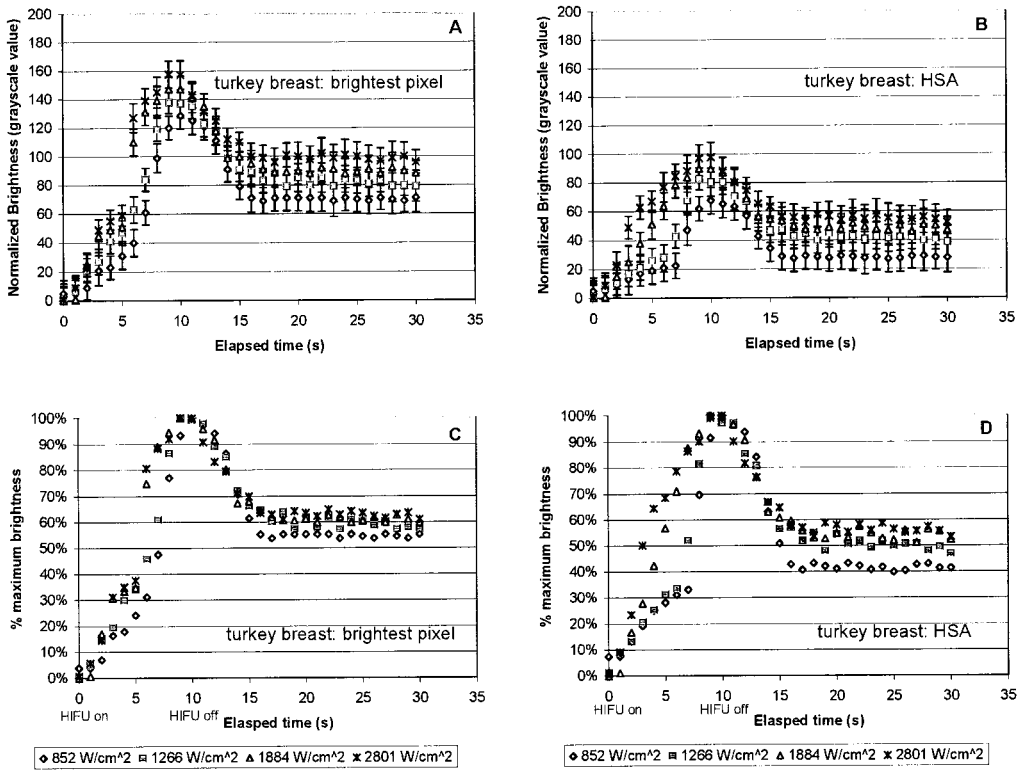

Figure 9.8 Hyperechoic spot normalized brightness over time: turkey breast lesions. A and B show the normalized brightness of the brightest pixel and average over the hyperechoic spot area (HSA) respectively. C and D show the data as a percent of maximum brightness.

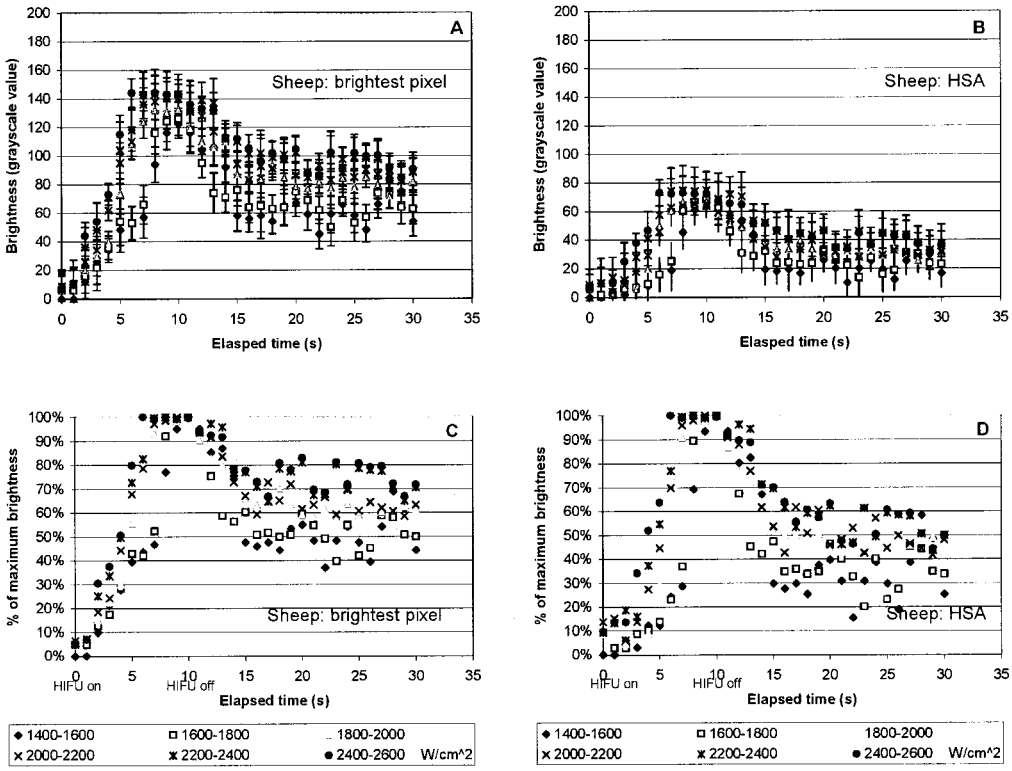

Figure 9.9 Hyperechoic spot normalized brightness over time: sheep uterus lesions. A and B show the normalized brightness of the brightest pixel and average over the hyperechoic spot area (HSA) respectively. C and D show the data as a percent of maximum brightness.

9.2.3 Discussions and conclusions

We have previously shown *in vitro* that there is a threshold intensity (I_{SATA} = 1250 W/cm^2) above which lesions will be visualized as hyperechoic spots in the ultrasound image (Section 5.2.3). Below this threshold, the likelihood of lesion visualization decreased proportionally to the intensity applied. For *in vivo* experiments, the threshold intensity was determined to be approximately 2200 W/cm^2. This was higher than the threshold intensity *in vitro* due to factors present *in vivo* that may affect the formation of a visible hyperechoic spot such as respiratory motion and perfusion.

The formation of a hyperechoic (bright white) spot at the lesion location is thought to be due to changes in tissue acoustic properties, tissue vaporization and gas bubble activity at the focus (Vaezy, Shi et al. 2001). After the HIFU was turned off, the hyperechoic spot still remained but appeared less bright. This was critical to distinguish between treated and non-treated regions. However, the visibility of a hyperechoic spot is not solely due to its brightness value, but also dependant on its contrast with surrounding tissue. The pre-existing bright areas in the uterus do not allow for an easy visual identification of the hyperechoic spot. The problem is exacerbated by tissue motion due to respiration or device movement. Three-dimensional tracking of the treated area is a future development to be incorporated in the device that would enhance the identification of treated areas.

The gain controls on the ultrasound machine can be used to adjust the contrast and brightness levels of the display, aiding identification of hyperechoic spots. However, by varying these gain controls, a basis for comparison and quantification of hyperechoic spots may be lost. Thus, quantifying lesions using the brightness of the hyperechoic spot is a method that is good for experimental purposes only in a controlled environment. However, it may not be ideal for *in vivo* unless real time signal processing and image processing is used.

10.0 CHAPTER 10 CLINICAL CONSIDERATIONS

10.1 INTRODUCTION

The work presented in this dissertation provides a strong justification for this HIFU device and treatment modality to be further investigated for use in humans. This chapter provides insight into suitable patients for this treatment, considerations for use of this device in humans, and the HIFU intensities that may be possible in treatment of humans.

10.2 INDICATIONS FOR TREATMENT

Although ultrasound image-guided HIFU has been shown in this dissertation to be potentially minimally-invasive treatment for uterine anomalies, it may not be suitable for all patients. This section explores why this treatment may be better suited for certain individuals.

First, the patient should be suffering from the presence of a symptomatic fibroid, confirmed using ultrasound or MRI. A careful diagnosis should be performed prior to treatment to distinguish the fibroid from a cancerous tumor or other abnormal mass (cyst or polyp). Although HIFU can be used to treat any tissue, treatment parameters may be different for each type and should be optimized based on the diagnosis.

HIFU treatment is recommended for ablation of smaller-sized fibroids, such as submucosal fibroids since the lesion volume resulting from a single treatment is small due to the small size of the HIFU focus. Most likely, the patient will need to be anesthetized, at least locally, so a shorter treatment time is recommended. Also, a physician performing this procedure would not want it to require more time than a hysterectomy or myomectomy (2-3 hours maximum). Based on calculated treatment rates in Section 8.7, a three hour treatment would be sufficient to ablate a fibroid of approximately 3.9 cm^3 in volume. If shorter off-times were used, and with a greater ultrasound absorption by fibroid tissue as discovered in section 8.7.3, a larger fibroid may be ablated in this 3 hour time frame.

Excess body fat may be a hindrance to image-guidance using ultrasound since ultrasound energy would be attenuated by a large layer of fat reducing image quality. In the ergonomic study (Section 5.3), we confirmed visualization of pelvic structures and the HIFU transducer up to a body mass index of 29.9. It would be of interest to determine if the presence of body fat in obese patients would result in poorer visualization of the pelvic structures. The transvaginal HIFU treatment would presumably be unaffected by the amount of body fat since the HIFU would still be radiated via a direct path into the uterus.

The orientation of the uterus may also determine the feasibility of using the device. There are several orientations of the uterus as discussed in Section 5.3.3. Fibroids can also be located in many areas of the uterus. The positioning of a HIFU transducer will likely depend on uterus size, fibroid location, and whether or not a woman has given birth. However, there may be some fibroids that would be too difficult to treat using a vaginal HIFU transducer due to uterus orientation and fibroid location. In these cases, a variable focus transducer or a transabdominal HIFU treatment could be more versatile. Alternatively, ablation of vasculature leading to the fibroid may be another method of treating hard-to-reach fibroids.

Since successful visualization and treatment of the uterus required a full bladder, catheterization of the urethra may be necessary, especially if local or general anesthesia is to be administered prior to treatment. Therefore, women with urinary tract infections or bladder anomalies may not be able to undergo HIFU treatment. Also, pregnant women and women with contraindications to ultrasound imaging should not partake in the treatment. Finally, a transvaginal HIFU transducer may not be feasible for patients that have vaginal complications or are uncomfortable with the idea of a transvaginal treatment.

10.3 PROTOCOL CONSIDERATIONS

Knowledge and insight into planning a successful human treatment protocol has been gained from the studies presented in this dissertation. This section will explore considerations relating to HIFU transducer preparation and treatment procedures for human treatment.

Anesthesia will most likely be necessary in the HIFU treatment procedure due to two main reasons. First, the patient may be able to feel localized HIFU energy and second, it is important for the patient to remain as still as possible during HIFU treatment to ensure accurate delivery of HIFU energy. The sensation of HIFU energy may be due to sympathetic innervation in the uterus from the hypogastric nerve (Gray 1918).

It is crucial for the patient to have a full bladder prior to treatment. This will ensure that the bowel is pushed out of the HIFU treatment area and that the bowel will not interfere with ultrasound visualization of the uterus and surrounding pelvic structures. It may be necessary to insert a balloon catheter into the urethera to prevent urine loss from the bladder, especially if the patient is under anesthesia.

It is essential for the HIFU transducer to be sterile, and that there be sufficient water (approximately 40-60 mL) in the condom prior to insertion into the vagina. The water filled condom would provide a cushion, easing entry of the HIFU transducer. Water should be approximately equivalent to body temperature and sufficient warm ultrasound gel should be applied onto the condom before insertion to prevent discomfort.

Next, the device should be manipulated so that an optimal field of view using the abdominal probe is possible. This may include adjusting the image probe vertically or horizontally, or slight rotation of the probe. Once optimal visualization is obtained, the device should be locked in place and the targeting system used to determine if all areas intended for treatment can be reached with the fixed focus. This may involve inflating and deflating the water filled condom to obtain an optimal stand off between the transducer and the uterus or changing the depth of insertion into the vagina. Treatment planning software, a potential future development, would be useful in determining optimal treatment patterns and positioning.

Once the system is positioned for treatment, a final check should be performed to ensure that the condom is not leaking, the electronics are set for proper HIFU parameters, and all wires are properly connected. During treatment, the transducer temperature should be carefully monitored and should not exceed 37°C. A sudden change in temperature may be indicative of condom leakage or transducer failure.

Since respiratory motion may cause the uterus to move during treatment, some form of respiratory gating or breathing control may be helpful in localizing treatment. Techniques that could be used include having the patient hold her breath for 5-10 seconds during which time HIFU would be administered. If the patient is under general anesthesia, treatment only on the exhalation or inhalation phase may provide consistency in treatment location.

After treatment, caution should be taken when removing the HIFU transducer. The water in the condom should be reduced to the amount present during transducer insertion. Post-treatment monitoring of the uterus using ultrasound should be performed. Signs of patient discomfort or medical anomalies (such as bleeding, tissue adhesions, swelling) should be noted.

10.4 INSIGHT INTO *IN SITU* HIFU ENERGY FOR HUMAN TREATMENTS

At this pre-clinical stage of developing a transvaginal HIFU treatment for fibroids, it was of interest to determine the treatment intensities that may be encountered if the device was to be used in a human. Although empirical data may not be available, treatment intensities can be predicted with the knowledge of HIFU treatment parameters and the physical and acoustic properties of the various media encountered.

10.4.1 Ultrasound Path Losses

The two extreme paths that the HIFU will encounter, representing minimal and maximal intensity loss as shown in Figure 10.1, were examined and intensities at the focus calculated. Intensities for treatment paths between these two extremes can then be interpolated.

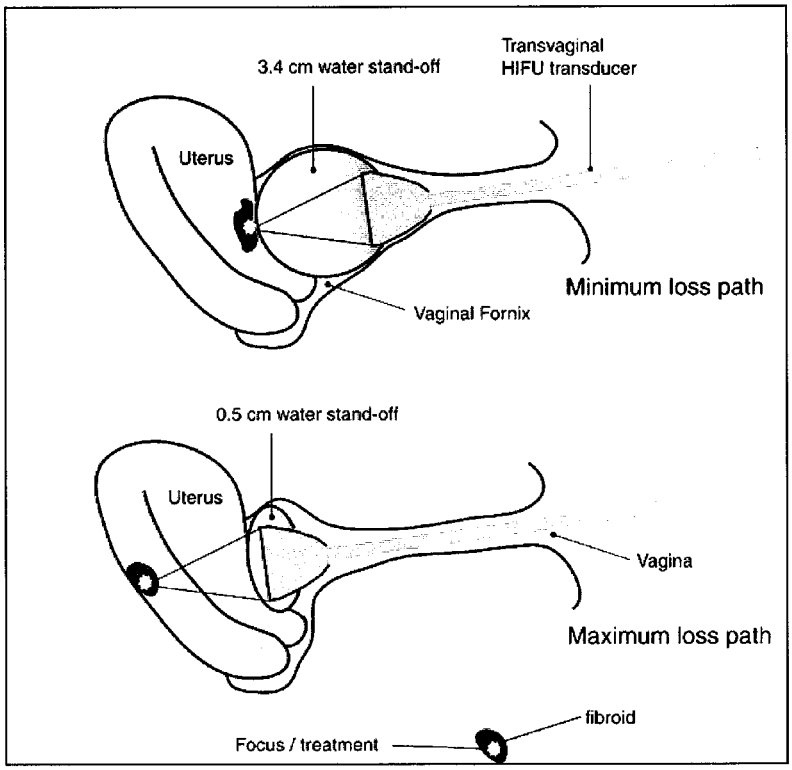

Figure 10.1 The two extreme ultrasound paths encountered during treatment

These two paths are described as follows (a) Minimal loss path: the tumor is on the side of the uterus adjacent to the condom and immediately under the mucosal layer. The condom is filled with water to a diameter of 3.4 cm. (b) Maximum loss path: the tumor is on the side of the uterus furthest from the condom and immediately under the mucosal layer. The condom is filled with water to a diameter of 0.5 cm.

HIFU waves will first travel through water in the condom, encounter a layer of myometrium, and finally encounter the fibroid. It is assumed that the fibroid will be a small submucosal fibroid, 1 cm in diameter, and treatment will occur at the center (0.5 cm inside the fibroid). Losses mainly due to attenuation and slightly due to transmission between different media would need to be accounted for in order to predict the HIFU intensity and dose at the focus. Since the condom has shown not to contribute to acoustic losses (section 5.1.3), it will be neglected from loss calculations. The acoustic properties used in the calculations are shown in Table 10.1.

The intensity at the focus (I_{focus}) represents a spatial average temporal average intensity and can be calculated based on Eq. 10.1:

Eq. 10.1 $$I_{focus} = I_{transmit}(e^{-2(\alpha_w d_w + \alpha_m d_m + \alpha_f d_f)})(T_{wm})(T_{mf})$$

T_{wm} and T_{mf} are the transmission coefficients between water and myometrium, and between myometrium and fibroid respectively, calculated as:

Eq. 10.2 $$T_{wm} = \frac{4Z_w Z_m}{(Z_w + Z_m)^2} \quad \textbf{and} \quad T_{mf} = \frac{4Z_m Z_f}{(Z_m + Z_f)^2}$$

where Z_i represents the acoustic impedance in medium "i" and is calculated as $Z_i = \rho_i / c_i$.

The variables in the above equations and their values used for the loss calculations for the two extreme paths are described in Table 10.1 for a frequency of 3.5 MHz. Calculations will be performed assuming a water temperature of 25°C in the water filled condom.

Table 10.1 Values used for intensity calculations

Parameter	Description	Value (maximum loss)	Value (minimum loss)	Units
$I_{transmit}$	I_{SATA} transmitted intensity	At half pressure maximum - varies		W/cm^2
α_w	Attenuation of water (25°C)	0.00272 (Duck 1990)		Np/cm
α_m	Attenuation of myometrium[+]	0.2875		Np/cm
α_f	Attenuation of fibroid[+]	0.3910		Np/cm
d_w	Path distance in water	0.5	3.4	cm
d_m	Path distance in myometrium	3.0	0.1	cm
d_f	Path distance in fibroid	0.5	0.5	cm
ρ_w	Density of water (25°C)	998		kg/m^3
ρ_m	Density of myometrium	1048		kg/m^3
ρ_f	Density of fibroid	1070		kg/m^3
c_w	Sound speed in water (25°C)	1483		m/s
c_m	Sound speed in myometrium	1584		m/s
c_f	Sound speed in fibroid	1584		m/s

[+] *based on section 3.6*

10.4.2 Predicted Treatment Intensities

The ratio of focal to transmitted intensity was calculated to be 0.63 for the minimum loss path and 0.12 for the maximum loss path based on equation Eq. 10.1. The large variation in loss is due to the variation in path distance, and thus attenuation, in myometrium (transmission losses only account for 0.01% of the total loss). Figure 10.2a shows the correlation between the distance of travel through myometrium and the ratio of $I_{focus}/I_{transmit}$ assuming a constant distance of 0.5 cm through the fibroid - i.e. any increase in path distance through myometrium results in a decrease of path distance through water. This is the same as simulating a change in volume of the water in the condom.

Figure 10.2b provides an alternative interpretation of this data. It shows the intensity for various continuous wave acoustic power levels assuming a full width at half maximum focal width of 1.2 mm (area of 1.13 mm^3) determined in section 4.4.2.3.

As shown in Figure 10.2b, the range of focal intensities that can be achieved is larger for a smaller distance through myometrium. By establishing this relation between focal intensity and ultrasound path distance through myometrium, the types of lesions formed and the bioeffects *in vivo* may be predicted for treatment planning. It can be inferred that a longer treatment duration will be necessary to achieve the same thermal dose and/or bioeffects for treatments utilizing the maximum loss path as opposed to the minimum loss path. It should be noted that tissue inhomogeneities, perfusion, and circulation may result in different intensities achieved *in vivo*.

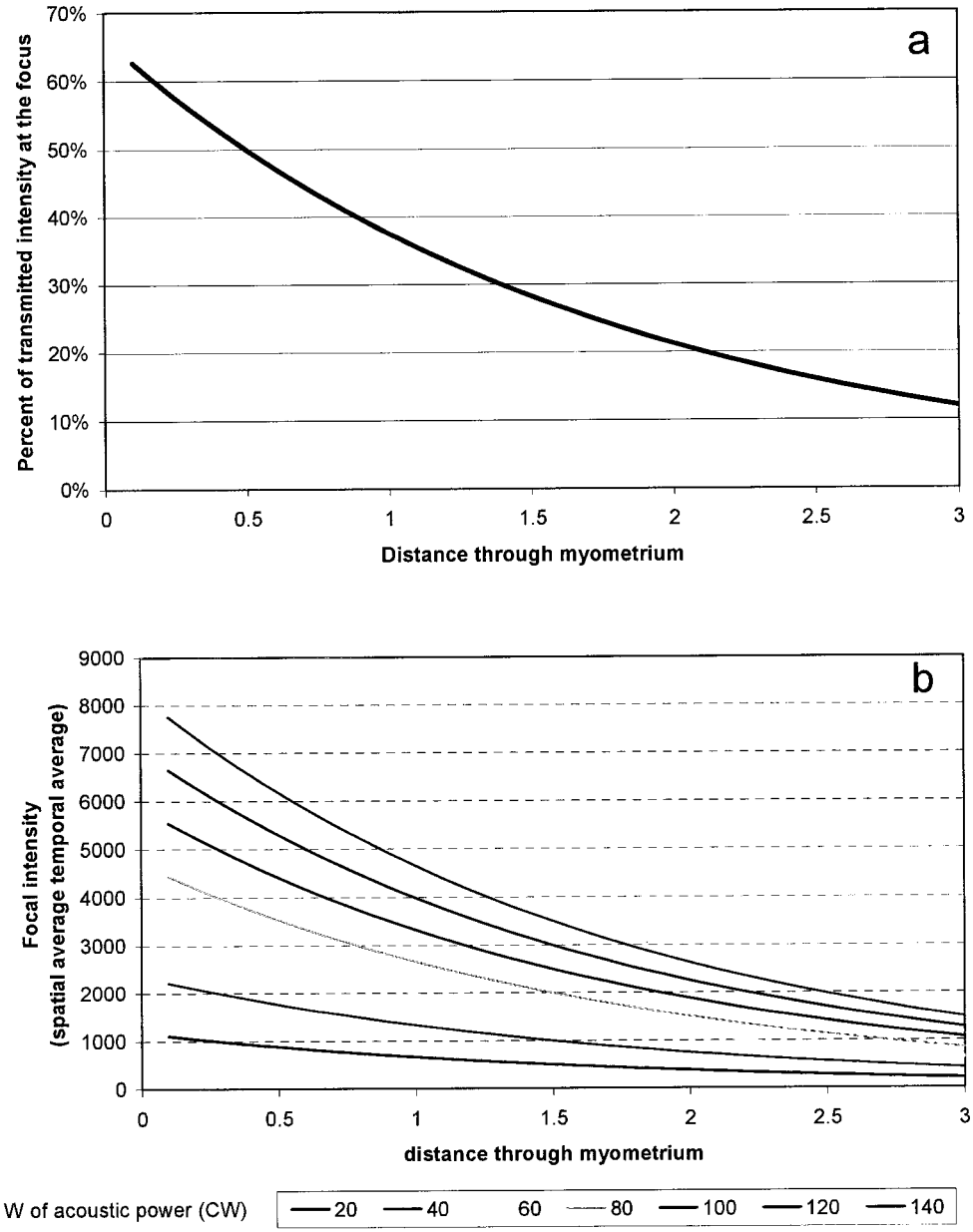

Figure 10.2 Effects of distance through myometrium and acoustic power on HIFU focal intensity

11.0 CONCLUSIONS AND FUTURE STUDIES

11.1 CONCLUSIONS

The work presented in this dissertation has taken ultrasound image-guided HIFU for leiomyoma from a concept to a stage where it is ready to be explored further in humans. All the principal goals and specific aims presented in Chapter 1 have been accomplished.

First, a device was designed that combined a commercially available abdominal ultrasound imaging device with a transvaginal HIFU transducer. This device was characterized using acoustic measurement techniques and was capable of performing image-guided therapy *in vitro* and *in vivo*. This device demonstrated the practicality and simplicity of an intracavitary HIFU transducer guided by external diagnostic ultrasound. An ergonomic study revealed that the device was comfortable and useable in humans for treating fibroids located in various parts of the uterus.

The device underwent improvements that enhanced efficiency and increased HIFU focal intensity. A targeting system was added, consisting of position transducers that were monitored in real-time by a computer. It was possible to determine the exact location of treatment prior to the onset of HIFU, and the system provided accurate indication of where the HIFU focus was at all times. The targeting system was tested *in vitro* and experimental errors were below theoretically determined error margins.

In vivo treatments using the device were performed in sheep *in vivo*. Eight sheep uteri were treated and evaluated at various times post-treatment. This large animal study showed that the treatment was safe and feasible. HIFU lesions were localized in intended treatment locations. With adequate cooling, a full bladder, and good visualization of the pelvic region, treatment of tissue surrounding the uterus was avoided. None of the animals suffered medical conditions (such as inflammation, bleeding, abnormal urinary and bowel movement) and at 30 days post-treatment, the treated uterus tissue had healed with the formation of scar tissue.

Image-guided HIFU therapy has the potential to be a minimally-invasive alternative to hysterectomy and other surgical procedures for women with symptomatic uterine fibroids and other uterine anomalies.

11.2 FUTURE DIRECTIONS

The work presented in this dissertation represents a major step forward in advancing the field of therapeutic ultrasound, and for using image-guided HIFU as a modality for treating uterine anomalies. However, the results and conclusions drawn from this work also lead to many unanswered questions and future directions for development. There is great potential for this project to be continued, and ideas for further exploration are presented.

11.2.1 Three-dimensional (3-D) lesion tracking and targeting

In Chapter 7, we showed that a computer monitored targeting system based on position sensor data was accurate and reliable in determining the HIFU focal location. However, a HIFU treated area is three dimensional. Depending on tissue characteristics, a HIFU lesion may spread in a direction within the image plane, perpendicular to the image plane, or many angles in between. Although two-dimensional B-mode ultrasound can be used to visualize a hyperechoic spot in the image plane, it cannot be used to determine the treatment effects in the other directions. With the advances of three-dimensional ultrasound, where adjacent image planes are scanned, recorded, and reconstructed to form a three-dimensional image, lesions may potentially be visualized in 3-D. 3-D ultrasound may improve HIFU treatment accuracy, and also be able to determine if HIFU energy is spreading into regions not intended for treatment in a manner undetectable by 2-D ultrasound imaging.

11.2.2 Means of treatment confirmation and tracking

Chapter 9 showed that the hyperechoic spot that appeared after HIFU lesion formation is a good visual indicator of whether or not treatment has taken place. However, the mechanisms that actually cause the hyperechoic spot phenomenon have not been fully understood. We have speculated that the hyperechoic spot is due to changes in tissue property, vaporization, and cavitation effects at the focus. It would be important to

understand these concepts better to determine if data obtained about the hyperechoic spot can be used to determine the extent of treatment. We also noted in Chapter 9 that the hyperechoic spot remained visible for at least 20 seconds after treatment. Unfortunately, the hyperechoic spots become difficult to track *in vivo* post treatment due to tissue movement and lack of contrast between the hyperechoic spot and surrounding tissue. Computerized image processing software may be used to keep track of treated tissue through developing an understanding of hyperechoic spot mechanisms and by having an electronic means to keep track of what areas of the tissue have exhibited hyperechoic appearance. If a large volume of tissue, such as a tumor, is to be treated, many individual lesions may be needed (Section 8.7.2). Therefore, it would be necessary to have a means of tracking which areas have already been treated.

Furthermore, the preexistence of one lesion may perturb and hinder the formation and intended placement of subsequent adjacent lesions due to a phenomenon known as lesion to lesion interaction. Perhaps the most noted efforts in studying lesion to lesion interaction were made by Chen et al. It was observed that when the HIFU focus was scanned over a target volume, viable cells were left between adjacent treated areas which could potentially result in the continued growth of tumor volume after treatment (Chen, ter Haar et al. 1997). A treatment confirmation and tracking system would detect such phenomena.

It would also be of interest to be able to obtain thermal measurements at the HIFU focus. This would enable the user of the HIFU device to determine whether or not coagulative necrosis would have taken place regardless of whether or not a hyperechoic spot appears on the ultrasound image. Being able to visualize thermal gradients would also prevent unwanted thermal damage to surrounding tissue, prevent over-treatment of tissue, reducing therapy time by optimizing the duration of each treatment, and provide a means of adjusting the HIFU intensity to optimize the degree of thermal effects produced.

11.2.3 Phased array transvaginal HIFU device for gynecological use

The device presented in this dissertation has shown the practicality, feasibility, efficacy and safety of a transvaginal HIFU device. The HIFU transducer was simple to

manufacture, and easily manipulated. Various areas of the uterus could be treated with the device by mechanical movement and changing the size of the water filled condom (Section 5.3.3). It may be advantageous to have a transducer with an electronically controlled focus allowing minimal device movement while moving the focal area. This would allow the ultrasound image to remain still while the treatment location was altered eliminating the difficulties in targeting the treatment area while simultaneously positioning the HIFU transducer. This could be accomplished with a phased array (section 2.11) transvaginal device. The device would have to be ergonomically designed for gynecological applications, and it would be ideal to minimize the electronics necessary to drive the phased array.

11.2.4 Study of HIFU complications

During dissection of sheep uterus, we discovered HIFU-affected areas not intended for treatment (Section 8.5) Fortunately, there were no medical complications that resulted from these undesired treatments. In continuing safety studies for uterus HIFU treatment, it would be of interest to purposely treat sensitive tissue near the uterus, such as the bladder, bowel, urethera, and ovaries to investigate the healing process. Tissue adhesion, bleeding, and loss of function would be specific complications of interest.

11.2.5 Study of post-HIFU pregnancy

It is important to study the possibility and complications of post-treatment pregnancies since women may elect HIFU therapy to preserve the uterus for future children. The study would determine if treated and healed uterus tissue can contain a developing fetus, and whether or not there is an increase in infertility after HIFU treatment. One method that could be used for this study is impregnating test sheep after their uterus has been treated.

11.2.6 Optimizing treatment parameters

For the *in vivo* study, five lesions were made in the uterus body (Section 8.3.2). However, it was shown that many more lesions would be needed to treat a small submucosal fibroid (section 8.7.2). It would be of interest to study optimal treatment parameters that would maximize the thermal and cavitation effects of the HIFU treatment and minimize the

treatment time. The individual treatment time, cooling time, amount of surrounding tissue to ablate, and lesion formation patterns should be studied.

It has also been suggested that the HIFU beam can be scanned either mechanically or electronically, or phased arrays can be used to generate multiple foci to cover the whole target volume versus using individual lesions (Hynynen 1992). The scanning beam method was tested by Chen et al. and it was stated that larger lesions were formed and lesion consistency was better than or as good as those achieved with a discrete array of overlapping ultrasound exposures (Chen, ter Haar et al. 1997). The development of software that can outline a tumor or other treatment area of interest, and automatically develop a treatment plan, would be very helpful in optimizing treatment efficiency.

11.2.7 Fixed system development

The device presented in this dissertation was designed to be a hand-held device to be used in office-based gynecological procedures. However, many HIFU treatment devices currently in use (ExAblate, InSightec, Dallas, TX; HAIFU Knife, Chongqing HAIFU Company, Chongqing, China; Sonoblate, Focus Surgery, Indianpolis, IN) employ an apparatus in which the HIFU device is mechanically fixed to stepper motors controlled by electronics. The stepper motors provide precise movement of the HIFU transducer to treat various areas. It may be of interest to develop a system where the transvaginal probe is computer controlled allowing for more precise targeting and treatment. Also, due to the length of time that may be required, a fixed device may be more pleasant for the physician to use than a handheld device. Although a handheld device seems more suited for transvaginal applications, Focus Surgery has demonstrated the feasibility of using a fixed rectal probe.

11.2.8 Uterine artery treatment and other gynecological conditions

HIFU has the potential to be used to ablate the vasculature feeding the uterus and fibroids. Similar to uterine artery embolisation, this treatment would potentially shrink large fibroids. The shrunken fibroids might alleviate pressure induced pain, and might then be subsequently treated with HIFU. A study to determine the positive and negative effects

of uterine artery occlusion using HIFU would provide insight into yet another means of fibroid treatment.

There is the opportunity for image-guided HIFU treatment to be used for treating other pelvic anomalies. These may include ovarian cysts, polyps, and endometriosis. HIFU has also been shown to be effective in treating uterine cancerous tumours, or leiyomyosarcoma, as proven in a previous study by Kesharvarzi et al. using a xenograft nude mouse model (Keshavarzi, Vaezy et al. 2002).

11.2.9 Use as an adjunct and complementary treatment

HIFU treatment may be studied as a joint treatment with another form of fibroid ablation. For example, fibroids which are too large for successful HIFU treatment might be first reduced by GnRH drugs and then subsequently treated with HIFU to allow complete ablation and prevent recurrence. HIFU might also be a second treatment option should fibroid re-growth occur after myomectomy or myolysis.

11.2.10 Treatment of human uterus

The ultimate goal of this research is to use image-guided HIFU to treat a diseased human uterus. As presented earlier in this chapter, there are certain individuals who would be most suitable and benefit most from this treatment. A study that would prepare this device and treatment for FDA (USA), CE mark (Europe) or other clinical use certification would be to treat humans with fibroids. It would be ideal to begin treatments on women who have an impending hysterectomy. Therefore, future pregnancies would not be a concern, and pathological changes to the fibroids and the uterus tissue could be studied. Once success in these patients has been shown, the treatment could be used on women interested in preserving their uterus.

BIBLIOGRAPHY

Adams, J. B., R. G. Moore, et al. (1996). "High-intensity focused ultrasound ablation of rabbit kidney tumors." J Endourol 10(1): 71-5.

Aharoni, A., A. Reiter, et al. (1988). "Patterns of growth of uterine leiomyomas during pregnancy. A prospective longitudinal study." Br J Obstet Gynaecol 95(5): 510-3.

Andersen, J. and R. L. Barbieri (1995). "Abnormal gene expression in uterine leiomyomas." J Soc Gynecol Investig 2(5): 663-72.

Apfel, R. E. (1982). "Acoustic cavitation: a possible consequence of biomedical uses of ultrasound." Br J Cancer Suppl 45(5): 140-6.

Arcangeli, S. and M. M. Pasquarette (1997). "Gravid uterine rupture after myolysis." Obstet Gynecol 89(5 Pt 2): 857.

Arefiev, A., F. Prat, et al. (1998). "Ultrasound-induced tissue ablation: studies on isolated, perfused porcine liver." Ultrasound Med Biol 24(7): 1033-43.

Ashush, H., L. A. Rozenszajn, et al. (2000). "Apoptosis induction of human myeloid leukemic cells by ultrasound exposure." Cancer Res 60(4): 1014-20.

Bailey, M. R., L. N. Couret, et al. (2001). "Use of overpressure to assess the role of bubbles in focused ultrasound lesion shape in vitro." Ultrasound Med Biol 27(5): 695-708.

Barkman, C. A., L. O. Almquist, et al. (1999). "Thermotherapy: feasibility study using a single focussed ultrasound transducer." Int J Hyperthermia 15(1): 63-76.

Beard, R. E., R. L. Magin, et al. (1982). "An annular focus ultrasonic lens for local hyperthermia treatment of small tumors." Ultrasound Med Biol 8(2): 177-84.

Bhatia, K. G. and V. R. Singh (2001). "Ultrasonic characteristics of leiomyoma uteri in vitro." Ultrasound Med Biol 27(7): 983-7.

Bloch, S. (1998). Ultrasonic tissue characerization towards high intensity focused ultrasound treatment monitoring. Bioengineering. Seattle, University of Washington.

Bohris, C., W. G. Schreiber, et al. (1999). "Quantitative MR temperature monitoring of high-intensity focused ultrasound therapy." Magn Reson Imaging 17(4): 603-10.

Brayman, A. A., L. M. Lizotte, et al. (1999). "Erosion of artificial endothelia in vitro by pulsed ultrasound: acoustic pressure, frequency, membrane orientation and microbubble contrast agent dependence." Ultrasound Med Biol 25(8): 1305-20.

Brentnall, M. D., R. W. Martin, et al. (2001). "A new high intensity focused ultrasound applicator for surgical applications." IEEE Trans Ultrason Ferroelectr Freq Control 48(1): 53-63.

Bronzo, J. and J. Anderson (1952). "The effectiveness of plastic focussing lenses with high intensity ultrasonic radiation." J Acoust Soc Am 24: 718-720.

Burov, A. and G. Andreevskaya (1956). "The effect of ultra-acoustic oscillation of high intensity on malignant tumors in animals and man." Dokl. Akad, Nauk. SSSR 106: 445-448.

Bush, N. L., I. Rivens, et al. (1993). "Acoustic properties of lesions generated with an ultrasound therapy system." Ultrasound Med Biol 19(9): 789-801.

Buttram, V. C., Jr. and R. C. Reiter (1981). "Uterine leiomyomata: etiology, symptomatology, and management." Fertil Steril 36(4): 433-45.

Chan, A. H., V. Y. Fujimoto, et al. (2002). "An image-guided high intensity focused ultrasound device for uterine fibroids treatment." Med Phys 29(11): 2611-20.

Chapelon, J. Y., J. Margonari, et al. (1992). "Effects of high-energy focused ultrasound on kidney tissue in the rat and the dog." Eur Urol 22(2): 147-52.

Chapelon, J. Y., J. Margonari, et al. (1992). "In vivo effects of high-intensity ultrasound on prostatic adenocarcinoma Dunning R3327." Cancer Res 52(22): 6353-7.

Chen, L., I. Rivens, et al. (1993). "Histological changes in rat liver tumours treated with high-intensity focused ultrasound." Ultrasound Med Biol 19(1): 67-74.

Chen, L., G. ter Haar, et al. (1997). "Influence of ablated tissue on the formation of high-intensity focused ultrasound lesions." Ultrasound Med Biol 23(6): 921-31.

Chen, L., G. ter Haar, et al. (1999). "Histological study of normal and tumor-bearing liver treated with focused ultrasound." Ultrasound Med Biol 25(5): 847-56.

Chen, W., Z. Wang, et al. (2002). "[High intensity focused ultrasound alone for malignant solid tumors]." Zhonghua Zhong Liu Za Zhi 24(3): 278-81.

Chen, W., Z. Wang, et al. (2002). "[High intensity focused ultrasound in the treatment of primary malignant bone tumor]." Zhonghua Zhong Liu Za Zhi 24(6): 612-5.

Chiaffarino, F., F. Parazzini, et al. (1999). "Use of oral contraceptives and uterine fibroids: results from a case- control study." Br J Obstet Gynaecol 106(8): 857-60.

Christensen, D. A. (1988). Ultrasonic Bioinstrumentation. New York, John Wiley and Sons.

Clement, G. T., J. Sun, et al. (2000). "A hemisphere array for non-invasive ultrasound brain therapy and surgery." Phys Med Biol 45(12): 3707-19.

Clevenger-Hoeft, M., C. H. Syrop, et al. (1999). "Sonohysterography in premenopausal women with and without abnormal bleeding." Obstet Gynecol 94(4): 516-20.

Cline, H. E., K. Hynynen, et al. (1995). "Focused US system for MR imaging-guided tumor ablation." Radiology 194(3): 731-7.

Cline, H. E., J. F. Schenck, et al. (1992). "MR-guided focused ultrasound surgery." J Comput Assist Tomogr 16(6): 956-65.

Coleman, D., F. Lizzi, et al. (1985). "Treatment of experimental lens capsular tears with intense focused ultrasound." Br J Ophthalmol 69: 645-9.

Colgan, T. J., S. Pendergast, et al. (1993). "The histopathology of uterine leiomyomas following treatment with gonadotropin-releasing hormone analogues." Hum Pathol 24(10): 1073-7.

Collins, R. (1957). "Theory and design of wide-band multisection quarter-wave transformers." Proc IRE 43: 179-185.

Connor, C. W. and K. Hynynen (2002). "Bio-acoustic thermal lensing and nonlinear propagation in focused ultrasound surgery using large focal spots: a parametric study." Phys Med Biol 47(11): 1911-28.

Coronado, G. D., L. M. Marshall, et al. (2000). "Complications in pregnancy, labor, and delivery with uterine leiomyomas: a population-based study." Obstet Gynecol 95(5): 764-9.

Coutinho, E. M. and H. S. Maia (1971). "The contractile response of the human uterus, fallopian tubes, and ovary to prostaglandins in vivo." Fertil Steril 22(9): 539-43.

Cramer, D. (1992). "Epidemiology of myomas." Seminars in Reproductive Endocrinology 10: 320-4.

Cramer, S. F. and A. Patel (1990). "The frequency of uterine leiomyomas." Am J Clin Pathol 94(4): 435-8.

Damianou, C. and K. Hynynen (1993). "Focal spacing and near-field heating during pulsed high temperature ultrasound therapy." Ultrasound Med Biol 19(9): 777-87.

Daum, D. R., N. B. Smith, et al. (1999). "In vivo demonstration of noninvasive thermal surgery of the liver and kidney using an ultrasonic phased array." Ultrasound Med Biol 25(7): 1087-98.

Deligdish, L. and M. Loewenthal (1970). "Endometrial changes associated with myomata of the uterus." J Clin Pathol 23(8): 676-80.

Donnez, J., P. E. Mathieu, et al. (1996). "Laparoscopic myomectomy today. Fibroids: management and treatment: the state of the art." Hum Reprod 11(9): 1837-40.

Dorr, L. N. and K. Hynynen (1992). "The effects of tissue heterogeneities and large blood vessels on the thermal exposure induced by short high-power ultrasound pulses." Int J Hyperthermia 8(1): 45-59.

Duck, F. A. (1990). Physical Properties of Tissue, a Comprehensive Reference Book. London, Harcourt Brace Jovanovich.

Dunn, F. and F. J. Fry (1971). "Ultrasonic threshold dosages for the mammalian central nervous system." IEEE Trans Biomed Eng 18(4): 253-6.

Dunn, F., J. E. Lohnes, et al. (1975). "Frequency dependence of threshold ultrasonic dosages for irreversible structural changes in mammalian brain." J Acoust Soc Am 58(2): 512-4.

Ebbini, E. S. and C. A. Cain (1991). "Optimization of the intensity gain of multiple-focus phased-array heating patterns." Int J Hyperthermia 7(6): 953-73.

Fan, X. and K. Hynynen (1996). "Ultrasound surgery using multiple sonications--treatment time considerations." Ultrasound Med Biol 22(4): 471-82.

Flynn, H. (1982). "Generation of transient cavities in liquids by microsecond pulses of ultrasound." J Acoust Soc Am 72: 1926-1932.

Fried, N. M., W. W. Roberts, et al. (2002). "Focused ultrasound ablation of the epididymis with use of thermal measurements in a canine model." Fertil Steril 78(3): 609-13.

Frizzell, L. A. (1988). "Threshold dosages for damage to mammalian liver by high intensity focussed ultrasound." IEEE Trans Ultrason Ferroelectr Freq Control 35: 578-581.

Frizzell, L. A., C. A. Linke, et al. (1977). "Thresholds for focal ultrasonic lesions in rabbit kidney, liver, and testicle." IEEE Trans Biomed Eng 24(4): 393-6.

Fry, F. (1965). "Recent developments in ultrasound at biophysical research laboratory and their application to basic problems in biology and medicine." Ultrasound Energy: 202-228.

Fry, F. and L. Johnson (1978). "Tumor irradiation with intense ultrasound." Ultrasound Med. Biol. 4: 337-341.

Fry, F., G. Kossoff, et al. (1970). "Threshold ultrasound dosages for structural changes in the mammalian brain." J. Acoust. Soc. Am 48: 1413-1417.

Fry, F. J. (1977). "Transskull transmission of an intense focused ultrasound beam." Ultrasound Med Biol 3: 179-184.

Fry, F. J., N. T. Sanghvi, et al. (1976). Ultrasound visualization and therapeutic computer controlled system. Ultrasound in Medicine. D. White and R. Barnes. New York, Plenum Publication Co. 4: 481-482.

Fry, W., J. Barnard, et al. (1942). "Ultrasonic lesions in the mammalian central nervous system." Science 122: 517-518.

Fry, W. and F. Dunn (1962). Ultrasound: analysis and experimental methods in biological research. Physical techniques in biological research, special methods. W. Nastuk. 4: 300-313.

Fry, W. and R. Fry (1954). "Determination of absolute sound levels and acoustic absorption coefficients by thermocouple probes-theory." J. Acoust. Soc. Am 26: 294-310.

Gelet, A., J. Y. Chapelon, et al. (2000). "Transrectal high-intensity focused ultrasound: minimally invasive therapy of localized prostate cancer." J Endourol 14(6): 519-28.

Gelet, A., J. Y. Chapelon, et al. (1993). "Prostatic tissue destruction by high-intensity focused ultrasound: experimentation on canine prostate." J Endourol 7(3): 249-53.

Goldfarb, H. A. (2000). "Myoma coagulation (myolysis)." Obstet Gynecol Clin North Am 27(2): 421-30.

Goodwin, S. C. and W. J. Walker (1998). "Uterine artery embolization for the treatment of uterine fibroids." Curr Opin Obstet Gynecol 10(4): 315-20.

Goss, S. and F. Fry (1984). "Tumor irradiation with intense ultrasound." IEEE Trans Sonics Ultrasonics 31: 491-496.

Goss, S. A., L. A. Frizzell, et al. (1979). "Ultrasonic absorption and attenuation in mammalian tissues." Ultrasound Med Biol 5(2): 181-6.

Graham, S. J., L. Chen, et al. (1999). "Quantifying tissue damage due to focused ultrasound heating observed by MRI." Magn Reson Med 41(2): 321-8.

Gray, H. (1918). Anatomy of the human body. Philadelphia, PA, Lea and Febiger.

Gruetzmacher, J. (1935). "Piezoelektrischer kristall mit ultraschallkonvergenz." Z Phys 96: 342-349.

Gunn, J., D. C. Cumberland, et al. (2001). "Ultrasound as treatment for coronary artery disease." Echocardiography 18(3): 213-7.

Hallez, J. P. (1996). "Myomectomies by endo-uterine resection." Curr Opin Obstet Gynecol 8(4): 250-6.

Hendrickson, M. and R. Kempson (1980). Smooth muscle neoplasms. Surgical Pathology of the Uterus. Philadelphia, Saunders.

Hill, C. R. (1994). "Optimum acoustic frequency for focused ultrasound surgery." Ultrasound Med Biol 20(3): 271-7.

Hill, C. R., I. Rivens, et al. (1994). "Lesion development in focused ultrasound surgery: a general model." Ultrasound Med Biol 20(3): 259-69.

Hill, C. R. and G. R. ter Haar (1995). "Review article: high intensity focused ultrasound--potential for cancer treatment." Br J Radiol 68(816): 1296-1303.

Holland, C. K. and R. E. Apfel (1990). "Thresholds for transient cavitation produced by pulsed ultrasound in a controlled nuclei environment." J Acoust Soc Am 88(5): 2059-69.

Huynh, G., A. Chan, et al. (2002). Minimization of transducer heating during focused ultrasound therapy. Seattle, WA, Department of Bioengineering, University of Washington.

Hynynen, K. (1991). "The threshold for thermally significant cavitation in dog's thigh muscle in vivo." Ultrasound Med Biol 17(2): 157-69.

Hynynen, K. (1992). "Methods and technologies of ultrasound heating." Ultrasonics 30: 114.

Hynynen, K., V. Colucci, et al. (1996). "Noninvasive arterial occlusion using MRI-guided focused ultrasound." Ultrasound Med Biol 22(8): 1071-7.

Hynynen, K., A. Darkazanli, et al. (1993). "Tissue thermometry during ultrasound exposure." Eur Urol 23(Suppl 1): 12-6.

Hynynen, K., A. Darkazanli, et al. (1993). "MRI-guided noninvasive ultrasound surgery." Med Phys 20(1): 107-15.

Hynynen, K. and D. DeYoung (1988). "Temperature elevation at muscle-bone interface during scanned, focused ultrasound hyperthermia." Int J Hyperthermia 4(3): 267-79.

Hynynen, K. and D. K. Edwards (1989). "Temperature measurements during ultrasound hyperthermia." Med Phys 16(4): 618-26.

Hynynen, K. and F. A. Jolesz (1998). "Demonstration of potential noninvasive ultrasound brain therapy through an intact skull." Ultrasound Med Biol 24(2): 275-83.

Hynynen, K., N. McDannold, et al. (2001). "Noninvasive MR imaging-guided focal opening of the blood-brain barrier in rabbits." Radiology 220(3): 640-6.

Hynynen, K., O. Pomeroy, et al. (2001). "MR imaging-guided focused ultrasound surgery of fibroadenomas in the breast: a feasibility study." Radiology 219(1): 176-85.

Hynynen, K., R. Roemer, et al. (1987). "A scanned, focused, multiple transducer ultrasonic system for localized hyperthermia treatments." Int J Hyperthermia 3(1): 21-35.

Hynynen, K., D. Shimm, et al. (1990). "Temperature distributions during clinical scanned, focused ultrasound hyperthermia treatments." Int J Hyperthermia 6(5): 891-908.

Ibbini, M. S. and C. A. Cain (1990). "The concentric-ring array for ultrasound hyperthermia: combined mechanical and electrical scanning." Int J Hyperthermia 6(2): 401-19.

Jaffe, B., R. Roth, et al. (1955). "Properties of piezoelectric ceramics in solid solution series lead titanate-lead zirconate-lead oxide: tin oxide and lead titanate-lead hafnate." J. Res. Nat. Bur. Stand. 55: 239.

Johnston, R. L. and F. Dunn (1976). "Ultrasonic absorbed dose, dose rate, and produced lesion volume." Ultrasonics 14(4): 153-5.

Kallel, F., R. J. Stafford, et al. (1999). "The feasibility of elastographic visualization of HIFU-induced thermal lesions in soft tissues. Image-guided high-intensity focused ultrasound." Ultrasound Med Biol 25(4): 641-7.

Keshavarzi, A., S. Vaezy, et al. (2001). "Attenuation coefficient and sound speed in human myometrium and uterine fibroid tumors." J Ultrasound Med 20(5): 473-80.

Keshavarzi, A., S. Vaezy, et al. (2002). "Treatment of uterine leiomyosarcoma in a xenograft nude mouse model using high-intensity focused ultrasound: a potential treatment modality for recurrent pelvic disease." Gynecol Oncol. 86(3):344-50.

Keshavarzi, A., S. Vaezy, et al. (2002). "Treatment of uterine fibroid tumors in Eker rats using high intensity focused ultrasound." Submitted publication.

Kincaide, L. F., N. T. Sanghvi, et al. (1996). "Noninvasive ultrasonic subtotal ablation of the prostate in dogs." Am J Vet Res 57(8): 1225-7.

King, R. L., G. T. Clement, et al. (2003). "Preliminary results using ultrasound transmission for image-guided thermal therapy." Ultrasound Med Biol 29(2): 301-7.

Kishi, M., T. Mishima, et al. (1975). "Experimental studies of effects of intense ultrasound on implantable murine glioma." Proceedings of the 2n European Congress on Ultraonics in Medicine: 28-33.

Kjerulff, K. H., P. Langenberg, et al. (1996). "Uterine leiomyomas. Racial differences in severity, symptoms and age at diagnosis." J Reprod Med 41(7): 483-90.

Kohrmann, K. U., M. S. Michel, et al. (2002). "High intensity focused ultrasound as noninvasive therapy for multilocal renal cell carcinoma: case study and review of the literature." J Urol 167(6): 2397-403.

Kossoff, G. (1979). "Analysis of focusing action of spherically curved transducers." Ultrasound Med Biol 5(4): 359-65.

Lafon, C., P. Kaczkowski, et al. (2001). Development and characterization of an innovative synthetic tissue-mimicking material for high intensity focused ultrasound (HIFU) exposures. Internation Congress on Acoustics, Rome, Italy.

Lagneaux, L., E. C. de Meulenaer, et al. (2002). "Ultrasonic low-energy treatment: a novel approach to induce apoptosis in human leukemic cells." Exp Hematol 30(11): 1293-301.

Lalonde, R., A. Worthington, et al. (1993). "Field Conjugate Acoustic Lenses for Ultrasound Hyperthermia." IEEE Trans Ultrason Ferroelectr Freq Control 40(5): 592-602.

Lele, P. (1962). "A simple method for production of trackless focal lesions with focused ultrasound: Physical factors." J Physiol 160: 494-512.

Lele, P. (1967). "Production of deep focal lesions by focused ultrasound - current status." Ultrasonics 5: 105-122.

Lele, P. (1977). "Thresholds and mechanisms of ultrasonic damage to "organized" animal tissues." Symposium on biological effects and characterizations of ultrasound sources FDA 78-8048: 224-239.

Lele, P. P. (1966). "Concurrent detection of the production of ultrasonic lesions." Med Biol Eng 4(5): 451-6.

Lepine, L. A., S. D. Hillis, et al. (1997). "Hysterectomy surveillance--United States, 1980-1993." Mor Mortal Wkly Rep CDC Surveill Summ 46(4): 1-15.

Li, C. X., G. L. Xu, et al. (2003). "[High intensity focused ultrasound for liver cancer]." Zhonghua Zhong Liu Za Zhi 25(1): 94-6.

Linke, C., E. Carstensen, et al. (1973). "Localized tissue destruction by high-intensity focused ultrasound." Arch. Surg 107: 887-891.

Lynn, J., R. Zwemer, et al. (1942). "A new method for the generation and use of focused ultrasound in experimental biology." J. Gen. Physiol. 26: 179-93.

Madersbacher, S., C. Kratzik, et al. (1998). "Transcutaneous high-intensity focused ultrasound and irradiation: an organ-preserving treatment of cancer in a solitary testis." Eur Urol 33(2): 195-201.

Madersbacher, S., M. Pedevilla, et al. (1995). "Effect of high-intensity focused ultrasound on human prostate cancer in vivo." Cancer Res 55(15): 3346-51.

Malone, L. J. (1969). "Myomectomy: recurrence after removal of solitary and multiple myomas." Obstet Gynecol 34(2): 200-3.

Marshall, L. M., D. Spiegelman, et al. (1997). "Variation in the incidence of uterine leiomyoma among premenopausal women by age and race." Obstet Gynecol 90(6): 967-73.

Marshall, L. M., D. Spiegelman, et al. (1998). "A prospective study of reproductive factors and oral contraceptive use in relation to the risk of uterine leiomyomata." Fertil Steril 70(3): 432-9.

Martin, R. W., S. Vaezy, et al. (1999). "Hemostasis of punctured vessels using Doppler-guided high-intensity ultrasound." Ultrasound Med Biol 25(6): 985-90.

Masaoka, H., N. Akamatsu, et al. (1987). Ultrasonic attenuation coefficient of uterine myomas. Euroson '87, Helsink, Finland.

McDannold, N. J., F. A. Jolesz, et al. (1999). "Determination of the optimal delay between sonications during focused ultrasound surgery in rabbits by using MR imaging to monitor thermal buildup in vivo." Radiology 211(2): 419-26.

Mesiwala, A. H., L. Farrell, et al. (2002). "High-intensity focused ultrasound selectively disrupts the blood-brain barrier in vivo." Ultrasound Med Biol 28(3): 389-400.

Meyers, R., W. Fry, et al. (1959). "Early Experiences with ultrasonic irradiation of the pallidofugal and nigral complexes in hyperkinetic and hypertonic disorders." J Neurosurg 16: 32-54.

Miller, D. L. and J. Quddus (2000). "Diagnostic ultrasound activation of contrast agent gas bodies induces capillary rupture in mice." Proc Natl Acad Sci U S A 97(18): 10179-84.

Miller, D. L. and J. Quddus (2001). "Lysis and sonoporation of epidermoid and phagocytic monolayer cells by diagnostic ultrasound activation of contrast agent gas bodies." Ultrasound Med Biol 27(8): 1107-13.

Moore, W. E., R. M. Lopez, et al. (1989). "Evaluation of high-intensity therapeutic ultrasound irradiation in the treatment of experimental hepatoma." J Pediatr Surg 24(1): 30-3; discussion 33.

Mulligan, E. D., T. H. Lynch, et al. (1997). "High-intensity focused ultrasound in the treatment of benign prostatic hyperplasia." Br J Urol 79(2): 177-80.

Nakamura, K., S. Baba, et al. (1997). "High-intensity focused ultrasound energy for benign prostatic hyperplasia: clinical response at 6 months to treatment using Sonablate 200." J Endourol 11(3): 197-201.

Neisius, D. and V. Moll (1989). "Renal ultrasonography in the management of calculus disease." Urologic Clin. North Am. 16: 829-840.

Nowak, R. A. (1999). "Fibroids: pathophysiology and current medical treatment." Baillieres Best Pract Res Clin Obstet Gynaecol 13(2): 223-38.

O'Brien, W. (1980). Biological effects of ultrasound. Medical physics of CT and ultrasound: tissue imaging and characterization. G. Fullerton and J. Zagzebski. New York, American Institute of Physics.

Oka, M. (1964). "Application of intense focused ultrasound in brain surgery and other fields." Clinica All-Round (Japan) 13: 1514.

Oka, M. (1977). "Progress in studies of the potential use of medical ultraonics." Wakayama Medical Report (Japan) 20: 1-50.

Oosterhof, G. O., E. B. Cornel, et al. (1997). "Influence of high-intensity focused ultrasound on the development of metastases." Eur Urol 32(1): 91-5.

Paterson, R. F., E. Barret, et al. (2003). "Laparoscopic partial kidney ablation with high intensity focused ultrasound." J Urol 169(1): 347-51.

Pelage, J. P., O. Le Dref, et al. (2000). "Fibroid-related menorrhagia: treatment with superselective embolization of the uterine arteries and midterm follow-up." Radiology 215(2): 428-31.

Pennes, M. (1948). "Analysis of tissue and arterial blood temperature in the resting human forearm." J. Appl. Physiol. 1: 93-122.

Pond, J. B. (1970). "The role of heat in the production of ultrasonic focal lesions." J Acoust Soc Am 47(6): 1607-11.

Prat, F., M. Centarti, et al. (1995). "Extracorporeal high-intensity focused ultrasound for VX2 liver tumors in the rabbit." Hepatology 21(3): 832-6.

Reilly, C. R. (1991). "Tissue heating measurements during high intensity focused ultrasound." J Ultrasound Med 10: S26.

Robboy, S. J., R. C. Bentley, et al. (2000). "Pathology and pathophysiology of uterine smooth-muscle tumors." Environ Health Perspect 108 Suppl 5: 779-84.

Roberts, W. W., D. Y. Chan, et al. (2002). "High intensity focused ultrasound ablation of the vas deferens in a canine model." J Urol 167(6): 2613-7.

Roberts, W. W., E. J. Wright, et al. (2002). "High-intensity focused ultrasound ablation of the epididymis in a canine model: a potential alternative to vasectomy." J Endourol 16(8): 621-5.

Robinson, T. and P. Lele (1972). "An analysis of lesion development in the brain and plastics by high-intensity focused ultrasound at low-megahertz frequencies." J Acoust Soc Am 51: 1333-1351.

Rosati, P., C. Exacoustos, et al. (1992). "Longitudinal evaluation of uterine myoma growth during pregnancy. A sonographic study." J Ultrasound Med 11(10): 511-5.

Rosecan, L., T. Iwamoto, et al. (1985). "Therapeutic ultrasound in the treatment of retinal detatchment: clinical observation and light and electron microscopy." Retina 5: 115-22.

Ross, R. K., M. C. Pike, et al. (1986). "Risk factors for uterine fibroids: reduced risk associated with oral contraceptives." Br Med J (Clin Res Ed) 293(6543): 359-62.

Rowland, I. J., I. Rivens, et al. (1997). "MRI study of hepatic tumours following high intensity focused ultrasound surgery." Br J Radiol 70: 144-53.

Sanghvi, N. T., R. S. Foster, et al. (1999). "Noninvasive surgery of prostate tissue by high intensity focused ultrasound: an updated report." Eur J Ultrasound 9(1): 19-29.

Sanghvi, N. T. and R. H. Hawes (1994). "High-intensity focused ultrasound." Gastrointest Endosc Clin N Am 4(2): 383-95.

Schechter, R., H. Chaskelis, et al. (1994). "Real-Time Parallel Computation and Visualization of Ultrasonic Pulses in Solids." Science 265: 1188-1192.

Schwartz, L. B., M. P. Diamond, et al. (1993). "Leiomyosarcomas: clinical presentation." Am J Obstet Gynecol 168(1 Pt 1): 180-3.

Seip, R. and E. S. Ebbini (1995). "Noninvasive estimation of tissue temperature response to heating fields using diagnostic ultrasound." IEEE Trans Biomed Eng 42(8): 828-39.

Selfridge, A. (1985). "Approximate material properties in isotropic materials." IEEE Trans Sonics Ultrasonics SU-32(3): 381-388.

Sette, D. (1949). "Ultrasonic Lenses of Plastic Materials." J Acoust Soc Am 21(4): 375-381.

Shaw, R. W. (1991). "New approaches to the management of fibroids." Curr Opin Obstet Gynecol 3(6): 859-64.

Shi, X., R. W. Martin, et al. (1999). "Detection of high-intensity focused ultrasound liver lesions using dynamic elastometry." Ultrason Imaging 21(2): 107-26.

Sibille, A., F. Prat, et al. (1993). "Extracorporeal ablation of liver tissue by high-intensity focused ultrasound." Oncology 50(5): 375-9.

Siddiqi, T. A., M. Miodovnik, et al. (1999). "In vivo ultrasonographic exposimetry: human tissue-specific attenuation coefficients in the gynecologic examination." Am J Obstet Gynecol 180(4): 866-74.

Siddiqi, T. A., W. D. O'Brien, Jr., et al. (1992). "Human in situ dosimetry: differential insertion loss during passage through abdominal wall and myometrium." Ultrasound Med Biol 18(8): 681-9.

Silverman, R., B. Vogelsang, et al. (1991). "Therapeutic ultrasound for the treatment of glaucoma." Am J Ophthalmol 111: 327-37.

Skyba, D. M., R. J. Price, et al. (1998). "Direct in vivo visualization of intravascular destruction of microbubbles by ultrasound and its local effects on tissue." Circulation 98(4): 290-3.

Smith, R. A. (1989). "Are hydrophones of diameter 0.5 mm small enough to characterise diagnostic ultrasound equipment?" Phys Med Biol 34(11): 1593-607.

Smith, S. J. (2000). "Uterine fibroid embolization." Am Fam Physician 61(12): 3601-7, 3611-2.

Sokka, S. D., R. King, et al. (2003). "MRI-guided gas bubble enhanced ultrasound heating in in vivo rabbit thigh." Phys Med Biol 48(2): 223-41.

Spies, J. B., A. R. Scialli, et al. (1999). "Initial results from uterine fibroid embolization for symptomatic leiomyomata." J Vasc Interv Radiol 10(9): 1149-57.

Stewart, E. A. (2001). "Uterine fibroids." Lancet 357(9252): 293-8.

Stewart, E. A. and R. A. Nowak (1996). "Leiomyoma-related bleeding: a classic hypothesis updated for the molecular era." Hum Reprod Update 2(4): 295-306.

Stewart, E. A. and R. A. Nowak (1998). "New concepts in the treatment of uterine leiomyomas." Obstet Gynecol 92(4 Pt 1): 624-7.

Stjernquist, M. (1997). "Treatment of uterine fibroids with GnRH-analogues prior to hysterectomy." Acta Obstet Gynecol Scand Suppl 164: 94-7.

Stovall, D. W. (2001). "Clinical symptomatology of uterine leiomyomas." Clin Obstet Gynecol 44(2): 364-71.

Strobelt, N., A. Ghidini, et al. (1994). "Natural history of uterine leiomyomas in pregnancy." J Ultrasound Med 13(5): 399-401.

Sullivan, L. D., M. G. McLoughlin, et al. (1997). "Early experience with high-intensity focused ultrasound for the treatment of benign prostatic hypertrophy." Br J Urol 79(2): 172-6.

Susani, M., S. Madersbacher, et al. (1993). "Morphology of tissue destruction induced by focused ultrasound." Eur Urol 23(Suppl 1): 34-8.

Swindell, W. (1985). "A theoretical study of nonlinear effects with focused ultrasound in tissues: an "acoustic bragg peak"." Ultrasound Med Biol 11(1): 121-30.

Szent-Gyorgi, A. (1933). "Chemical and biological effects of ultrasonic radiation." Nature 131: 278.

Tachibana, K., T. Uchida, et al. (1999). "Induction of cell-membrane porosity by ultrasound." Lancet 353(9162): 1409.

Tarnoczy, T. (1965). "Sound focussing lenses and waveguides." Ultrasonics Jul-Sep: 115-127.

Taylor, K. J. and C. C. Connolly (1969). "Differing hepatic lesions caused by the same dose of ultrasound." J Pathol 98(4): 291-3.

Tempany, C. M., E. A. Stewart, et al. (2003). "MR imaging-guided focused ultrasound surgery of uterine leiomyomas: a feasibility study." Radiology 226(3): 897-905.

ter Haar, G. (1988). Biological Effects of Ultrasound in Clinical Applications. Ultrasound: Its chemical, physical, and biological effects. K. Suslick. New York, VCH: 305-20.

ter Haar, G. (1999). "Therapeutic ultrasound." Eur J Ultrasound 9(1): 3-9.

ter Haar, G., S. Daniels, et al. (1986). "Evidence for acoustic cavitation in vivo: thresholds for bubble formation with 0.75 MHz continuous wave and pulsed beams." IEEE Trans Ultrason Ferroelectr Freq Control UFFC-33: 162-164.

ter Haar, G., I. Rivens, et al. (1991). "High intensity focused ultrasound for the treatment of rat tumours." Phys Med Biol 36(11): 1495-501.

ter Haar, G., D. Sinnett, et al. (1989). "High intensity focused ultrasound--a surgical technique for the treatment of discrete liver tumours." Phys Med Biol 34(11): 1743-50.

Thomas, J. and M. Fink (1996). "Ultrasound beam focusing through tissue inhomogeneities with a time reverasl mirror: application to transskull therapy." IEEE Trans Ultrason Ferroelectr Freq Control 43: 1122-1129.

Uchida, T., N. T. Sanghvi, et al. (2002). "Transrectal high-intensity focused ultrasound for treatment of patients with stage T1b-2n0m0 localized prostate cancer: a preliminary report." Urology 59(3): 394-8; discussion 398-9.

Vaezy, S., M. Andrew, et al. (2001). "Image-guided acoustic therapy." Annu Rev Biomed Eng 3: 375-90.

Vaezy, S., V. Y. Fujimoto, et al. (2000). "Treatment of uterine fibroid tumors in a nude mouse model using high- intensity focused ultrasound." Am J Obstet Gynecol 183(1): 6-11.

Vaezy, S., R. Martin, et al. (1999). "High Intensity Focused Ultrasound Used for Hemostasis of Liver and Spleen." Proceedings of Amer Ins Ultrasound Med 18: 42.

Vaezy, S., R. Martin, et al. (1999). "Use of high-intensity focused ultrasound to control bleeding." J Vasc Surg 29(3): 533-42.

Vaezy, S., R. Martin, et al. (1999). "Control of splenic bleeding by using high intensity ultrasound." J Trauma 47(3): 521-5.

Vaezy, S., R. Martin, et al. (1997). "Liver hemostasis using high-intensity focused ultrasound." Ultrasound Med Biol 23(9): 1413-20.

Vaezy, S., R. Martin, et al. (1998). "Hemostasis of punctured blood vessels using high-intensity focused ultrasound." Ultrasound Med Biol 24(6): 903-10.

Vaezy, S., X. Shi, et al. (2001). "Real-time visualization of high-intensity focused ultrasound treatment using ultrasound imaging." Ultrasound Med Biol 27(1): 33-42.

Vallancien, G., E. Chartier-Kastler, et al. (1991). "Focussed extracorporeal pyrotherapy: experimental results." Eur Urol 20(3): 211-9.

Vallancien, G., E. Chartier-Kastler, et al. (1993). "Focused extracorporeal pyrotherapy: experimental study and feasibility in man." Semin Urol 11(1): 7-9.

Visioli, A. G., I. H. Rivens, et al. (1999). "Preliminary results of a phase I dose escalation clinical trial using focused ultrasound in the treatment of localised tumours." Eur J Ultrasound 9(1): 11-8.

Vykhodtseva, N., N. McDannold, et al. (2001). "Apoptosis in ultrasound-produced threshold lesions in the rabbit brain." Ultrasound Med Biol 27(1): 111-7.

Wall, P., W. Fry, et al. (1951). "Changes produced in the central nervous system by ultrasound." Science 114: 686-687.

Wang, X. and J. Sun (2002). "High-intensity focused ultrasound in patients with late-stage pancreatic carcinoma." Chin Med J (Engl) 115(9): 1332-5.

Waterman, F. M., R. E. Nerlinger, et al. (1990). "Catheter induced temperature artifacts in ultrasound hyperthermia." Int J Hyperthermia 6(2): 371-81.

Watkin, N. A., S. B. Morris, et al. (1997). "High-intensity focused ultrasound ablation of the kidney in a large animal model." J Endourol 11(3): 191-6.

Wong, G. C., S. J. Muir, et al. (2000). "Uterine artery embolization: a minimally invasive technique for the treatment of uterine fibroids." J Womens Health Gend Based Med 9(4): 357-62.

Wood, R. and A. Loomis (1927). "The physical and biological effects of high frequency sound waves of greater intensity." The London, Edinburgh, and Dublin Philosophical Magazine and Journal of Science 4: 417-436.

Wu, F., W. Z. Chen, et al. (2001). "Pathological changes in human malignant carcinoma treated with high- intensity focused ultrasound." Ultrasound Med Biol 27(8): 1099-106.

Wu, F., W. Z. Chen, et al. (2002). "Tumor vessel destruction resulting from high-intensity focused ultrasound in patients with solid malignancies." Ultrasound Med Biol 28(4): 535-42.

Yang, R., K. K. Kopecky, et al. (1993). "Sonographic and computed tomography characteristics of liver ablation lesions induced by high-intensity focussed ultrasound." Invest Radiol 28(9): 796-801.

Yang, R., C. R. Reilly, et al. (1991). "High-intensity focused ultrasound in the treatment of experimental liver cancer." Arch Surg 126(8): 1002-9; discussion 1009-10.

Yang, R., C. R. Reilly, et al. (1992). "Effects of high-intensity focused ultrasound in the treatment of experimental neuroblastoma." J Pediatr Surg 27(2): 246-50; discussion 250-1.

Yang, R., N. T. Sanghvi, et al. (1992). "Extracorporeal liver ablation using sonography-guided high-intensity focused ultrasound." Invest Radiol 27(10): 796-803.

Yuen, J. (2001). Characterization of Lesion Formation in a Tissue-Mimicking Phantom for Focused Ultrasound Surgery. Bioengineering. Seattle, University of Washington.

Zanelli, C., S. DeMarta, et al. (1993). "Beam forming for therapy with high intensity focused ultrasound (HIFU) using quantitative schlieren." IEEE Ultrasonics Symp.: 1233-1238.

Zhong, P., Y. Zhou, et al. (2001). "Dynamics of bubble oscillation in constrained media and mechanisms of vessel rupture in SWL." Ultrasound Med Biol 27(1): 119-34.

Ziskin, M. C. and P. Lewan (1993). Ultrasonic Exposimetry. Boca Raton, Florida, CRC Press.

APPENDIX A COMPILATION OF HIFU STUDIES

Notes:
I_{SATA} is spatial average temporal average intensity
FWHM is full width at half maximum
G refers to the method of guidance used: V for visual, U for ultrasound, M for MRI

Year	First Author	Tissue, study type	Model (#)	Frequency Aperture Focal dist.	I_{SATA} (W/cm^2)	FWHM beam profile (mm)	G	Findings
1992	Yang (Yang *et al.*, 1991)	Liver, Survival	Morris rat hepa-toma (112)	4 MHz 5.5 cm 8 cm	550	7 x 0.6	V	Survival rate higher in HIFU treated animals
1992	Yang (Yang *et al.*, 1992)	Liver, testing guidance	NZ white rabbits (10)	4 MHz 30 x 13 mm 3.5 cm	1500	5 x 0.5	U	Coagulation necrosis visible, targeting with US feasible
1992	Yang et al. (Yang *et al.*, 1992)	Murine Neuro-blastoma	Ajax mice (60)	4 MHz 5.5 cm 8 cm	550	7 x 0.6	V	HIFU treatment inhibits tumor growth
1992	Vallancien (Vallancien *et al.*, 1993)	BPH, (28) bladder tumors (12) kidney (8) liver (2)	Human (50)	1 MHz ? 32 cm		10 x 1.5	U	Tissue laceration, hyperemia with few skin burns noticed
1992	Chapelon (Chapelon *et al.*, 1992)	Prostatic adenocarci noma	Rat (50)	1 MHz	300 - 2750	10 x 2		Reduced tumor growth and prolonged host survival
1993	Ter Haar (ter Haar *et al.*, 1993)	Liver, histology analysis	Rat	1.7 MHz 10 cm 14 cm	300	15 x 1.5	V	Cellular destruction at center of lesion, rim 10 cells wide surround damage
1993	Gelet (Gelet *et al.*, 1993)	Prostate	Dog (37)	2.25 MHz 3.5 cm 3.5 cm	720 – 2300		U	Lesions created in prostatic tissue through rectal wall
1993	Sibille (Sibille *et al.*, 1993)	Liver tissue, dosimetry	Rabbit (74)	1 MHz 10 cm 10 cm	1000 – 5500	14 x 1.8	U	Lesion volume increased with exposure time and intensity
1995	Uchida (Uchida *et al.*, 1995)	BPH	Human (28)	4 MHz 30 x 13 mm 3.0, 3.5	1680	10 x 2	U	Prostate symptom score and quality of life showed improvement

1995	Prat (Prat *et al.*, 1995)	VX2 liver tumors	Rabbit (14)	1 MHz 10 cm 10 cm	1000	10 x 2	U	Tumor destruction, proliferation and tumorigenesis decreased
1995	Vallancien (Vallancien *et al.*, 1996)	Bladder tumors	Human (25)	1 MHz ? 32 cm		10 x 2	U	Ablation of superficial bladder tumor with minimal recurrence
1995	Madersbacher (Madersbacher *et al.*, 1995)	Prostate Cancer	Human (29)	4 MHz ? 3, 3.5, 4 cm	1260 – 2000		U	Sharply delineated coagulative necrosis with no alerations of periprostatic structure
1996	Adams (Adams *et al.*, 1996)	Renal tumors	Rabbit (18)	4 MHz 3 cm 3 cm			U	HIFU effective for cell death in renal tumors, imaging not adequate
1996	Kincaide (Kincaide *et al.*, 1996)	Prostate	Dog (4)	4 MHz 30 x 20 mm 2.5, 3, 3.5	1680 – 2100	10 x 2	U	Hemorrhagic liquefactive necrosis shown, cystic cavities developed
1997	Vaezy (Vaezy *et al.*, 1997)	Liver hemostasis	Rabbits (10)	3.3 MHz 2.84 cm 4 cm	3000		V	Coagulative necrosis and controlled bleeding achieved
1998	Madersbacher (Madersbacher *et al.*, 1998)	Testis	Human (1)	4.0 MHz 3 – 4 cm	1600 – 2000	10-20 x 2	U	Cellular necrosis in HIFU treated areas
1999	Visioli (Visioli *et al.*, 1999)	Prostate, renal and bladder carcinoma, melanoma	Human (14)	1.69 MHz 10 cm 15 cm	1500		U	HIFU safe, well tolerated, more clinical trials needed
1999	Gelet (Gelet *et al.*, 1999)	Prostate cancer	Human (50)	2.25 MHz ? 4.25 cm			U	Morbidity assoc. with HIFU is minimal. complication rates as low as 17%.
1999	Daum (Daum *et al.*, 1999)	Liver and kidney	Pig (7)	1.1 MHz 12 cm 10 cm			M	Focal lesions created using single 20 s sonication

1999	Vaezy (Vaezy *et al.*, 1999)	Longitudinal incisions in vein, arteries	Pigs (4)	3.5 MHz 3.5 cm 3.5 cm	2500 – 3000	9 x 1	V	Major / complete hemostasis achieved
1999	Vaezy (Vaezy *et al.*, 1999)	Spleen hemostasis	Pigs (5)	5.0 MHz 3.5 cm 3.5 cm	6000	13.5 x 0.67	V	Bleeding from incisions stopped within one minute
1999	He (He *et al.*, 1999)	Variety of tumors	Human (160)	1.04 MHz 2-15 cm	1000 – 2000	3 x 8 to 6 x 10	U	Successful in 97%, no skin burns
1999	Chen (Chen *et al.*, 1999)	Liver (histology)	Rat (1)	1.7 MHz 10 cm 14 cm	382 – 479	21 x 2.1	V	Indirect tissue damage outside treatment volume due to blood vessel damage
1999	Vaezy (Vaezy *et al.*, 2000)	Uterine fibroid tumors	Mouse (28)	3.5 MHz ? 5.5cm	2000	9 x 1	V	Complete tumor shrinkage after 1 or 2 treatments observed, no recurrence
2001	Hynynen (Hynynen *et al.*, 2001)	Breast fibroadenomas	Human (9)	1.5 MHz 100 mm 80 mm	40 W	4.8 x 1	M	Coagulation of fibroadenomas observed
2001	Wu (Wu *et al.*, 2001)	Liver, breast, bone tumor, soft tissue sarcoma	Human (164)	0.8 – 3.2 MHz 12 cm 9 – 16 cm	5000 – 20000	3.3 x 1.1	U	Treatments safe and feasible, accurate treatment of targeted areas
2002	Kesharvarzi (Keshavarzi *et al.*, 2002)	Uterine fibroid tumors	Eker rat (29)	3.5 MHz 2.3 cm 3.5 cm	2000	10 x 2	V	70% showed significant tumor volume reduction
2002	Kesharvarzi (Keshavarzi *et al.*, 2002)	Uterine leiomyo-sarcoma	Mouse (65)	2 MHz 3.5 cm 5.5 cm	2000	16 x 2	V	Reduction in tumor volume after HIFU, sham tumor growth
2002	Noble (Noble *et al.*, 2002)	Spleen hemostasis	Rabbit (21)	9.6 MHz 1.9 cm 2.5 cm	3000		V	
2002	Chen (Chen *et al.*, 2002)	Malignant solid tumors	Humans (30)					Side effects of skin injury, nerve damage, new metastases
2002	Fried (Fried *et al.*, 2002)	Epididymis	Dogs (4)		3-7 W			Potential for male sterilization

2002	Kohrmann (Kohrmann *et al.*, 2002)	Renal cell carcinoma		Parabolic reflector				Thermal ablation in 2/3 tumors
2002	Uchida (Uchida *et al.*, 2002)	Localized prostate cancer	Humans (20)	? ? 2.5 – 4.5 cm			U	Complete response in all patients
2002	Wang (Wang *et al.*, 2002)	Pancreatic cancer	Humans (15)					HIFU destroyed carcinoma and alleviated abdominal pain
2002	Wu (Wu *et al.*, 2002)	Tumor blood vessels	Humans (164)	0.8, 1.6, 3.2 MHz 12 cm 9,13,16 cm	5000-20000	3.3 x 1.1 (1.6 MHz)	U	Tumor cells necrosed, small vessles feeding tumor ablated
2003	Paterson (Paterson *et al.*, 2003)	Kidney	Pigs (13)				U	Homogeneous and complete tissue necrosis
2003	Tempany (Tempany *et al.*, 2003)	Uterine Fibroids	Humans (6)				M	

APPENDIX B MATLAB CODE TO GENERATE ACOUSTIC LENS

```
% acoustic lens design file
% aclens.m
%get inputs
clear
d=input('Enter the Diameter of the Disk (cm) :');
xf=input('Enter the Focal Length (cm) :');
c1=input('Enter the speed of sound in the lens media (m/s) :');
c2=input('Enter the speed of sound in the external media (m/s) :');
iter=input('Enter number of steps :');
%calculations for all y values
r=d/2;
cr=c2/c1;
yr=0;
x(1)=0;
y(1)=0;
dy=r/iter;
for i=2:(iter)+1
  yr=yr+dy;
  y(i)=yr;
  a=(1-cr^2);
  b=(2*xf*(cr-1));
  c=(yr^2);
  xpos=(-b+sqrt(b^2-4*a*c))/(2*a);
  xneg=(-b-sqrt(b^2-4*a*c))/(2*a);
  if (xpos<=xneg) x(i)=xpos;
  else
    x(i)=xneg;
  end
  z(i)=0;
end
%plot lens
figure
plot(xf,0,'*',x,y,'b',x,-y,'b')
xlabel('Axial Distance (cm)')
ylabel('Radial Distance (cm)')
title('Acoustic Lens Simulation')
grid
%print values
scurve=1/2.54*[z' -x' y'];
```

APPENDIX C HUMAN ERGONOMIC STUDIES: PATIENT AND SONOGRAPHER SURVEY

Human Volunteer Feedback:

Responses to the post-study survey are as follows. Study participants can answer one of five responses to each question (strongly agree, agree, undecided, disagree, strongly disagree) and provide comments. Comments are compiled and are in no particular order.

Question 1: The entrance of the probe in the vagina was comfortable

Response (Number)	Comments
Agree (5)	- when condom was filled with water and lubricant used, entrance was not painful - no worse than typical for a vaginal ultrasound, better than a speculum - coaching and good feedback by study staff was helpful - using warmed gel helped but the probe was cold
Disagree (1)	- entrance was uncomfortable, felt blunt and large, not smooth (note - water balloon may not have been sufficiently filled. Subject also had a longer duration of transvaginal imaging than other volunteers where the probe was moved around significantly)

Question 2: While the probe was in the vagina, it did not cause any discomfort

Response (Number)	Comments
Strongly Agree (4)	- slight pressure when locating fundus, may have been due to full bladder - could barely feel it, only when it was moved or when water was added - movements were slow and felt no discomfort
Agree (2)	- a little uncomfortable at times - slight pinching, watching the monitor helps to know what to anticipate

Question 3: The exit of the probe from the vagina was comfortable

Response (Number)	Comments
Strongly Agree (6)	- couldn't feel anything, no discomfort

Sonographer Feedback:

Responses provided by our sonographer (Marla Paun) have been compiled from five of the volunteer studies. A feedback form was not supplied for the first volunteer.

Question 1: The entrance of the probe in the vagina was easy

Response (Number)	Comments
Strongly Agree (4)	- slight resistance in all cases except in one volunteer who took a deep breath and relaxed
Undecided (1)	- one volunteer had discomfort upon entrance after a lengthy transvaginal exam where the probe was moved around significantly

Question 2 : While the probe was in the vagina, it was not difficult to maneuver and move it

Response (Number)	Comments
Strongly Agree (4)	- probe was easy to maneuver in all directions
Agree (1)	- some difficulty in imaging probe since the distance between the HIFU probe and imaging probe was greater than in previous studies (note subject BMI was higher than others in study)

Question 3: The exit of the probe from the vagina was easy

Response (Number)	Comments
Strongly Agree (5)	- exit was easy

Imaging capability of the abdominal imaging probe ranked on a scale of 1-5 with 1 being the best

Response (Number)	Comments
1 (5)	- good diagnostic quality

Other comments provided

- probe was easily moved
- one volunteer had larger bladder than others and visualization of HIFU probe not as good
- caution must be taken for insertion of HIFU probe if volunteer experienced discomfort in transvaginal imaging

APPENDIX D POSITION SENSOR SPECIFICATIONS

POTENTIOMETER SPECIFICATIONS

Potentiometer Type	1-turn, conductive plastic
Resistance: Value, Tolerance	5K ohms, ±10%
Travel: Electrical, Mechanical	340°, 340° minimum
Mechanical Life	100 million shaft revolutions
Power Rating	0.75 watts at 158° F (70° C); maximum input voltage of 38 V
Max. Indep. Linearity Error	±0.5% per VRCI-P-100A
Output Smoothness	0.1%
Insulation Resistance	1000 Mohms at 500 VDC minimum
Dielectric Strength	500 VDC minimum
Resolution	infinite signal
Operating Temperature	-65° to +257° F (-65° to +125° C)
Shock, Vibration	100 g for 6 ms, 10 to 2000 Hz at 15 g per Mil-R-39023
Temperature Coefficient (Max.)	±400 ppm/°C
Output Signal	analog signal from 0 to supply voltage (voltage divider circuit)
Max. Wiper (Signal) Current	20 µA
Max. Supply Voltage	35 VDC / 35 VAC (using voltage divider circuit)

OTHER SPECIFICATIONS

Case Materials	precision-machined anodized 2024 aluminum
Displacement Cable	0.018-inch (0.46-mm) dia., 7-by-7 stranded stainless steel, 40-lb (177-N) min. breaking strength. A minimum of 12 inches (305 mm) of displacement cable is provided with an uncrimped loop sleeve and pull ring for connection to the application. The 160001-01 installation kit is available if you do not have a suitable crimping solution.
Electrical Cable	A minimum of 18 inches (457 mm) of electrical cable is provided. Electrical cable is terminated with flying leads (no electrical connector). Cable is 30 gauge diameter (minimum) with Teflon insulation.

		Series 173			Series 174		Series 175		Series 176	
Approximate Weight		1 oz.	28 g		2 oz.	57 g	3 oz.	85 g	4 oz.	113 g
Displacement Cable	Min	0.5 oz.	0.1 N	Opt. 1	3 oz.	0.8 N	2 oz.	0.6 N	2.5 oz.	0.7 N
Tension and Max. Cable	Max	4 oz.	1.1 N	8 g's max.	12 oz.	3.3 N	10 oz.	2.8 N	8 oz.	2.2 N
Acceleration	Min	2 oz.	0.6 N	Opt. 2	8 g's max.		8 g's max.		8 g's max.	
	Max	10 oz.	2.8 N	17 g's max.						

Environmental Protection: NEMA 3S / IP 54, DO-160D Env. Cat. E1E1ABSHXFDXSAXXXXXXXXXX

MODEL NUMBERS

173-0241-abc	position transducer (3.00-inch (76-mm) range)
174-0321-abc	position transducer (4.00-inch (102-mm) range)
175-0401-abc	position transducer (5.00-inch (127-mm) range)
176-0521-abc	position transducer (6.50-inch (165-mm) range)

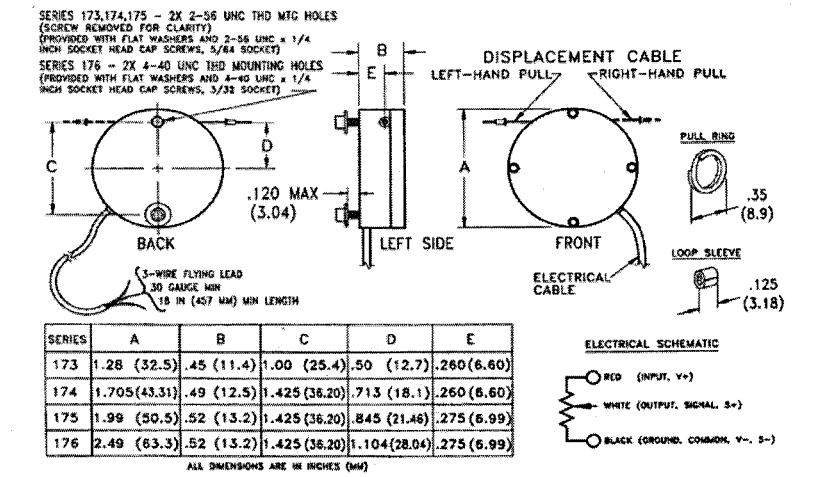

SERIES	A	B	C	D	E
173	1.28 (32.5)	.45 (11.4)	1.00 (25.4)	.50 (12.7)	.260 (6.60)
174	1.705 (43.31)	.49 (12.5)	1.425 (36.20)	.713 (18.1)	.260 (6.60)
175	1.99 (50.5)	.52 (13.2)	1.425 (36.20)	.845 (21.46)	.275 (6.99)
176	2.49 (63.3)	.52 (13.2)	1.425 (36.20)	1.104 (28.04)	.275 (6.99)

ALL DIMENSIONS ARE IN INCHES (MM)

A Small, Flexible Alternative to LVDTs and Linear Potentiometers

SpaceAge Control, Inc. 661-273-3000 email@spaceagecontrol.com
38850 20th Street East, Palmdale, CA 93550 USA Fax: 661-273-4240 www.spaceagecontrol.com ISO

Linear displacement sensors (Space Age Control, Model 173)

Package Dimensions

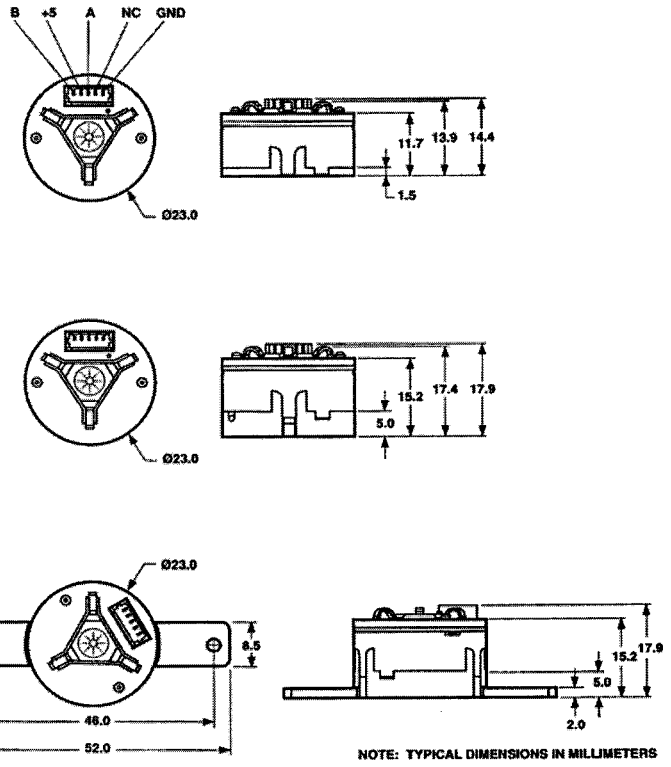

Output Waveforms

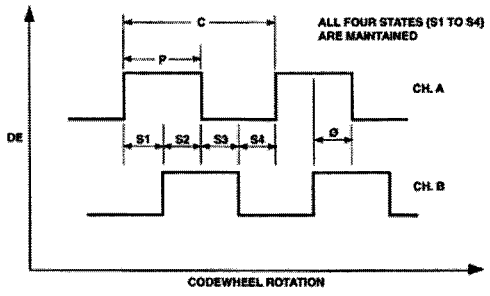

Direction of Motor Rotation

When the codewheel rotates in the clockwise direction (as viewed from the encoder end of the motor), channel A will lead channel B. If the codewheel rotates in the counterclockwise direction, channel B will lead channel A.

Optical rotation encoder (Agilent HEDR-5420)

Absolute Maximum Ratings

Storage Temperature	–40°C to +85°C
Operating Temperature	0°C to 85°C
Supply Voltage	–0.5 V to 7 V
Output Voltage	–0.5 V to V_{CC}
Output Current per Channel	–2.0 mA to 12 mA
Shaft Axial Play	±0.25 mm
Shaft Eccentricity Plus Radial Play	0.04 mm
Radial Play between Housing and Cover	0.2 mm – 0.5 mm
Distance between Tip of Codewheel Shaft and PC Board	0.4 mm – 0.5 mm
Distance between Codewheel and Stopper before Reset	0.25 mm – 0.35 mm
Distance between Codewheel and Stopper after Reset	0.75 mm
Concentricity Misalignment between Mounted Base Plate Center Bore and Motor Shaft	0.12 mm
Frequency	16 kHz

Electrical Characteristics
(Over recommended operating conditions. Typically at 25°C)

Parameter	Symbol	Min.	Typical	Max.	Units	Notes
Supply Current	I_{CC}		18	33	mA	
High Level Output Voltage	V_{OH}	2.4			V	I_{OH} = –2 mA min.
Low Level Output Voltage	V_{OL}			0.4	V	I_{OL} = 12 mA max.

Encoding Characteristics

Parameter	Symbol	Typical	Max.	Units
Pulse Width Error	ΔP	7	75	°e
State Width Error	ΔS	15	60	°e
Phase Error	Δϕ	15	60	°e
Position Error	Δϴ	50	120	arcmin
Cycle Error	ΔC	10	45	°e

Mechanical Characteristics

Parameter	Dimension	Tolerance	Units
Codewheel Fits these Standard Shaft Diameters			
Press Fit/Adhesive Mount Hub	2, 3, 4	+0/–0.01	mm
Set Screw Hub	2, 3, 4, 5, (1/8)	(+0/–0.0005)	(in.)
Allowable Motor Shaft Length			
Press Fit/Adhesive Mount Hub	Between 7.5 and 8.0		mm
Set Screw Hub (uses size M1.5 Allen wrench, not included)	Between 7.5 and 11.5		
Bolt Circle Diameter (2 holes)	16 to 20		mm
Mounting Screw Size	M2 M2.5, (2-56) for external mounting ears		mm (in.)

Electrical Interface
Pull up resistors on output pins 2, 3, and 5 have already been integrated into the mid-sized encoder. Each of the three encoder outputs can drive a single TTL load in this configuration.

Connectors
The connector to be used with the mid-sized encoder is Molex Part Number 51021-0500. This is a 5 connector crimp wire to board connector.

Pins configuration HEDR-542x series.

Pin 1	GND
Pin 2	NC
Pin 3	Ch.A
Pin 4	5 V
Pin 5	Ch.B

Optical rotation encoder (Agilent HEDR-5420) - continued

APPENDIX E LABVIEW CODE

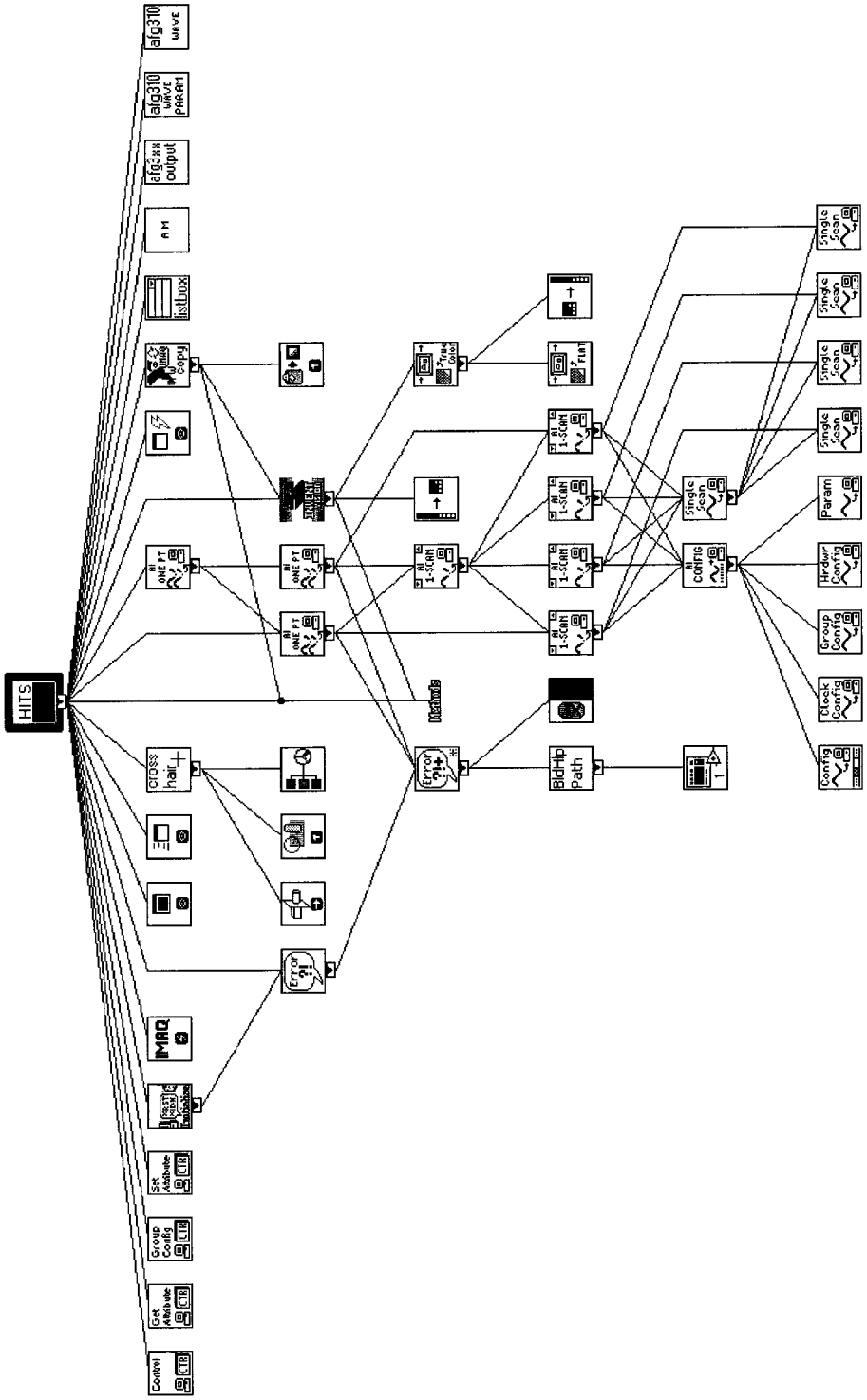

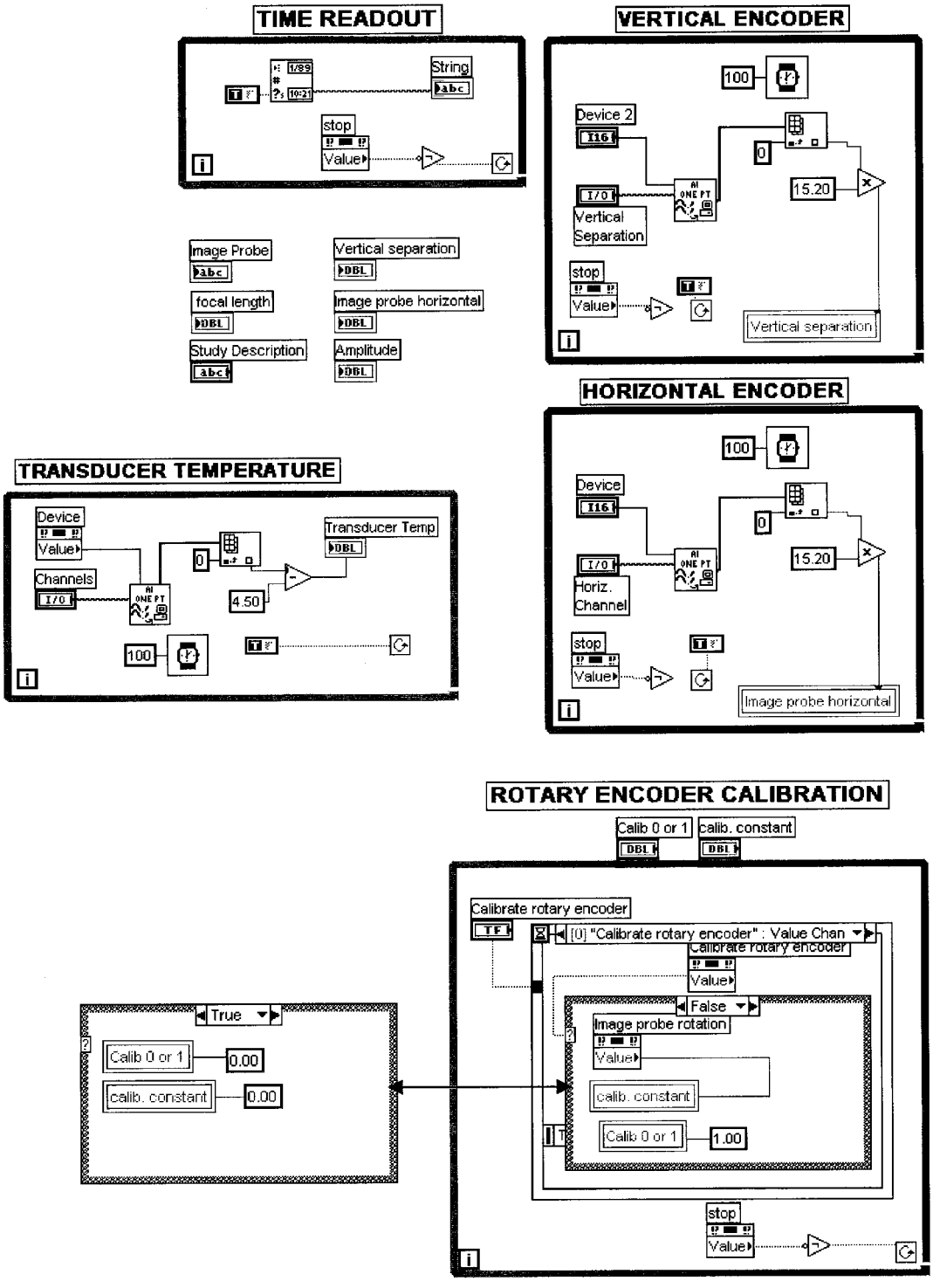
TIME READOUT
String
stop
Value
VERTICAL ENCODER
100
Device 2
I16
0
15.20
I/O
Vertical Separation
stop
Value
Vertical separation
Image Probe
Vertical separation
focal length
Image probe horizontal
Study Description
Amplitude
HORIZONTAL ENCODER
100
Device
I16
0
15.20
I/O
Horiz. Channel
stop
Value
Image probe horizontal
TRANSDUCER TEMPERATURE
Device
Value
Transducer Temp
Channels
I/O
0
4.50
100
ROTARY ENCODER CALIBRATION
Calib 0 or 1
calib. constant
Calibrate rotary encoder
[0] "Calibrate rotary encoder" : Value Chan
Value
False
Image probe rotation
Value
calib. constant
Calib 0 or 1
1.00
stop
Value
True
Calib 0 or 1
0.00
calib. constant
0.00

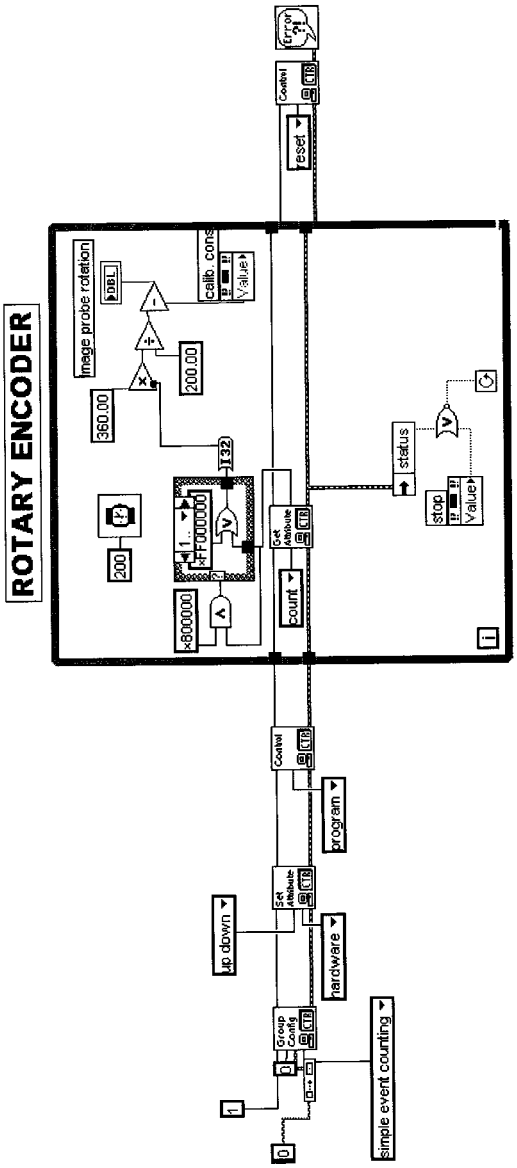
ROTARY ENCODER
image probe rotation
calib. cons
Value
200.00
360.00
I32
200
x800000
x7F000000
count
status
stop
Value
error
Control
reset
Control
program
up down
hardware
Simple event counting
1
0

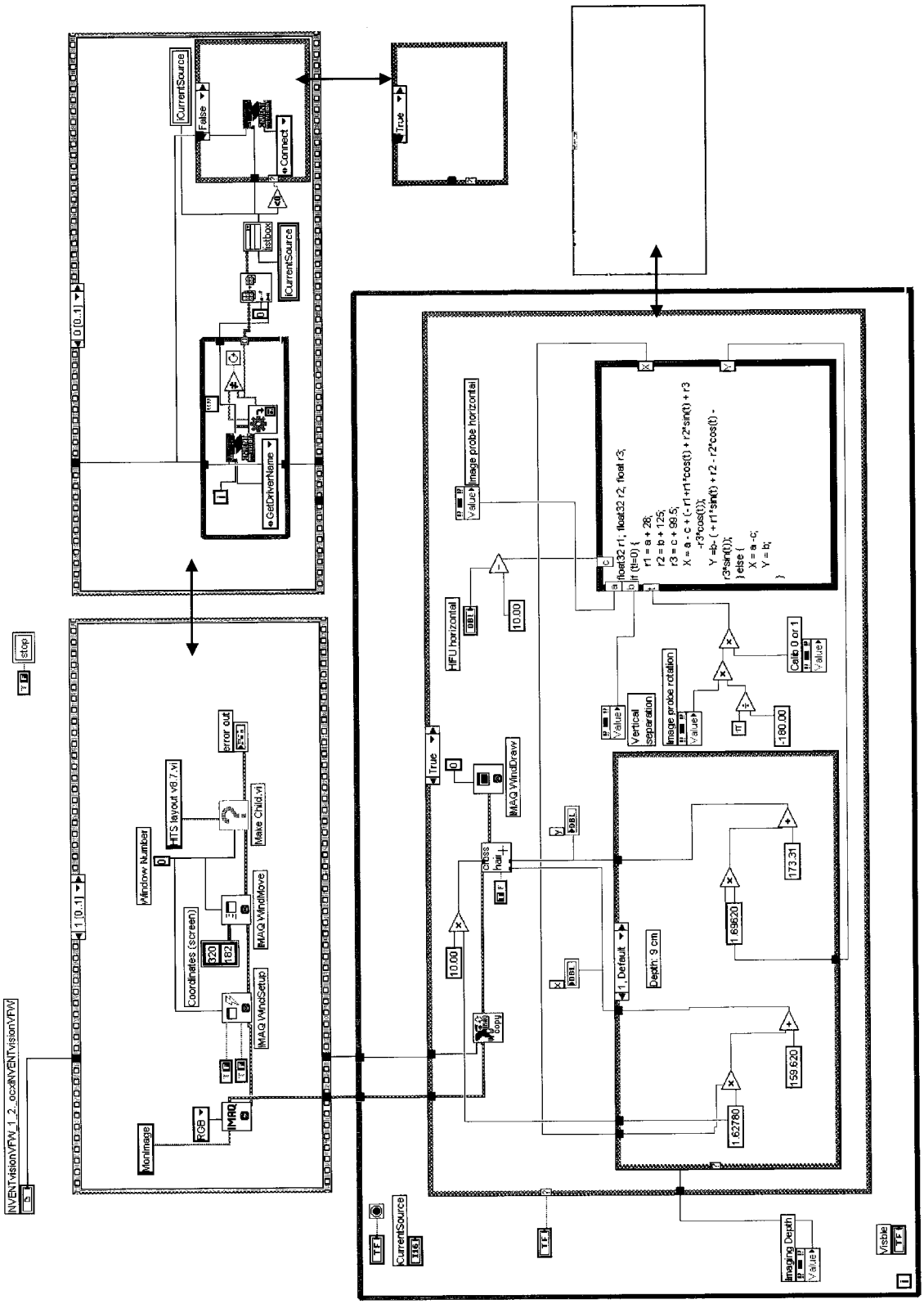
NIVENTvisionVFW_1_2_ocxINVENTvisionVFW
stop
Minimage
RGB
IMAQ
Coordinates (screen)
320
182
Window Number
HTS layout v9.7.vi
error out
Make Child.vi
IMAQ WindMove
IMAQ WindSetup
1 [0..1]
0 [0..1]
CurrentSource
False
Connect
listbox
GetDriverName
True
HFU horizontal
10.00
Image probe horizontal
Vertical separation
Image probe rotation
Calib 0 or 1
-180.00
IMAQ WindDraw
Cross hair
Copy
1, Default
Depth: 9 cm
1.62780
159.620
1.69620
173.31
Imaging Depth
Visible
float32 r1, float32 r2, float r3;
if (tt=0) {
r1 = a + 28;
r2 = b + 125;
r3 = c + 99.5;
X = a - c + (- r1 +r1*cos(t) + r2*sin(t) + r3
-r3*cos(t));
Y =b- (+r1*sin(t) + r2 - r2*cos(t) -
r3*sin(t));
} else {
X = a -c;
Y = b;
}

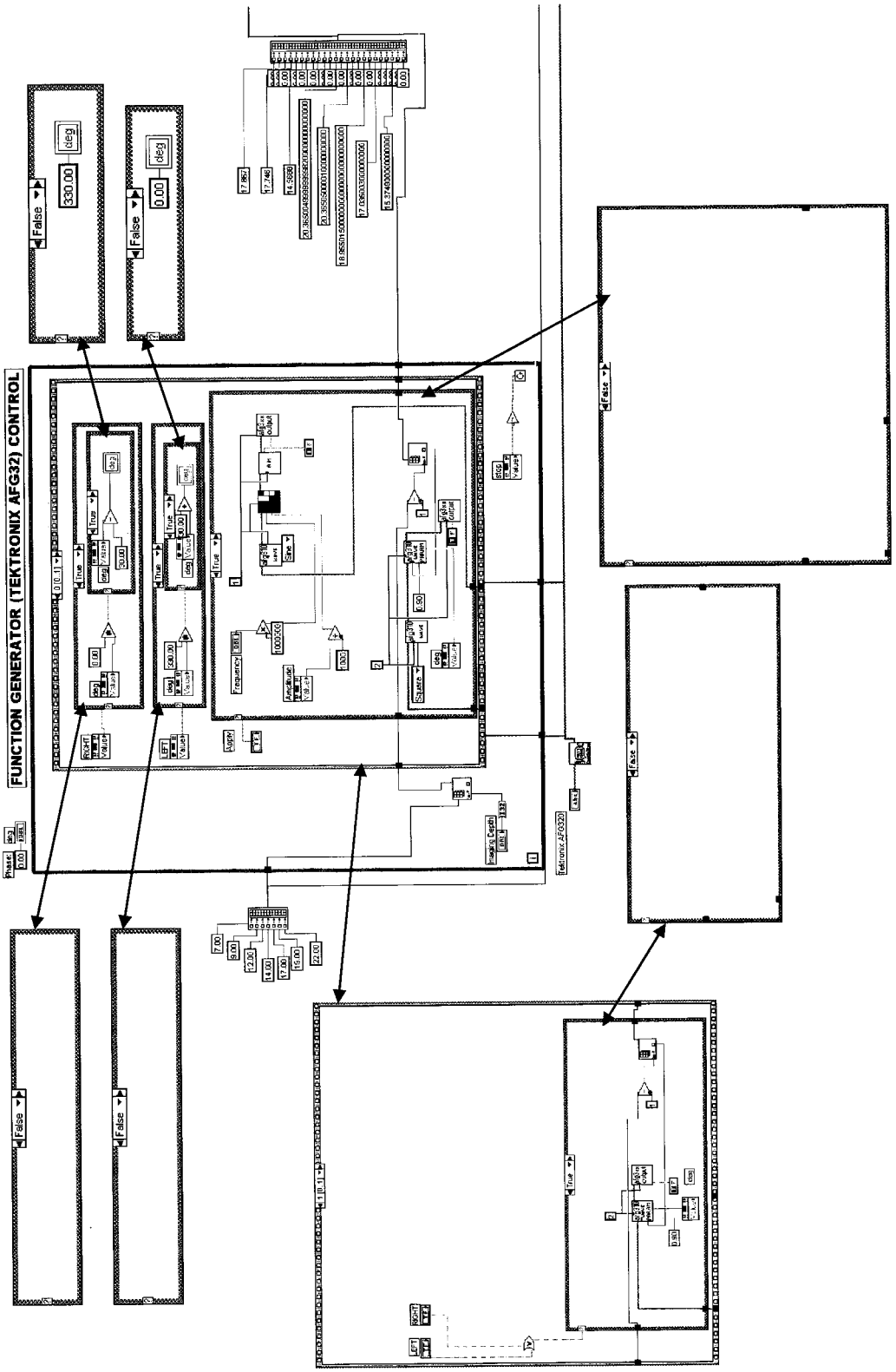
FUNCTION GENERATOR (TEKTRONIX AFG32) CONTROL
False
deg
330.00
0.00
Frequency
Amplitude
Square
Tektronix AFG320

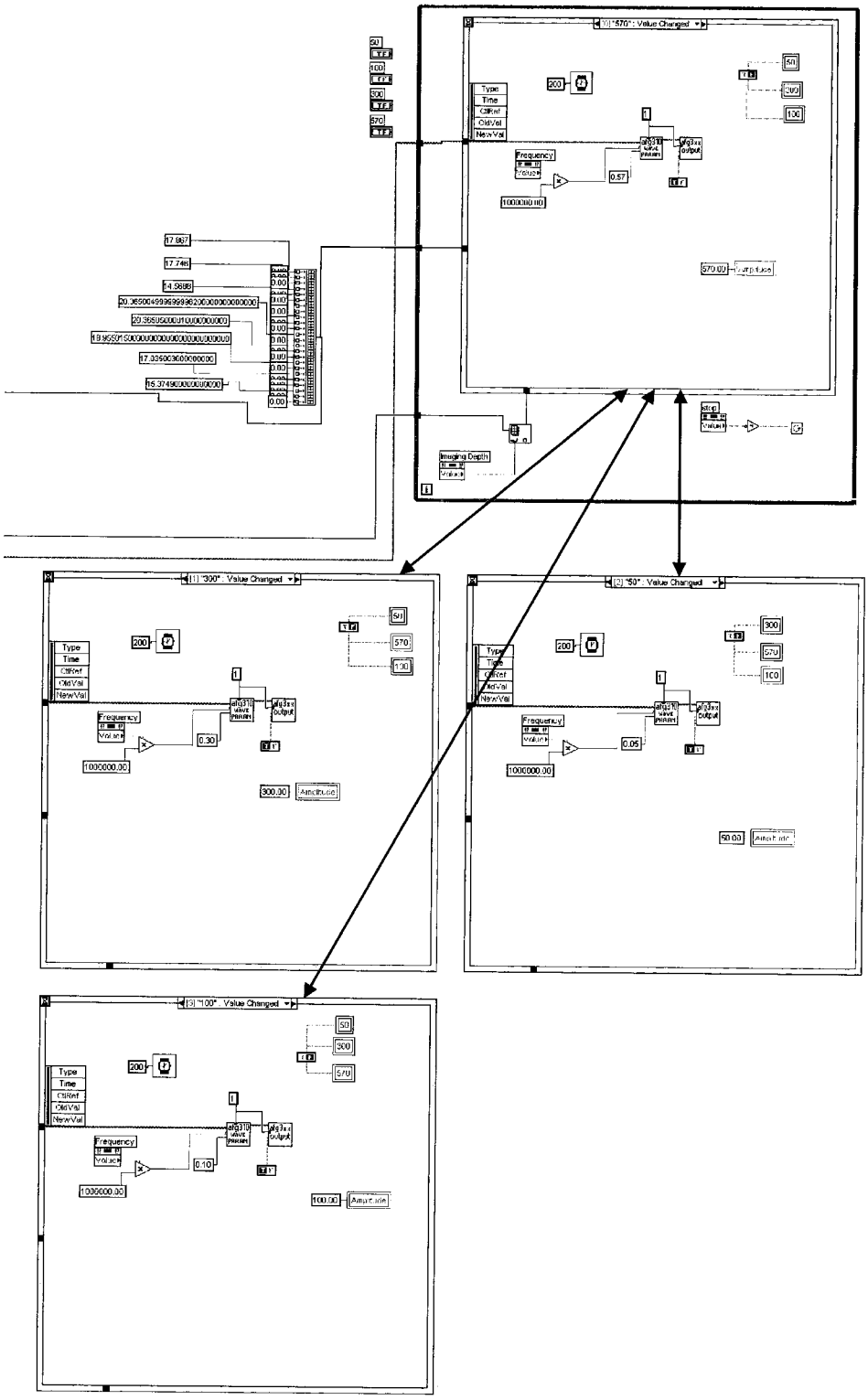
[0] "570" : Value Changed
[1] "300" : Value Changed
[2] "50" : Value Changed
[3] "100" : Value Changed
Type
Time
CtlRef
OldVal
NewVal
Frequency
Value
Imaging Depth
Value
Amplitude
570.00
300.00
50.00
100.00
1000000.00
0.57
0.30
0.05
0.10

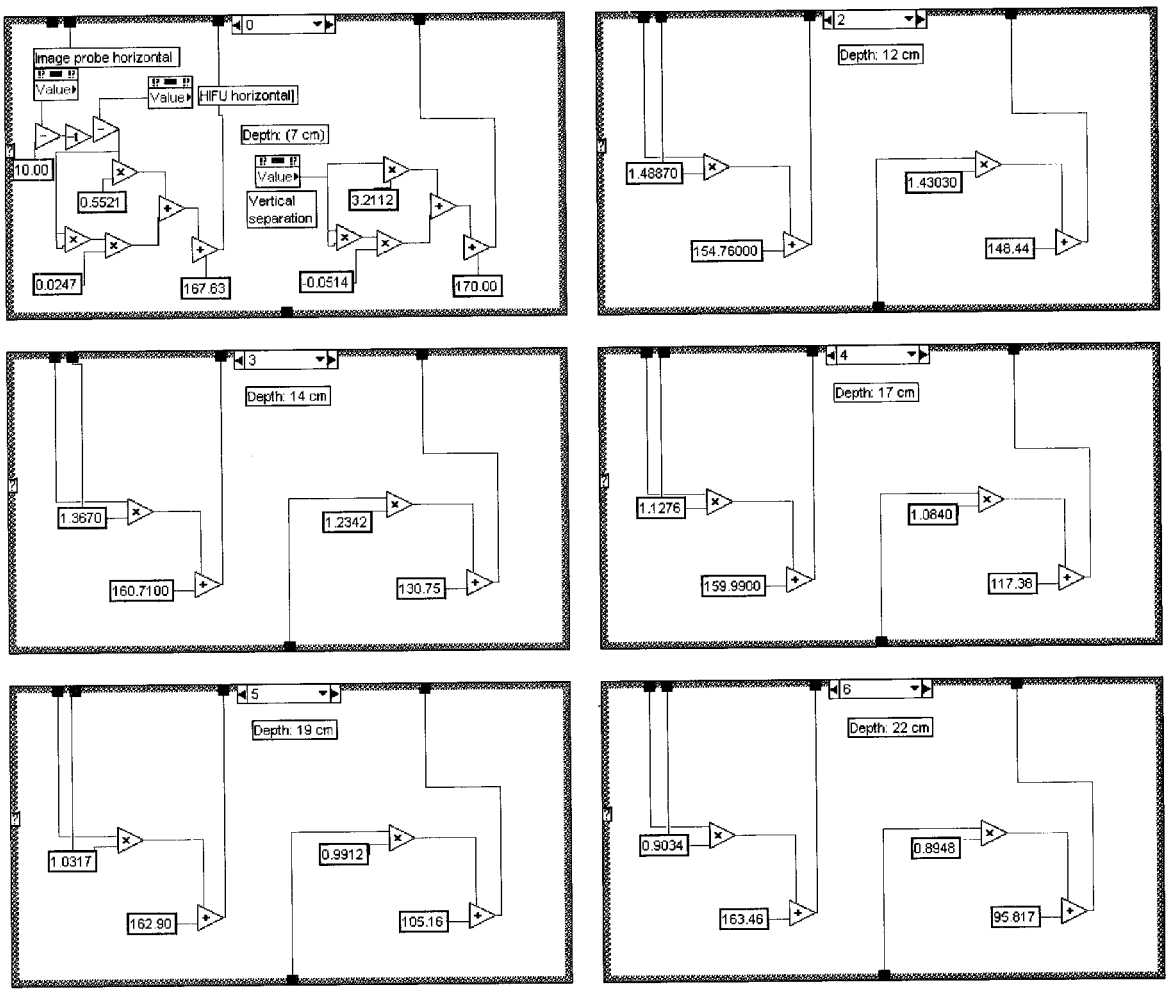
0
Image probe horizontal
Value
Value
HIFU horizontal
Depth: (7 cm)
Value
Vertical separation
10.00
0.5521
3.2112
0.0247
167.63
-0.0514
170.00
2
Depth: 12 cm
1.48870
1.43030
154.76000
146.44
3
Depth: 14 cm
1.3670
1.2342
160.7100
130.75
4
Depth: 17 cm
1.1276
1.0840
159.9900
117.36
5
Depth: 19 cm
1.0317
0.9912
162.90
105.16
6
Depth: 22 cm
0.9034
0.8948
163.46
95.817

List of programmed variables

Imaging Depth – the depth setting on the SonoSite ultrasound machine

Study Description – allows the user to type in the name of the experiment

HIFU horizontal – the horizontal setting of the HIFU transducer

stop – If "True", will terminate the targeting program

Visble – If "True" will show the visual target superimposed on the ultrasound image

AcqPic – If "True" will capture the ultrasound image from the SonoSite

Frequency – the operating frequency of the HIFU transducer

Apply – activates the changes made to the HIFU operating parameters

LEFT – moves the spatially stable HIFU interference bands on the ultrasound image to the left by adjusting the HIFU wave phase

RIGHT – moves the spatially stable HIFU interference bands on the ultrasound image to the right by adjusting the HIFU wave phase

Horiz. Channel (abc) Channel: defines the data acquisition (DAQ) board channel that reads from the horizontal position encoder

Vertical Separation (abc) Channel: defines the data acquisition (DAQ) board channel that reads from the horizontal position encoder

Device (I16) Device: The device number assigned to the DAQ board during configuration.

50 – sets the function generator amplitude to 50 mV-pp

100 – sets the function generator amplitude to 100 mV-pp

300 – sets the function generator amplitude to 300 mV-pp

570 – sets the function generator amplitude to 570 mV-pp

Calib 0 or 1 – activates (1) or deactivates (0) rotation encoder position sensing

Calibrate rotary encoder – If "true", begin rotary encoder calibration routine

Image Probe – allows user to enter the make and model of the image probe

focal length – the distance to the HIFU focus from the HIFU transducer

Image probe horizontal – the horizontal position sensor reading

Vertical separation – the vertical position sensor reading

Image probe rotation – the rotation encoder reading

Amplitude – the function generator amplitude setting

Transducer Temp – the temperature acquired by the HIFU transducer's internal thermocouple

error out error out is a cluster that describes the error status after the VI executes.

x – the position of the visual target, in pixels, on the screen

y – the position of the visual target, in pixels, on the screen

List of LabVIEW built-in subroutines used

Crosshair.vi
C:\HITS\Drivers\Custom Made\Crosshair.vi

Methods - SHELLdrvINVENTvisionVFW.ctl
C:\HITS\inventvisionVFW\LV6_0\Methods - SHELLdrvINVENTvisionVFW.ctl

ListBoxSelect.vi
C:\HITS\inventvisionVFW\LV6_0\ListBoxSelect.vi

IMAQ WindDraw
C:\Program Files\National Instruments\LabVIEW 6.1\vi.lib\Vision\Display1.llb\IMAQ WindDraw

AI Sample Channels.vi
C:\Program Files\National Instruments\LabVIEW 6.1\vi.lib\daq\1easyio.llb\AI Sample Channels.vi

AI Sample Channels (scaled array).vi
C:\Program Files\National Instruments\LabVIEW 6.1\vi.lib\DAQ\1easyio.llb\AI Sample Channels (scaled array).vi

TKAFG3xx Initialize.vi
C:\HITS\Drivers\afg3xx.llb\TKAFG3xx Initialize.vi

TKAFG3xx Waveform type.vi
C:\HITS\Drivers\afg3xx.llb\TKAFG3xx Waveform type.vi

TKAFG3xx Waveform parameters.vi
C:\HITS\Drivers\afg3xx.llb\TKAFG3xx Waveform parameters.vi

TKAFG3xx AM modulation.vi
C:\HITS\Drivers\afg3xx.llb\TKAFG3xx AM modulation.vi

TKAFG3xx Output.vi
C:\HITS\Drivers\afg3xx.llb\TKAFG3xx Output.vi

Simple Error Handler.vi
C:\Program Files\National Instruments\LabVIEW 6.1\vi.lib\Utility\error.llb\Simple Error Handler.vi

Counter Control.vi
C:\Program Files\National Instruments\LabVIEW 6.1\vi.lib\DAQ\zadvdctr.llb\Counter Control.vi

Counter Get Attribute.vi
C:\Program Files\National Instruments\LabVIEW 6.1\vi.lib\DAQ\zadvdctr.llb\Counter Get Attribute.vi

Counter Set Attribute.vi
C:\Program Files\National Instruments\LabVIEW 6.1\vi.lib\DAQ\zadvdctr.llb\Counter Set Attribute.vi

Counter Group Config.vi
C:\Program Files\National Instruments\LabVIEW 6.1\vi.lib\DAQ\zadvdctr.llb\Counter Group Config.vi

_SHELLdrvINVENTvisionVFW_1_2.vi
C:\HITS\inventvisionVFW\LV6_0_SHELLdrvINVENTvisionVFW_1_2.vi

INVENTvisionVFWcopy.vi
C:\HITS\inventvisionVFW\IMAQexamples\INVENTvisionIMAQexample_1_2_Clipboard_Method.llb\INVENTvisionVFWcopy.vi

IMAQ Create
C:\Program Files\National Instruments\LabVIEW 6.1\vi.lib\Vision\Basics.llb\IMAQ Create

IMAQ WindMove
C:\Program Files\National Instruments\LabVIEW 6.1\vi.lib\vision\Display1.llb\IMAQ WindMove

IMAQ WindSetup
C:\Program Files\National Instruments\LabVIEW 6.1\vi.lib\Vision\Displays.llb\IMAQ WindSetup

APPENDIX F DESIGN DRAWINGS

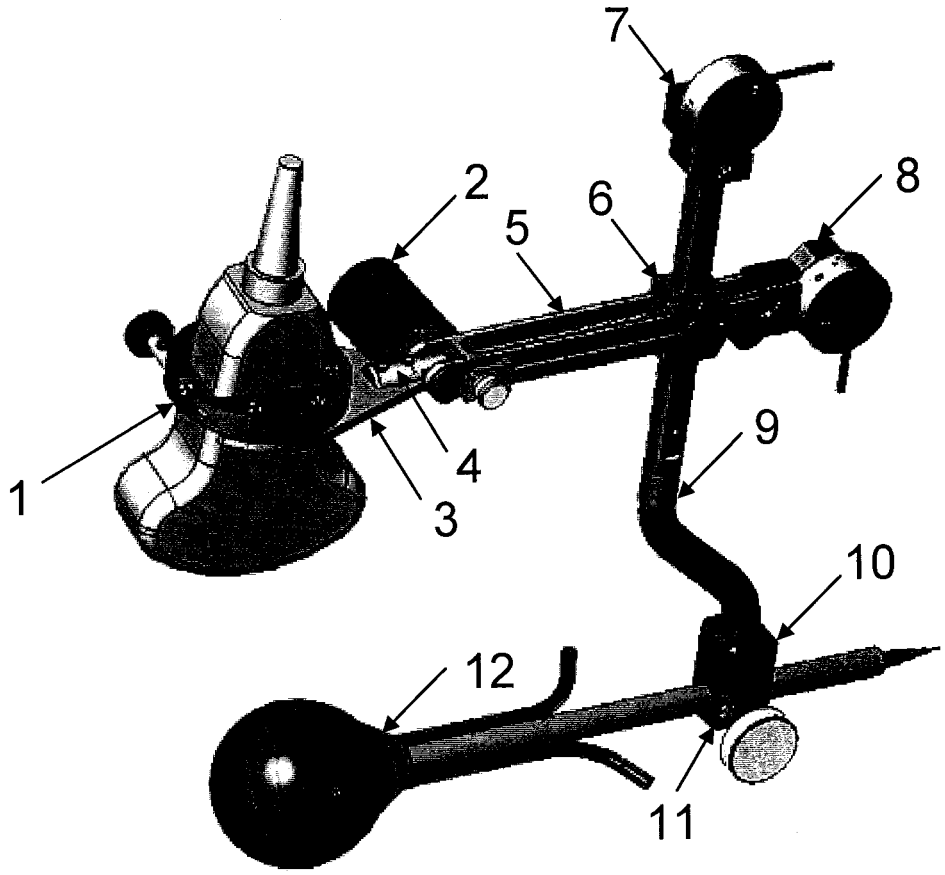

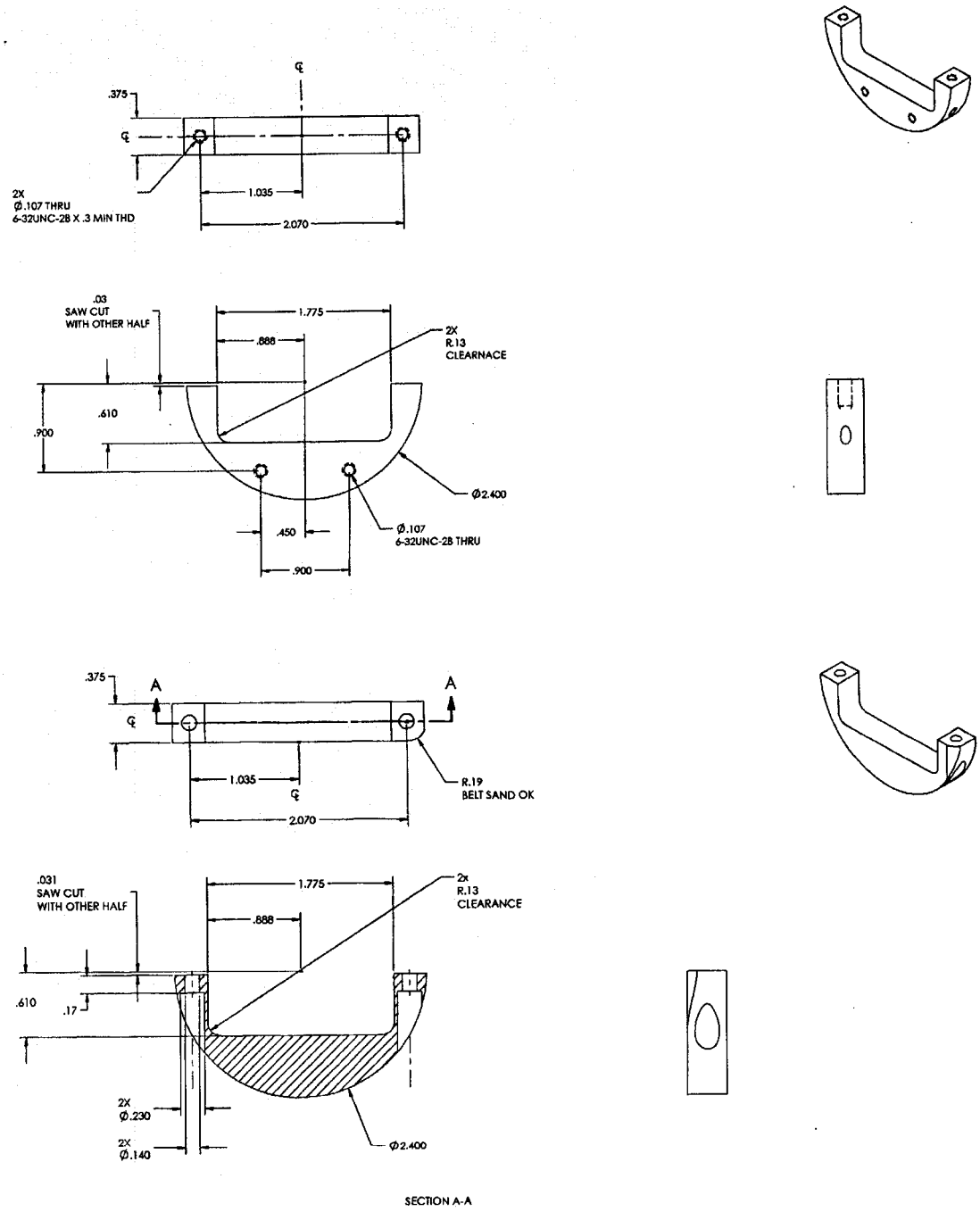

1. Image probe locking bracket

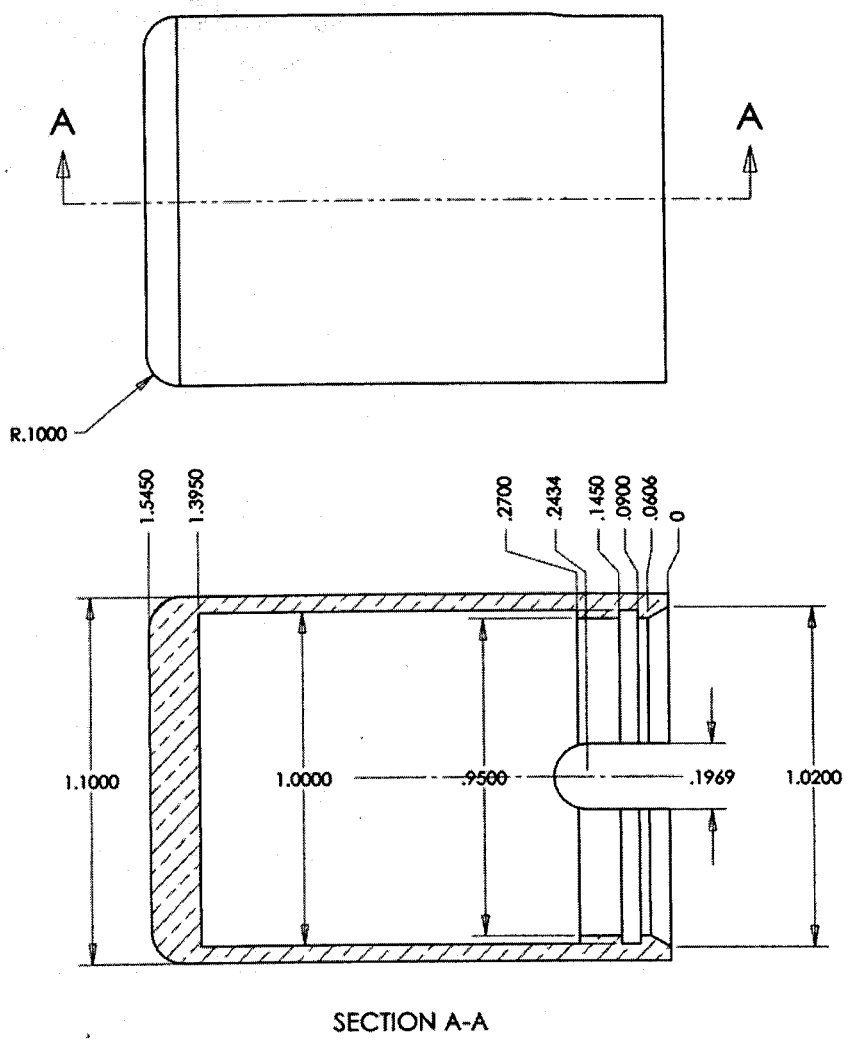

2. Rotation encoder cap

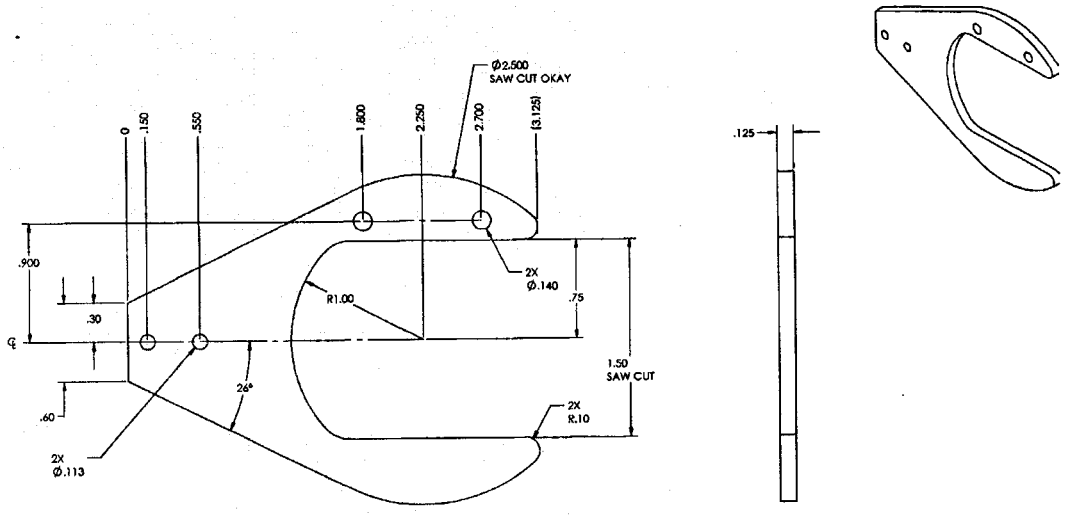

3. Image probe mounting plate

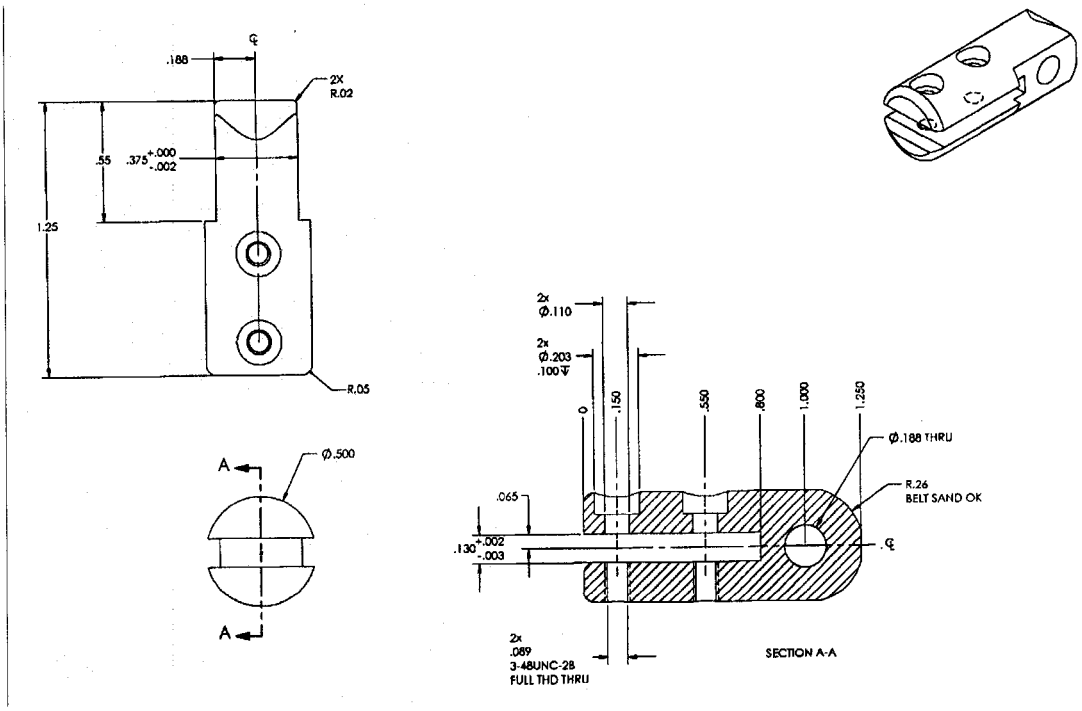

4. Mounting plate joint

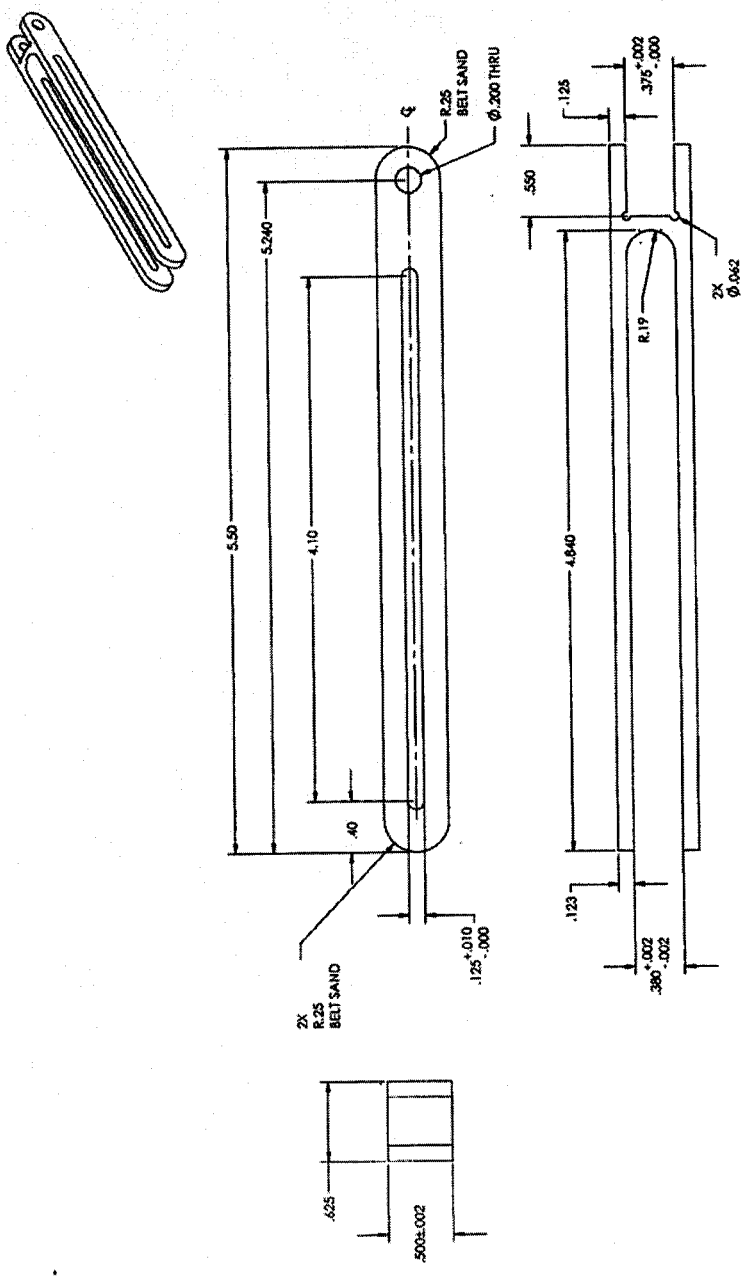

5. Horizontal rod

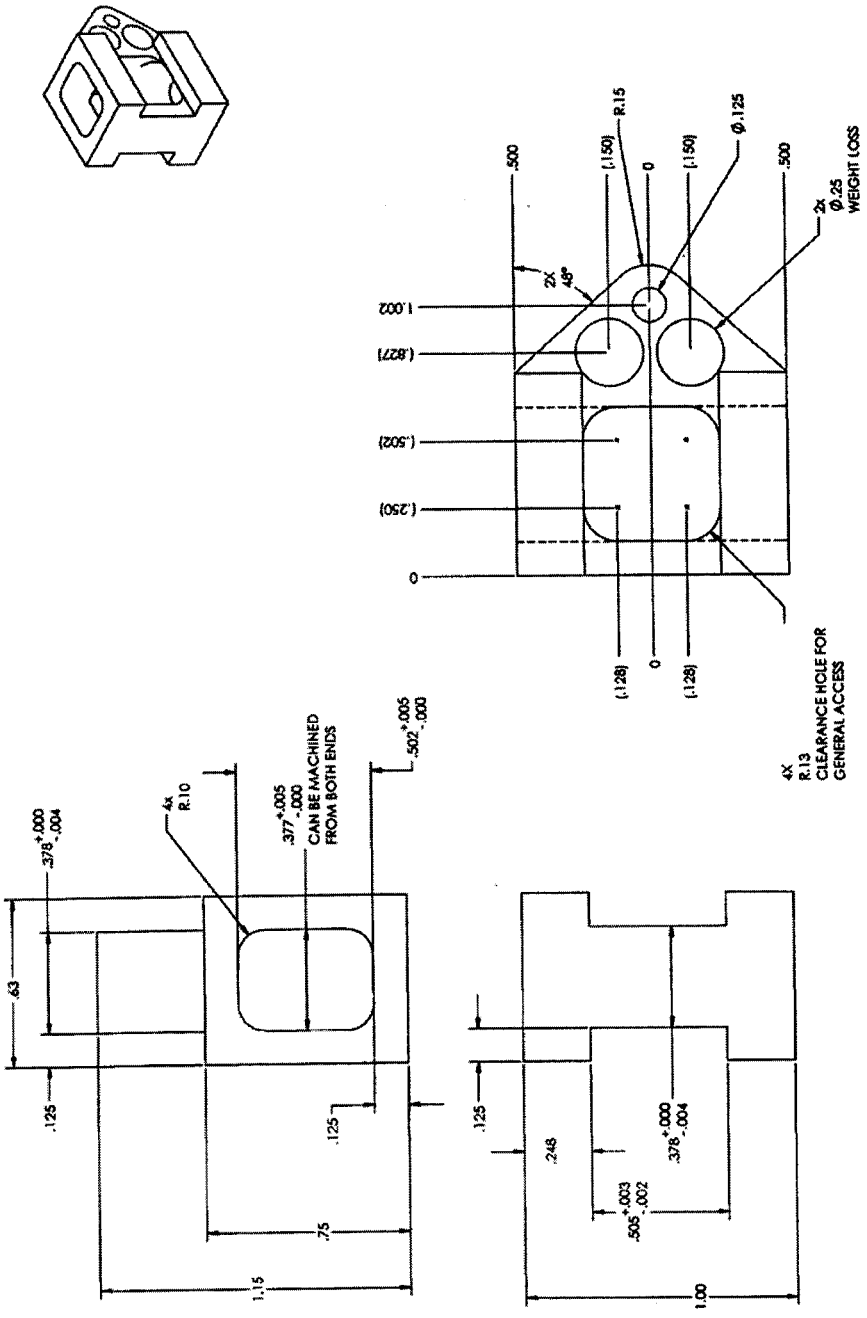

6. Center bracket

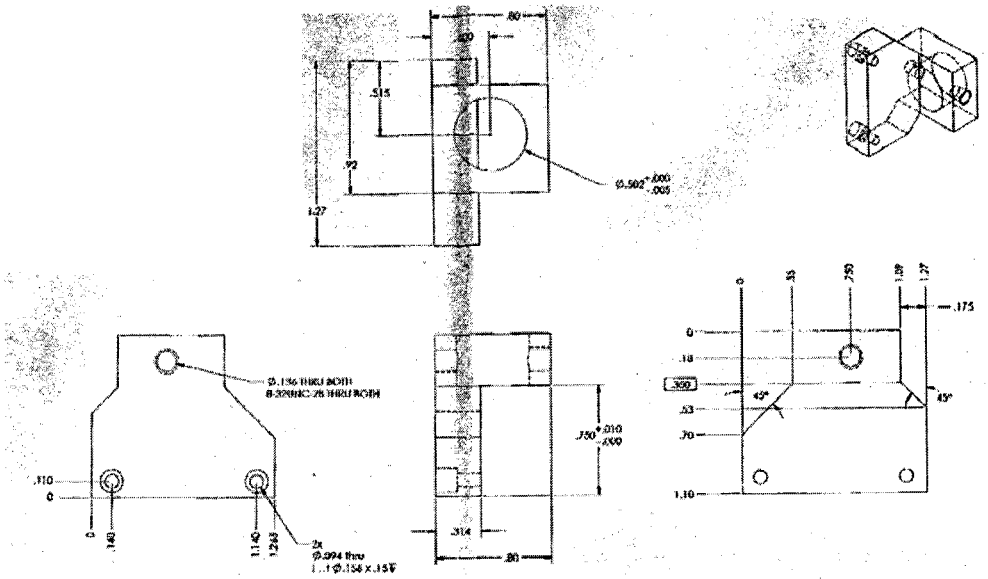

7. Vertical displacement sensor mount

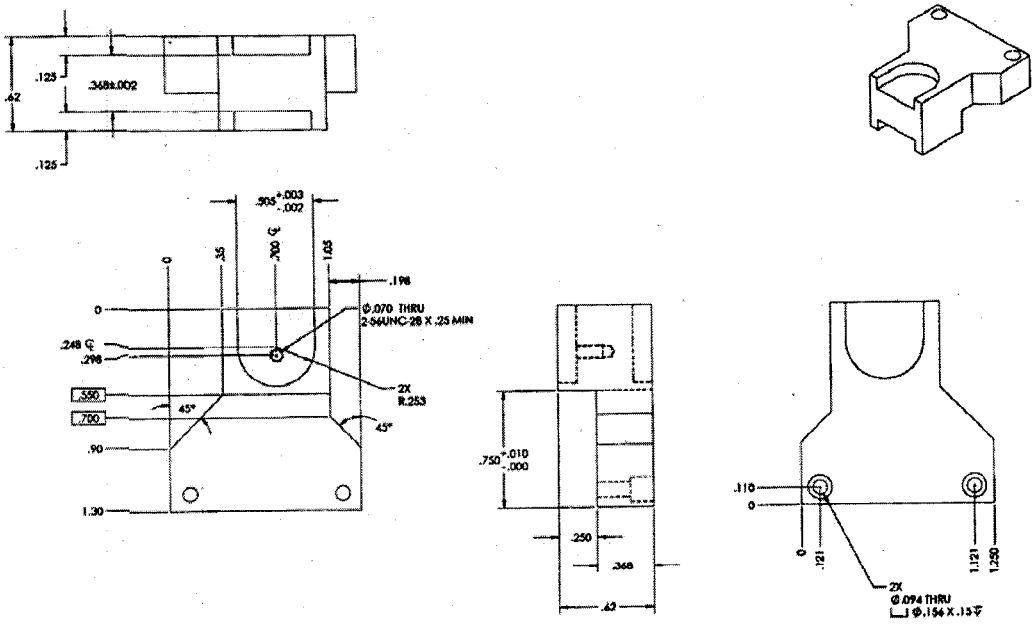

8. Horizontal displacement sensor mount

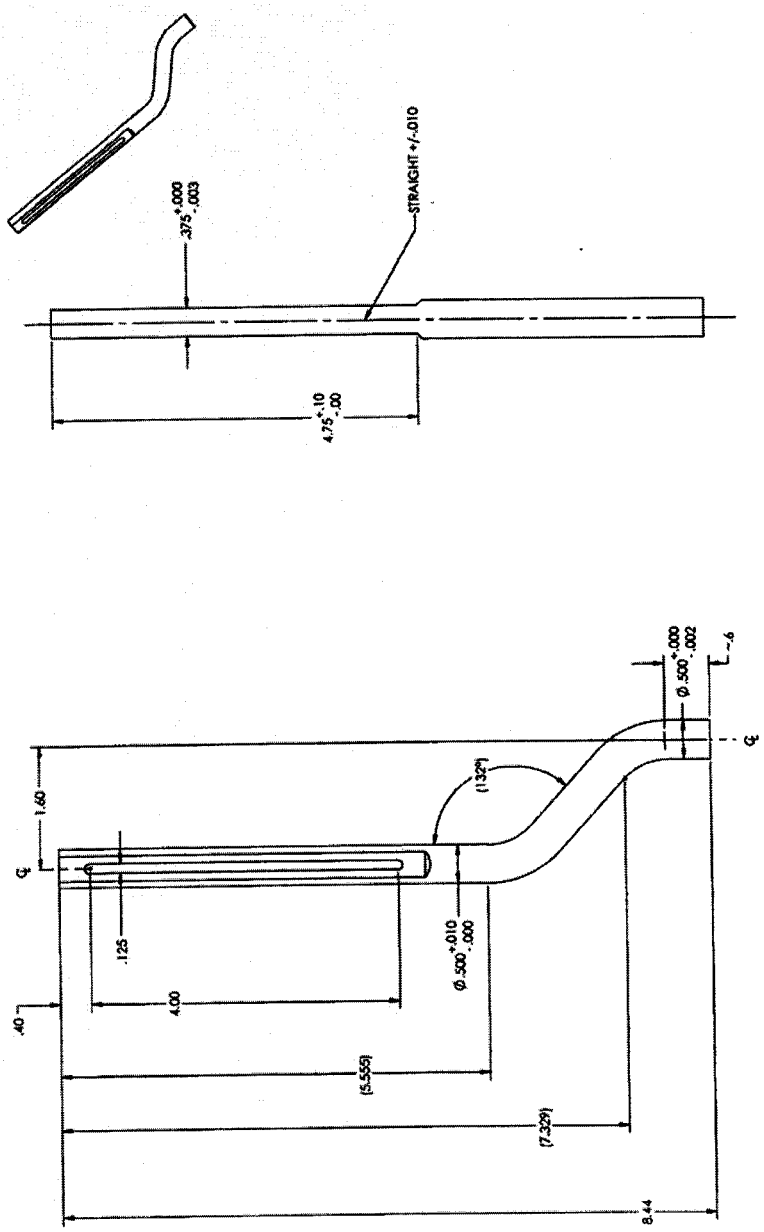

9. Vertical rod

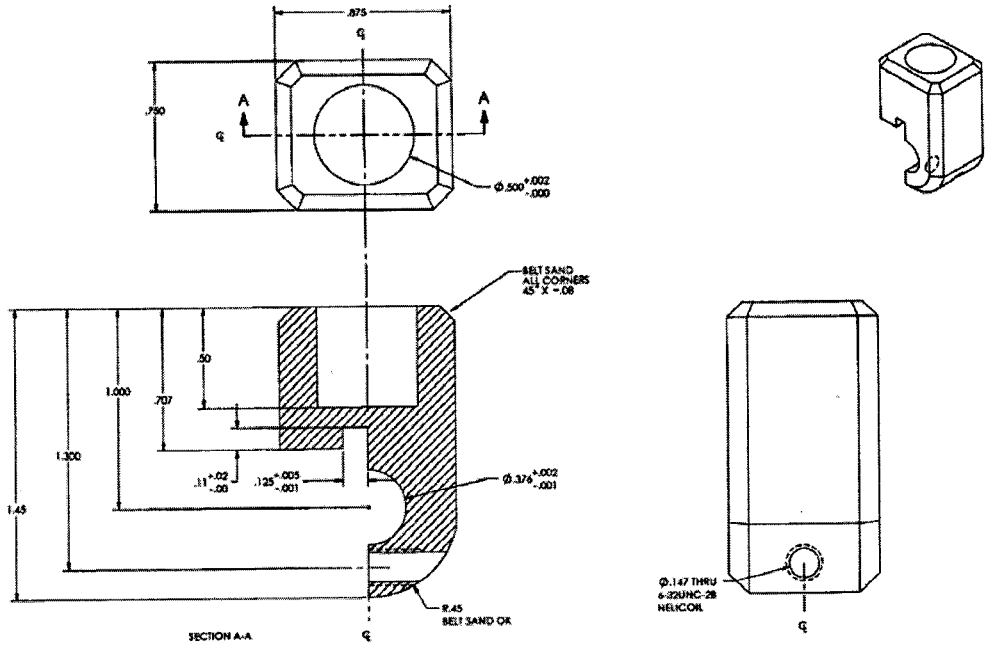

10. HIFU transducer bracket (1)

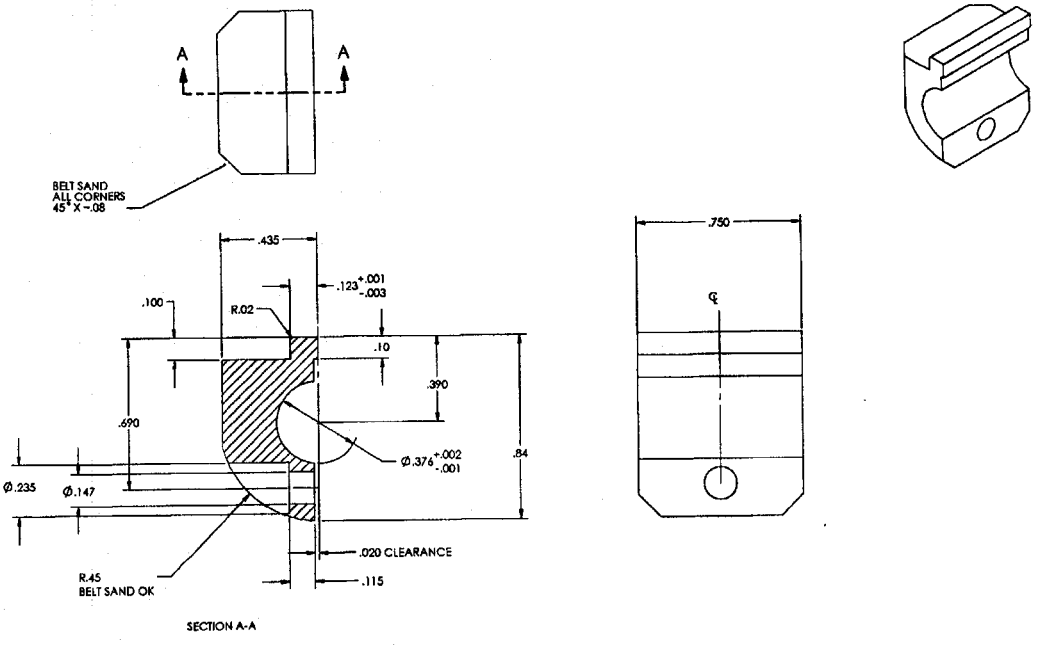

11. HIFU transducer bracket (2)

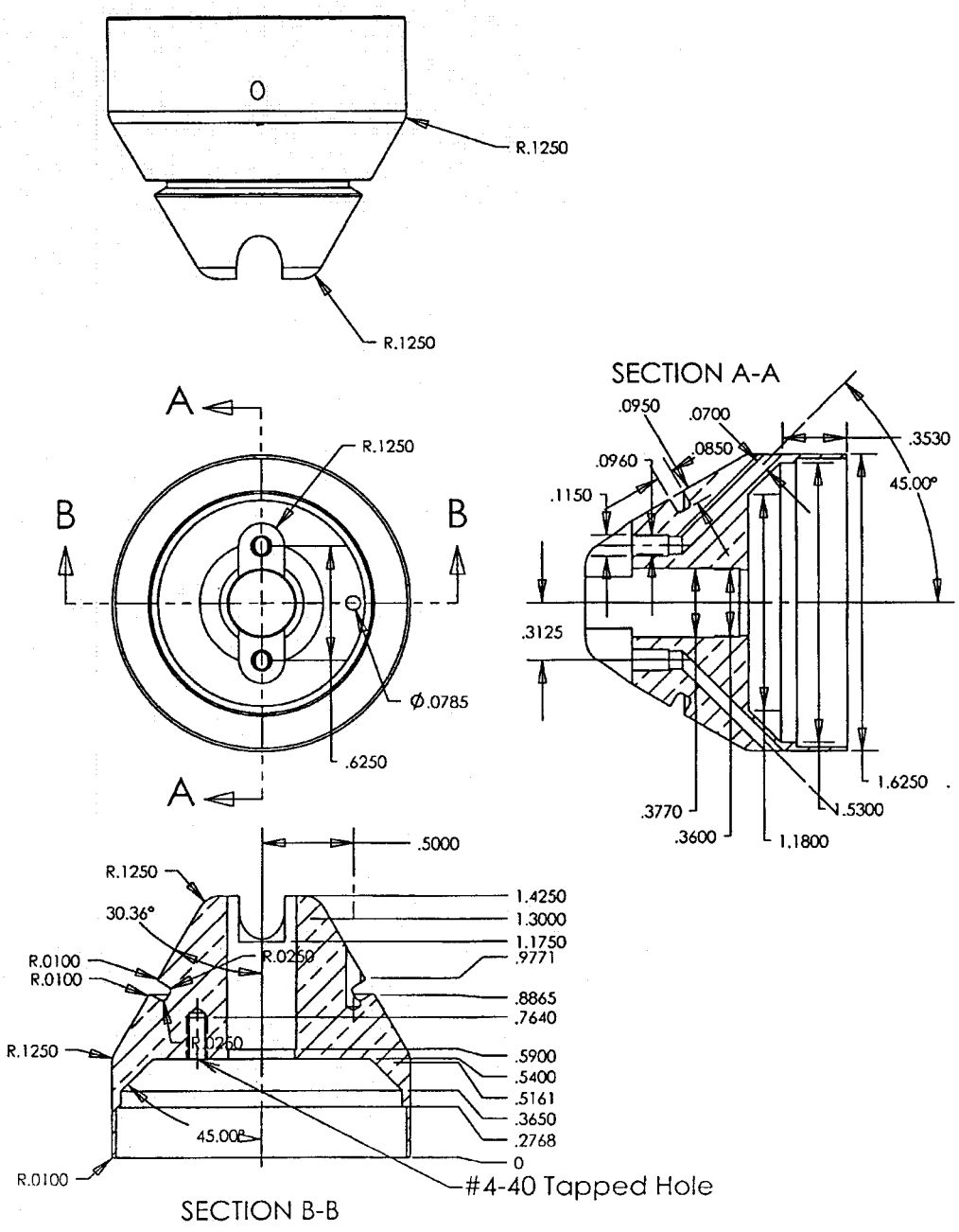

12. HIFU transducer brass housing

Vita

ARTHUR H. CHAN

ahchan@u.washington.edu

University of Washington Bioengineering Ph.D., graduation June 2003
Certificate in Technology Entrepreneurship from University of Washington MBA Program

Expertise in ultrasound device modeling, design, fabrication, and testing
Exceptional time management, organization, marketing abilities and leadership
Strong entrepreneurial sense with technical aptitude, project management and presentation skills

Seeking challenging position in a medical device company with leadership and business development role combined with engineering responsibilities, working in a team-environment.

EMPLOYMENT HISTORY

06.03 - Clinical Applications Development Engineer
InSightec, Dallas, TX

- Engineering and business development to company specializing in MRI guided focused ultrasound surgery
- Conduct clinical trials, educate patients and doctors
- Project management and marketing of novel medical device and treatment
- Work closely with the FDA

06.02 – 10.02 WRF Capital / Gates Technology Fellow
Center for Technology Entrepreneurship
University of Washington, Seattle WA

- Evaluated University technology for commercialization potential
- Led new biotechnology venture creation, formulate and present business plans
- Mentored Singapore entrepreneurship students, team won business plan competition

12.01 – 06.02 Product Development / Acoustics Engineer
EKOS Corporation, Bothell WA

- Aided in the design and development of an ultrasonic device for thrombolysis
- Led thermodilution study, performed acoustic and device performance testing
- Taught acoustic theory, developed simulation software, project management

01.98 – 09.98 Optimization and Operations Engineer
05.97 – 09.97 British Petroleum, PLC (Amoco Canada Petroleum Company Ltd.), Calgary, AB Canada

- Implemented new steam injection strategy for increase oil recovery
- Studied steam quality and distribution, designed and tested optimization methods

05.96 – 12.96 Pipeline Design Engineer
Canadian Utilities (Northwestern Utilities Ltd.), Edmonton, AB, Canada

- Optimized preparation of work procedures, design drawings and work orders
- Supervised operations and construction of new gas pipeline installations

EDUCATION

09.99 – present University of Washington (GPA 3.7 / 4.0)
Ph.D. in Bioengineering
Thesis: Image-guided high-intensity focused ultrasound treatment of leiomyoma
Technology in Entrepreneurship Certificate (Business school)

09.94 – 09.99 University of Alberta (GPA 3.8 / 4.0)
B.Sc. Mechanical Engineering, Co-op program, With distinction

RESEARCH EXPERIENCE

Doctoral
09.99 – 06.03 Department of Bioengineering, University of Washington
Advisor: Shahram Vaezy, Ph.D.

- Design, construct, characterize image-guided therapeutic ultrasound device for uterine fibroids treatment
- Conduct acoustic measurements, ergonomic, in vitro and in vivo experiments
- Integrate, develop and validate medical device hardware and software

Undergraduate
01.99 – 09.99 Biomedical Engineering, University of Alberta
Advisor: Brian Andrews, Ph.D.

- Develop improved orthosis: spinal motion to aid paraplegic walking
- Performed human gait analysis to test device and validate model

Undergraduate
09.96 – 12.98 Mechanical Engineering, University of Alberta
Advisor: Gary Faulkner, Ph.D.

- Studied craniofacial implant mobility using the Periotest dental tool
- Designed and tested an active-eye prosthesis using smart memory alloys

ACTIVITIES

- Mentoring bioengineering undergraduate students
- Executive of curriculum committee, science and engineering business association, student advisory board
- Past-president of Bioengineering Students' Association and BioMedical Engineering Society (BMES)
- Board member: Life Enrichment Foundation, providing disabled people athletic opportunities
- Special Olympics coach: skiing and track and field
- Presented science and engineering to schools through Set-Up, Gear-Up, APEGGA outreach programs
- Co-founder and PR director of University of Alberta's first Solar Vehicle Project
- Assistant director of sponsorship for the Canadian Congress of Engineering Students

AWARDS

- WRF Capital / Gates Technology summer fellowship to aid in new venture creation
- Research awards from department of Bioengineering and American Society of Reproductive Medicine
- Natural Sciences and Engineeering Research Council of Canada fellowship
- Arnold Edinborough Scholarship, International Scholarship Foundation
- Valedictorian, Mechanical Engineering class of 1999, University of Alberta
- Awarded 4 leadership scholarships and 3 academic scholarships from University of Alberta
- Awarded Faculty of Engineering Dean's Research Award from University of Alberta
- Two patents pending from Ph.D. thesis work

ARTICLES PUBLISHED IN REFEREED JOURNALS

Chan,A.H., Fujimoto,V.Y., Moore,D.E., Held,R.T., Paun,M., Starr,F.R., Vaezy,S., Image-guided transvaginal focused ultrasound therapy: in vivo safety and potential for leiomyoma treatment, Submitted to Medical Physics, May 2003

Chan,A.H., Fujimoto,V.Y., Moore,D.E., Martin,R.W., Vaezy,S., Image-guided high intensity focused ultrasound device for uterus treatment. Medical Physics Nov 2002;29(11): 2611-20

Faulkner, M.G., Wolfaardt, J.F., and Chan, A., Measuring abutment/implant joint integrity with the Periotest instrument. International Journal of Oral and Maxillofacial Implants Sep-Oct;14(5):681-8 (undergraduate work)

OTHER REFEREED CONTRIBUTIONS

Chan,A.H., Vaezy,S., Crum,L.A., High Intensity Focused Ultrasound. McGraw Hill Yearbook of Science and Technology, 2003.

CONFERENCE PROCEEDINGS

Chan,A.H., Held,R.T., Fujimoto,V.Y., Moore,D.E., Paun,M., Vaezy,S., Safety and efficacy of transvaginal image-guided focused ultrasound therapy for uterus treatment, World Federation for Ultrasound in Medicine and Biology and American Institute of Ultrasound in Medicine, joint conference, Montreal, PQ (6/03) *Nominated for new investigator award*

Chan,A.H., Vaezy,S., Moore,D.E., Huynh,G., Paun,M., Fujimoto,V.Y., Image-Guided High Intensity Focused Ultrasound: Potential for Minimally-Invasive Treatment of Uterine Fibroids, 58th annual meeting of the American Society of Reproductive Medicine, Seattle, WA (10/02) *Nominated for AIUM Prize Paper*

Chan,A.H., Huynh,G, Paun,M, Fujimoto,V.Y., Moore,D.E., Vaezy, S., Focused ultrasound therapy of the uterus: A device for potential treatment of leiomyoma, 2nd symposium of the International Society of Therapeutic Ultrasound, Seattle, WA (7/02)

Chan,A.H., Fujimoto,V.Y., Martin,R.W., Moore,D.E., Vaezy,S., An Image-Guided High Intensity Focused Ultrasound Device for Treating Uterine Fibroids, American Institute of Ultrasound in Medicine, Nashville, TN (7/02)

Chan,A.H., Vaezy,S., Martin,R.W., Keilman,G., Fujimoto,V.Y., Image-Guided HIFU device for Transvaginal Treatment of Fibroids, IEEE-UFFC, San Juan, Puerto Rico (10/00)

Chan,A.H., Vaezy,S., Martin,R.W., Keilman,G., Fujimoto,V.Y., Non-Invasive Therapy for Uterine Fibroids, BioMedical Engineering Society, Seattle, WA (9/00)

TECHNOLOGY TRANSFER

Pseudo-Fresnel lenses for Therapeutic Ultrasound Applications (UW IPTT 2031-3799)

Therapeutic Ultrasound for use in veterinary and agricultural application (UW IPTT 2031-3763)

Targeting system for ultrasound image-guided HIFU treatment (UW IPTT 2031-3886)

Graphite Embedded Epoxy Acoustic Impedance Matching Layer for Ultrasound Transducers (UW IPTT 2031-3764 USPTO Serial 60/411,687)

Image-guided High Transvaginal Intensity Focused Ultrasound Device for Uterine Fibroids, US Patent Pending (UW IPTT 2031-3714, USPTO Serial 60/381,183)